Growth of self-catalyzed GaAs nanowires using molecular-beam-epitaxy and structural characterization by *in-situ* X-ray diffraction

DISSERTATION

zur Erlangung des Grades eines Doktors

der Naturwissenschaften

vorgelegt von

Dipl.- Phys. Philipp E. Schroth

eingereicht bei der Naturwissenschaftlich-Technischen Fakultät

der Universität Siegen

Siegen 2016

Gutachter:
Prof. Dr. Ullrich Pietsch
Prof. Dr. Tilo Baumbach

Tag der mündlichen Prüfung:
26.09.2016

Gedruckt auf alterungsbeständigem holz- und säurefreiem Papier.

Zusammenfassung

In der vorliegenden Arbeit werden dynamische Prozesse während des epitaktischen Wachstums selbstkatalysierter GaAs-Nanodrähte mittels zeitaufgelöster Röntgenbeugung an Synchrotronstrahlungsquellen untersucht. Umfassendes Verständnis der grundlegenden Wachstumsprozesse ist Voraussetzung für eine optimale zukünftge Integration von GaAs-Nanodrähten in die complementary-metal-oxide-semiconductor Technologie u.a. als hocheffiziente vertikale Transistoren.

Zur Vorbereitung dieser Experimente werden Wachstumsstudien in einer auf *in-situ* Röntgenstudien spezialisierten, portablen Molekularstrahlepitaxie-Anlage durchgeführt. Das Ziel ist es, vertikale GaAs-Nanodrähte epitaktisch auf Silizium-Substraten herzustellen, und gleichzeitig das sogenannte parasitäre GaAs-Inselwachstum zu minimieren. Mittels *ex-situ* Rasterelektronenmikroskopie wird der Einfluss elementarer Wachstumsparameter wie Gallium- und Arsenflüsse, Substrattemperatur und Oberflächenpräparation auf das Wachstum der Nanodrähte sowie auf die flüssigen Galliumtropfen, welche als Katalysator eine zentrale Rolle im Nanodrahtwachstum wahrnehmen, untersucht.

Des Weiteren wird die Mikrostruktur dieser GaAs-Nanodrähte mit Röntgenbeugungsmethoden *ex-situ* untersucht. Aus Messungen einzelner Nanostrukturen mittels hochfokussierter Synchrotronstrahlung werden Unterschiede im Streusignal zwischen parasitären GaAs-Inseln und GaAs-Nanodrähten herausgestellt. Damit wird die Trennung der Beiträge von parasitischen GaAs-Inseln und GaAs-Nanodrähten in Ensemble-Röntgenmessungen ermöglicht und Einblicke in die Eigenschaften der unterschiedlichen Kristallphasen in den Nanodrähten gewährt.

Auf Grundlage dieser Erkenntnisse, wird mittels zeitaufgelöster *in-situ* Röntgenbeugung in symmetrischer Geometrie die Entwicklung des sogenannten Wurtzit-Zinkblende Polytypismus in selbst-katalysierten GaAs-Nanodrähten während des epitaktischen Wachstums verfolgt. Auf Basis eines statistischen Modells mit zeitabhängigen Übergangswahrscheinlichkeiten werden Einsichten in die Entwicklung der mittleren Segmentlänge sowie des Volumenanteils beider GaAs-Polytypen Wurtzit und Zinkblende gewonnen und Unterschiede in deren Nukleationsbarrieren abgeleitet.

Die Ausbildung von Kristallstruktur und Form von GaAs-Nanodrähten während des Wachstums wird mittels zeitaufgelöster Röntgenbeugung an phasenselektiven Bragg-Reflexionen untersucht. Dabei gelingt die Trennung radialer Wachstumsprozesse in katalytische und nichtkatalytische Beiträge. Dies ermöglicht erstmals den direkten Abgleich mit theoretischen Modellen des katalytischen radialen Wachstums in Abhängigkeit der Wachstumsparameter. Dadurch können Rückschlüsse auf die Entwicklung des flüssigen Galliumtropfens während des Wachstums getroffen werden.

Abstract

In the present thesis, dynamical processes during the epitaxial growth of self-catalyzed GaAs nanowires are investigated by means of time-resolved *in-situ* X-ray scattering methods at synchrotron radiation facilities. Comprehensive knowledge of their fundamental growth processes is pre-requisite for the optimized integration of GaAs nanowires into the complementary-metal-oxide-semiconductor technology, e.g. as highly efficient vertical transistors.

First, growth studies employing a portable molecular-beam-epitaxy system specially designed for *in-situ* X-ray investigations are carried out. The aim is to epitaxially grow vertical GaAs nanowires onto silicon substrates with minimal parasitic GaAs island growth. Employing *ex-situ* scanning-electron-microscopy, the effect of the growth parameters on the growth and the properties of GaAs nanowires, as well as the liquid Ga-droplet is investigated. The growth parameters are comprised of the material fluxes of Ga and As, the substrate temperature as well as surface-oxide preparation.

Further, the microstructure of GaAs nanowires is investigated by means of *ex-situ* X-ray scattering methods. Employing highly focused X-ray radiation, the difference of the scattering signals from individual GaAs nanowires and parasitic GaAs islands is demonstrated. This allows the separation of the contributions of parasitic GaAs islands and GaAs nanowires in X-ray measurements averaging over a statistical ensemble of nanostructures and gives insight into the crystallographic properties of the nanowires.

On this basis, the evolution of the so-called wurtzite/zinc-blende polytypism during the growth of self-catalyzed GaAs nanowires is monitored by means of time-resolved *in-situ* X-ray scattering in symmetric geometry. Using a statistical model with time-dependent transition-probabilities between the polytypes, insights into the evolution of key-parameters of polytypism, such as mean polytype segment length and polytype fraction, are obtained. Moreover, differences in the nucleation barriers are estimated.

The formation of microstructure and shape of GaAs nanowires during growth is monitored *in-situ* via time-resolved X-ray scattering at phase-sensitive Bragg reflections. Thereby, the separation of radial growth processes in non-catalytic and catalytic contributions is achieved. This allows for the direct comparison to theoretical models for catalytic radial growth. In dependence of the growth parameters, conclusions on the evolution of the liquid catalyst particle during growth become possible.

Contents

Introduction

Nanomaterials such as fullerenes, nanotubes, nanofibers or crystalline nanoparticles already have a large number of applications in our everyday life, e.g in water purifiers, lotions, paints or tear resistant textiles. The great potential of nanomaterials arises from their small size resulting in unique properties which can differ substantially from the bulk counterparts. Essentially, the large surface to volume ratio increases the influence of surface effects, causing e.g. an increased chemical reactivity. In case of semiconductor nanomaterials, the size-reduction leads to special optical and electronic properties caused by quantum mechanical effects related to charge carrier confinement. In particular, crystalline III/V compound semiconductor nanostructures are highly attractive for optoelectronic applications, as in light emitting devices or detectors. For combining the advantages of III/V nanostructures with Complementary Metal-Oxide-Semiconductor (CMOS) technology for optoelectronic applications (e.g. as fast transistor channels), the epitaxial integration of III/V nanostructures on silicon is required. Ideally for this purpose, the nanostructures should have a small epitaxial interface with the substrate, which is given for vertical III/V nanowires. For bulk or thin-layer systems such an integration is not yet feasible due to the large lattice mismatch between the different materials.

For synthesis and epitaxial integration of the respective nanostructures on silicon, special *bottom-up* fabrication methods such as molecular beam epitaxy (MBE), based on self-assembly, are required. By bottom-up fabrication, the final properties of the nanostructures are a result of a complex interplay between various factors and dynamical processes that are taking place during growth. Therefore, understanding of the growth dynamics is a prerequisite for tailoring the final properties of semiconductor nanostructures for further applications.

In this context, the time-resolved, non-destructive monitoring of the growth process would grant valuable insights into the growth dynamics. Such *in-situ* experiments are however highly challenging from the experimental point of view, since they require the integration of suitable growth equipment and non-destructive measurement technique. For the non-destructive characterization of semiconductor nanostructures (ensembles as well as individual objects), especially of their crystalline structure and their shape, diffraction methods based on X-ray radiation (electromagentic radiation with an energy of several keV) provided by synchrotron radiation facilities, have proven as powerful tools. Presently, only few pioneering setups for such *in-situ* X-ray based growth studies exist worldwide and corresponding experiments are yet rare.

The aim of this work is to gain a comprehensive understanding of dynamical processes during growth of GaAs nanowires on silicon by use of non-destructive time-resolved *in-situ* X-ray scattering methods. Therefore, we will employ a special portable MBE system optimized for simultaneous growth and *in-situ* X-ray experiments at synchrotron radiation facilities. We will calibrate this MBE system and establish protocols for the reproducible growth of GaAs nanowires. Further, we will develop and apply *in-situ* X-ray scattering methods for the time-resolved characterization of the structural evolution of growing GaAs nanowires. From the obtained results we will be able to draw conclusions on various important aspects of the growth dynamics.

In chapter 1, we will give an introduction in the growth of GaAs nanowires. We will discuss their crystal-structure with focus on the polytypism between wurtzite and zin-blende, as well as X-ray scattering resulting from such polytypic structures. Further, we introduce a statistical model for the generation of the polytypic crystal structure of nanowires. Finally, the portable MBE system, used for the growth and *in-situ* X-ray characterization, will be introduced.

In chapter 2, we will present MBE growth studies of self-catalyzed GaAs nanowires. In particular, the influence of the basic growth parameters such as material fluxes, growth temperature, as well as growth time and substrate preparation will be addressed. As a result, we will obtain a parameter window suitable for the growth of GaAs nanowires in the portable MBE system, optimized with respect to time-resolved *in-situ* X-ray diffraction experiments.

In chapter 3, results of *ex-situ* as well as *in-situ* X-ray experiments will be presented. First, we will discuss scattering from an ensemble of GaAs nanowires with polytypic crystal structure. We will discuss, how information on polytype fraction and mean polytype segment length can be extracted from the X-ray scattering data. Further, we will analyze signals of individual polytypic nanowires and obtain values for the difference of the lattice spacing in the two GaAs polytypes. Additionally, we will identify the contribution of parasitic growth (island-like GaAs crystallites that did not grow to vertical nanowires) to the scattering signal (Paper 1). By time-resolved *in-situ* X-ray diffraction experiments in so-called symmetric geometry, we will monitor the crystal structure of a growing ensemble of GaAs nanowires. Employing a statistical model for the generation of the crystal structure, we will obtain estimates on the change of the polytype phase fraction, and the mean segment length during growth. Moreover, we will infer quantitative values for the difference in the nucleation barriers of the polytypes and their evolution (Paper 2). By so-called asymmetric X-ray diffraction, we will be able to investigate phase-sensitive Bragg reflections during the growth of GaAs nanowires. We will demonstrate, how to characterize the crystalline properties of the nanowires without requiring a model for the generation of the crystal structure. In combination with *ex-situ* scanning electron microscopy, we will disentangle processes of radial growth responsible for tapering and side-wall growth. Thereby, we will facilitate the direct application of recent growth models to our experimental data which allows insights into the dynamics of the liquid Ga-droplet during growth (Paper 3, in preparation).

Finally, a conclusion of the manuscript and an outlook are given.

Results presented in chapter 3 have been published in:

- Paper 1: M. Köhl, P. Schroth, A.A. Minkevich, J.-W. Hornung, E. Dimakis, C. Somaschini, L. Geelhaar, T. Aschenbrenner, S. Lazarev, D. Grigoriev, U. Pietsch and T. Baumbach, *Polytypism in GaAs nanowires: Determination of the interplanar spacing of wurtzite GaAs by X-ray diffraction*, Journal of Synchrotron Radiation, 22, 67–75, 2015
- Paper 2: P. Schroth, M. Köhl, J.-W. Hornung, E. Dimakis, C. Somaschini, L. Geelhaar, A. Biermanns, S. Bauer, S. Lazarev, U. Pietsch and T. Baumbach, *Evolution of Polytypism in GaAs Nanowires during Growth Revealed by Time-Resolved in situ X-ray Diffraction*, Physical Review Letters, 114, 055504, 2015
- Paper 3: P. Schroth, M. Köhl, J. Jakob, L. Feigl, M. Kashani, J. Vogel, J. Strempfer, T. Keller, A. Stierle, U. Pietsch, and T. Baumbach, *In-situ X-ray investigation of radial growth processes of self-catalyzed GaAs nanowires*, in preparation.

Other co-authored publications:

- T. Slobodskyy, P. Schroth, D. Grigoriev, A. A. Minkevich, D. Z. Hu, D. M. Schaadt, und T. Baumbach, *A portable molecular beam epitaxy system for in situ X-ray investigations at synchrotron beamlines*, Review of Scientific Instruments 83, 105112, 2012
- M. Helfrich, P. Schroth, D. Grigoriev, S. Lazarev, R. Felici, T. Slobodskyy, T. Baumbach, und D. M. Schaadt, *Growth and characterization of site-selective quantum dots*, Physica Status Solidi (A) 209, 2387–2401, 2012
- P. Schroth, T. Slobodskyy, D. Grigoriev, A. Minkevich, M. Riotte, S. Lazarev, E. Fohtung, D.Z. Hu, D.M. Schaadt, T. Baumbach, *Investigation of buried quantum dots using grazing incidence X-ray diffraction*, Materials Science and Engineering B 177, 721–724, 2012
- M. Köhl, P. Schroth, A. A. Minkevich, T. Baumbach, *Retrieving the displacement of strained nanoobjects: the impact of bounds for the scattering magnitude in direct space*, Optics Express 21, 27734–27749, 2013
- T. Slobodskyy, P. Schroth, A. Minkevich, D. Grigoriev, E. Fohtung, M. Riotte, T. Baumbach, M. Powalla, U. Lemmer, A. Slobodskyy, *Three-dimensional reciprocal space profile of an individual nanocrystallite inside a thin-film solar cell absorber layer*, Journal of Physics D: Applied Physics 46, 475104, 2013
- D. Grigoriev, S. Lazarev, P. Schroth, A.A. Minkevich, M. Köhl, T. Slobodskyy, M. Helfrich, D.M. Schaadt, T. Aschenbrenner, D. Hommel and T. Baumbach, *Asymmetric skew X-ray diffraction at fixed incidence angle: application to semiconductor nano-objects*, Journal of Applied Crystallography 49, 961–967, 2016

- M. Köhl, P. Schroth, and T. Baumbach, *Perspectives and limitations of symmetric X-ray Bragg reflections for inspecting polytypism in nanowires*, Journal of Synchrotron Radiation 23, 487–500, 2016

1 Introduction to GaAs nanowires

At the outset of this manuscript, we will give a brief overview on semiconductor nanowires. We thereby introduce concepts employed for their fabrication and further elaborate the *vapor-liquid-solid* growth process for the *bottom-up* synthesis of free-standing GaAs nanowires. The crystal-structure of GaAs nanowires, especially structural polytypism (the occurrence of different crystalline phases of the same material within the same nanowire) will be detailed, and a model for polytypism based on a Markov-chain for the stacking will be presented. In the end of this chapter, we will discuss X-ray diffraction as a probe for crystal-structure and polytypism in GaAs nanowires, and discuss the possibility for time-resolved *in-situ* growth studies employing X-ray diffraction in combination with specialized growth equipment.

1.1 Synthesis of GaAs nanowires

Semiconductor nanowires are quasi one-dimensional structures with a radius usually ranging from 10 nm – 100 nm, and lengths in the range from 100 nm – 20 μm. The unique properties of semiconductor nanowires offer vast opportunities for designing novel devices [1, 2] exploiting for instance quantum confinement [3], surface effects [4, 5], and their thermoelectric [6] and strain relaxation properties [7]. By use of current fabrication methods, challenging structures ranging from nanowires with nearly perfect crystal quality [8], to sophisticated multilayer heterosystems interfacing dissimilar materials within the nanowire geometry [9]. As a consequence of extensive study, devices integrating nanowires range from transistors [10, 11], solar cells [12, 13], light-emitting diodes [14], and Lasers [15, 16, 17, 18, 19] towards bio sensors [20, 21]. The great potential of semiconductor nanowires is not limited to applicatory aspects, but has also inspired fundamental research [22, 23, 24] on e.g. qubits [25], and single photon sources [26].

Methods for the fabrication of nanowires structures can be divided into two general strategies *top-down* and *bottom-up* [27]. Whereas the *top-down* approach requires pre-processing and structuring methods such as electron-beam-lithography [28] defining the nanostructures, the *bottom-up* approach relies on a self-assembly of the nanostructres. In addition, pre-processing steps like substrate patterning [29] as applied in *top-down* fabrication could be integrated in the *bottom-up* synthesis of nanowires. The work presented in this manuscript employs the *bottom-up* strategy for the fabrication of GaAs nanowires by MBE.

The *bottom-up* synthesis of semiconductor nanowires by modern MBE techniques often involves a metallic droplet on top of the nanowire, that remains liquid during the entire growth process. This metal droplet acts as a catalyst for the nanowire growth and serves as a material reservoir. The growth species, supplied by direct impingement from the molecular-beams or by diffusion, get adsorbed by the liquid droplet until a certain critical supersaturation inside the droplet is reached. Then, the growth species are successively incorporated from the liquid droplet into the nanowire by forming a new crystalline layer at the liquid-solid interface shifting the droplet upwards [30, 31, 32, 33, 34, 35].

The growth of crystalline semiconductor structures via such a process was demonstrated by Wagner and Ellis in 1964 by the gold-catalyzed (Au-catalyzed) growth of freestanding silicon micro-whiskers on Si(111) substrates [36]. They figured out, that the Au-droplet mediates the unidirectional nanowire growth along the [111] – direction of the solid Si whisker and defines its position on the substrate, and its radius.

Today, the vapor-liquid-solid (VLS) growth method is applied by various groups, in order to synthesize one-dimensional structures at the nanoscale [20, 37, 12, 38, 39, 40]. Using MBE or MOVCD, Au-catalyzed nanowires with a radius of 10 nm − 100 nm and a length up to several μm can be grown in several material systems, including the group IV semiconductors Si [20, 41] and Ge [42, 43] and several compounds of the III-V [44, 33, 45, 46] and II-VI [47, 48] semiconductors.

In the case of Au-catalyzed GaAs nanowires, the growth follows a procedure including the following steps:

- At UHV conditions, the substrates are covered with a thin solid Au layer (usually 1nm).
- Formation of Au droplets by annealing of the Au layer.
- Growth of GaAs nanowires by deposition of GaAs above the melting point of the Au-Ga alloy.

These steps can only be performed at certain growth conditions. Usually, growth temperatures 500 °C $<$ T_S $<$ 620 °C are employed for the growth of Au-catalyzed GaAs nanowires [49]. At these temperatures the diffusivity of Ga adatoms is very high and allows the Ga adatoms to migrate from the surface towards the nanowire top [50, 38]. At the same time, the desorption-rate of the group V element exceeds the one of the group III element by far, effectively suppressing diffusion of As adatoms. Thus, surface diffusion of the group III element has to be considered in the description of the nanowire growth rates in the frame of the VLS growth model [51, 31], whereas for the group V element, re-evaporation processes have to be considered [52]. In particular, the radial and axial growth rates of the nanowires are of interest, since by optimizing those, nanowires with extreme aspect ratios can be obtained [38, 53]. For example, in MBE the length of the nanowire can, by several orders of magnitude, exceed the nominal thickness of an equivalent 2D layer grown under the same conditions [54, 52], whereas the radial growth rates are small [55]. Under constant growth conditions, the length of the final nanowires, is approximately

proportional to the growth time [38, 56], whereas the growth-rate depends on the supplied As-flux [38, 57]. For sufficiently small radii (below 100 nm) nanowires grow in a layer-by layer mode (mono-nuclear mode). Each nucleation of a new layer decreases the amount of Ga and As in the liquid droplet. Thus, the next nucleation event can only take place after the material reservoir has been refilled and a critical supersaturation with As has been reached. The axial growth-rate is thus tied to the waiting-time between two successive nucleation events, which in turn depends on the supplied As-flux [58, 59]. Differences in the Ga-flux do not effect the axial growth-rate [56], but influence the radial-growth, and the diameters of the final nanowires, leading to tapered nanowire-geometries [60]. Additionally, at radii below 100 nm, size-dependent effects like the so-called Gibbs-Thomson-effect play a limiting role and need to be taken into account in the VLS growth model [30, 61, 62, 63].

However, the Au-catalyzed approach has a severe drawback, since the incorporation of Au strongly affects the optical and electrical properties if incorporated into a semiconductor, and thus renders the Au-catalyzed approach incompatible with standart CMOS technology [64, 65]. The effects of Au impurities in semiconductor nanowires have been investigated in several works, e.g. Breuer [40] investigated PL properties of Au-catalyzed GaAs/(Al,Ga)As core-shell nanowires and demonstrated a strongly reduced minority carrier lifetime due to Au incorporation.

In case of Si nanowires Kodambaka et al. [66, 67] have shown, that Au can diffuse away from the droplet onto the sidewalls of the nanowire during growth. The droplet shrinks, and thereby reduces the diameter of the nanowire until the VLS growth stops as the droplet is finally consumed. Xu et al. [68] found Au atoms which have been incorporated into Si nanowires during the growth, creating defect sites in the Silicon.

Hence, there has been an increasing interest in substituting Au as catalyst material. Besides Au, other metals like Al [69] and Cu [70], Ti [71] have been found to support a stable VLS growth mode. In order to fully avoid unwanted impurities in compound semiconductor nanowires (like III–V nanowires) caused by foreign materials, the catalyst metal needs to be replaced by the group III material. In 2008, Fontcuberta et al. [72] demonstrated the self-catalyzed (or Ga-catalyzed in the case of GaAs nanowires) growth of GaAs nanowires on GaAs substrates covered by a Si–oxide layer. The grown GaAs nanowires feature a spherical Ga droplet on top which was formed during the initial stage of the growth. There have been several follow-up investigations, focusing on the growth of Ga-catalyzed GaAs nanowires on GaAs substrates [38, 73], until the first growth of self-catalyzed III–V nanowires on Si was reported by [74]. Since Si is cost-effective and compatible with the processing chains of the CMOS industry, this sparked further intensive research on the integration of self-catalyzed III–V nanowires on Si substrates e.g. [75], especially for GaAs nanowires [76, 56, 77] or for InAs nanowires [78, 46].

The process of the self-catalyzed growth of nanowires will be discussed in the following referring to self–catalyzed GaAs nanowires on Si(111) covered by a native Si–oxide layer as model system, and can be summarized in the following points:

- The growth species, Ga and As, supplied by the vapor, impinge on the substrate. Due to

its high volatility at usual growth temperatures around 500 °C to 600 °C, As immediately evaporates. Ga atoms instead stick to the surface, accumulate and form liquid droplets on the surface. This step may be enhanced by the high surface mobility of Ga. The droplets then stick to certain regions at the surface, likely at inhomogeneities or defects in the thin Si–oxide layer.

- At these sites, the Ga can etch away the Si-oxide and can establish contact with the crystalline Si, given that the oxide–layer is sufficiently thin.
- After the Ga droplets have formed, As gets adsorbed in the liquid phase until a critical supersaturation necessary for nucleation is reached. Under these conditions, the nucleation of a 2D layer happens at the liquid–solid interface directly below the droplet, rapidly forming a complete GaAs monolayer covering the whole interface area. After the nucleation step, the material reservoir in the droplet is refilled, until the necessary supersaturation of As is reached again.

In order to model the growth process in its entirety one has to take into account the interactions between objects in the vapor, liquid and solid phases with each other. In Fig. 1.1 we give a short overview of the most important factors. The vapor phase acts as a source of the growth species, available for the growth in general. The atoms and molecules in the vapor phase impinge on the substrate, where adsorption, desorption and diffusion processes take place – primarily depending on the temperature of the substrate. Here the flux-ratio of As and Ga is an important parameter for tailoring the nanowire morphology, as we will see later. The amount of the provided material which does not desorb participates in the growth of GaAs nanostructures (which can be wires or bulky parasitic crystallites). The crystallographic orientation of the substrate, defines the orientation of the wires relative to the surface normal. Most importantly the thin oxide–layer on the substrate and its properties such as thickness, roughness, porosity and chemical composition are important parameters which can considerably affect the nanowire growth [79, 80]. The nanowire itself consists of a solid phase of GaAs that forms the columnar wire–structure with a hexagonal base, faceted side-walls and a liquid Ga–droplet on its tip. Whereas the solid wire is well defined by radius and length, surface–facets and its crystallographic structure. The properties of the side-walls are important when considering surface–effects like side-wall diffusion towards and away from the droplet or the substrate, and radial growth–rates, whereas the crystal–structure address defects in the nanowire, such as impurity atoms, stacking faults or polytypism. Inside liquid droplet the growth species for the axial nanowire growth are solved. A complicated interplay of its size and geometry, especially the morphology of the liquid-solid-interface, and its supersaturation define the properties of the growing nanowire e.g. diameter, axial growth–rate, and the resulting crystalline structure [81, 82, 60, 83, 84, 80].

An overview of kinetic processes involved in the VLS growth of a single nanowire is depicted in Fig. 1.1. Ga adatoms may be incorporated into the droplet by (1) direct impingement (for the effective influx, the desorption from the droplet (2) has to be taken into account), (3) diffusion

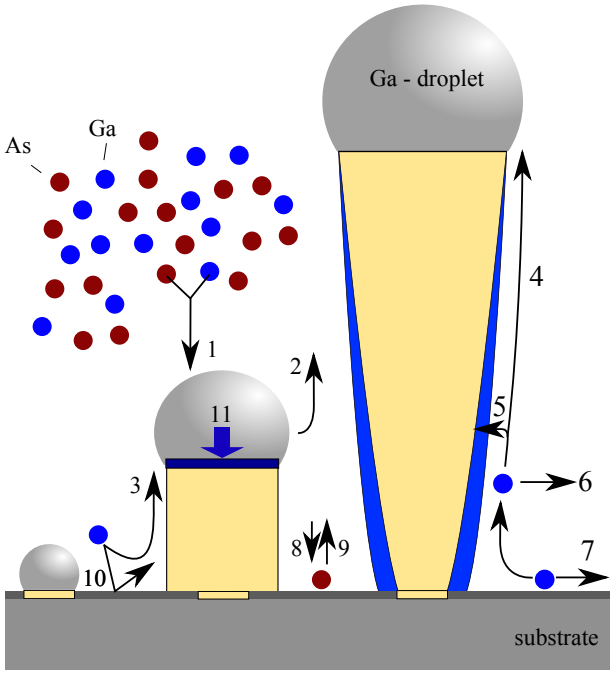

Figure 1.1: Kinetic processes during VLS growth of a self-catalyzed GaAs nanowire. For description, see text.

of Ga adatoms which have impinged at the sidewalls, and (4) diffusion from the surface via the sidewalls. Depending on the balance of material fluxes in and out of the droplet, it may vary its size during growth and cause (inverse) tapering. Some adatoms may not reach the droplet, if they (5) become incorporated into the sidewalls and contribute to side-wall growth (blue), or (6) evaporate from the sidewalls, or (7) form parasitic crystallites on the substrate. In case of As, the direct impingement (1) leads to an increase of the group V concentration in the droplet, since otherwise As is immediately re-evaporated (8 and 9). Growth species, which evaporate from the surface or the side facets can return to the vapor phase, and can again be collected by nearby nanowires (10). In case of As, re-evaporation may provide an additional source of material, in addition to the direct flux into the droplet. In process (11) Ga and As is incorporated into the nanowire via layer-by-layer nucleation. Only the growth species (provided by the fluxes 1, 3, 4 and 10) solved in the liquid Ga droplet contribute to the axial growth. Growth species incorporated into the side-walls will cause the nanowire to grow in radial direction (5), whereas adatoms involved in the parasitic growth (7) will not participate in nanowire growth.

III/V nanowires preferably grow along the [111] – direction, which will result in forests of oblique nanowires if grown on substrates with [001] – or [110] – surface orientation [85]. Thus, using [111] – oriented substrates will facilitate the growth of vertical, freestanding nanowires.

For a more comprehensive overview and further details on practical and theoretical aspects of the growth of VLS grown nanowires, we refer the reader to the PhD thesis of S. Breuer [86], the

reviews of P. Krogstrup [87] and P. Caroff [88], or the extensive growth study of F. Bastiman [89] as well as to the book of V. G. Dubrovskii *Nucleation Theory and Growth of Nanostructures* [63]. One aim of this work is the controlled fabrication of self-catalyzed GaAs nanowires on Si(111) substrates with focus on the investigation of the evolution of the nanowire morphology during the growth process. Therefore, we will now discuss the crystal structure of GaAs nanowires in detail, especially the wurtzite-zinc-blende polytypism. Later, we introduce X-ray diffraction as a non-destructive probe of the crystal structure for time-resolved *in-situ* measurements.

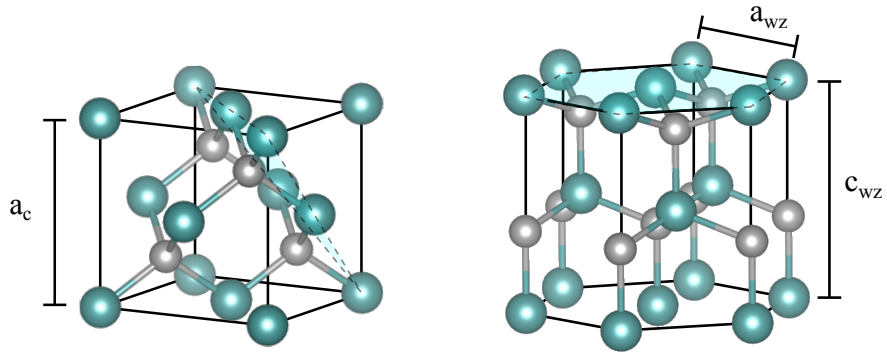

(a) Zinc-blende unit cell composed of As atoms at the corners, and Ga atoms. An atomic layer of As atoms perpendicular to the $[111]_c$ direction is depicted.

(b) Wurtzite structure of GaAs. An atomic layer of As atoms perpendicular to $[111]_c = [00.2]_{h,wz}$ is depicted.

Figure 1.2: Zinc-blende and wurtzite structures of GaAs.

1.2 Polytypism and crystal structure of GaAs nanowires

In this section, we will describe the crystalline structure of GaAs nanowires, their epitaxial relation to the Si(111) substrate, and the polytypism between wurtzite and zinc-blende. This polytypism, the coexistence of different crystal phases in the same nanowire, is not exclusive for GaAs nanowires, but has also been observed for nanowires grown by other III/V materials e.g. InAs [90, 91], GaP [35] or InP [82]. GaAs nanowires grow along the [111]–direction, which in our case is the same principal direction as the substrate-orientation (compare e.g. RHEED in Sec. 2). Ideally, the wires grow free-standing and vertical to the substrate surface and are truncated by (110)-type facets in case of Ga-catalyzed GaAs nanowires, or (112)-type facets if Gold is chosen as a catalyst material instead (see Ref. [86], and references therein).

The stable crystalline phase of bulk GaAs and bulk Si crystals at ambient conditions is the cubic zinc-blende and the cubic diamond structure respectively. For both structures, the atoms within the cubic unit cell can be found at positions defined by two superposed face-centered cubic (fcc) unit cells with lattice parameter a_c shifted by $(1/4, 1/4, 1/4)\ a_c$. Whereas for Si in the diamond structure, the positions $(0, 0, 0)\ a_c$ and $(1/4, 1/4, 1/4)\ a_c$ are both occupied by Si atoms, they are occupied only by As or Ga ions in case of the zinc-blende structure.

A cubic zinc-blende crystal such as GaAs can be decomposed into hexagonal close packed atomic sub-layers stacked in a certain sequence along the [111]-direction. These sub-layers are perpendicular to the [111]-direction and contain either only Ga or only As atoms, for which the atomic species is alternating for each neighboring layer. For illustration, these atomic sub-layers are depicted within the unit cells of cubic and hexagonal GaAs in Fig. 1.2. For the following discussion, we will refer to a "layer" to be composed by two neighboring atomic sub-layers of Ga and As atoms, so that the stacking of the GaAs nanowire can be described as a periodic repetition

of a certain stacking sequence of these (bi-atomic) GaAs layers along the [111]-direction.

Polytypism in GaAs nanowires refers to the observation of extended segments with cubic (zinc-blende) or hexagonal (wurtzite) stacking of the GaAs layers - even within the same wire. For a cubic zinc-blende crystal the stacking along $[111]_c$ can be described as a periodic repetition of three layers 'ABC' as depicted in Fig. 1.3(a). Since the growth on nanowires occurs in a layer-by-layer mode, stacking faults are the most often observed defect structure causing an interruption of the 'ABCABCABC'-type sequence of zinc-blende. As we observe by RHEED (see Sec. 2) also wurtzite and twinned zinc-blende segments are present in the GaAs nanowires. The crystal structure of the zinc-blende twin corresponds to a 180° rotation of the non-twinned structure around the $[111]_c$-growth axis, which causes an inversion of the 'ABCABC'-type stacking sequence to 'CBACBA'-type one. Therefore, a stacking fault in the layer-sequence needs to be generated, the twin-boundary, e.g. 'ABCA|CBACBA' where the twin boundary is indicated by the vertical line (compare also Fig.1.3(b)). This single stacking fault generates a local 'ABA'- type (or like 'BCB', or 'CAC') layer sequence. Atoms arranged in a stacking sequence of two alternating layers '...ABABABA...' are hexagonally close packed (hcp) and constitute the wurtzite poltytype of GaAs. Consequently, repeated twin-boundaries cause formation of extended segments of wurtzite (as shown in Fig. 1.2(b) and Fig. 1.3(c)).

In analogy to Refs. [92, 93], we now introduce a surface coordinate system that accounts for the hexagonal symmetry of the (111)-planes in which the cubic $[111]_c$ direction corresponds to the $[00.2]_{h,wz}$ direction of wurtzite. The hexagonal basis for zinc-blende structures and for wurtzite structures are given by the following convention

cubic basis for zinc-blende	hexagonal basis zinc-blende	hexagonal basis wurtzite
$a_c \cdot \begin{bmatrix} 1 & 0 & 0 \\ 0 & 1 & 0 \\ 0 & 0 & 1 \end{bmatrix}$	$a_{wz} \cdot \begin{bmatrix} \frac{1}{2} & \frac{1}{2} & 0 \\ -\frac{\sqrt{3}}{2} & \frac{\sqrt{3}}{2} & 0 \\ 0 & 0 & \sqrt{6} \end{bmatrix}$	$a_{wz} \cdot \begin{bmatrix} \frac{1}{2} & \frac{1}{2} & 0 \\ -\frac{\sqrt{3}}{2} & \frac{\sqrt{3}}{2} & 0 \\ 0 & 0 & \sqrt{\frac{8}{3}}\,(1+\frac{d_{wz}}{d_{zb}}) \end{bmatrix}$
notation: $[111]_c$	notation: $[00.3]_{h,zb}$	notation: $[00.2]_{h,wz}$

Table 1.1: Cubic and hexagonal bases for describing zinc-blende and wurtzite structures in GaAs nanowires. The vertical lattice parameter c_{wz} of the hexagonal structure is by a factor 2/3 shorter than the vertical lattice parameter of the cubic GaAs, if $d_{wz}/d_{zb} = 1$, since the number of layers in the hexagonal unit cell is 2 instead of 3 for the cubic structure. Else, the difference $d_{wz} \neq d_{zb}$ of the layer-spacing of wurtzite and zinc-blende has to be taken into account.

Where a_c is the lattice constant of the cubic lattice, $a_{wz} = a_c/\sqrt{2}$ is the lattice constant for the hexagonal lattice. The ratio of the layer-distance between wurtzite and zinc-blende GaAs in $[111]_c$ direction is d_{wz}/d_{zb}. The distance d_{hkl} between two crystallographic planes can be calculated by

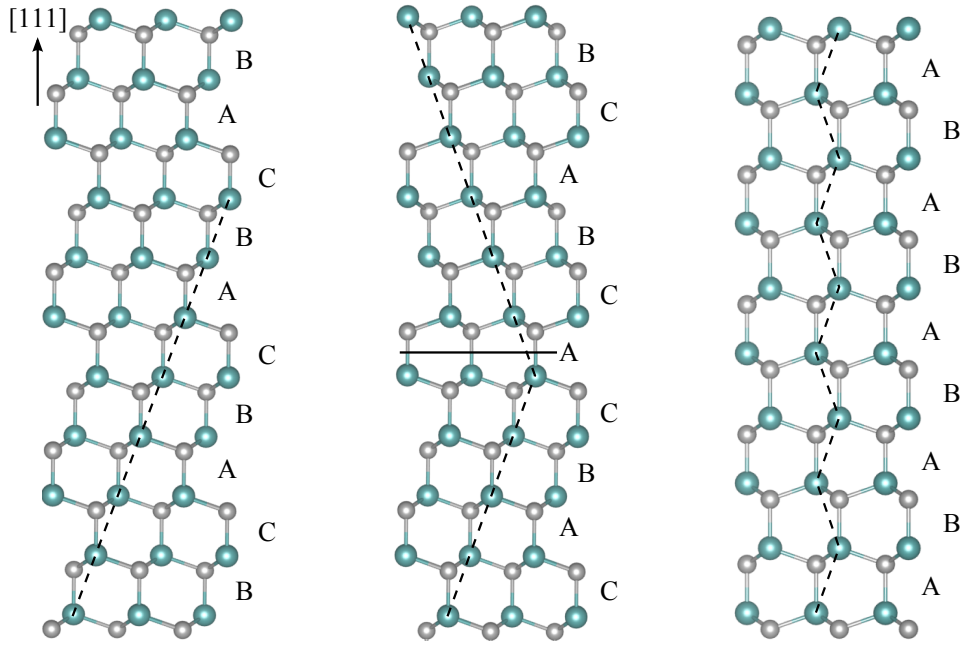

(a) zinc-blende stacking

(b) mixed zinc-blende and twinned zinc-blende stacking

(c) wurtzite stacking

Figure 1.3: Stacking sequences of atomic bi-layers along the $[111]_c$ direction viewed along $[10\bar{1}]_c$. The zinc-blende stacking is a periodic repetition of the '...ABC...' sequence. The twinned zinc-blende structure is described by an inversion of this sequence into '...CBA...'. The twin-boundary is marked by a horizontal line. The wurtzite stacking is a sequence of alternating layers e.g. '...ABAB...' that can be created by successive nucleation of twin-boundaries.

$$d_{[hkl]_c} = \frac{a_c}{\sqrt{h^2+k^2+l^2}}; \quad \text{and } d_{[hkl]_{h,wz}} = \frac{a_{wz}}{\sqrt{\frac{4}{3}\left(h^2+k^2+hk\right)+\left(\frac{a_{wz}}{c_{wz}}\right)^2 l^2}} \tag{1.1}$$

for the cubic and hexagonal structure respectively [92, 93, 94, 95].

The Miller-indices of $[hkl]_c$-planes can be transformed into the hexagonal basis by the following transformation matrix ([92, 93])

$$\begin{pmatrix} h \\ k \\ l \end{pmatrix}_{h,zb} = \mathbf{M_{c\to h,zb}} \begin{pmatrix} h \\ k \\ l \end{pmatrix}_{c} \quad \text{with} \quad \mathbf{M_{c\to h,zb}} = \begin{bmatrix} 1/2 & 0 & -1/2 \\ -1/2 & 1/2 & 0 \\ 1 & 1 & 1 \end{bmatrix} \tag{1.2}$$

and for the wurtzite structure

$$\begin{pmatrix} h \\ k \\ l \end{pmatrix}_{h,wz} = \mathbf{M_{h,zb\to h,wz}} \begin{pmatrix} h \\ k \\ l \end{pmatrix}_{h,zb} \quad \text{with} \quad \mathbf{M_{h,zb\to h,wz}} = \begin{bmatrix} 0 & 0 & 0 \\ 0 & 0 & 0 \\ 0 & 0 & 2/3 \end{bmatrix}. \tag{1.3}$$

The positions of As and Ga atoms in cubic and hexagonal notation for GaAs zinc-blende and wurtzite respectively are given in Tab. 1.2.

cubic basis zinc-blende	hexagonal basis zinc-blende	hexagonal basis wurtzite
As atoms	As atoms	As atoms
$(0\ 0\ 0)$ $(\frac{1}{2}\ \frac{1}{2}\ 0)$ $(\frac{1}{2}\ 0\ \frac{1}{2})$ $(0\ \frac{1}{2}\ \frac{1}{2})$	$(0\ 0\ 0)$ $(\frac{2}{3}\ \frac{1}{3}\ \frac{1}{3})$ $(\frac{1}{3}\ \frac{2}{3}\ \frac{2}{3})$	$(0\ 0\ 0)$ $(\frac{2}{3}\ \frac{1}{3}\ \frac{1}{2})$
Ga atoms	Ga atoms	Ga atoms
$(\frac{1}{4}\ \frac{1}{4}\ \frac{1}{4})$ $(\frac{3}{4}\ \frac{3}{4}\ \frac{1}{4})$ $(\frac{3}{4}\ \frac{1}{4}\ \frac{3}{4})$ $(\frac{1}{4}\ \frac{3}{4}\ \frac{3}{4})$	$(0\ 0\ \frac{1}{4})$ $(\frac{2}{3}\ \frac{1}{3}\ \frac{7}{12})$ $(\frac{1}{3}\ \frac{2}{3}\ \frac{11}{12})$	$(0\ 0\ \frac{3}{8})$ $(\frac{2}{3}\ \frac{1}{3}\ \frac{7}{8})$

Table 1.2: Relative atomic positions in the cubic zinc-blende unit cell and the unit cells for zinc-blende and wurtzite in hexagonal basis.

For illustration, we depict the unit cells for the GaAs zinc-blende and wurtzite structure in the hexagonal basis in Fig. 1.4.

Another important difference between wurtzite and zinc-blende GaAs is a slight variation in the vertical spacing of the atomic layers in $[111]_c$ direction. However, different values for the ratio $(d_{wz} - d_{zb})/d_{zb}$ have been reported in literature which span a wide range: In 1992, Yeh et al. [96] predict the ratio to be -1.3%, whereas 2011 Panse et al. [97] obtain a value of 0.55%. In experimental reports, the values range from 0.52% to 1.49% ([32, 98, 99, 100, 92, 86]). Interestingly, values reported for bulk GaAs (0.554%) by McMahon and Nelmes [99] are close to the theoretical values from Panse et al. [97] (0.55%). For wurtzite in GaAs nanowires only one the value obtained by Tchernycheva et al. [32] is with 0.52% close to these reports. All other values for wurtzite in GaAs nanowires are larger than for bulk GaAs: 0.62% [86]; 0.7% [92], and 1.49% [98]. In Sec. 3.1 we will therefore investigate the difference in the vertical spacing of wurtzite and zinc-blende GaAs by means of X-ray diffraction in detail.

In this section, we described the geometrical properties of the two polytypes zinc-blende and wurtzite GaAs. We introduced a hexagonal coordinate system which accounts for the surface orientation of the substrate and the principal growth direction of the nanowires. In the following we will briefly discuss the occurrence of polytypism in GaAs nanowires from a thermodynamic and a kinetic point of view, analogous to [63].

Usually III/V materials in bulk adopt the cubic zinc-blende crystal structure. An exception are nitrides, e.g. GaN which exhibit the hexagonal wurtzite structure in their bulk form. In

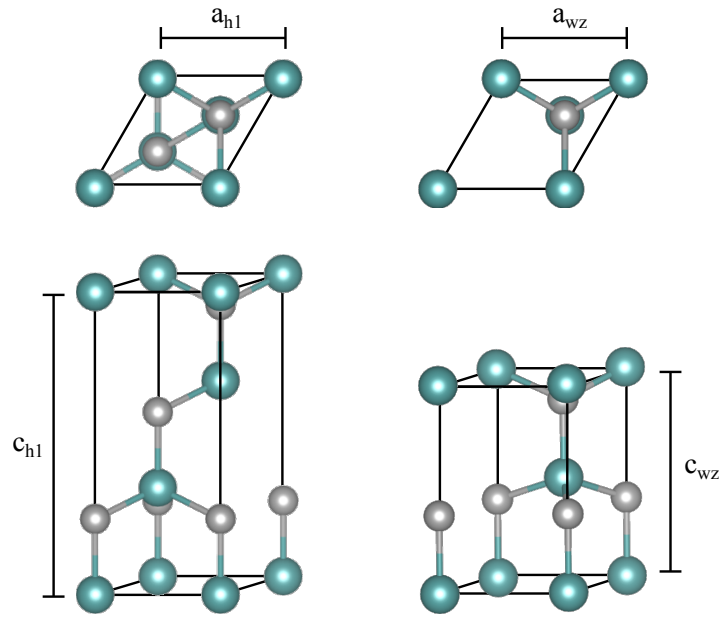

(a) zinc-blende unit cell in hexagonal basis

(b) wurtzite unit cell in hexagonal basis

Figure 1.4: Unit cell of zinc-blende (1.4(a)) and wurtzite (1.4(b)) in hexagonal basis. On top, the unit-cells are displayed with view along the [111]-direction. The lattice constants $a_{h,zb} = a_{wz} = a_c/\sqrt{2}$, and $c_{h,zb} = \sqrt{6}a_{h,zb} = \sqrt{3}a_c$. The c-lattice constant for wurtzite is $c_{wz} = a_{wz}\sqrt{\frac{8}{3}}(1+\frac{d_{wz}}{d_{zb}})$.

case of GaAs the reported differences in the cohesive binding energies between wurtzite and zinc-blende are about $\delta E = E_{wz} - E_{zb} = 24\,\text{meV/pair}$ [96] which makes zinc-blende the energetically favourable structure. This difference for GaN, $\delta E = -36.8\,\text{meV/pair}$ is negative [96] and consequently GaN should obtain the hexagonal wurtzite structure. However, for $[111]_c$ oriented nanowires with hexagonal cross-section, wurtzite phase has been observed for various III/V materials (e.g. GaAs [91, 37, 101], InAs [91, 101, 46, 102], InP [101] and GaP [101]).

Early explanations for the existence of wurtzite in III/V nanowires were based on the lower surface energies of the side-wall facets of wurtzite nanowires caused by the lower number of dangling bonds as compared to the facets of zinc blende. Depending in the nanowires' composition (i.e. the inonicity of the III/V compound), Akiyama et al. [103] estimate a critical radius ranging from 1-22 nm for which wurtzite nanowires are energetically preferred. Moreover the authors report on an intermediate regime ranging from 12-32 nm for which both polytypes, zinc-blende as well as wurtzite can coexist in the same structure. Similarly, Magri and Rosini [104, 105] find a critical diameter for the wurtzite-zinc-blende transition in GaAs nanwire of 6.3 nm below which the cost to create a solid wurtzite volume is overcompensated by the gain in surface energy of the respective wurtzite facets. However, these values are too small to explain experimental observations of polytypism im GaAs nanowires with diameters up to 285 nm [92].

Consequently, solely thermodynamic considerations might be insufficient for a description of the wurtzite-zincblende polytypism. Therefore, we now consider polytypism by kinetic aspects of nanowire growth.

For gold-seeded GaAs nanowires, wurtzite segments are often observed at the very bottom of the wire close to the substrate, and at the tip, just below the droplet [92, 86]. Accordingly, these segments were formed at the beginning and at the end of growth. As observed for self-catalyzed GaAs nanowires by Rieger et al. [83] wurtzite controllably formed during the consumption of the liquid Ga-droplet. This means, that the growth parameters such as the substrate temperature or the V/III ratio and therefore the supersaturation and the shape of the catalyst are important parameters for describing and understanding polytypism. Consequently, a kinetic approach to polytypism which is able to describe above observations needs to take into account important values like the supersaturation [106], the shape of the droplet [81] and the geometry of the nucleation site [107] (and thereby the surface energies of the involved facets [108]) defining the energy barrier E for creating critical nucleus [63].

The nucleation energy barrier is related to the layer-nucleation rate J by [63]

$$J = J_0 \ \exp^{-\frac{E}{k_B T}} . \tag{1.4}$$

The absolute value of E and the substrate temperate T define the growth rate of the wire (i.e. number of layers per time [58, 57]). In general, E depends on the current polytype and the polytype of the new nucleus or layer respectively. In the frame of the wurtzite-zinc-blende polytypism, we therefore have to consider at least four nucleation barriers: $E_{WZ|ZB}$ and $E_{ZB|WZ}$ - the energy required to grow a wurtzite layer on top of a zinc-blende layer or vice versa; and $E_{WZ|WZ}$ and $E_{ZB|ZB}$ - adding a new layer of the current polytype without changing the stacking sequence. By the differences of these energy barriers $\delta E_{WZ|ZB} = E_{WZ|ZB} - E_{ZB|ZB}$ and $\delta E_{ZB|WZ} = E_{ZB|WZ} - E_{WZ|WZ}$ we can describe the polytypic behaviour of the growing nanowire in a statistical way as they define the probabilities for nucleating a new layer of the other polytype, or resuming growth in the current polytype. Already, we can estimate limiting cases: if $\delta E_{ZB|WZ} \ll \delta E_{WZ|ZB}$ the nanowires will exhibit almost pure zinc-blende phase with (or almost pure wurtzite for $\delta E_{ZB|WZ} \gg \delta E_{WZ|ZB}$). At the same time, the observation of stacking-faults and polytypism suggests $\delta E_{ZB|WZ}, \delta E_{WZ|ZB} \gtrsim k_B T$. However, the differences in the nucleation energies are hard to quantify since they require exact modeling of the nucleation mechanisms and droplet dynamics. One way to characterize structural polytypism in nanowires in a non-destructive way and to get access to the differences in the nucleation energies on a statistical level is X-ray diffraction.

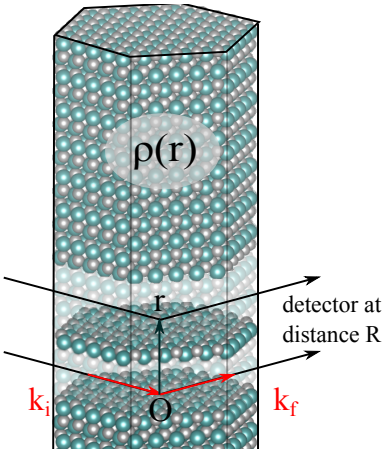

Figure 1.5: Illustration of a scattering process of incoming wave with wave-vector k_i at different positions r in the crystal with electron density $\rho(r)$. The different scattering centers cause a phase difference between the scattered waves $r(k_f - k_i)$ and lead to interference at the detector position R.

1.3 X-ray scattering from nanowires

Here, we shortly discuss X-ray scattering from surface nanostructures such as nanowires. In the following description we restrict to elastic scattering. Since our nanowires are comparably small (1 to 4 μm in length and 20 to 200 nm in diameter), we discuss scattering within the kinematic approximation (1. order Born approximation). Thereby, we neglect multiple scattering which has to be considered in case of large, defect-free crystals or X-ray experiments under grazing incidence conditions [109, 110]. As typical sample-detector distances R are in the range of meters and the size of our inspected sample r is in the range of several μm we consider to be in the far-field limit, $r \ll R$ so that the Fraunhofer approximation is valid. The size of the X-ray beam is sufficiently large, to illuminate a large number N_{NW} of nanostructures. We consider the coherence volume of the X-ray beam to be sufficient for complete coherent illumination of a single nanostructure, but to be smaller than the size of the X-ray beam.

For elastic scattering, we have energy conservation: $|\mathbf{k}_i| = |\mathbf{k}_f| = \frac{2\pi}{\lambda}$ and the scattering vector writes $\mathbf{q} = \mathbf{k}_f - \mathbf{k}_i$. Here, λ is the wavelength, and $\mathbf{k}_{i,f}$ are the wave-vectors of incident and outgoing waves. With the above assumptions, the amplitude of the scattering amplitude is given by [110]

$$S(\mathbf{q}) \propto \int \rho(\mathbf{r}) e^{i\mathbf{q}\mathbf{r}} d\mathbf{r} \tag{1.5}$$

and is proportional to the Fourier transform of the electron density $\rho(\mathbf{r})$ of the nanostructure. For an infinite, defect-free crystal, $S(\mathbf{q})$ is zero (within the 1. order Born approximation) unless the scattering vector is equal to a reciprocal lattice vector $\mathbf{G}_{hkl}$, with $\mathbf{G}_{hkl} \cdot \mathbf{r} = 2\pi m$, $m \in \mathbb{Z}$.

The diffraction condition $\mathbf{q} = \mathbf{G}_{hkl}$ is equivalent to Bragg's law.

For X-rays the location of the scattering center $\mathbf{r}$ is given by the location of the electrons in the solid crystal (the X-ray photons also interact with the atomic cores, however to a much lesser extent, which we will therefore neglect). For crystals with finite size composed of N_{uc} unit cells, the integral 1.5 reduces to a sum over all electron contributions contained therein. For a certain scattering center, $\mathbf{r}$ can then be expressed by the location of the unit cell in the crystal $\mathbf{r}_{uc}$, the location of an atom in the unit cell $\mathbf{r}_\alpha$, and the electron-distribution around this atom $\mathbf{r'}_\alpha$ as

$$\mathbf{r} = \mathbf{r}_{uc} + \mathbf{r}_\alpha + \mathbf{r'}_\alpha \tag{1.6}$$

and

$$S(\mathbf{q}) \propto \sum_{N_{\text{cell}}} e^{i\mathbf{q}\mathbf{r}_{uc}} \sum_\alpha \left(\int \rho(\mathbf{r'}_\alpha) e^{i\mathbf{q}\mathbf{r'}_\alpha} d\mathbf{r'}_\alpha \right) e^{i\mathbf{q}\mathbf{r}_\alpha} = \sum_{N_{\text{cell}}} e^{i\mathbf{q}\mathbf{r}_{uc}} \sum_\alpha f_\alpha(\mathbf{q}) e^{i\mathbf{q}\mathbf{r}_\alpha}. \tag{1.7}$$

Here, $f_\alpha(\mathbf{q})$ is the atomic form factor. We write the structure factor

$$F_{hkl}(\mathbf{q}) = \sum_\alpha f_\alpha(\mathbf{q}) e^{i\mathbf{q}\mathbf{r}_\alpha} \tag{1.8}$$

and the geometrical factor

$$L(\mathbf{r}_{uc}) = \sum_{N_{\text{cell}}} e^{i\mathbf{q}\mathbf{r}_{uc}}. \tag{1.9}$$

The structure factor $F_{hkl}(\mathbf{q})$ expresses the strength of a Bragg reflection, and the geometrical factor $L(\mathbf{r}_{uc})$ defines possible locations of allowed Bragg reflections in the reciprocal space.

Following [93], we will now derive the scattering from a single nanostructure, e.g. a single nanowire for a symmetric Bragg reflection $\mathbf{Q}_B$. Accounting for the finite size and the shape of the nanowire, we introduce the shape function $\Omega(\mathbf{r})$ which is unity inside the nanowire, and zero elsewhere. We split the nanowire into N_l bi-atomic layers consisting of Ga and As atoms perpendicular to the $[111]_c$ growth direction. The electron density of a nanowire writes then

$$\rho(\mathbf{r})_{NW} = \sum_l^{N_l} \Omega_l(\mathbf{r}_\perp) \sum_{\alpha \in \{Ga,As\}} \rho_{l\alpha}(\mathbf{r}_\perp, z_{l\alpha}). \tag{1.10}$$

$\Omega_l(\mathbf{r}_\perp)$ corresponds to the cross section of the wire in the $(111)_c$-plane and is defined by the diameter of the nanowire at layer l. The electron density of a single atomic sub-layer $l\alpha$ at height $z_{l\alpha}$ is $\rho_{l\alpha}$. The height $z_{l\alpha}$ depends on the atomic species and can be expressed as

$$z_{l\alpha} = z_l + \delta z_\alpha = \sum_{l=0}^{l-1} d_l + \delta z_\alpha \tag{1.11}$$

where z_l is the beginning of bi-layer l and δz_α is a vertical shift of the sub-layer, depending on the atomic species. For Ga atoms $\delta z_\alpha = 3/4 d_l$, whereas $\delta z_\alpha = 0$ for As atoms. d_l is the thickness of layer l and depends on the local polytype

$$3/4\ d_l = \begin{cases} 1/4\ c_{h1} & \text{for zinc} - \text{blende} \\ 3/8\ c_{wz} & \text{for wurtzite.} \end{cases} \tag{1.12}$$

We now restrict to q_z-profiles ($\mathbf{q}_\perp = 0$) in the close vicinity of a symmetric reflection $\mathbf{Q}_B$ and consequently approximate the atomic form factor with its value at the Bragg reflection $f_\alpha(\mathbf{q}) \approx f_\alpha(\mathbf{Q}_B)$. The scattering amplitude of a single nanowire then only depends on q_z

$$S_{NW}(\mathbf{q}) = S_{NW}(\mathbf{q}_\perp = 0, q_z) \propto \sum_l^{N_l} \tilde{\Omega}_l(\mathbf{q}_\perp = 0, q_z)\ e^{-iq_z z_l} \sum_{\alpha \in \{Ga,As\}} f_\alpha(\mathbf{Q}_B)\ e^{-iq_z \delta z_\alpha} \tag{1.13}$$

with the two-dimensional Fourier transform of the shape function $\tilde{\Omega}_l$. For our nanowires, we assume constant diameter over the whole length, therefore the shape function is layer-independent and becomes a constant pre-factor.

Finally we sum up all N_{NW} illuminated nanowires incoherently and obtain the intensity distrubution along q_z in the vicinity of a symmetric Bragg reflection $\mathbf{Q}_B$

$$I(q_z) \propto \sum_{N_{NW}} |S_{NW}(q_z)|^2. \tag{1.14}$$

As we can see from Eq. 1.9, the magnitude of the structure factor depends on the relative atomic positions in the respective unit cell. In Sec. 1.2 we have discussed the geometric differences between the GaAs polytypes zinc-blende, twinned-zincblende and wurtzite. Due to their different symmetry, the structure factors of wurtzite and zinc-blende GaAs differ. Here we approximate the atomic form factors by their atomic number and give the structure factor of a certain cubic reflection $(h,k,l)_c$ for cubic zinc-blende GaAs F^c_{hkl}:

$$F_{(hkl)_c} = (1 + e^{i\pi(h+k)} + e^{i\pi(h+l)} + e^{i\pi(k+l)}) \cdot (f_{As} + f_{Ga}\ e^{i\frac{\pi}{2}(h+k+l)}) \tag{1.15}$$

$$F_{(hkl)_c} = 4 \cdot \begin{cases} f_{As} + f_{Ga} \text{ if } h,k,l \text{ even and } h+k+l = 4n; n \in \mathbb{Z} \\ f_{As} - f_{Ga} \text{ if } h,k,l \text{ even and } h+k+l \neq 4n; n \in \mathbb{Z} \\ f_{As} \pm i f_{Ga} \text{ if } h,k,l \text{ odd} \\ 0 \text{ else} \end{cases} \tag{1.16}$$

and the structure factor of a wurtzite reflection $(hk.l)_{h,wz}$ for hexagonal wurtzite GaAs $F^{h,wz}_{hk.l}$

$$F_{(hk.l)_{h,wz}} = (f_{As} \cdot (1 + e^{-2\pi i(\frac{h+2k}{3}+\frac{1}{2}l)}) + f_{Ga} \cdot (e^{-2\pi i(\frac{3}{8}l)} + e^{-2\pi i(\frac{h+2k}{3}+\frac{7}{8}l)}). \tag{1.17}$$

If we restrict to symmetric reflections, $(00.l)_{h,wz}$, Eq. 1.17 becomes

$$F_{(00.l)_{h,wz}} = \begin{cases} 2 \cdot (f_{As} + f_{Ga}\ e^{-i\frac{3}{4}\pi l}) \text{ if } l \text{ even} \\ 0 \text{ else} \end{cases} \tag{1.18}$$

The structure factors of zinc-blende and wurtzite allow us to calculate the strength and the position in reciprocal space of Bragg-reflections suitable for studying polytypism in GaAs nanowires. Further discussions and detailed lists of allowed $(h, k, l)_c$ and $(hk.l)_{h,wz}$ reflections can be found in [93].

1.4 Modeling the vertical stacking of polytypic nanowires

In this section we briefly introduce a statistical model for the generation of stacking sequences of the atomic layers in a nanowire: a discrete-time Markov chain. The obtained structure will then be the basis for calculation of the X-ray scattering signal thereof using Eq. 1.14. The choice of a Markov model is motivated by the results from Johannson et al. [44, 111]. This Markov model and the thereby generated stacking sequences, as well as simulations of resulting X-ray scattering profiles of the $[\mathrm{nnn}]_\mathrm{c}$ reflection have been systematically studied by Martin Köhl. We now summerize his result provided in his PhD thesis [93] and in Ref. [112] insofar as they are required for the remainder of this manuscript.

The growth of GaAs nanowires can be described by successive nucleation of layers at the vapor-liquid-solid interface a the top of the nanowire [58]. Depending on the properties of the liquid-droplet and the liquid-solid interface there is a certain probability for a new layer to nucleate in wurtzite or zinc-blende phase [81]. However, modeling these probabilities requires certain assumptions on the dynamics of the nucleation process.

Since the transition probabilities for switching between the polytypes depend on the current polytype (compare Sec. 1.2), we have to consider at least the three topmost layers of the nanowire if we want to identify the type of a new layer to be added. This method is however not applicable for the beginning of the growth i.e. when the nanowire is composed of less than three layers. Hence, we assume a probability $p(0)_{wz}$ for the first three layers to nucleate in wurtzite stacking. After the initial three layers, we can identify the current polytype on top of which the next layer is added. If the type of layers n-1 and n-3 is the same (e.g. both are layers of type 'A'), then the current polytype is wurtzite. If the type of the layers differs, the current polytype is zinc-blende. The probability to add a new layer of wurtzite on top of a zinc-blende segment is $0 \leq p_{zb\to wz} \leq 1$, whereas the probability to continue in zinc-blende stacking is $1 - p_{zb\to wz}$. The same holds for the opposite case $0 \leq p_{wz\to zb} \leq 1$ of adding a zinc-blende layer on top of a wurtzite segment. This process in continued until a maximum number N_l of layers is reached. A schematic of this process is depicted in Fig. 1.6(a). Exemplary, stacking sequences of nanowires with $N_l = 4000$ layers have been created. This corresponds to a nanowire length of approx. $1.3\,\mu$m. The resulting distributions of wurtzite and zinc-blende segments obtained by the Markov-process considering layer-independent, static transition probabilities are shown in Fig. 1.6(b). Comparing the distributions of the three depicted examples for each set of parameters, a considerable fluctuation in the distribution of the segments can be observed. For the transition probabilities $p_{zb\to wz} = p_{wz\to zb} = 1\%$ longer segments are more likely than for $p_{zb\to wz} = p_{wz\to zb} = 3\%$, where the nanowires are built from many short segments. If we introduce asymmetric transition probabilities $p_{zb\to wz} \neq p_{wz\to zb}$ (e.g. $p_{wz\to zb} = 3\%$ and $p_{zb\to wz} = 1\%$) we observe that zinc-blende segments become longer than the wurtzite segments and the fraction of zinc-blende clearly exceeds that of wurtzite. Segment distributions for various parameters generated by the Markov-process introduced here can be found in Refs. [93, 112, 113].

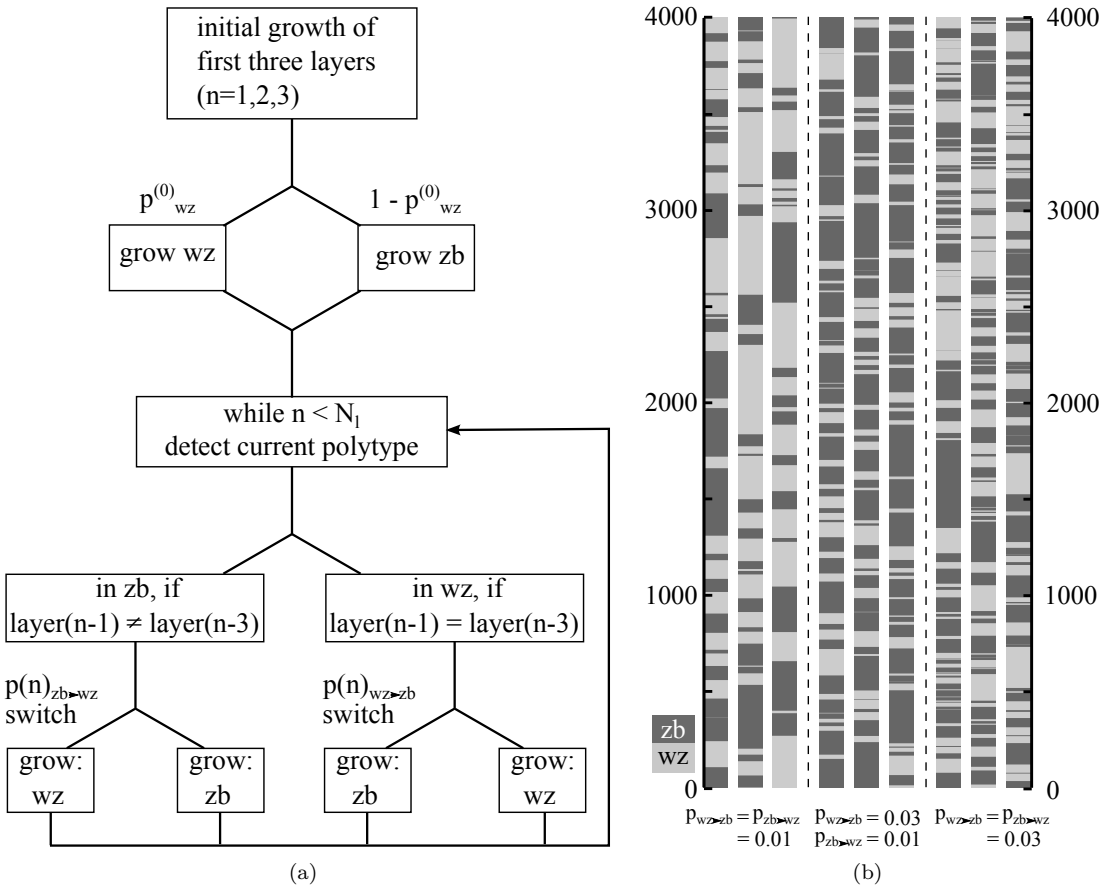

Figure 1.6: Illustration of the Markov-process for the generation of the stacking sequences (1.6(a)). Distribution of wurtzite and zinc-blende segments, obtained by a Markov-process for $p(0)_{wz} = 0.5$ and various transition probabilities $p_{zb\to wz}$ and $p_{wz\to zb}$. The generated stacking sequence contains $N_l = 4000$ layers (1.6(b)).

The transition probabilities $p_{zb\to wz}$ and $p_{wz\to zb}$ can be either static for the whole process or depend on the actual layer n. Thereby changes in external growth conditions which may affect polytypism can be incorporated in the model.

We now consider the probability for a faultless wurtzite segment of $n \geq 1$ layers starting from layer $n = 1$ in case of static transition probabilities. Therefore, the wurtzite stacking has to continue for n layers and switch to zinc-blende at layer $n + 1$:

$$p_{wz}(n) = C_N \left[\prod_{k=2}^{n}(1 - p_{wz\to zb})\right] p_{zb\to wz} \tag{1.19}$$

with C_N being the normalization constant of the probability distribution. For $n > 0$ we have an exponential distribution for

$$p_{wz}(n) = C_N(1 - p_{wz\to zb})^{n-1} p_{zb\to wz} \tag{1.20}$$

$$= C_N \frac{1}{1 - p_{wz\to zb}} e^{n \log(1-p_{wz\to zb})} \tag{1.21}$$

$$= \tilde{C}_N^{(wz)} e^{-\frac{n}{b_{wz}}} \tag{1.22}$$

with the decay-length

$$b_{wz} = \frac{-1}{\log(1 - p_{wz\to zb})} \overset{p_{wz\to zb}\ll 1}{\approx} \frac{1}{p_{wz\to zb}}. \tag{1.23}$$

In Eq. 1.19, n is an integer. The interpretation of Eq. 1.19 as an exponential distribution with mean segment length $\mu_{wz} = b_{wz}$ and $\tilde{C}_N^{(wz)} = 1/b_{wz}$ is however only valid for $n \in \mathbb{R}$ and is therefore an approximation. This approximation is valid for $b_{wz} \gg 1$ which is equal to the condition $p_{wz\to zb} \ll 1$ in Eq. 1.23.

We remain in the frame of layer independent transition probabilities, which allows us to define stationary limit of the wurtzite fraction $\tilde{p}_{wz}$ of the nanowires for $N_l \to \infty$ [93, 112]:

$$\tilde{p}_{wz} = \frac{1}{1 + \frac{p_{wz\to zb}}{p_{zb\to wz}}}. \tag{1.24}$$

The stationary limit of the wurtzite fraction does therefore not change upon simultaneous scaling of $p_{wz\to zb}$ and $p_{zb\to wz}$ and is always in the range $0 \leq \tilde{p}_{wz} \leq 1$. If the transition probabilities $p_{wz\to zb} = p_{zb\to wz} = 0$, the stationary limit of the wurtzite fraction is given by the initial probability $\tilde{p}_{wz} = p(0)_{wz}$. The influence of the initial probability causes a deviation of the average wurtzite fraction from the stationary limit. This deviation is the more pronounced the smaller the values of the transition probabilities and is discussed in detail in the PhD thesis of M. Köhl [93]. In the context of this thesis, the influence of the initial probabilities for cases $p_{wz\to zb} + p_{zb\to wz} \geq 0.015$ and $N_l \geq 2000$ is negligible.

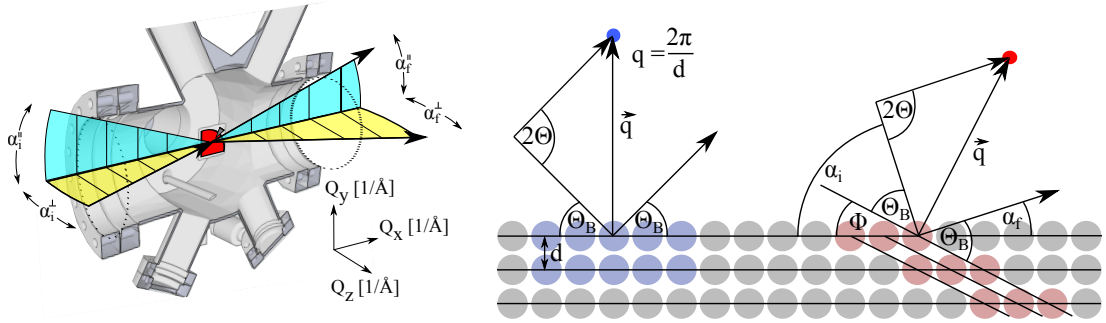

(a) The Be-windows of the growth chamber installed at opposite sides of the sample (sample depicted in red) limit the angular range accessible in X-ray experiments to $0° \leq \alpha_i^{\perp}, \alpha_f^{\perp} \leq 18°$ and $-18° \leq \alpha_i^{\parallel}, \alpha_f^{\parallel} \leq 18°$.

(b) Illustration of symmetric and asymmetric coplanar scattering geometry. In asymmetric coplanar geometry, the inclination angle ϕ of the Bragg planes towards the surface additionally increase or decrease incidence angle $\alpha_i^{\perp} = \Theta_B \pm \phi$ or outgoing angle $\alpha_f^{\perp} = \Theta_B \mp \phi$).

Figure 1.7: Accessible angular range for X-ray diffraction in the pMBE, and illustration of symmetric and asymmetric scattering geometry.

1.5 Capabilities of the portable MBE system for X-ray analysis

In this section we will discuss the capabilities of the portable MBE (pMBE) system [114] for X-ray analysis. This system is equipped with effusion cells for As, In and Ga as source materials and has been designed by the company Createc as a compact device which is easily transportable. The growth chamber features Be-windows transparent for X-ray radiation at opposite sides of the growth chamber (see Fig. 1.7(a)) which open an angular range of ±18° for X-ray measurements. In contrast to common MBE reactors, this system has a small and compact growth chamber in order to be compatible with heavy-load goniometer setups at synchrotron radiation facilities. As a result of the small size, a special design of the growth chamber and optimized arrangement of the components is required. The most obvious difference to common MBE growth chambers, besides the small volume of the growth chamber, is the sample position with the sample normal lying in the horizontal plane.

Previously, the pMBE system has been applied for *in-situ* grazing incidence diffraction and grazing incidence small angle X-ray scattering experiments at the surface diffraction beamline ID03 at the European Synchrotron Radiation Facility [114, 115, 116]. Subsequently, and supported by the epitaxy group of the Paul Drude Institut für Festkörperelektronik in Berlin, the system has been calibrated for the growth of GaAs nanowires on Si(111). For the present work, X-ray diffraction experiments at the NANO beamline at ANKA and the beamline P09 at DESY have been conducted.

The pMBE system features circular Be-windows which are transparent for X-ray radiation and thus facilitate X-ray experiments during MBE growth. In contrast to common MBE reactors,

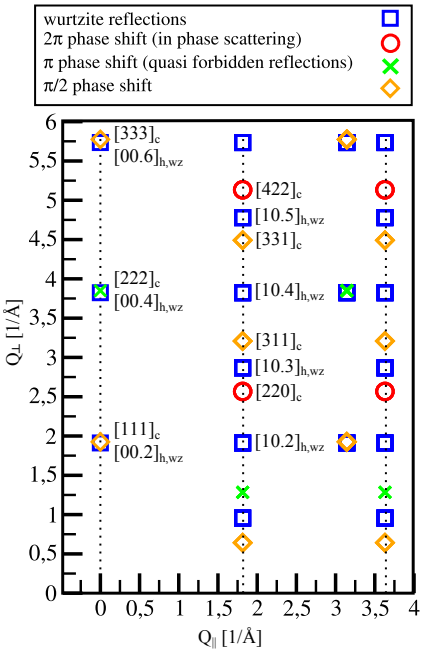

Symmetric coplanar geometry		
Reflection	Bragg angle	Angle to surface
$(111)_c$	7.27°	0
$(222)_c$	14.67°	0
$(333)_c$	22.32°	0
Asymmetric coplanar geometry		
Reflection	Bragg angle	Angle to surface
$(220)_c$	11.93°	35.26°
$(10.3)_{h,wz}$	13.17°	32.14°
$(311)_c$	14.03°	29.50°

Figure 1.8: Left: Reciprocal space of $[111]_c$-oriented GaAs nanowires (adapted from [93]). Some reflections of interest along the symmetric and the lowest order asymmetric truncation rod have been indexed. Right: Bragg angles for selected Bragg reflections and the angles to surface for the respective Bragg planes calculated for an X-ray energy of E = 15keV. For the limits imposed by the Be-windows, only the $(111)_c$ and $(222)_c$ reflections are accessible within coplanar geometry.

this system has a small and compact growth chamber in order to be compatible with heavy-load goniometer setups at synchrotron facilities in terms of weight and dimensions. As a result of the small size, a special design of the growth chamber and optimized arrangement of the components was required.

The angular range accessible in X-ray experiments is shown in Fig. 1.7(a). The x- and y-axes are parallel to the sample surface. The sample normal points in the direction of the z-axis. In case of GaAs nanowires grown on Si(111), the sample normal coincides with the $[111]_c$ direction. The out-of-plane angles $\alpha_i^\perp$ and $\alpha_f^\perp$ are bound from above by 18° and limit the accessible Bragg-reflections in symmetric co-planar geometry to reflections with $0 < \Theta_B \leq 18°$ at the respective X-ray energy. For the symmetric case, the Bragg planes are parallel to the surface and $\alpha_i^\perp = \alpha_f^\perp$ and are equal to the Bragg angle Θ_B if the Bragg condition is fulfilled. If we however consider asymmetric reflections in coplanar geometry we additionally have to account for the inclination angle ϕ of the Bragg planes towards the surface (and thereby increasing or decreasing incidence angle $\alpha_i^\perp = \Theta_B \pm \phi$ or outgoing angle $\alpha_f^\perp = \Theta_B \mp \phi$). This angular range alone sets limitations to accessible Bragg-reflections in coplanar geometry. Fig. 1.8 depicts Bragg reflections of GaAs nanowires grown on Si(111) substrates. The reflections for wurtzite

and zinc-blende GaAs coincide at the symmetric truncation rod with $Q_{\parallel} = 0$ Å^{-1} and can only be distinguished by the small difference in their vertical lattice constants. Since zinc-blende and its twin have the same lattice constants, they cannot be distinguished in a symmetric reflection. At the asymmetric truncation rod ($Q_{\parallel} \neq 0$ Å^{-1}), polytype *specific* reflections are located at different, well separated positions which allows obtaining information on each polytype (including twinned zinc-blende) separately. Here, only reflections in Bragg-geometry ($\alpha_{i,f}^{\perp} > 0°$) are considered (reflections in GID geometry, strictly Laue-geometry, are not depicted). As can be seen from the table in Fig. 1.8, the only reflections that are within the limits of the Be-windows are the $(111)_c$ and the $(222)_c$ reflection of which the $(222)_c$ is a quasi-forbidden reflection for GaAs, and strictly forbidden for Si. The asymmetric reflections are not available in *coplanar* geometry due to the large angle between the Bragg-planes and the surface.

Later we will discuss results of first *in-situ* X-ray experiments performed in symmetric geometry. Moreover, we will show and discuss data obtained later during *in-situ* studies of the $(220)_c$, $(311)_c$, $(1.03)_{h,wz}$ reflections performed in a special asymmetric *non-coplanar* geometry with a fixed incidence angle. Scans in the reciprocal space using this measurement geometry are possible by using only a rotation around the sample normal, and thus compatible with the angular range provided by our growth equipment. The geometry for these particular scans was developed by M. Köhl and is described in detail in his PhD thesis [93].

Comparable equipment for the growth of semiconductor nanowires compatible with *in-situ* X-ray methods is rare, and only few *in-situ* X-ray experiments investigating the growth of semiconductor nanowires exist presently [90, 117, 118].

2 Growth of self-catalyzed GaAs nanowires on Si(111)

The growth experiments presented in this section have been performed in the pMBE system introduced in Sec. 1.5. At the time this work started in 2011, there was no experience at ANKA in the growth of GaAs nanowires. Moreover, these experiments constituted the first attempts to grow nanostructures in such a pMBE system at all. For the first growth calibrations, this system was transferred to the Paul-Drude Institut für Festkörperelektronik in Berlin. As a result of this work, the growth of self-catalyzed GaAs nanowires on Silicon (111) has been established and the growth procedure was successfully transferred and repeated at the UHV-laboratory at ANKA. In this chapter, the routines for sample preparation and the growth experiments in the pMBE will be given. Effects of the substrate preparation, and the growth parameters on the morphology of the self-catalyzed nanowires will be discussed on the basis of SEM investigations and RHEED, and compared to reports from literature.

2.1 Sample preparation and growth protocol

All nanowires presented here have been grown in the self-catalyzed mode, where a liquid Ga droplet serves as material reservoir and induces the uniaxial growth according to the VLS model. As substrates p-doped Si (111) wafers provided by Crystek covered with a thin layer of silicon oxide have been used. This silicon oxide layer is of crucial importance for the formation of the Ga-droplets [78, 80], since it pins the droplets at certain positions on the surface. When applied on oxide-covered GaAs substrates, the Ga-droplets nucleate at pinholes in the oxide layer where an epitaxial relation to the substrate for the GaAs nanowire can be established, given that the oxide thickness does not exceed 30 nm [72]. Moreover, it has been found that the properties of the oxide layer like thickness, roughness and the chemical composition have a strong impact on the success of the growth and the morphology of the grown nanowires [119]. In order to control the thickness of the silicon oxide - layer a first series of Si(111) substrates were treated with HF which completely removed the native oxide. Subsequently the substrates were re-oxidised in a bath of 80 °C warm DI H_2O, continuously stirred and supplied by controlled flow of O_2 for several hours. Alternatively, the substrates could be exposed to air. This way, a silicon oxidelayer will

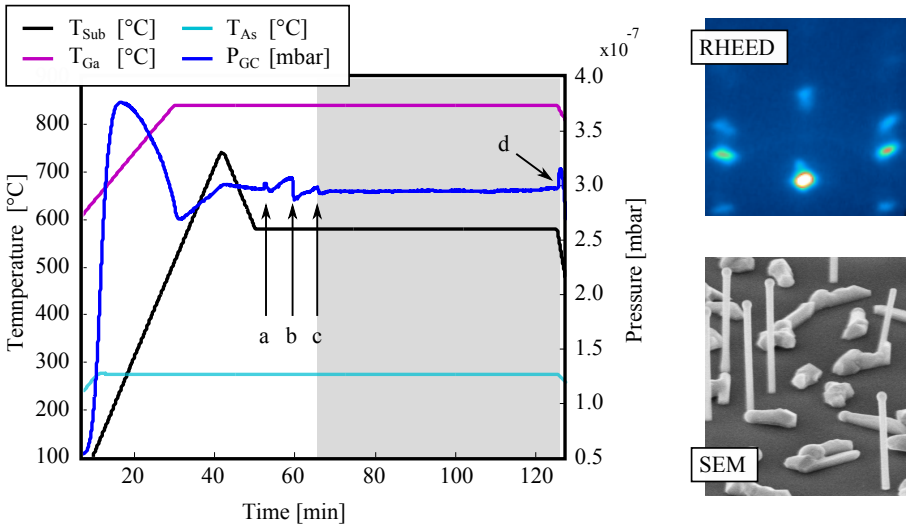

Figure 2.1: Background pressure in the growth chamber and temperatures of substrate heater and effusion cells, and motor actions during a representative NW growth cycle. The growth (gray area) is initiated with the opening of the Ga-shutter and stopped after 60 min by the simultaneous closing of all shutters. RHEED shows a typical electron diffraction pattern obtained at the end of the growth cycle indicating GaAs ZB and ZB-twin structures. Post-growth SEM images reveal vertical Nanowires featuring pronounced Ga-droplets and structures formed by lateral growth on the substrate surface.

grow up to approx. 1.5 nm under ambient conditions, in a couple of days [86, 120, 121].

The growth procedure will be discussed in the following on the example of a substrate that was re-oxidised for 5 hours by the water bath method. The substrate was loaded into UHV and degassed for 15 minutes. The substrate temperature was $T_S = 580\,°C$, the Ga flux was equivalent to a Ga limited 2D GaAs growth rate of $R_{GaAs} = 30\,nm/h$ and the ratio of As to Ga was approx. 2, calibrated by RHEED. The growth process has been recorded by the pressure and temperature sensors of the pMBE growth chamber and is displayed in Fig. 2.1: the substrate was heated to $T_S = 700\,°C$. This temperature was set in order to remove any residual impurities from the HF etching. After this step the substrate temperature was lowered to the growth temperature of $T_S = 580\,°C$. The shutter of the As evaporation cell was opened which causes the background pressure inside the growth chamber P_{GC} to increase until it stabilized at approximately $P_{GC} = 3 \cdot 10^{-7}$mbar (a). Until this step, a main shutter was protecting the substrate which was opened after the pressure stabilized (b). Subsequently, the Ga shutter was opened and the growth was initiated (c). After 60 minutes of growth, the growth was stopped by closing all shutters and decreasing the cell-temperatures T_{Ga} and T_{As} to their standby value and T_S to room temperature (d). At this time, the movement of the shutters causes a peak in the background pressure P_{GC}. After 5 minutes the background pressure reaches $P_{GC} = 6 \cdot 10^{-8}$mbar and $T_S = 200\,°C$. Approximately 30 minutes after the growth was finished, the substrate was

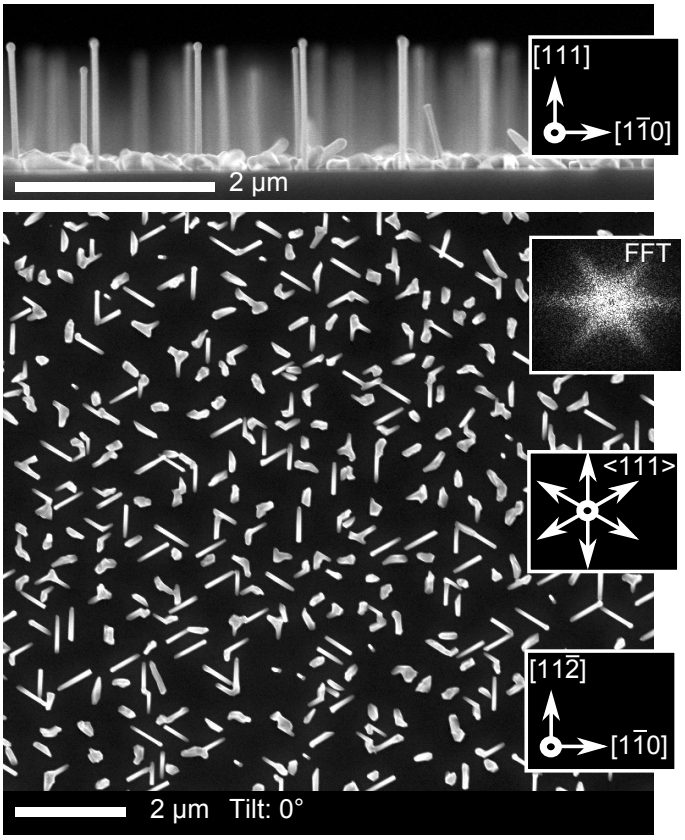

Figure 2.2: Epitaxial alignment: A fast-Fourier-transform (FFT) of the top-view SEM image indicates a sixfold symmetry, implying the existence of preferred growth-directions of GaAs structures besides the [111] surface-normal. The [111]-oriented silicon surface has equivalent directions <111>, which are here projected in the (111)-plane as shown in the inset. Most tilted nanowires grow along these alternative directions. The majority of the in-plane growth is oriented along [11$\bar{2}$] and [$\bar{1}$1$\bar{2}$] and equivalent directions.

taken out of ultra-high vacuum for SEM characterization.

In Fig. 2.1, a RHEED image is depicted which was taken at the final growth stage. The beam was incident along the [1$\bar{1}$0] azimuth and shows the characteristic diffraction patterns of the cubic zinc blende structure with rotational twins. This implies, that the grown GaAs structures have epitaxial alignment with the substrate and have grown predominantly in cubic zinc-blende. The SEM image shows the structures grown in the central region of the substrate. Besides faceted crystallite-like structures, elongated wires can be observed. Some of the wires have grown along the [111]-direction and are vertically oriented, whereas others seem to grow along certain directions parallel to the surface. All vertical nanowires, as well as their counterparts lying on the substrate show a spherical droplet on their tips. In case of the vertical nanowires, the droplet makes a contact angle $\beta = 115° \pm 6°$ with the (111)-top facet. The droplet diameter exceeds

the diameter of the vertical nanowires. In average the droplets are approximately $90\,\mathrm{nm} \pm 8\,\mathrm{nm}$ in diameter. The vertical nanowires have a large aspect ratio corresponding to a height of $h = 1.1\,\mu\mathrm{m} \pm 0.2\,\mu\mathrm{m}$ and a diameter of $d = 62\,\mathrm{nm} \pm 5\,\mathrm{nm}$.

Fig. 2.2 shows a side-view as well as a top-view SEM image which gives a better overview of the grown sample. For SEM, the wafers were cleaved in order to obtain images of the center region of the sample. From the side-view, we can nicely identify the vertical non-tapered nanowires with pronounced Ga-droplets on top. Close to the surface, a layer of non-vertical GaAs crystallites can be seen. In contrast to Au-catalyzed GaAs nanowires grown on GaAs, the crystallites do not form a coherent layer but remain individual objects, as can be seen from the top-view image. Here, a distinct orientation of the traces on the surface can be observed, implying an epitaxial relation of the grown traces to the Si(111) substrate. Why these traces, which obviously grow in VLS mode, too, did not grow into vertical nanowires is most likely caused by the morphology of the nucleation site and the wetting angle of the Ga-droplet. Besides these elongated VLS grown traces, other GaAs crystallites are visible which are not connected to a Ga-droplet and show a rather complicated shape.

2.2 Epitaxial alignment, polytypism and faceting of self-catalyzed GaAs nanowires observed by in-situ RHEED

RHEED as a highly surface-sensitive technique is commonly applied in MBE in order to monitor the growth of thin films at the monolayer scale, or in order to investigate near surface nanostructures like quantum dots. RHEED, due to the high energy and the large scattering cross section of the electrons with matter, allows to measure e.g. a 2D-layer growth-process with single monolayer resolution, and moreover gives information on the atomic ordering of the surface of the substrate. In this thesis, RHEED has been applied to calibrate the pMBE system's 2D layer growth rate of GaAs as well as the ratio of arsenic vs gallium for certain substrate temperatures. In case of vertical free-standing nanowires, the information obtained by RHEED is contained in diffraction spots, similar to X-ray diffraction in the Laue case (transmission geometry), and includes information on epitaxial alignment of the GaAs structures, polytypism and faceting. In case of epitaxial alignment with the crystalline Si(111) substrate, the diffraction spots are aligned along truncation rods perpendicular to the substrate surface. Is the epitaxial alignment missing, a Debye-Scherrer ring would be observed – like in powder X-ray diffraction – indicating randomly oriented GaAs crystallites. Whether a GaAs crystallite can be epitaxially connected with the substrate and will evolve to a nanowire or not, crucially depends on the nucleation site and thus the oxide layer covering the crystalline Si(111) substrate. If the oxide layer is too thick, no nanowire growth may be possible. In a study of Fontcuberta i Morral et al. [72], the authors investigated the growth of GaAs NWs using a sputtered oxide layer on top of GaAs(111) substrate. They found a critical oxide layer thickness of $d_{crit} = 30\,\text{nm}$ above which no epitaxial alignment could be obtained.

The thickness of the oxide layers used in the present study are well below this critical value. Thus, epitaxial alignment with the underlying Si(111) substrate is expected to be possible. As an example, we show two different RHEED measurements obtained from samples grown on different substrates under different conditions, in order to discuss the epitaxial alignment of the nanowires and crystallites, polytypism and faceting of the nanowire side-walls. Fig. 2.3 shows RHEED patterns taken during growth of GaAs nanowires on Si(111). The Ga flux was set to obtain a 2D growth rate of $R_{GaAs} = 30\,\text{nm/h}$ which results in a V/III ratio of approx. 2. The oxide of the substrate used for this growth was removed and then re-oxidised as described above resulting in a very thin oxide layer.

Due to the thin oxide cover, diffuse elongated streaks in RHEED can be observed in the $[1\bar{1}0]$ azimuth instead of the 7x7 reconstruction which would be expected for a clean Si(111) surface, prior to the growth. During the growth of GaAs nanowires, the streaks transform into diffraction spots which can be attributed to zinc-blende and twinned zinc-blende GaAs in the nanowires as well as in the crystallites. Additional weak spots are visible in the $[1\bar{1}0]$ azimuth at positions

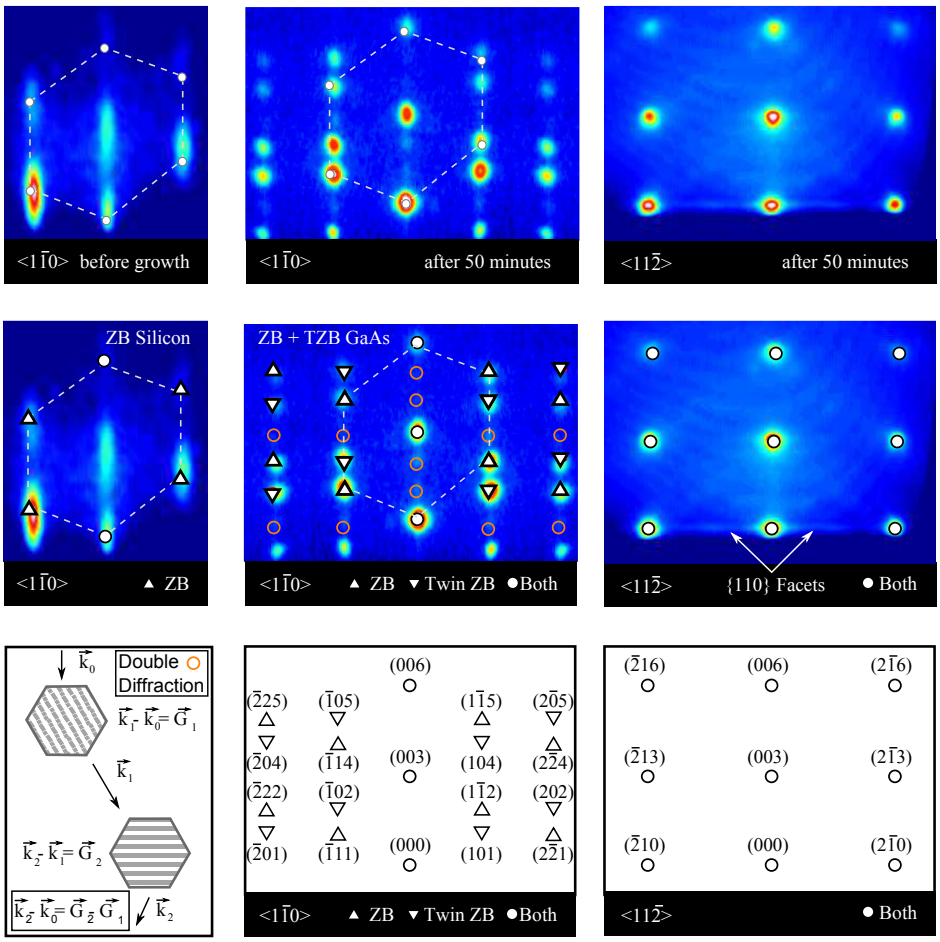

Figure 2.3: RHEED pattern containing reflection spots originating from zinc-blende and twinned-zinc-blende segments during growth

that correspond to forbidden reflections of zinc-blende and twinned zinc-blende. The presence of these diffraction spots can be readily explained by double or multiple diffraction at twinned and non-twinned zinc-blende GaAs. In case of double diffraction, the incident electron diffracts at a zinc-blende element and afterwards diffracts again at a twinned zinc-blende element which is rotated with respect to the first element by 60°.

The reflections are indexed in the hexagonal surface coordinate system $[h,k,l]_h$. The translation rule from the cubic $(h,k,l)_c$ to hexagonal surface system is performed via

$$\begin{pmatrix} h \\ k \\ l \end{pmatrix}_h = \mathbf{M_{c\to h}} \begin{pmatrix} h \\ k \\ l \end{pmatrix}_c \quad \text{with} \quad \mathbf{M_{c\to h}} = \begin{bmatrix} 1/2 & 0 & -1/2 \\ -1/2 & 1/2 & 0 \\ 1 & 1 & 1 \end{bmatrix} \tag{2.1}$$

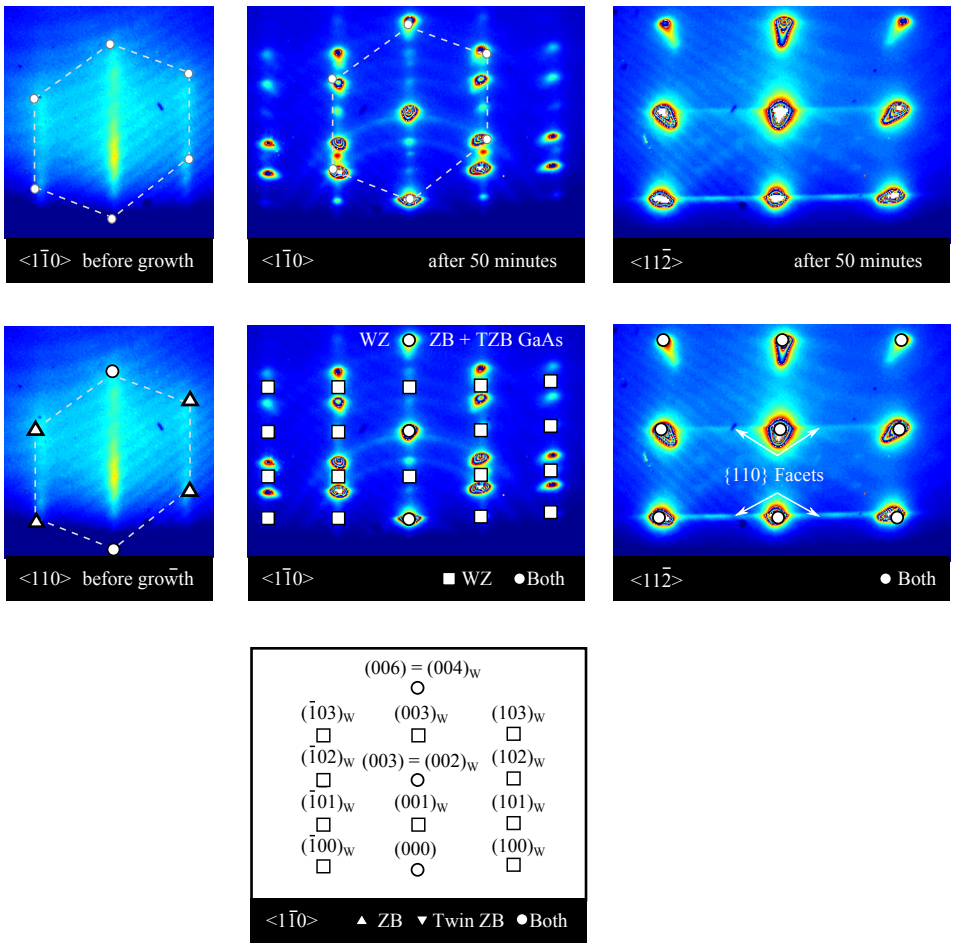

Figure 2.4: RHEED pattern showing wurtzite signals as well as zinc-blende and twinned zinc-blende during growth.

Let $\vec{k_0}$ be the incident wave vector of the electron. After diffraction at the first zinc-blende element, the wave vector writes $\vec{k_1} = \vec{k_0} - \vec{G_1}(h_1, k_1, l_1)_h$ and becomes $\vec{k_2} = \vec{k_1} - \vec{G_2}(h_2, k_2, l_2)_h$ after diffraction at the second element. If the second zinc-blende element is twinned, then $\vec{k_0} - \vec{k_2} = \vec{G}(H, K, L)_h$, where $H = h_1 - k_2, K = k_1 + k_2 + h_2$ and $L = l_1 + l_2$. The diffraction spot at the forbidden $(004)_\mathrm{h}$ reflection is thus the result of double-diffraction at $\vec{G_1} = (2, 0, 2)_h$ and $\vec{G_2} = (\bar{2}, 2, 2)_h$.

The $[11\bar{2}]$ azimuth on the other hand, shows no spots arising from double diffraction since here, the reflections of twinned zinc-blende and zinc-blende, and wurtzite coincide at the screen. Interestingly, another feature is visible in this particular substrate orientation: originating from reflections at the symmetric (0,0,l) truncation rod, horizontal streaks are visible which can be attributed to un-polar GaAs (110)-type facets constituting the vertical nanowire side walls.

Fig. 2.4 shows RHEED patterns of the growth of another sample. Here, the nanowires

were grown on a native oxide layer using a Ga flux equal to $R_{GaAs} = 50\,\mathrm{nm/h}$ layer growth rate and a V/III Ratio of approx. 7. In addition to zinc-blende and twinned zinc-blende GaAs diffraction spots in the $[1\bar{1}0]$ azimuth, we observe signals arising from the hexagonal wurtzite GaAs, indicating that high V/III ratios favor the nucleation of wurtzite in this case. Comparing the RHEED patterns in Figs. 2.3 and 2.4, we find that the WZ reflections of the (k 0 l) - truncation rods, for $k \neq 0$ and $l = 0, 2, 4, ...$ coincide with the spots from double diffraction, and therefore both scattering mechanisms contribute to the intensity of these reflections and have to be taken into account if a quantitative analysis of the RHEED patterns is to be done.

Besides the diffraction spots of twinned zinc-blende and zinc-blende, and wurtzite, Debye-Scherrer rings are visible, passing through the twinned zinc-blende and zinc-blende diffraction spots, but no rings, passing through the wurtzite peaks can be detected. Comparing the $[11\bar{2}]$ azimuth, the Debye-Scherrer rings are present as well. Since the presence of these rings therefore does not depend on the azimuth, they can be attributed to scattering from randomly oriented twinned zinc-blende and zinc-blende structures on the substrate surface, similar to the diffraction signal known from powder X-ray diffraction.

In summary, we shortly explained the RHEED patterns of GaAs nanowires grown on 111 oriented Silicon substrates. We discussed the epitaxial relation of the grown GaAs structures and observed the GaAs wurtzite-zinc-blende polytypism. In case of the native oxide layer, twinned zinc-blende and zinc-blende structures give rise to a Debye-Scherrer signal indicating missing epitaxial relation to the substrate, whereas no Debye-Scherrer ring for the wurtzite polytype occurs. We attribute the sharp diffraction spots of wurtzite, twinned zinc-blende and zinc-blende GaAs to the epitaxially grown nanowires, and the Debye-Scherrer signal to randomly oriented crystallites at the surface. As second indication for the epitaxial alignment of the nanowires, we observe pronounced streaks in the [11-2] azimuth originating from the symmetric diffraction spots. These streaks are caused by the truncation of the crystalline volume by the nanowire (110)-type side facets equal to the crystal truncation rods, as commonly observed in RHEED for e.g. flat crystalline GaAs(001) surfaces.

2.3 The silicon oxide layer: the role of substrate preparation

In the growth process of self–catalyzed III–V nanowires, the thin oxide layer constitutes an important free parameter [122]. Properties like its chemical composition, thickness, and roughness, have impact on the nucleation site of the Ga droplets and influence the size, and the density of the grown nanowires [119, 79, 53, 77, 123]. Eventually, it is the thin oxide–layer that decides whether the nanowire growth succeeds or fails (given, that the growth conditions like V/III ratio and substrate temperature are within a growth window otherwise suitable for nanowire growth [119]). There are various approaches for the preparation of the surface Silicon oxide layer, for example the sputter–deposition and successive etching using a Hydrofluoric–acid (HF) solution [72, 38], or preparation steps that involve the use of Hydrogen Silsesquioxane (HSQ) together with a subsequent annealing step [124, 75]. Common for both approaches was the observation of a critical layer–thickness, above which no wire growth was observed. For the above two cases, these critical thicknesses differed: $d_{crit} = 30\,\text{nm}$ was found for the sputtered oxide [72] and $d_{crit} = 5\,\text{nm}$ was found for the oxide obtained by thermal sublimation [75]. Another way to achieve very thin oxide–layers consists of an etching step using 5%HF in order to completely remove the oxide from the Si(111) wafer. In a subsequent step, the oxide is regrown by exposing the wafers to air for several days or insertion in a warm water bath for several hours. With such regrowth preparation, usually very thin oxide layers below the critical thickness can be prepared [86, 120, 121].

If the oxide-layer is too thin, the growth of nanowires may still be possible, however the density of parasitic crystallites is strongly increased [77].

2.3.1 Growth of nanowires on oxide-layers with varying thickness

For *in-situ* X-ray growth studies a high yield of vertical nanowires at minimal parasitic growth of crystallites is favorable. In the following section, we therefore compare density and crystal sizes of the parasitic growth on several nanowire samples in dependence of the oxide thickness. Oxide layers with varying thickness were achieved by adjusting the time for which the substrates were kept in 80 °C warm water from 180 minutes to 465 minutes, after the samples have been etched for minutes in 5% HF. All samples have been grown under otherwise identical growth conditions for 60 minutes using a Ga flux of 30 nm/h equivalent 2D GaAs growth rate and a high V/III ratio of approx. 5, at $T_S = 580\,°\text{C}$. These samples are then compared to a sample grown on native oxide.

Representative side-view SEM images of these samples in Fig. 2.5(a) show vertical, thin nanowires without visible tapering and surface near crystalline chunks with a surface density of approx. $1/\mu\text{m}^2$. Since the growth parameters were the same for these samples, the influence on the diameter of the nanowires is a result of teh varying oxide thickness. Consequently, we

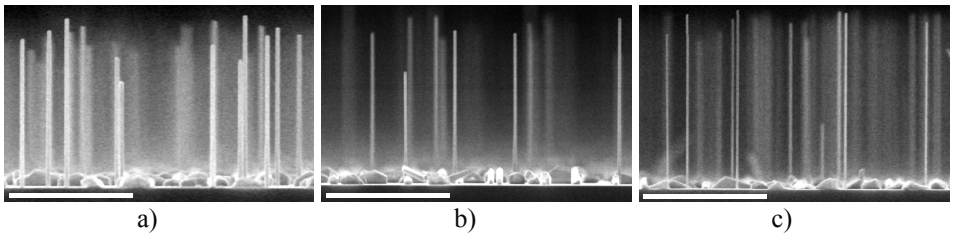

(a) Nanowire ensembles grown by identical f_{As} and f_{Ga} and T_S on substrates with different oxidation time: a) 180 minutes, b) 300 minutes and c) 465 minutes. The length scale is 2 µm.

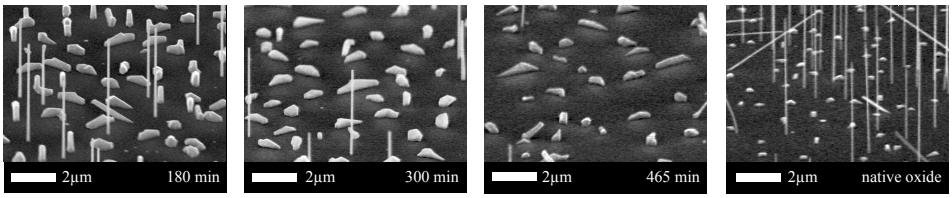

(b) Tilt-view SEM images of the oxidation time series. From such images, the density as well as the size and shape of the crystallites can be estimated. The growth of parasitic crystallites for a fixed set of growth parameters was influenced by the conditioning of the oxide layer only. For 180 min oxidation time, long and thick cystallites can be observed. By increasing the oxidation time, the parasitic growth is suppressed and the crystallites shrink in size.

Figure 2.5: In Fig. 2.5(a), side-view SEM images of the grown nanowires which are part of the oxidation series are depicted. On the bottom in Fig. 2.5(b), SEM images are shown from which the parasitic growth can be estimated. For comparison, a nanowire sample grown under the same conditions on Si(111) covered native oxide is depicted at the right.

evaluated the diameters and heights of nanowire ensembles grown on substrates with different oxidation time in detail. The result regarding the diameter obtained from measuring at least 10 nanowires per sample and is presented in Fig. 2.6(a). Starting from $d_{180min} = 61\,\text{nm} \pm 7\,\text{nm}$ the diameter decreases monotonously over $d_{300min} = 50\,\text{nm} \pm 4\,\text{nm}$ to $d_{465min} = 41\,\text{nm} \pm 5\,\text{nm}$. For comparison, the mean diameter of nanowires grown on native oxide $d_{native} = 25\,\text{nm} \pm 2\,\text{nm}$ is depicted. In contrast to the diameter, the height of the nanowires is less affected by the difference in substrate preparation. As depicted in Fig. 2.6(b), the mean height of the nanowires after 30 and 60 minutes of growth on native oxide are $h_{native,30min} = 1161\,\text{nm} \pm 198\,\text{nm}$ and $h_{native,60min} = 2456\,\text{nm} \pm 355\,\text{nm}$ respectively, which is reproduced by the nanowires grown on re-oxidised substrates.

Given, that the substrate temperature T_S and fluxes of gallium and arsenic are the same for these samples presented here, the observed effects relate to the difference of the oxide layers. For the diameter of a nanowire, the initial size of the Ga-droplet is relevant. The size of the Ga-droplet can be increased by both direct impingement of Ga atoms from the molecular beams and arrival of Ga adatoms via surface diffusion. Since the direct impingement can be controlled by the Ga-flux and is kept constant, we consider the latter factor to be responsible for the change in diameter: At constant T_S the chance of a Ga adatom to get incorporated into the liquid depends

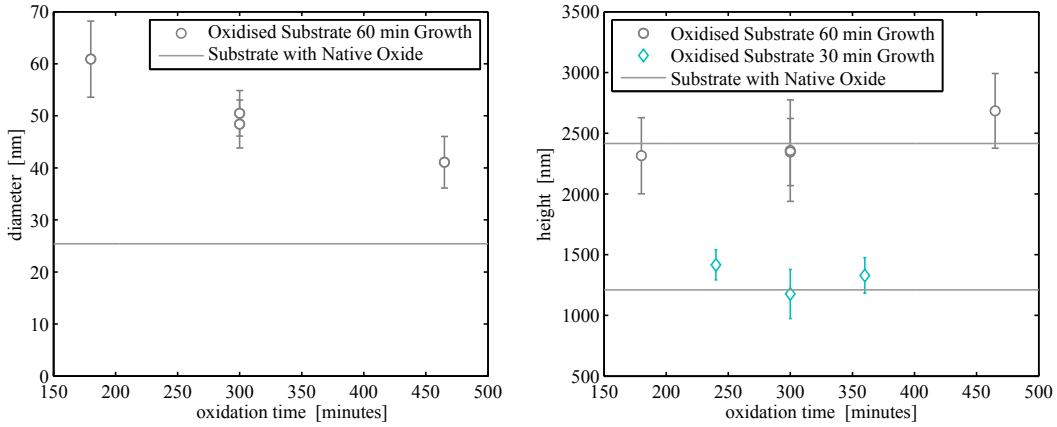

(a) Mean diameter of nanowire ensembles grown on substrates after various oxidation times. The mean diameter corresponding to nanowires grown on SI(111) covered by native oxide is given by the solid line.

(b) Mean heigth of nanowire ensembles grown on substrates after various oxidation times. Circles correspond to a growth time of 60 minutes, diamonds show the height after 30 minutes of growth. The solid line gives the mean heigth of nanowires grown for 30 minutes and 60 minutes on native oxide.

Figure 2.6: Mean height and diameter of nanowire ensembles grown on substrates after various oxidation times. The solid line indicates the mean value obtained for GaAs nanowires grown on native oxide. As the nanowire diameter decreases monotonously with increasing oxidation time and oxide layer thickness, approximating the value obtained for native oxide, the final height of the nanowires seems to be unaffected by the thickness of the oxide layer.

on its lifetime (until the adatom gets desorbed) and on the adatom's surface mobility, which in turn depends on the surface roughness [125, 126, 127]. Consequently, an increase in surface roughness with increasing oxidation time and oxide layer thickness causes the adatom mobility to decrease which results in a reduced size of the Ga-droplet after a certain time. This implies that the oxides grown in the re-oxidation procedure have a lower thickness than the native oxide layer but gradually approach the thickness of the native oxide by increasing the oxidation time. In contrast to the diameter, the final height and therefore the axial growth rate of the nanowires remains unaffected by the substrate preparation within the margins of error.

After inspecting the geometrical properties of the grown *nanowires*, we now evaluate, if the growth of *crystallites* is effected by the different oxidation times. Since the geometry of the nucleation site decides whether a Ga-droplet grows into a vertical nanowire or becomes a crystallite [119, 79], a variation of the oxide-layer thickness and its roughness is likely to show an effect. In Fig. 2.5(b), SEM images recorded at 60° angle of view give an idea of the morphology of the crystallites. The sample with the lowest oxidation time shows large, and elongated crystallites measuring approximately 500 nm by 100 nm by 200 nm. These crystallites are elongated in-plane along the $[11\bar{2}]$ and $[\bar{1}\bar{1}2]$ or equivalent directions. With increasing of the oxidation time, the aspect ratio decreases until a minimal value is reached for the growth on native oxide. In Fig. 2.7(a) the length distribution of the crystallites is depicted. Here, the length corresponds to the

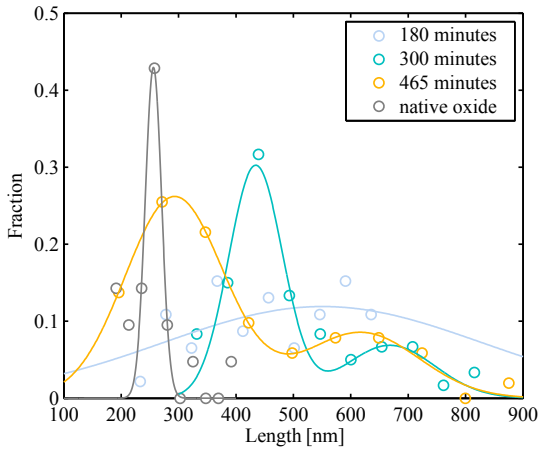

(a) Length distribution of the parasitic crystallites grown on substrates with oxide-layers obtained by different oxidation-times and a growth on native-oxide as reference (circles). The solid lines are Gaussian-fits. In two cases the length-distribution is bi-modal (see discussion in the text).

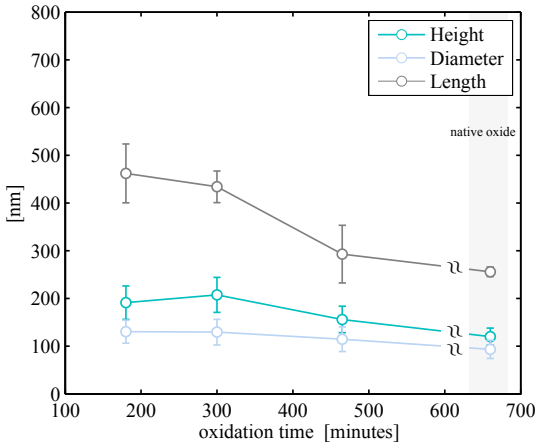

(b) Mean values of length, diameter and height of the crystallites grown on different substrates with different oxidation time, and the native oxide as reference.

Figure 2.7: The length distribution and mean length, height and diameter of parasitic crytallites are depicted. A bi-modal distribution is observed for the samples which have been re-oxidised for 300 min and 465 min. This is most likely caused by a merger of neighboring crystallites growing in opposite directions on the surface. In general the mean volume of the parasitic crystallites decreases with increasing oxidation time. The best result for the applied growth conditions was obtained for native-oxide substrates.

largest in-plane extension of the respective crystallite. For each sample up to 60 but at least 20 crystallites have been investigated. Starting with a length of $l_{180min} = 462\,\text{nm} \pm 62\,\text{nm}$ the length decreases to the minimal value of $l_{nat.oxide} = 250\,\text{nm} \pm 10\,\text{nm}$ in case of the native oxide. The length distributions for the oxidation times of 300 and 465 minutes exhibit a second maximum at approx. two times of the value of the mean length respectively. Many of these longest crystallites show a slope towards their center where they exhibit a peak and may be the result of coalescence of two crystallites growing laterally in opposite directions, visible in SEM. In Fig. 2.5(b) several of such mergers can be observed.

In contrast to these two samples, the bi-modal length distribution is not observed for the lowest oxidation time, although such long crystallites are visible in the SEM pictures. In case of the native oxide layer, the length distribution is sharp which suggests that lateral growth of the crystallites has been hindered, therefore the coalescence of crystallites is unlikely and a bi-modal length distribution is not observed. By measuring the height and the extension perpendicular to the elongation direction as shown in Fig. 2.7(b), we can estimate the average volume of a crystallite depending on the oxidation time. By further increasing the oxidation time, the average crystallite volume could be reduced by a factor of 2. By using substrates covered by native oxide, the average volume could even be reduced by a factor of 4, for these particular growth conditions.

2.3.2 The effect of Ga pre-deposition on the growth of self-catalyzed GaAs nanowires grown on substrates with varying oxide-layer thickness

Another way to condition the oxide layer is the so-called Ga polishing [128, 86] also referred to as Ga pre-deposition. In this procedure, the Si substrate is exposed to a Ga beam in the MBE growth chamber and subsequently heated before the GaAs nanowires are grown. During the heating, the silicon-oxide is converted to gallium-oxide by the following processes [129, 122]:

$$SiO_2 + 4Ga \rightarrow Si + 2Ga_2O$$

$$SiO_2 + 2Ga \rightarrow SiO + Ga_2O$$

The gallium-oxide is thermally less stable and evaporates from the substrate at around $T_S = 582\,°C$ [130]. If not the complete gallium is used up in this reaction, the remaining Ga will form small liquid droplets, which will act as possible nucleation sites for GaAs nanowires or crystallites. On the substrates treated with this procedure 4 monolayer (ML) of Ga were deposited at $T_S = 580\,°C$. Afterwards, the substrate was heated above $T_S = 700\,°C$ and cooled down to $T_S = 580\,°C$ again where the growth of GaAs nanowires was performed. The samples have been grown for 60 minutes using a Ga flux of 30 nm/h GaAs growth rate and a V/III ratio of approx. 5. The SEM images in Fig. 2.8 show GaAs nanowires and crystallites grown on a 300min re-oxidised substrate. The left panel of Fig. 2.8 shows the result of a regular growth, whereas the grown structures after additional Ga pre-deposition are depicted in the right panel. Although no effect on the final length of the nanowires is visible, the number density of wires as well as of crystallites changes dramatically. In the same field of view, four times more nanowires, 164 compared to 40, have been grown using the Ga pre-deposition on the 300 min re-oxidised substrate and the number of crystallites has reduced from 884 to 472 objects. Effectively the overall nucleation density has been reduced by a factor of 2/3. Further, the mean diameter of the nanowires grown after Ga pre-deopsition have increased from $d_{regular} = 50.5\,\text{nm} \pm 4.4\,\text{nm}$ to $d_{Ga-pre} = 60.9\,\text{nm} \pm 10.8\,\text{nm}$. With regard to the total number of nanowires, the volume represented by GaAs in vertical wires could be increased by factor or 6.

In average, we observe an increase of the nanowire diameter in case of Ga pre-deposition about $\delta d = 9.7\,\text{nm} \pm 2.7\,\text{nm}$ equivalent to an increase of approx. 22% compared to the nanowire diameters obtained by regular growth without any change in nanowire length. The average increase in diameter of approx. +22% leads to an average volume increase of approx. +49% for the wires. If we finally assume, that the average volume increase also holds for the crystallites, the reduction of the overall nucleation density is compensated by the average volume increase each individual nanostructure resulting in a preservation of the deposited GaAs material. This effect however, is most pronounced at the re-oxidised substrates. For nanowires grown on the Si substrates with native oxide for instance, the diameter increase was approx. $\delta d = 3\,\text{nm}$ or +12%.

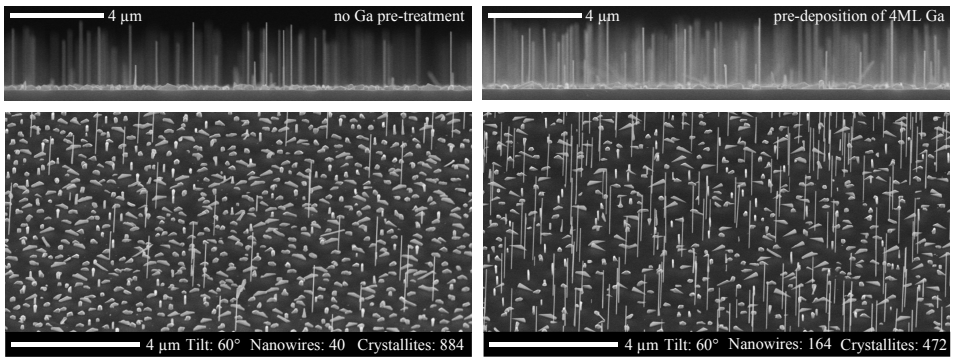

Figure 2.8: Morphology of grown nanowires on Si(111) substrates, reoxidised for 300 minutes without (left) and with gallium pre-deposition (deposition of 4ML Ga and successive annealing, right). For this sample, the gallium pre-deposition shows a positive effect on vertical yield of nanowires and reduces the parasitic growth. In the same area, 40 nanowires could be counted if the sample was grown regularly. In case of gallium pre-deposition, the number of nanowires was increased to 164. At the same time, the number of crystallites has been reduced from 884 to 472.

We now investigate the effect of oxidation time and Ga pre-deposition on the nucleation density. Therefore, nanowire and crystallite densities in the center of the wafer have been evaluated from several SEM images resulting in inspected areas ranging from $150\,\mu m^2$ to $350\,\mu m^2$. In Fig. 2.9 these results are summarized. The nanowire density decreases with increasing oxidation time if Ga pre-deposition is applied. Although Ga pre-deposition has a positive effect on the nanowire density at the wafers with thin oxide, the effect becomes negative and reduces the nanowire density in case growing on the native oxide. Similar observations can be made for the crystallites. Whereas Ga pre-deposition reduces the crystallite density for the 300 min re-oxidised sample, the density increases drastically when the Ga pre-deposition is applied to the substrate covered by native oxide. Regarding the overall nucleation density, the effect of the Ga pre-deposition treatment is most pronounced on the native oxide, whereas only little changes in the overall nucleation density in case of the re-oxidised substrates can be observed. The drastic increase in nucleation density on the native oxide could be explained by the etching process described above. Due to the high lattice mismatch, the deposited gallium will not form a wetting layer on the oxide, but will form small liquid droplets [123]. At growth temperature, these droplets will move around on the surface until they get pinned to defects on the oxide layer. At these positions, the gallium can locally etch the silicon oxide and thus create additional nucleation sites. However, it appears, that under the investigated growth conditions, these additional nucleation sites and the increased size of the Ga-droplets due to the additional supply of Ga favor the growth of crystallites and tilted nanowires.

Regarding the re-oxidised substrates, almost no change in the overall nucleation density can be observed. This could be due to the fact, that the oxide layer is already very thin and there are sufficient nucleation sites available where the droplets can settle even without any etching. Here

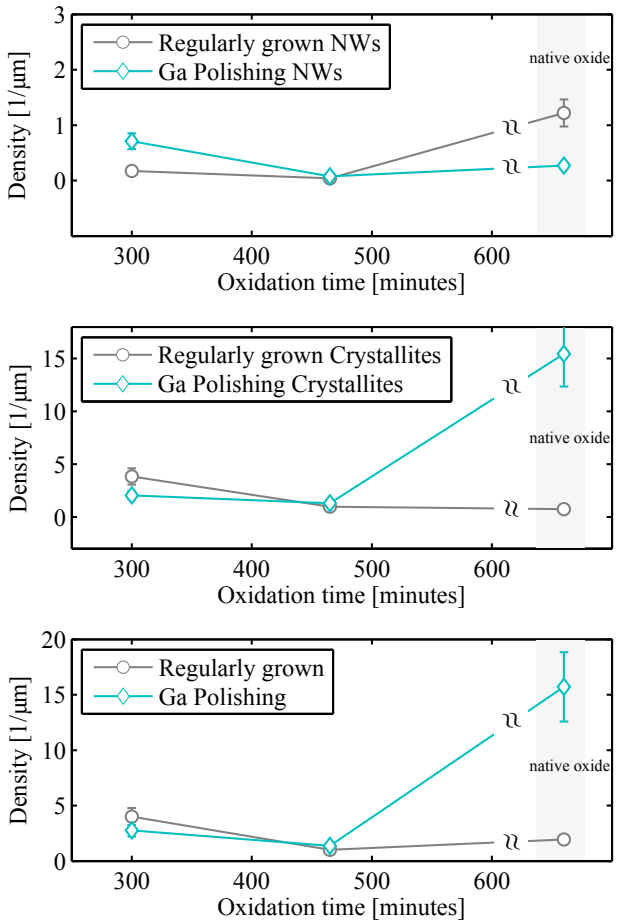

Figure 2.9: Nucleation density of nanowires, crystallites and both structures obtained for regular growth and growth after Ga pre-deposition with successive annealing. Whereas the vertical yield increases by additional gallium in case of very thin oxide layers, it promotes crystalline growth when applied on native oxide substrates.

the additional gallium apparently causes a higher yield of vertical nanowires, which grow with larger diameter as compared to the regularly grown nanowires at the same growth conditions. The latter observation is qualitatively in agreement with [79] which found a connection between Ga-flux needed to maintain a certain nanowire density and surface roughness. A lower surface roughness will enable a higher Ga-diffusion [127] resulting in less but vertical nanowires with increased diameter.

The results shown here indicate, that the optimal growth conditions for the growth of vertical nanowires depend on the oxidation time and thus the thickness and the roughness of the oxide layer. Whereas gallium pre-deposition favors the growth of vertical nanowires with larger diameters for very thin and smooth oxides, oxides with high roughness require high V/III - ratios or less Ga-flux, resulting in thin vertical nanowires.

We will now discuss the above observations in the framework of oxide layer thickness, its roughness and droplet size which can affect their wetting behavior [131, 132, 133] and thus have a strong impact on the wetting angle of the Ga-droplets forming prior to nanowire growth. Matteini et al. [80] have shown in particular, that the wetting angle of a Ga-droplet β with the substrate increases with increasing the oxide layer thickness from $\beta = 50°$ for 0.1 nm oxide thickness to $\beta = 116°$ for 1.5 nm thick oxide layers. From the presented growth experiments in [80], Matteini et al. conclude that vertical nanowire growth is possible only if the droplet reaches wetting angles above 80° with an optimal value for vertical yield around 90°. Above 90° they found, that growth of tilted nanowires becomes more pronounced.

Whether a droplet wets the surface or not, depends on the surface energies of the involved phase boundaries. Following Ref. [63], we write the surface energy G of a spherical liquid droplet on a planar surface

$$G = \gamma_{lv}\frac{2\pi R^2}{1+\cos\beta} + \gamma_{sl}\pi R^2 + \gamma_{sv}(S_0 - \pi R^2) \tag{2.2}$$

with the liquid-vapor, solid-liquid and solid-vapor surface energies γ_{lv},γ_{sl} and γ_{sv}, the base radius of the droplet R and the surface area $S_0 = const$ of the solid. The system is in equilibrium if G is minimal. For fixed droplet volume

$$V = \frac{\pi R^3}{3}\frac{(1-\cos\beta)2+\cos\beta}{(1+\cos\beta)\sin\beta} = const \tag{2.3}$$

the differential dG writes

$$dG_{V=const} = (\gamma_{sl} - \gamma_{sv} + \gamma_{lv}\cos\beta)\ 2\pi\ R\ dR. \tag{2.4}$$

This expression becomes minimal if the wetting angle β satisfies the Young's equation [134]:

$$\gamma_{sv} = \gamma_{sl} + \gamma_{lv}\cos\beta \tag{2.5}$$

and the system is in equilibrium.

Since for nano-sized droplets, β becomes size dependent, the Young's equation has been modified [135, 136]

$$\gamma_{sv} - \gamma_{sl} = \gamma_{lv}\cos\beta + \frac{\gamma_{slv}}{r} \tag{2.6}$$

where γ_{slv} is the line tension at the triple-phase-line and r the drop base radius.

By varying the amount of Ga, the droplet volume can change by varying R and thus β or by varying only the base contact area by r. We assume that the droplet is, due to roughness, pinned to the surface, so the base radius might not change and the volume increase effectively changes β and the droplet radius R. We therefore neglect the line tension term as well as the change in base radius r in the following considerations.

We evaluate now $\gamma_{sv} - \gamma_{sl}$ for constant and positive γ_{lv}. $\gamma_{sv} - \gamma_{sl} < 0$ results in $\beta > 90°$ and

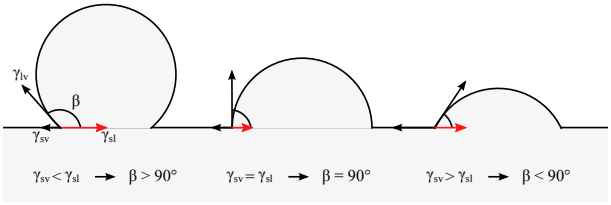

(a) Liquid Ga-droplet on a plane surface with equilibrium wetting angles $\beta > 90°$, $\beta = 90°$, $\beta < 90°$ and the forces acting on the triple phase line.

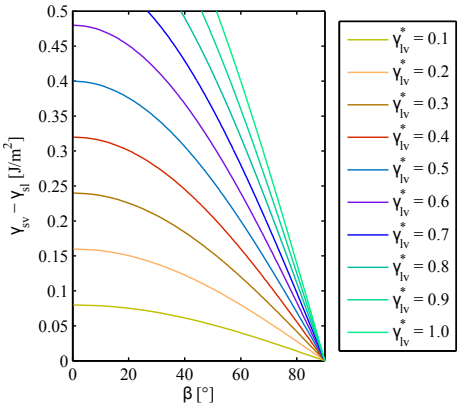

(b) Surface energies for different oxide layer thicknesses and corresponding equilibrium wetting angle calculated by Eq. 2.6. We qualitatively evaluate the effect of variation of the droplet size by changing γ^*_{lv} from 0.1 to 1.0.

Figure 2.10: For the same oxide layer thickness, we obtain smaller equilibrium wetting angles for smaller droplet volume at same base radius. For constant droplet volume, a decrease of the oxide thickness (increasing $\gamma_{sv} - \gamma_{sl}$) leads to a decrease of the equilibrium wetting angle as well. Therefore, for a given oxide thickness below 0.8 nm, an increase of the droplet volume may result in larger wetting angles closer to the conditions favorable for vertical nanowire growth.

$\gamma_{sv} - \gamma_{sl} > 0$ to $\beta < 90°$. We limit our considerations to thin oxide layers, and $\gamma_{sv} - \gamma_{sl} \geq 0$ (see Fig, 2.10(a)). Analogous to Ref. [80], we now express the oxide layer thickness by use of $\gamma_{sv} - \gamma_{sl}$ and investigate the impact of changing the droplet's volume at constant base radius r (pinned case) by use of 2.5. As an example of the results in Ref. [80] we list the corresponding oxide thicknesses for $\gamma_{sv} - \gamma_{sl} = [0.0, 0.2, 0.4]$: $D_{ox} = [0.8, 0.4, 0.0]$ nm. We refer to Refs. [137, 132] and [138], and employ $\gamma_{lv} = 0.7\,\mathrm{J/m^2}$ and $\gamma^*_{lv} = \frac{\gamma(R)}{\gamma_{lv}} < 1$ and $\gamma(R) \to \gamma_{lv}$ if $R \to \infty$ at $\frac{\gamma_{slv}}{r} << 1$ and *const*. Here, $\gamma(R)$ is the size dependent surface energy of a small liquid droplet with radius R as proposed by Refs. [139, 140]. As depicted in Fig. 2.10(b) a volume increase via the droplet liquid-volume surface at constant r leads to an increase of the equilibrium wetting angle β at same $\gamma_{sv} - \gamma_{sl}$.

With the behavior of the wetting angle as depicted in Fig. 2.10, the observed increase in the vertical yield of nanowires in case of the growth on the 300 minutes re-oxidised substrate can be explained, in case that $D_{ox} \leq 0.8\,\mathrm{nm}$. With additional material available after the Ga pre-deposition, the droplets can increase their average wetting angle such, that the majority exhibits values favorable for vertical nanowire growth. Without the additional gallium in case of the regular growth, many droplets have wetting angles which are too small for nanowire growth, and therefore a large number of crystallites is observed.

In summary, the influence of the substrate preparation e.g. oxide thickness and roughness on the size, shape and density of nanowires and crystallites has been investigated. Therefore, a series

of self-catalyzed GaAs nanowires has been grown under identical arsenic rich growth conditions and investigated by SEM. In order to study the effect of the oxide layer thickness, Si substrates were re-oxidised in warm water after HF etching. By varying the re-oxidation time from 180 to 465 minutes, various oxide layer thicknesses below the thickness of the native oxide could be achieved. The oxide layer thickness has an effect on the nanowire diameter, which decreases with increasing oxide thickness in case of our very thin nanowires with diameters below 60 nm. Additionally, the size of the crystallites decreases with increasing oxide thickness, which is a very positive effect since we aim to minimize parasitic growth for *in-situ* X-ray studies. In another growth series a Ga pre-deposition step was applied as additional free parameter to condition the oxide layer further and to deposit small Ga-droplets which may act as favorable nucleation sites for nanowires. Here we observed a positive effect on the vertical yield of nanowires and a reduction of parasitic growth for samples with very thin oxide, whereas the Ga pre-deposition caused additional nucleation of crystallites and a reduction of the vertical yield of nanowires when growing on Si substrates covered by native oxide. We discussed on a qualitative level, that by introducing additional gallium, the wetting angle of the Ga droplets could be increased, improving the vertical yield in case of thin oxide layers. At the native oxide, the Ga pre-deposition caused the growth of tilted nanowires and increased the density of crystallites drastically. We found that the optimal parameters for growth of vertical nanowires depend on the oxide layer thickness. Whereas an increased amount of Ga is beneficial for thin oxides in our case, a high V/III ratio delivered better results for oxide thicknesses in the range of the native oxide which usually exhibits a thickness of approx. $D_{nat.ox} \approx 1.5\,\mathrm{nm}$ [80].

Consequently further experiments on Si(111) wafers covered by native oxide were conducted with the aim to map the growth-parameter space in detail. The choice for the native oxides was motivated by simple sample preparation and better growth results for our growth conditions in the high V/III ratio regime.

2.4 The parameter window for the growth of self-catalyzed GaAs nanowires grown on Si(111) covered with native oxide

In this section we investigate the parameter window suitable for the growth of self-catalyzed GaAs nanowires on Si(111) wafers covered by native oxide in the pMBE system. We will discuss the effect of the growth time, the As- and Ga-fluxes, on diameter, length and axial growth rate of the nanowires. Also, we will consider the substrate temperature as a way of influencing the nucleation density. Further we will observe the influence of the V/III-ratio on the wetting angle of the liquid droplet as observed after the growth. Finally, we will identify the optimal substrate temperature for the growth of self-catalyzed GaAs nanowires in the pMBE system.

The growth of GaAs nanowires is only possible in a limited growth window defined by MBE growth parameters and conditions (Ga- and As- fluxes, substrate temperature and the surface oxide layer). *Within* this growth window, the growth process is *highly sensitive* to these parameters, especially in the case of Ga-catalyzed nanowires, since in this case the volume of the catalyst droplet is not necessarily constant during growth. For example, once the growth species are supplied to the liquid Ga-droplet, they can reach the droplet by direct impingement and surface diffusion, resulting in the corresponding material influxes driven by the difference in chemical potential. Once a critical supersaturation in the liquid is reached, excessive GaAs starts to precipitate at the liquid-solid interface, reducing the amount of Ga N_{Ga} and As N_{As} in the droplet. The requirements for a steady state growth with constant droplet volume are then: $dN_{Ga}/dt = dN_{As}/dt$. This condition can only be obtained at certain V/III ratios. If we consider a too small V/III-ratio on the one hand, $dN_{Ga}/dt > dN_{As}/dt$ and the droplet volume would increase, resulting in enhanced radial growth and tapering. On the other hand, the droplet would shrink at too large V/III-ratios, at $dN_{Ga}/dt < dN_{As}/dt$. Both scenarios eventually lead to a collapse of the nanowire growth. Either the droplet volume increases critically and becomes unstable, or it gets completely consumed [60].

2.4.1 Nanowire length and diameter as a function of growth-time

There are several post-growth SEM based reports in literature on the growth rate of nanowires: e.g. [30, 33, 141, 38, 56, 142, 63]. The essential message of these reports is, that the axial nanowire growth rate is arsenic limited and thus the final nanowire height depends linearly on the effective influx of As $I_{As,eff}$ into the droplet, at constant growth time t:

$$H = \Omega_{GaAs} f_{As,eff} t = Ct. \tag{2.7}$$

The effective influx of As, $f_{As,eff}$ contains all contributions from 1.1 and is in particular directly proportional to the arsenic limited 2D GaAs growth rate calibrated by RHEED. Ω_{GaAs} is the

volume occupied by a GaAs pair in the solid.

Alternatively to the reports mentioned above, Glas et al. [58, 45] investigate the number of nucleation events in a certain time-interval in a single nanowire, explaining the observed linear relation of growth-time and nanowire length. They observe a self-regulatory mechanism regarding the time between two nucleation events. This mechanism is responsible for minimizing the fluctuations around an expectation value for the number of layer nucleation events in a certain time t_{NE}. In simple words, this mechanism works as follows: The probability of nucleating new layers is proportional to the Boltzmann factor $e^{-E/(k_B T_s)}$, where k_B is the Boltzmann constant and T_s is the substrate temperature in Kelvin. E is the energy barrier for nucleation and depends on the supersaturation of the droplet with arsenic [58]. If the layer-by-layer nucleation rate is due to statistical fluctuations, larger than expected by t_{NE}, dN_{As}/dt becomes negative, resulting in a reduction of N_{As} in the droplet, thus decreasing supersaturation N_{As}. Therefore the expectation time for the next nucleation event increases. If otherwise, the nucleation rate becomes lower than t_{NE}, the supersaturation and N_{As} in the droplet increases, therefore the probability of nucleation of subsequent layers increases as well and fluctuations of the grown layers after a certain growth time t is minimized. A more thorough discussion of this so-called antibunching effect can also be found in Ref. [58] and Ref. [93].

Since the growth rates depend on As-flux and substrate temperature, a measurement of a growth-time series allows for both, crosschecking the above growth-laws and benchmarking the stability of growth parameters in the pMBE system.

A series of four samples, grown for 30, 60 (two samples) and 120 minutes serve as a basis for these investigations. In Fig. 2.11 representative SEM side view images show the growth results with a Ga flux corresponding to $R_{GaAs,100} = 30\,\mathrm{nm/h}$ GaAs growth rate and a high V/III ratio of approx. 5. at $T_S = 580\,^{\circ}\mathrm{C}$. Mostly vertical nanowires with uniform diameter, without pronounced tapering have been grown. Also parasitic growth and tilted nanowires are observed. For the evaluation of height and diameter, more than 100 nanowires have been investigated. The height can be sufficiently described by the linear relation given in Eq. 2.7: $H = C(t - t_{inc}) = 41.43\,\mathrm{nm/min} \cdot (t - 1.57\,\mathrm{min})$ by introducing the incubation time t_{inc} which accounts for the delay of the GaAs nucleation [72, 80] in Fig. 2.12(b). Although, the error on the value for the incubation time is large and t_{inc} is compatible with zero as well, it seems to be reasonable for such thin oxide–layers. Comparing our value to values for the incubation time of self-catalyzed GaAs nanowires from literature, our value is quite low. For example, Fontcuberta et al. [72] found $t_{inc} = 4.3\,\mathrm{min}$ for self-catlyzed GaAs nanowires grown on sputtered silicon–oxide up to a thickness of 30 nm, and Rieger et al. [124] observed $t_{inc} = 15\,\mathrm{min}$ for his GaAs nanowires grown on silicon–oxide, obtained by annealing a HSQ layer, with a thickness up to 12 nm. As in our case, Rieger et al. [124] does not observe an effect of the oxide–layer thickness on the incubation time, implying that rather the porosity, roughness or the number–density of possible nucleation sites (e.g. given by sub-nanometer pinholes) than the actual thickness of the oxide is an important factor causing the incubation time. Besides that, the

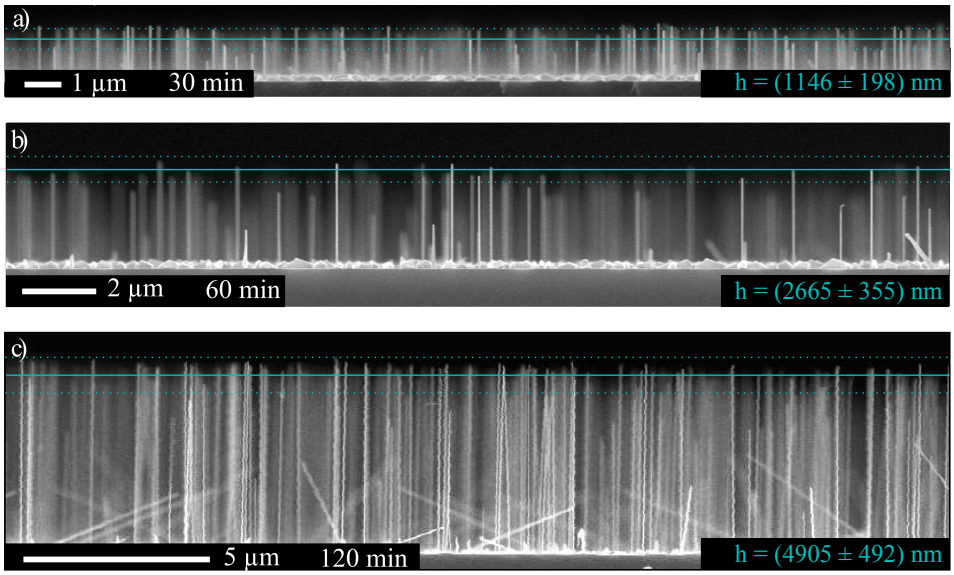

Figure 2.11: Side-view SEM images of nanowires grown with the same growth parameters for a) 30, b) 60 and c) 120 minutes. The growth was initiated by opening the Ga-shutter at constant As background pressure, and ended by simultaneously closing the Ga-, As- and main-shutters. The nanowires in c) appear to be wiggled along their growth axis. This is a scanning artifact produced by the SEM system. The mean nanowire height and standard deviation therefor are given by the horizontal solid and dotted lines respectively.

incubation time should also depend on the growth parameters like substrate–temperature, Ga–flux and V/III – ratio. From the gradient of the linear fit, we obtain the mean nucleation rate $t_{NE}^{-1} = (41.43\,\mathrm{nm/min} \pm 7.36\,\mathrm{nm/min})/d_{GaAs,111} = 2.1\ \mathrm{layer/s} \pm 0.4\ \mathrm{layer/s}$.

The value of the axial nanowire growth rate $C = 41.43\,\mathrm{nm/min}$ exceeds the applied flux of Ga, given by the nominal 2D layer growth rate of $\mathrm{R}^{\mathrm{Ga}}_{\mathrm{GaAs},100} = 30\,\mathrm{nm/h} = 0.5\,\mathrm{nm/min}$ and the flux of As (equivalent to approx $R^{As}_{GaAs,100} = 2.5\,\mathrm{nm/min}$) by far. Therefore, we will shortly discuss the discrepancy regarding the Ga-fluxes. The As-flux and its effect on the growth rate will be discussed later. The difference between $R_{GaAs,100}$ and t_{NE}^{-1} can be explained, if we consider diffusion of Ga-adatoms from inside a collection area around the GaAs nanowire towards the nanowire tip and into the Ga-droplet. Therefore, the Ga-adatoms have to be able to reach the droplet before they get desorbed or incorporated into the nanowire sidewall and the radius of the collection area needs to be smaller than half the next-neighbor distance between GaAs nanowires or GaAs crystallites. Otherwise neighboring nanowires will compete for Ga-adatoms which may result in the termination of the growth process by consumption of the droplets of both or one of the corresponding nanowires.

In the following discussion, we neglect desorption and assume that all Ga-adatoms deposited in an area $S_c = \pi R_c^2$ around a nanowire will diffuse into the Ga-droplet. We also neglect radial growth due to Ga incorporation at the nanowire side-walls for the moment. For a steady state

growth, the incorporation rate of Ga-atoms into the nanowire due to axial growth has then to be equal to the deposition rate of Ga-atoms onto S_c :

$$t_{NE}^{-1} \frac{S_{NW,111}}{\Omega_{GaAs}} = R_{GaAs,100}^{Ga} \frac{S_c}{\Omega_{GaAs}} \tag{2.8}$$

with $S_{NW,111} = \pi R_{NW}^2$ being the area of the nanowire top facet (if we approximate the nanowire by a cylinder) and Ω_{GaAs} being the volume of a GaAs pair in the solid. With the values given above, and $R_{NW} = 10\,\text{nm}$ we obtain the radius of the collection area

$$R_c = \sqrt{\frac{R_{GaAs,100}^{Ga}}{t_{NE}^{-1}}} = 91\,\text{nm}. \tag{2.9}$$

This value is only an approximation and constitutes a lower bound, since we neglected desorption and incorporation processes. From Ref. [143] we obtain an experimental value for the diffusion length of Ga-adatoms on SiO: $\lambda_{Ga,SiO} = 5\,\mu\text{m}$ at $T_S = 663\,^\circ\text{C}$, which is in the same range as the diffusion length on GaAs (110)-type side walls [50], an in both cases by far larger than R_c in our case. Therefore, the discrepancy between direct Ga-flux and Ga incorporation into the nanowire can easily compensated by an increased collection area for Ga-atoms including the substrate and the nanowire side-walls.

Concomitant to the axial growth, we observe an increase of the nanowire diameter over growth time, depicted in Fig. 2.12(a). The increase can be sufficiently described as linear with $d(t) = 0.2019\,\text{nm/min} \cdot t + 12.31\,\text{nm}$. Interestingly this fit implies a minimal diameter $d(t = 0) = 12.31\,\text{nm}$ which might be related to the initial diameter to the Ga-droplets before the start of GaAs nucleation. Within the resolution of SEM, the diameter of the nanowires along the growth axis does not change. Therefore an inflation of the droplet due to increasing effective influx of Ga $f_{Ga,eff}$ is unlikely to be the reason for this radial growth, which leads us to Ga-diffusion as a possible factor for the uniform radial growth.

We now consider the radial GaAs growth rate $R_{GaAs,110} = 0.101\,\text{nm/min}$, which we find to be approx. 5 times lower than the applied nominal GaAs growth rate $R_{GaAs,100} = 0.5\,\text{nm/min}$. We explain this difference by an additional Ga-supply into the Ga-droplet provided by surface diffusion: Let us consider the Einstein-relation $\lambda^2 = \Delta\tau$, with Δ being the diffusion coefficient, λ the diffusion length and τ the life-time of the adatom. A Ga-adatom with $\lambda >> h$ seated on the side-wall of a nanowire with height h will rather be incorporated into the liquid droplet, or leave the nanowire via the substrate, before it gets incorporated into the side wall and will therefore not contribute to the radial growth. Indeed, the diffusion length $\lambda_{Ga,110}$ of Ga-adatoms on GaAs (110)-facets can exceed $10\,\mu\text{m}$ [50] which is well below the height of the nanowires discussed here.

Using the approximate relation [144], and expanding it for a geometrical factor α which accounts for the directional molecular beams in the pMBE

$$\frac{R_{GaAs,110}}{R_{GaAs,100}} \approx \alpha \frac{1}{\sqrt{2}} \left(\frac{\lambda_{Ga,100}}{\lambda_{Ga,110}} \right)^2 \tag{2.10}$$

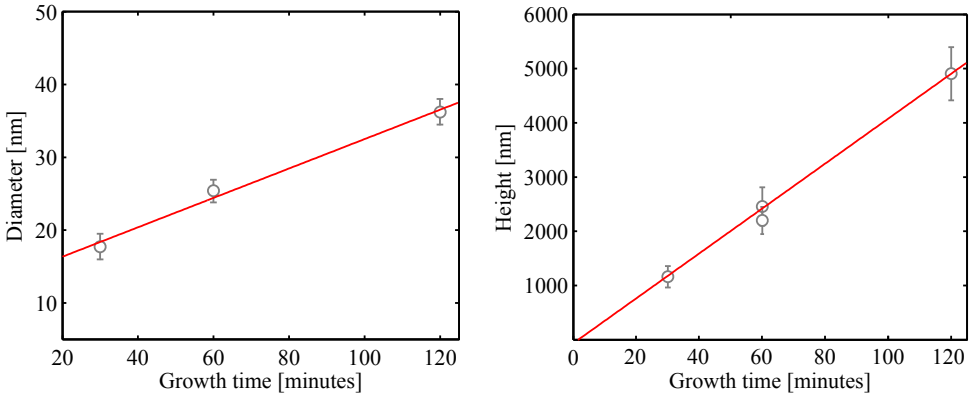

(a) Evolution of the nanowire diameter with growth time and linear fit: $d(t) = 0.2019\,\text{nm/min} \cdot t + 12.31\,\text{nm}$

(b) Increase of the nanowire height with growth time and linear fit: $h(t) = 41.43\,\text{nm/min} \cdot t - 65.24\,\text{nm}$

Figure 2.12: The mean diameters as well as the mean height increases with growth time and can be sufficiently described by a linear relation. The y-intercept in 2.12(a) $d(0) = 12.31\,\text{nm}$ may be close to the size of the Ga-droplets at t_{inc}. The incubation time t_{inc} may be extracted from the x-intercept in 2.12(b). Additionally, a second sample has been grown for 60 minutes in order to estimate the reproducibility of the growth. As there is virtually no difference in diameters, the difference in height is in the range of error.

with the GaAs 2D growth rates $R_{GaAs,110} = \frac{0.2019}{2}\frac{nm}{min}$ and $R_{GaAs,100} = 30\frac{nm}{h} = 0.5\frac{nm}{min}$ and $\alpha = \frac{sin(28)}{sin(62)}$, we obtain

$$\left(\frac{\lambda_{Ga,100}}{\lambda_{Ga,110}}\right)^2 \approx \frac{1}{2}. \tag{2.11}$$

Meaning, at our growth conditions, the diffusion length of Ga-adatoms at the nanowire side facets $\lambda_{Ga,110}$ is approximately four times larger than $\lambda_{Ga,100}$ resulting in a reduced growth rate of the (110) side facets compared to the nominal growth rate $R_{GaAs,100}$. This also implies, that the radial growth rate may be controlled by the supplied Ga-flux - as in regular 2D layer growth, but is governed by the large diffusion length of Ga-adatoms at the nanowire side walls and therefore Ga-diffusion in general [145]. Further, Ga-diffusion depends on the As-partial pressure and the respective growth temperatures. The effective As-partial pressure however may differ from its nominal value given by the growth parameters, due to e.g. re-evaporation processes [52]. Also the temperature along the nanowire growth axis may depend on the nanowire height [53]. Therefore, a quantitative prediction of the facet growth rate is complicated, even in the absence of tapering. As we will discuss in chapter 3, *in-situ* X-ray diffraction grants experimental access to these radial growth rates.

In summary, we found a linear relation between nanowire growth time and height. For growth times ranging from 30 to 120 minutes, we obtained heights from $h_{30min} = 1146\,\text{nm} \pm 198\,\text{nm}$ up to $h_{120min} = 4905\,\text{nm} \pm 492\,\text{nm}$ resulting in a mean nucleation rate of $t_{NE}^{-1} = 2.1\,\text{layer/s}$ along

the 111 growth direction, which is approx. 40 times larger than the applied Ga-flux equivalent to a 2D nominal GaAs growth rate $R_{GaAs,100}$. Extrapolating the linear relation of nanowire height and growth time, to $t = 0\,\text{min}$ leads to an incubation time of $t_{inc} = 1.57\,\text{min} = 94.2\,\text{s}$. The results found here are also in good agreement with the heights obtained and depicted in Fig. 2.6(b). Additionally, we found an increase in nanowire radius with growth time. Different from the axial growth rate, being the result of a VLS mechanism, the radial growth rate of the [110] side facets $R_{GaAs,110}$ is smaller, but in the order of the 2D nominal GaAs growth rate. The difference in growth rates has been explained by the different diffusion lengths of Ga-adatoms on the respective facets.

2.4.2 Nanowire length and diameter as a function of the Ga-flux

The diameter of the final nanowire is tied to the size of the Ga-droplet. Since in the self-catalyzed growth of GaAs nanowires, the droplet size crucially depends on the incoming As- and Ga- fluxes, a variation of the latter gives means to tailor the nanowire diameter [60, 142, 146, 145]. In the following section, we evaluate the effect of Ga-Flux variation on the diameter and height of the grown nanowires. We therefore grew a series of samples using a Ga-Flux corresponding to a 2D GaAs growth rate ranging from $R^{Ga}_{GaAs,100} = 24\,\text{nm/h}$ to $R_{GaAs,100} = 72\,\text{nm/h}$ at the same time, keeping the As-Flux and the substrate temperature constant equivalent to a arsenic limited growth rate of $R^{As}_{GaAs,100} = 150\,\text{nm/h}$. The samples have been grown for 30 minutes at a substrate temperature $T_S = 580\,°\text{C}$.

The considerations in Refs. [147, 148] and [31] will provide a model for the liquid Ga-droplet defining the nanowire diameter d. For a given supersaturation ζ there is a minimal critical radius $r_0 = \frac{\gamma_{lv} V_l}{RTln\zeta}$ depending on the supersaturation ζ, below which no stable VLS growth is possible. Since the arsenic flux $f_{As} = const$, also $r_0 = const$. At this point, we assume the droplet consists of $N_0 = N_{Ga} + N_{As}$ catalyst atoms. In general $N_{Ga} >> N_{As}$ thus we consider the droplet to be constituted mainly by Ga atoms: $N_0 \approx N_{Ga}$. If N is the number of atoms additionally deposited by increasing the Ga-flux, we can write $x = \frac{N}{N_0+N}$ being the fraction of additionally deposited Ga-atoms. Each Ga-atom occupies the same liquid volume Ω_l, thus we can express the volume of an e.g. semi-spherical droplet:

$$V = \frac{2}{3}\pi r^3 = (N_0 + N)\Omega_l \tag{2.12}$$

and

$$V(1-x) = \frac{2}{3}\pi r_0^3 = N_0\Omega_l. \tag{2.13}$$

We then arrive at an expression for the nanowire diameter

$$d = \frac{d_0}{[1-x]^{1/3}} \tag{2.14}$$

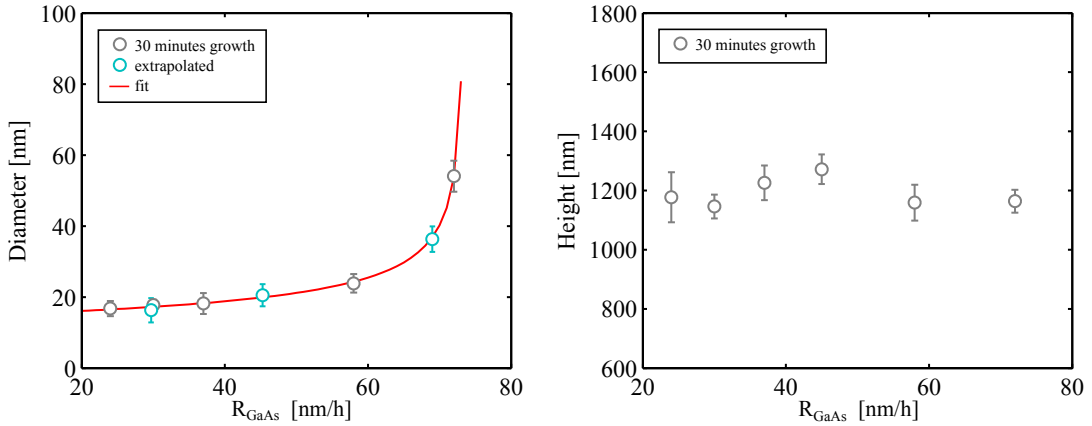

(a) Nanowire mean diameter after 30 minutes of growth as function of the Ga-flux. The red solid line depicts the fit by Eq. 2.15.

(b) Mean heights of nanowires grown at various Ga-fluxes but at constant As-fluxes for 30 minutes. In contrast to the diameter, the height remains unaffected by the Ga-flux within the investigated range.

Figure 2.13: As the Ga-flux increases, the diameter of the nanowires increase - a result rather caused by a difference in the sizes of the Ga-droplets at t_{inc} than by an increased radial growth rate of the nanowire side-walls. The axial growth rate and therefore the final length of the wires is unaffected by the increased Ga-flux. Pronounced tapering did not occur in the investigated samples.

with $d_0 = 2r_0 = const$ the initial diameter of the liquid droplet. Following Ref. [56], x is proportional to the Ga-flux and can be expressed by f_{Ga} as $x = af_{Ga}$ and

$$d = \frac{d_0}{[1 - af_{Ga}]^{1/3}}. \tag{2.15}$$

In Fig. 2.13(a), we depict diameters of vertical nanowires obtained under different Ga-fluxes. As the Ga-flux increases, the final diameter increases as well. Using Eq. 2.15 we obtain the best fit for the 30 min growth samples in grey with $d_0 = 14.46\,\text{nm} \pm 0.52\,\text{nm}$ and $a = 0.136 \pm 0.004$. Indeed, we did not observe nanowires with diameters $d < d_0$, even for the lowest $R_{GaAs,100} = 24\,\text{nm/h}$ applied. Lowering the growth rate further to $R_{GaAs,100} = 16\,\text{nm/h}$ did not result in the growth of nanowires and it is possible that by lowering $R_{GaAs,100}$ desorption processes at $T_S = 580\,°\text{C}$ avoided the building of a Ga-droplet with $d \geq d_0$. In addition to the mean diameters of nanowire samples grown for 30 minutes in Fig. 2.13(a), we depict three values for mean diameters obtained from samples grown for 60 minutes. For these samples grown with $R_{GaAs,100} = 30\,\text{nm/h},\ 45\,\text{nm/h},\ 72\,\text{nm/h}$, the measured diameters $d_{30\,\text{nm/h}} = 22.3\,\text{nm}$, $d_{45\,\text{nm/h}} = 26.5\,\text{nm}$ and $d_{72nm/h} = 42.3\,\text{nm}$ have been extrapolated to 30 minutes growth time using the linear fit given in Fig. 2.12(a). As we can see, Eq. 2.15 describes the relation diameter to Ga-flux well. Consequently, we argue, that at constant f_{As}, the two factors which contribute to the nanowire diameter - the Ga-flux by defining the initial size of the droplet, and the radial growth - are independent from each other, at least in the frame of measurements regarded here.

In contrast to the nanowire diameter d, the height of the nanowires seems not to be affected by varying the Ga-flux, as can be seen in Fig. 2.13(b), resulting in a mean height $h_{mean} = 1175\,\text{nm} \pm 31\,\text{nm}$. This implies, that the growth rate of our self-catalyzed GaAs nanowires is, above a critical value $16\,\text{nm/h} < R^{Ga,crit}_{GaAs,100} < 24\,\text{nm/h}$ independent of the supply of the group III material for the investigated growth conditions.

2.4.3 Nanowire length and diameter as a function of the As-flux

The axial growth rate of GaAs nanowires is governed by the flux of the group V element f_{As} [56, 58, 52, 63]. Consequently, we investigate the effect of changing f_{As} at constant T_S in our pMBE system by keeping f_{Ga} constant. The influence on the diameter has been investigated on basis of a series of samples grown at constant f_{Ga} (see Fig. 2.15(a)), since f_{Ga} has impact on the nanowire diameter as well. As we observed before, f_{Ga} does not affect the axial growth rate and the final height of our nanowires at equal growth time, thus additional samples with larger f_{Ga} for f_{As} equal to an arsenic limited growth rate of $R^{As}_{GaAs,100} > 200\,\text{nm/h}$ contribute to Fig. 2.15(b). The samples have been grown at $T_S = 580°$ for 60 minutes.

As we can see in Fig. 2.14 a), at a low V/III - Ratio of $f_{Ga} \approx f_{As}$ we observe short but thick GaAs nanowires with a pronounced Ga droplet on top with mean heigth $h = 504.8\,\text{nm} \pm 42.6\,\text{nm}$ Besides the vertical nanowires, tilted wires as well as crystallites with large Ga droplets on the surface are present. As the arsenic flux is increased $f_{Ga} < f_{As}$, the axial growth rate of the wires increases resulting in a mean height of $h = 1166.8\,\text{nm} \pm 157.3\,\text{nm}$ – seen in Fig. 2.14 b) – after 60 minutes of growth. Still pronounced droplets are seated at the nanowire tips, however, the Ga-droplets at the surface vanished. Therefore crystallites with faceted side-walls appear. Comparing with Fig. 2.14 a), also the nanowire diameter decreased visibly. For $f_{Ga} << f_{As}$ depicted in Fig. 2.14 c), the nanowires grow even faster resulting in $h = 2706.4\,\text{nm} \pm 194.9\,\text{nm}$ whereas their diameter decreases further. Now, no Ga-droplets can be observed at the NW tip anymore: Some nanowires show flat (111) top facets, whereas other wires seem to exhibit a sharp tip instead which is a result of consumption of the droplet after stopping the group III supply at the end of growth [56]. Besides some needle like tips, we found no indication of tapering along the wire growth axis which implies that a stable steady state growth mode was maintained for all investigated samples.

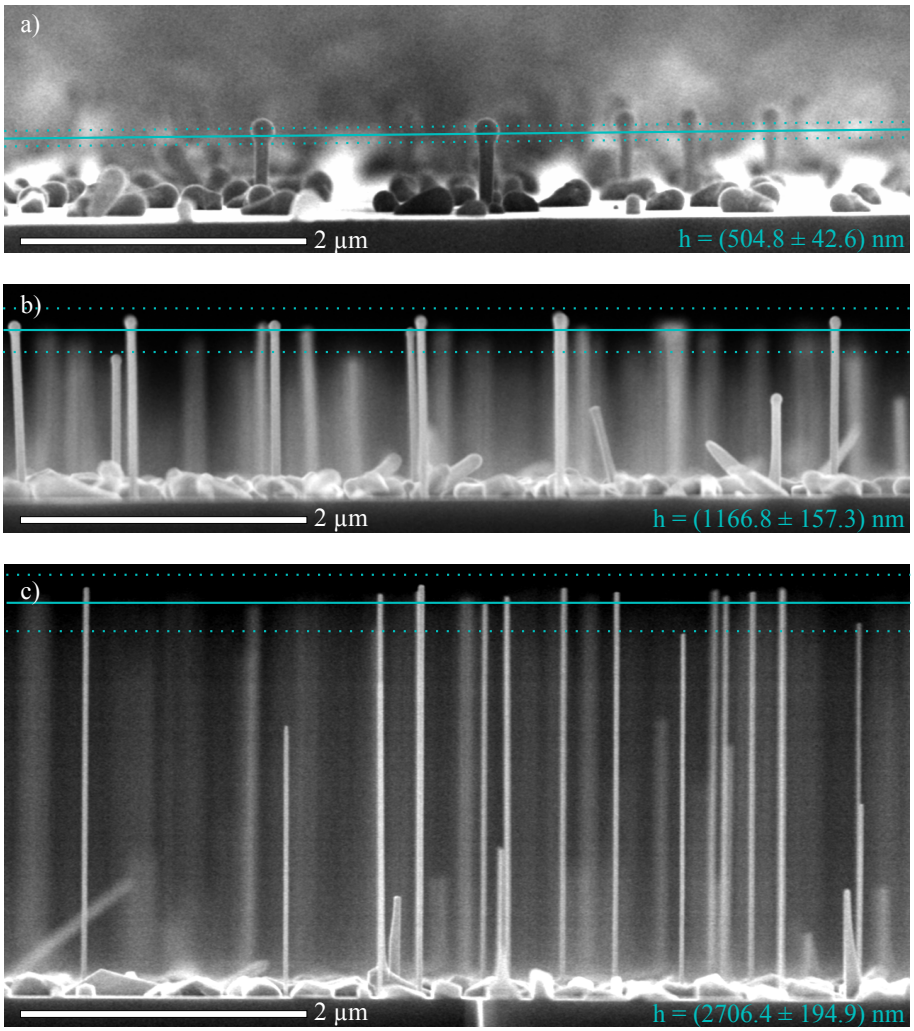

Figure 2.14: Side-view SEM images of nanowire samples grown at constant Ga-flux but different As-fluxes for a fixed growth time of 60 minutes. The mean height and corresponding standard deviation are depicted by the horizontal solid and dotted lines respectively.

In Fig. 2.15(a), we express f_{As} in the equivalent As-limited 2D growth rate of GaAs $R^{As}_{GaAs,100}$ and depict the obtained mean diameters of the nanowire ensembles as a function thereof. This is possible due to our prior growth calibrations. With increasing f_{As} at constant f_{Ga}, the wire diameter decreases sufficiently described by a linear function. As we observed before, the diameter is homogeneous along the wire growth axis, which is the same for the Ga-flux series discussed above. Moreover, the contribution of non-catalytic side-wall growth, which may depend on f_{Ga} and growth time, is supposed to be similar in the considered samples. So it is likely, that the difference in nanowire diameters, is a result of different initial sizes of the Ga-droplets before nucleation.

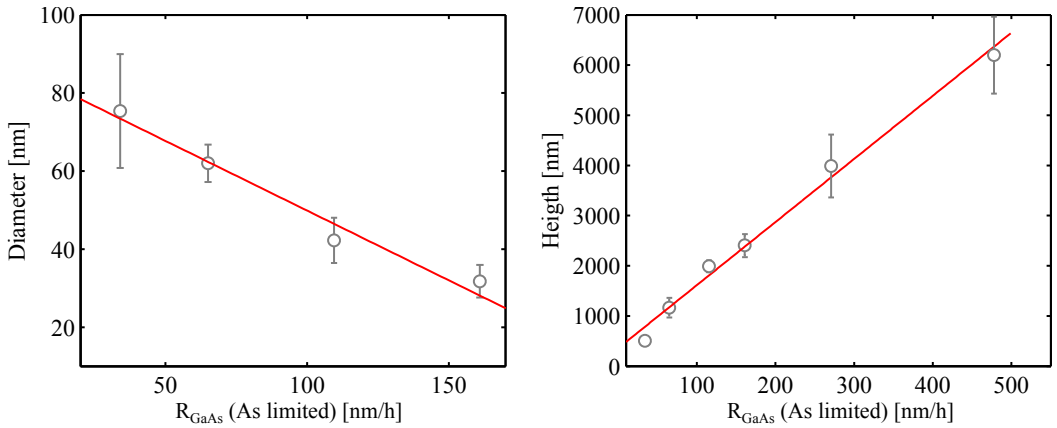

(a) Mean nanowire diameters grown at the same Ga-flux and growth time for various As-fluxes. The solid line is a linear fit, as guide for the eyes.

(b) Mean nanowire height as function of the As-flux. In the range of the investigated parameters, the relation is sufficiently described by a linear function. The positive y-intercept is most likely an offset caused by crystallization processes after the growth was stopped.

Figure 2.15: Diameter and height of the grown nanowires as a function of the As-flux at constant Ga-flux and growth time.

In addition to post-growth SEM, the growth of the nanowire samples has been monitored in-situ by RHEED which is very sensitive to processes on the surface. From RHEED we observe a time-delay between opening the Ga-shutter and the nucleation of GaAs, exemplarily shown in Fig. 2.16 for two samples grown at f_{As} equivalent to $R^{As}_{GaAs,100} = 30\,\mathrm{nm/h}$ (Fig. 2.16(a)) and $R^{As}_{GaAs,100} = 160\,\mathrm{nm/h}$ (Fig. 2.16(b)). With increasing f_{As} the time-delay decreases considerably from 180 s down to below 30 s for the lowest and highest f_{As} applied. Lets call this time-delay 'incubation time': The time t_{inc} in which the Ga-droplet can accumulate material until it reaches steady state conditions, in particular a sufficient size for stable VLS growth and the critical supersaturation of arsenic [141, 72, 63]. We already considered the existence of t_{inc} from a growth time series (compare Fig. 2.12(b)). With RHEED, a direct observation of the incubation time is possible. Since arsenic can reach the droplet mainly by direct impingement from the vapor, the time in which the critical supersaturation of arsenic in the droplet is reached therefore depends on f_{As}, if $T_S = const.$ Consequently, with decreasing incubation time at constant f_{Ga} and T_S the droplet has less time to accumulate gallium and therefore its final size decreases.

In Fig. 2.15(b), the final height after 60 minutes of growth scales linearly with the equivalent arsenic limited growth rate $\mathrm{R}^{\mathrm{As}}_{\mathrm{GaAs}}$, implying that Eq. 2.7 sufficiently describes the growth within the investigated parameter window. The non-negative y-intercept could be a result of GaAs crystallization after the end of the growth by closing the shutters. The linear relation between As-flux and nanowire height also suggests, that the local growth conditions in the Ga-droplet are Ga-rich, meaning that the growth rate is indeed As-limited, despite of As over-pressure in the vapor.

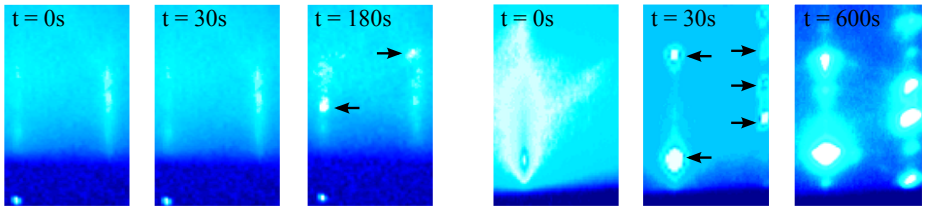

(a) The first 180 seconds after opening the Ga-shutter. At $t = 0\,\mathrm{s}$ and $t = 30\,\mathrm{s}$, only diffuse background of the oxide covered Si(111) substrate is observed. After $t = 180\,\mathrm{s}$, GaAs reflections (indicated by arrows) become visible. The sample was grown at $f_{As} \approx f_{Ga} \propto 30\,\mathrm{nm/h}$. In the lower left, the direct reflected beam is visible.

(b) Already at $t < 30\,\mathrm{s}$, GaAs reflecions appear. After $t = 30\,\mathrm{s}$ even higher order reflections are visible. The sample was grown at $f_{As} > f_{Ga}$ with f_{As} equivalent to $R^{As}_{GaAs,100} = 160\,\mathrm{nm/h}$.

Figure 2.16: RHEED during the growth shows, that the delay between opening the Ga-shutter and the GaAs nucleation depends on the As-flux, given that the Ga-flux, oxide layer and substrate temperature are identical. This indicates that the incubation time is reached faster, reducing the time to build up the liquid Ga-droplet. As a result, the Ga-droplets at t_{inc} become smaller for high As-fluxes, reducing the final diameter of the grown nanowires.

If so, the growth rate should then be proportional to the number of As atoms arriving at the droplet with a collection area S:

$$\frac{dN_{As}}{dt} = f_{As} S. \tag{2.16}$$

via direct impingement from the vapor. The volume increase of a cylindrical nanowire by axial growth then writes

$$\pi r_{NW}^2 \frac{dh}{dt} = \Omega_{GaAs} \frac{dN_{As}}{dt} \tag{2.17}$$

with the volume $\Omega_{GaAs} = 0.0452\,\mathrm{nm}^3$ occupied by a pair of Ga and As atoms in the solid nanowire of radius r_{NW}. The growth rate $\frac{dh}{dt}$ is

$$dh = \Omega_{GaAs} f_{As} dt \tag{2.18}$$

and the nanowire height

$$h = \Omega_{GaAs} f_{As} t = Ct \tag{2.19}$$

with the axial nanowire growth rate $dh/dt = C = \Omega_{GaAs} f_{As}$. For the presented growth experiments here, C exceeds the nominal R_{GaAs} by far.

Comparing Fig. 2.12(b), we obtain $C = 41\,\mathrm{nm/min} = 0.68\,\mathrm{nm/s}$ axial nanowire growth rate at an arsenic flux corresponding to $R^{As}_{GaAs} = 2.67\,\mathrm{nm/min} = 0.044\,\mathrm{nm/s}$ resulting in $C/R^{As}_{GaAs} = 15.3$. For this comparison however, we considered equal collection areas for nanowire planar

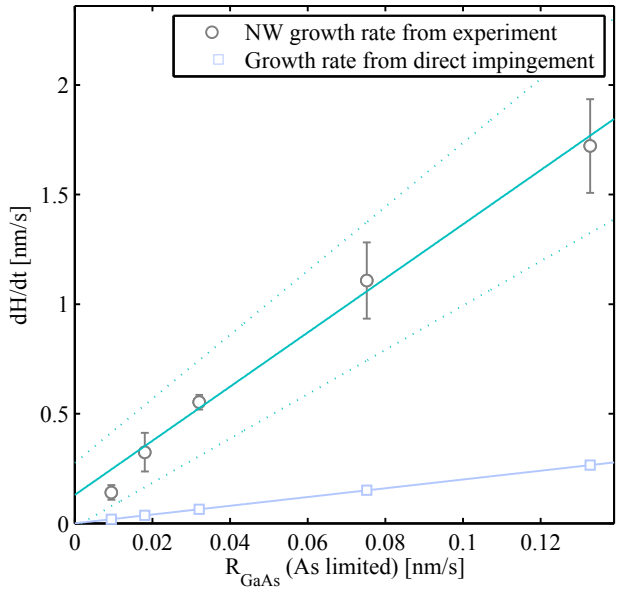

Figure 2.17: Nanowire growth rate C = dh/dt as function of the As-flux given by R^{As}_{GaAs} and linear fit using Eq. 2.19 with upper and lower error bound. The calculated growth rate from direct impingement of As onto the droplet is depicted for comparison. The nanowire growth rate exceeds the calculated one by far, implying an additional source of As.

growth neglecting the shape of the Ga-droplet. The exact value for the collection area S can be obtained by geometrical considerations, including the incoming angle of the As-flux, the nanowire radius and the droplet wetting angle [54, 52]. Since values for the latter during growth can only be estimated, we consider $S = 2\pi r^2_{drop}$, the surface of a semisphere with radius r_{drop} as an approximation. The number of As atoms collected by the droplet over time by direct impingement can then be written

$$\frac{dN_{As}}{dt} = f_{As}\ 2\pi r^2_{drop} \tag{2.20}$$

and

$$\frac{dh}{dt} = 2\ \Omega_{GaAs}\ f_{As}\ \frac{r^2_{drop}}{r^2_{NW}} \tag{2.21}$$

which allows us to directly compare the rate of As atoms built in the solid nanowire with the number of As atoms arriving at the droplet surface by direct impingement. In Fig. 2.17 we depict the axial nanowire growth rate as function of the As-flux, expressed by the corresponding arsenic limited 2D GaAs growth rate and compare it to the growth rate estimated by the As-flux into the droplet by direct impingement. For simplicity we set $\frac{r_{drop}}{r_{NW}} = 1$, keeping in mind that $1 < \frac{r_{drop}}{r_{NW}} < 2$ has been observed after the growth (see next section). Still, after geometrical corrections, the axial nanowire growth rate exeeds the growth rate feeded by the direct As-beam

and collected by the droplet. Therefore, a second source of As, besides direct impingement has to be considered in order to compensate for this discrepancy. Indeed, Rieger et al. [60] and Ramdani et al. [52] argue that As re-evaporation from nanowire side-walls and from the Silicon surface significantly contribute to the axial nanowire growth rate. Therefore we have to write

$$dh = \Omega_{GaAs} f_{As,eff} dt \tag{2.22}$$

with $f_{As,eff} = f_{As} + f_{As,re}$. In our case, re-evaporation is the major contribution to $f_{As,eff}$.

With re-evaporation being the main component of $f_{As,eff}$, it is likely, that the axial nanowire growth rate is influenced by the surface density of the nanowires as well [149]. This so-called shadow effect however has not been investigated in this work, since a certain control of positioning and thus nanowire density, as obtained by various patterning methods for site-elective nanowire growth are required. From recent reports [150] the shadow effect seems to play an important role at surface densities $\rho_{\mathrm{NW}} >> 1\,\mu\mathrm{m}^2$. In this work, the obtained surface densities are in the range of $\rho_{\mathrm{NW}} \approx 1\,\mu\mathrm{m}^2$, so the effect of shadowing is considered to be small, which is also supported by the linear dependence of $dh/dt(R_{GaAs})$.

2.4.4 The wetting angle of Ga-droplets after growth

The liquid Ga-droplet serves as catalyst and material reservoir for the VLS growth. Since nucleation takes place directly at the interface between the liquid droplet and the solid below the shape of the droplet, i.e. its wetting angle and the type of the involved facets play a crucial role in the growth process [8, 81, 117, 59, 151, 63, 80]. We therefore investigated the tips of nanowires grown under different V/III ratios for the presence of Ga-droplets and measured the wetting angle between droplet and the top (111)-plane. In all cases, the growth was stopped by closing the shutters and ramping down the temperatures of the effusion-cells and of the substrate. Since the molecular beam from the solid source effusion cell of arsenic can only be controlled by a fast shutter and not by a needle valve, it was not possible to cut off the As-supply after growth completely. Therefore we have to consider that the droplets may have been partially consumed to a certain degree after growth, depending on the As-flux used. Consequently, the measured wetting-angles might not correspond to the wetting angles during or at the end of the growth.

A selection of the observed droplets for different V/III ratios is depicted in Fig. 2.18(a). As the V/III ratio is increased from 1 to 5, the droplets become less pronounced and even vanish for V/III > 5. Interestingly, the nanowires of this sample were terminated by flat top facets, and not needle-shaped as observed elswhere [56]. For V/III < 3 the mean wetting angles range from $\beta = 126°$ to $\beta = 107°$.

Analogous to [108, 63] we consider a Ga droplet with wetting angle $\beta > 90°$ being seated at the tip of a cylindrical nanowire. The triple-phase-line is in contact with the side walls, the liquid droplet and the vapor phase. For equilibrium conditions, it holds for the surface energies

$$\gamma_{lv}\sin\beta + \gamma_{sl} = \gamma_{wv} \tag{2.23}$$

and

$$-\gamma_{lv}\cos\beta = \gamma_{sl} \tag{2.24}$$

with the surface energy of the nanowire side-walls γ_{wv}. These equalities describe the condition of thermal equilibrium, where the triple-phase-line does not move, which is fine if the nanowire does not grow by nucleation of successive layers at the liquid-solid-interface. If a nucleus forms, as schematically depicted in Fig. 2.18(d), there needs to be an upward directed force, parallel to γ_{sl} in this case, shifting the triple-phase-line back to the level of the liquid-solid interface, in order to keep the growth stable. Consequently Eq. 2.23 turns to

$$\gamma_{lv}\sin\beta + \gamma_{sl} > \gamma_{wv}. \tag{2.25}$$

If this inequality in Eq. 2.26 is inverted, the droplet tends to wet the nanowire side walls further, sliding down the nanowire, thereby increasing β eventually resulting in unstable growth conditions. Eqs. 2.24 and 2.25 have also been used by Nebol'sin and Shetinin [152] and Glas [107] for a description of stable VLS growth conditions. Combining 2.24 and 2.25 we obtain the condition for stable VLS growth of a cylindrical nanowire:

$$\frac{\gamma_{wv}}{\gamma_{lv}} < sin\beta - cos\beta. \tag{2.26}$$

In order to quantitatively estimate stable conditions from the above relation, we employ the value $\gamma_{\mathrm{wv}}^{\mathrm{zb}} = 0.83\,\mathrm{J/m^2}$ for the surface energy of the (110)-type nanowire side-walls. This value has been obtained by DFT calculations for zinc-blende GaAs surfaces [153, 105, 86]. Together with the surface energy of the liquid Ga droplet $\gamma_{\mathrm{lv}} = 0.67\,\mathrm{J/m^2}$ [137, 63] resulting in $\frac{\gamma_{\mathrm{wv}}^{\mathrm{zb}}}{\gamma_{\mathrm{lv}}} = 1.2388\,\mathrm{J/m^2}$ as an estimate for zinc blende nanowires. As depicted in Fig. 2.18(d), Eq. 2.26 is satisfied for wetting angles $106° < \beta < 164°$. We note, that according to [63] Ga-catalyzed nanowires can not grow under the stable conditions given here. This may however be the result of employing $\gamma_{\mathrm{wv}} = 1.5\,\mathrm{J/m^2}$ which has been obtained by the counting of surface dangling bonds [154] whereas the values employed here are the result of ab-initio DFT calculations [153, 105]. Further, γ_{wv} also depends on the local polytype. Inserting the value $\gamma_{\mathrm{wv}}^{\mathrm{wz}} = 0.73\,\mathrm{J/m^2}$ for $\{11\bar{2}0\}$ sidewalls [105] we obtain a range for stable VLS growth if $96° < \beta < 175°$, implying that droplets with wetting angles smaller than 100° may still be able to sustain stable VLS growth, if the wurtzite phase is grown. Evaluating Eq. 2.24 with $\gamma_{sl} = 0.39\,\mathrm{J/m^2}$ [155], we can further estimate the equilibrium wetting angle $\beta^{eq} = 125°$.

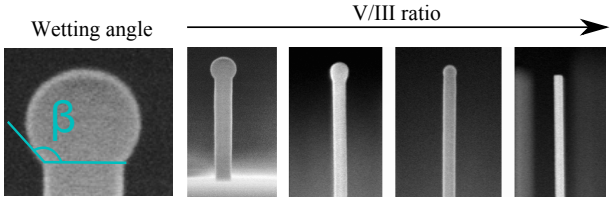

(a) Close-up SEM images of nanowire tips.

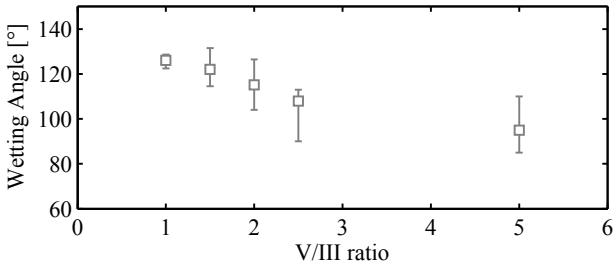

(b) Measured wetting angles for various V/III ratios.

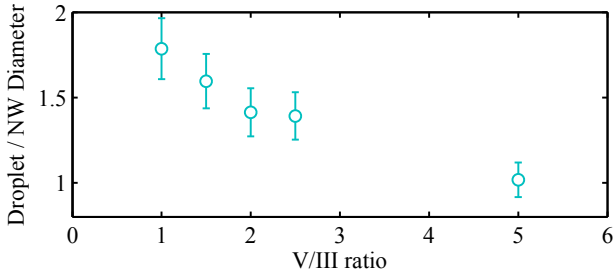

(c) Ratio between droplet diameter and nanowire top diameter.

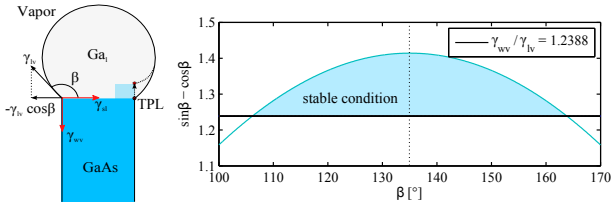

(d) Stable conditions of Ga-droplet for VLS growth, assuming (110)-type side walls.

Figure 2.18: The wetting angle with the (111)-plane β is indicated in the left (a) from post-growth SEM. With increasing V/III ratio, the droplets become smaller and, eventually vanish.

Summarizing, we investigated Ga-droplets on the tip of self-catalyzed GaAs nanowires with post-growth SEM and found wetting angles ranging from $\beta = 107°$ to $\beta = 126°$. Depending on the applied V/III ratio, the observed wetting angle changes. With increasing V/III ratio, the wetting angle decreases as well as the volume of the droplet and the diameter of the grown nanowire. Above V/III = 5, the droplets vanish completely after growth. This may be caused

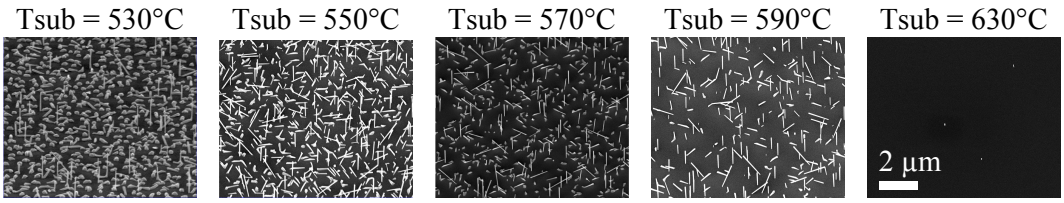

Figure 2.19: Growth results for various substrate temperatures

by crystallization as a result of the remaining As in the droplet as well as in the vapor, even after the shutters of the Ga- and As-cell have been closed. Therefore, the wetting angle observed *after* growth may differ from the wetting angle *during* growth. Considering the surface energies of the nanowire sidewalls and of the droplet, we evaluated the stability condition for VLS growth. The experimental values presented here are all within the calculated range for zinc-blende sidewalls. Other groups found similar values for the wetting angles ranging from 90° to 140° for self-catalyzed GaAs nanowires [72, 86, 80]. A thorough discussion of the surface energies and wetting conditions for VLS grown nanowires can be found in Ref. [86] and Ref. [63].

2.4.5 Influence of the substrate temperature

The temperature of the substrate is an important growth parameter, since it influences the desorption rates and the diffusion lengths of the deposited materials arsenic and gallium. Consequently, the substrate temperature effects the effective material influx into the Ga droplet. We varied the Substrate temperature from $T_S = 530\,°\mathrm{C}$ to $T_S = 630\,°\mathrm{C}$ at constant As- and Ga-fluxes. The As-flux corresponded to a As-limited 2D layer growth rate of $R^{As}_{GaAs,100} = 115\,\mathrm{nm/h}$ and the Ga-flux was equivalent to $R^{Ga}_{GaAs,100} = 45\,\mathrm{nm/h}$. The samples depicted in Fig. 2.19 have been grown for 60 minutes. The substrate temperature was calibrated by RHEED for the value of GaO desorption $T_{GaO,des} = 583.5\,°\mathrm{C}$ using a GaAs(100) substrate and by the visual observation the melting of a thin indium pillar at $T_{ind,l} = 156.6\,°\mathrm{C}$ glued on a GaAs(100) substrate.

For $T_S = 530\,°\mathrm{C}$ a large fraction of the surface is covered by crystallites, and besides tilted wires only few vertical nanowires can be observed. The tips of these wires are facetted without any Ga-droplet which has most probably been consumed after closing the Ga-shutter. This is reasonable, due to the reduced desorption rate of As at lower T_S resulting in an increased $f_{As,eff}$ in the droplet. At the same time, the nanowires are roughly $h = 2\mu m$ long which is close to the expected length $h = 1.8\mu m$ for equal f_{As} but higher T_S. If we assume $f_{As,eff}(T_S = 530\,°\mathrm{C}) > f_{As,eff}(T_S = 580\,°\mathrm{C})$ an increased axial growth rate is expected for the lower substrate temperature. As the substrate temperature is increased further the density of crystallites reduces significantly, whereas the vertical yield of the nanowires increases reaching optimal conditions for $570\,°\mathrm{C} \leq T_S \leq 590\,°\mathrm{C}$. At $T_S = 630°C$ no nanowire growth was observed.

Rieger et al. [60] performed a similar experiment obtaining comparable results. He also observes pronounced growth of crystalline GaAs at lower substrate temperatures and explains

this by the comparably high sticking coefficient of Ga-adatoms on the silicon oxide layer at these temperatures. In another study by Heiß et al.[143] the sticking coefficient is held responsible for the nucleation of the poly-crystalline GaAs as well.

For the used growth conditions, we found a window of substrate temperatures in the range of $570\,^{\circ}\mathrm{C} \leq T_S \leq 590\,^{\circ}\mathrm{C}$ suitable for the growth of self-catalyzed GaAs nanowires. Below these range, the growth of crystalline GaAs is enhanced, and the vertical yield of nanowires decreases. Above this temperature window, the density of the grown structures decreases until no nanowire growth was observed at temperatures around $T_S = 630\,^{\circ}\mathrm{C}$.

2.5 Summary: growth of self-catalyzed GaAs nanowires on Si(111)

In Summary, we performed a growth parameter study for self-catalyzed GaAs nanowires using MBE. Therefore, the whole process-line for nanowire growth was set up at the PDI in Berlin and then transferred to the UHV-lab at ANKA, beginning with the commissioning and calibration of a special portable MBE system, followed by substrate preparation process of the Si(111) wafer and post-growth SEM characterization.

We shortly commented on in-situ RHEED as a tool for fast *in-situ* feedback on the crystalline structure, epitaxial alignment and faceting of the grown structures. It is worth to note, that RHEED may become a valuable technique in order to investigate the evolution of polytypism in nanowires during the growth if employed simultaneous to *in-situ* X-ray diffraction.

We investigated different types of oxide layer-thicknesses below the thickness of the native oxide and their effect on the growth of self-catalyzed GaAs nanowires. We found, that the oxide layer thickness has an effect on the final nanowire diameter. As the oxide thickness decreased, the nanowire diameter increased. This observation could be explained by an increase of the Ga-droplet volume prior to GaAs nucleation by enhanced Ga-surface diffusion for thin oxide-layers. At the same time, the growth of parasitic crystallites could be reduced by increasing the oxide-layer thickness. Good results have been obtained for the growth on native oxide.

A Ga pre-deposition step has been introduced and its effect on the nucleation density, the vertical yield of nanowires, as well as the obtained nanowire diameter has been investigated. In our case, Ga pre-deposition leads to an increase in vertical yield of nanowires in case of a very thin oxide layer, and to a reduction of parasitic growth. However, as the oxide layer thickness approaches the one of native oxide, the effect was reversed and favored the growth of parasitic crystallites instead. At the same time, the Ga pre-deposition caused an increase of the final nanowire diameter implying larger Ga-droplets prior to growth as compared to the regular growth without Ga pre-deposition. We discussed the influence of Ga pre-deposition together with the different oxide-layer thickness in the framework of a model for the equilibrium wetting angle of Ga-droplets on Silicon oxide, which allowed to explain the observed increase in vertical yield for thin oxides.

For a systematic study of the growth parameter window for self-catalyzed GaAs nanowires, we chose Si(111) wafers covered by native oxide. We investigated the effects of Ga-flux and As-flux and substrate temperature on the nanowire's morphology and discussed our findings in the context of actual literature, both experimental an theoretical. As a result, we obtained a reliable chart of possible growth parameters for self-catalyzed GaAs nanowires for the portable MBE system.

These studies have been performed in preparation of the following *in-situ* investigations of the evolution of the morphology of self-catalyzed GaAs nanowires during growth.

3 X-ray studies of self-catalyzed GaAs nanowires

In this chapter we will report on the structural properties of self-catalyzed GaAs nanowires and their evolution during growth obtained by *ex-situ* and *in-situ* X-ray diffraction techniques. Time-resolved *in-situ* X-ray diffraction, opens up new routes for structure characterization of GaAs nanowires during growth. Therefore, we will discuss methodical aspects of our approach for structure characterization of GaAs nanowires in detail. In particular, different strategies for data evaluation for the determination of the mean polytype fraction, mean polytype segment length, and nanowire radius will be introduced and applied on results obtained by X-ray diffraction experiments performed in symmetric and asymmetric scattering geometry.

In Sec. 3.1 we will focus on the *symmetric* $(111)_{\mathrm{c}}$ and $(00.2)_{\mathrm{h,wz}}$ reflections. These reflections are accessible within the limits of the pMBE chamber and are the lowest indexed symmetric reflections in our case, providing a reasonable intensity also suitable for time-resolved measurements. Given a sufficient resolution in reciprocal space, scattering originating from wurtzite and zinc-blende will be distinguishable due to the small difference between their spacing of (111)-layers. We will introduce the measurement geometry, and describe how a scan will be performed. Then, we show exemplary results of measurements of a statistical ensemble of nanowires, which we relate qualitatively to simulated X-ray profiles for an ensemble of nanowires. By this example, we will demonstrate the sensitivity of the scattered intensity-distribution in the vicinity of the $(111)_{\mathrm{c}}$ GaAs reflection to the structural properties of the GaAs nanowires in terms of mean polytype fraction, mean segment length and statistical fluctuations thereof.

Next, we will present results obtained by *ex-situ* X-ray diffraction employing a *nano-focused* X-ray beam in order to resolve scattering signals from *individual* nanostructures in Sec. 3.2. From this experiment, we will be able to distinguish the contribution of individual nanowires and crystallites in the X-ray signal. Thereby, we also obtain valuable information for the interpretation of X-ray data obtained from ensemble measurements. In particular, we will obtain a way how to account for the contribution of the parasitic GaAs islands to the scattering.

In Sec. 3.3, we will show results obtained by *time-resolved in-situ* X-ray diffraction in symmetric geometry during the growth of an ensemble of GaAs nanowires. We evaluate our results in the frame of a time-dependent Markov model for the generation of the polytype segment

distribution in the nanowires, and discuss implications of our findings on the growth dynamics.

Later, we present results obtained in an *asymmetric non-coplanar* X-ray diffraction geometry. Both *ex-situ* and time-resolved *in-situ* experiments during the growth process of self-catalyzed GaAs nanowires will be discussed. For measurements in asymmetric geometry, the contributions of zinc-blende, twinned zinc-blende and wurtzite structures split into well separated Bragg peaks located at different positions along a truncation rod, compare e.g. the zinc-blende $(311)_{\mathrm{c}}$, the wurtzite $(10.3)_{\mathrm{h,wz}}$ and the twinned zwinc-blende $(220)_{\mathrm{c}}$ reflections in Fig. 1.8. The reflections of zinc-blende and its twin are determined by the orientation of the substrate. In our measurements we use the $(311)_{\mathrm{c}}$ reflection of Silicon as reference.

Exploiting advantages of the asymmetric measurement geometry, we will separate the contributions to the scattering signal originating from tilted structures (mainly GaAs crystallites) and the scattering of $[111]_c$-oriented epitaxial GaAs nanowires in Sec. 3.4. Since parasitic growth of crystallites is usually present, the separation of the crystallite signal from the scattering is of great importance for determining the phase fractions in the nanowires presented in Sec. 3.5. From measurements in asymmetric geometry, we will be able to obtain the phase fraction from the integrated intensity of the Bragg peaks without requiring a model for the stacking as in the symmetric case. In addition, we will be able to distinguish twinned zinc-blende from non-twinned zinc-blende which is impossible in the symmetric geometry.

In Sec. 3.6 we present time-resolved *in-situ* X-ray experiments in asymmetric scattering geometry. Besides the evolution of the phase fractions, we will investigate radial growth processes of the growing vertical nanowires, by the scattering features originating from the nanowire side-facets in Sec. 3.7.

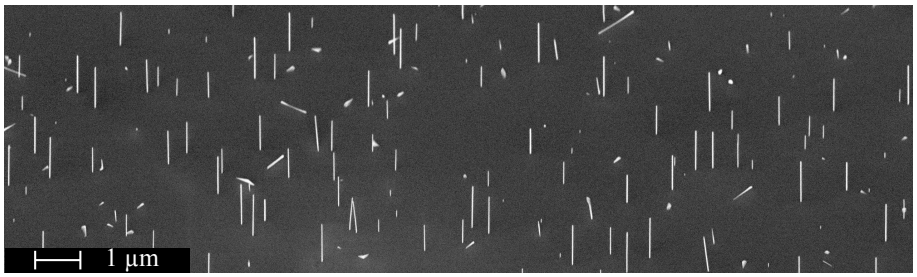

Figure 3.1: SEM image taken in a 30° view angle with respect to the sample normal. Straight and vertical GaAs nanowires have grown. Some appear to bend due to charging effects. The density of parasitic islands is very low.

3.1 Characterization of an ensemble of GaAs nanowires by *ex-situ* X-ray diffraction in symmetric scattering geometry

Here we will discuss the intensity distribution in reciprocal space around the $(111)_c$ Bragg reflection of Si and GaAs originating from the Si(111) substrate and the grown GaAs nanostructures. By comparing the measured intensity profiles to simulations, we elaborate how the structural properties (namely wurtzite fraction and mean segment length) of the GaAs nanowires are related to the scattered intensity distribution.

Sample The sample under investigation has been grown in the pMBE system prior to the measurements. The growth was performed at $T_S = 590\,°C$ substrate temperature on n-type Si(111) and a V/III ratio $F_{V/III} \approx 5$. Prior to the growth, the substrate was annealed for 30 minutes. Afterwards, Ga-droplets were deposited on the substrate. The nanowire growth was then initiated by increasing the As-flux. As the GaAs spots in RHEED appeared, the Ga shutter was opened. After 1 hour, the growth was stopped by closing the shutters and rampdown. SEM shows approx. 2000 nm long and 30-40 nm thick nanowires present at the surface, as well as some parasitic growth (see Fig. 3.1).

Experiment The X-ray measurements have been performed at a photon energy E = 15 keV at the beamline P09 at PETRA III with a beam size of $145\,\mu m x 50\,\mu m$. A Pilatus 300K detector has been placed with approx. 80 cm distance to the sample. The corresponding Bragg angles for GaAs and Si are $\Theta^{GaAs}_{(111)_c} = 7.27°$ and $\Theta^{Si}_{(111)_c} = 7.57°$ respectively. By accounting for the incidence angle, an ensemble containing approximately 50 000 nanowires are illuminated by the X-ray beam, each single nanowire with unique a stacking sequence of wurtzite and zinc-blende segments (as illustrated in Fig. 1.6(b)).

Results & Discussion For this measurement, the sample was mounted inside the pMBE chamber. By a rotation about the y-axis (see Fig. 1.7(a)) using the heavy load goniometer of the diffractometer a sufficiently large angular-range around the Bragg angles for Si and GaAs have

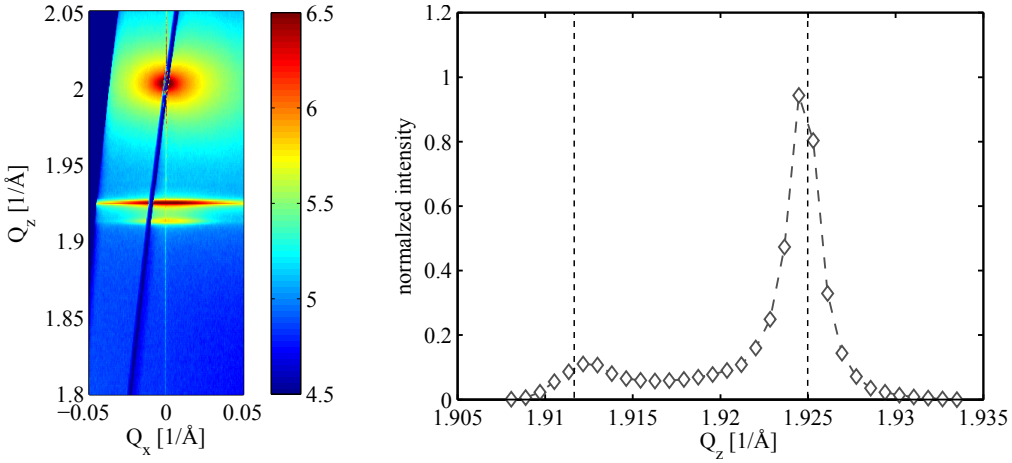

(a) RSM of the $(111)_c$ Bragg reflections of Si and GaAs.

(b) Intensity profile of the vicinity of the GaAs $(111)_c$ reflection along Q_z.

Figure 3.2: In 3.2(a), the intensity distribution in reciprocal space around the $(111)_c$ Bragg reflections of Si and GaAs is depicted in logarithmic colorscale. 3.2(b) shows the normalized intensity profile along Q_z,integrated from $-0.01 \leq Q_y \leq 0.01$ and corrected for background. The reference Q_z-values for wurtzite [92] and zinc-blende GaAs are indicated by dotted vertical lines.

been sampled. The obtained data has been transformed into reciprocal space and integrated along the q_x-direction in order to obtain a 2 dimensional map of the intensity distribution in the Q_y, Q_z- plane. Q_z is the momentum transfer perpendicular to the $(111)_c$ planes and therefore this reflection is sensitive to the stacking of wurtzite and zinc-blende segments since the vertical spacing of wurtzite and zinc-blende layers differs. The reciprocal space map is depicted in Fig. 3.2(a). Apart from the $(111)_c$ Si Bragg peak at $Q_z = 2.0038\,\text{Å}^{-1}$ we observe two separated clouds of intensity close to each other. Both signals have a large aspect ratio $\delta Q_y/\delta Q_z$ which is expected from long and thin nanowires. The most pronounced signal of these two is located very close to the Bragg peak of zinc-blende GaAs ($Q_z^{GaAs,zb} = 1.9251\,\text{Å}^{-1}$) at $Q_z^e = 1.9245\,\text{Å}^{-1} \pm 0.0001\,\text{Å}^{-1}$. A second, weaker signal is located below at $Q_z^e = 1.9125\,\text{Å}^{-1} \pm 0.0008\,\text{Å}^{-1}$. The superscript 'e' indicates that these values have been obtained from a measurement of an ensemble of nanowires. We attribute these signals to zinc-blende GaAs and wurtzite GaAs. The corresponding vertical spacing is $d_{zb}^e = 3.2648\,\text{Å} \pm 0.0001\,\text{Å}$ and $d_{wz}^e = 3.2853\,\text{Å} \pm 0.0013\,\text{Å}$, and the ratio $(d_{wz}^e - d_{zb}^e)/d_{zb}^e = 0.63\% \pm 0.04\%$. This ratio is below the reported 0.7% in [92] but are close to the value of 0.62% [86] and the value of 0.66%±0.02% reported in Sec. 3.2 and in [156]. Regarding the intensity profile in Fig. 3.2(b) however, we observe that the peaks do not exactly coincide with the positions expected by the tabular values of GaAs zinc-blende ($d_{zb}^t = 1/\sqrt{3} \cdot 5.65325\text{Å} = 3.2639\text{Å}$) and wurtzite ($d_{wz}^t = 3.2858\text{Å}$ from [92]), but appear closer to each other. This shifts are not the result of an error in the transformation to reciprocal space. Such an error causing a shift to a lower Q_z-value for zinc-blende for example, would also shift the position of wurtzite peak

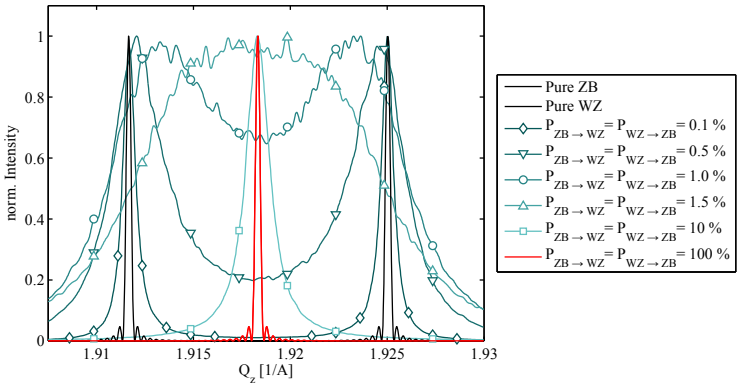

Figure 3.3: Simulations of the Q_z-intensity profiles near the $(111)_c$-GaAs Bragg reflection based on stacking sequences generated by the Markov model restricting to symmetric, static transition probabilities.

to lower Q_z-values and therefore cannot explain the observed peak positions. Another source of error could be the signal arising from the parasitic growth, although the density of parasitic islands is rather low at the actual sample. The crystallites consist of GaAs, too and therefore contribute to the measured intensity distribution around the GaAs Bragg peak. However, in an ensemble measurement of the $(111)_c$- reflection the contribution of the crystallites cannot be identified or separated without further knowledge of their individual signals. The contribution of parasites is therefore analyzed in a separate experiment using a nano-focused X-ray beam and discussed in Sec. 3.2.

In the following, we stay with the ensemble of nanowires and explain the shape and the peak positions of measured intensity profile in a qualitative way without knowing the contribution of the crystallites yet. Accounting for the average number of nanowires illuminated by the beam, and the number of layers in a nanowire of approx. 2 µm length, we simulate the stacking sequences of sets of 3000 nanowires consisting of 4000 layers using the Markov model introduced in Sec. 1.4 with varying mean wurtzite fraction and phase purity (mean lengths of zinc-blende and wurtzite segments). The simulation tool which we use has been developed and implemented by Martin Köhl [93] as part of his PhD thesis. Subsequently, we calculate the corresponding Q_z-profiles and discuss the effect of wurtzite fraction and phase purity on the X-ray scattering signal. The initial probability for wurtzite was $p(0)_{wz} = 0.5$. The intensity of the resulting Q_z-profiles has been normalized to one.

Fig. 3.3 shows the Q_z-profiles for symmetric transition probabilies in the range from 0% to 100%. For all symmetric cases the wurtzite fraction is $\tilde{p}_{wz} = 0.5$, however the phase purity varies. The extreme cases for ensembles of pure wurtzite and zinc-blende nanowires show sharp peaks with size oscillations centered at $Q_z^{GaAs,wz}$ and $Q_z^{GaAs,zb}$ respectively. Increasing the transition probability to 0.1%, the size oscillations vanish and the two peaks broaden due to fluctuations in the sizes of wurtzite and zinc-blende segments. Increasing the transition probabilities further, the

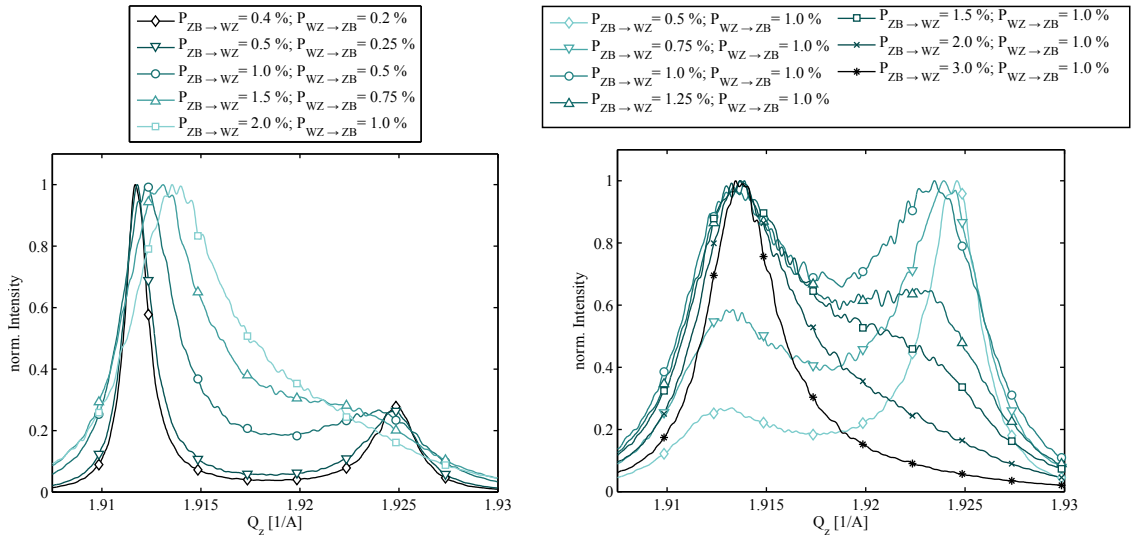

(a) Asymmetric transition probabilities with fixed asymmetry and wurtzite fraction.

(b) Asymmetric transition probabilities with varying wurtzite fraction

Figure 3.4: Simulations of the Q_z-intensity profiles near the $(111)_c$-GaAs Bragg reflection based on stacking sequences generated by the Markov model obtained for asymmetric transition probabilities.

peaks broaden further and begin to move away from their original positions towards each other. Thereby an overlap causes the intensity between the signals to increase. This overlap increases further until the two peaks merge into a broad plateau at $p_{wz\to zb} = p_{zb\to wz} = 1.5\%$. For higher transition probabilities, the plateau transforms into a single peak at $0.5 \cdot (Q_z^{GaAs,wz} + Q_z^{GaAs,zb})$ which gets sharper as the transition probabilities increase further. For $p_{wz\to zb} = p_{zb\to wz} = 50\%$ we obtain nanowires with a fully random stacking: the probability for resuming the stacking is equal to the probability to switch to the other polytype.

Since the corresponding peak is rather sharp, this means that the observation of a single sharp peak in an X-ray experiment does not necessarily imply nanowires with high phase purity. The third extreme case is reached for $p_{wz\to zb} = p_{zb\to wz} = 100\%$, where the nanowires are composed of alternating zinc-blende and wurtzite layers with a stacking sequence as '...ABCBABCBACBC...' forming pure nanowires of the 4H-polytype.

Now, we model nanowires with $\tilde{p}_{wz} \neq 0.5$. Consequently, $p_{wz\to zb} \neq p_{zb\to wz} = 1.5\%$ for which we can consider two cases: fixed $\tilde{p}_{wz}$ and free $\tilde{p}_{wz}$. The cases depicted in Fig. 3.4(a) have $\tilde{p}_{wz} = 0.67$ and the transition probabilities scale with $p_{wz\to zb} = 0.5 \cdot p_{zb\to wz}$. Similar to the symmetric cases in Fig. 3.3, we observe the merging of two peaks into one single peak for decreasing phase purity (with increasing the transition probabilities). However, the peaks are highly asymmetric regarding their maximum intensity owing to the value of the wurtzite fraction. As the transition probabilities increase, the peaks drift towards each other and their simultaneous

broadening causes an increase of intensity between the peaks. For $p_{wz\to zb} = 0.5 \cdot p_{zb\to wz}$ no individual peak close to $Q_z^{GaAs,zb}$ is visible anymore, but a plateau. Further, the broad shape of the peak close to $Q_z^{GaAs,wz}$ is highly asymmetric with pronounced weight at the right flank. The maximum of this peak shifts towards the center for increasing transition probabilities. Now, we let the wurtzite fraction vary and consider the cases depicted in Fig. 3.4(b). Here $p_{wz\to zb} = 1\%$ is fixed and $p_{zb\to wz}$ varies from 1% to 3%. Starting at a wurtzite fraction of $\tilde{p}_{wz} = 0.33$ for $p_{zb\to wz} = 0.5\%$, we see a pronounced peak near the zinc-blende position and a small peak close to the position of wurtzite. Both broad peaks show considerable overlap due to the small segment size. For $\tilde{p}_{wz} = 0.43$ for $p_{zb\to wz} = 0.75\%$, the peak close to wurtzite becomes stronger. At the same time the peak at zinc-blende broadens and both peaks shift towards the center. The symmetric condition is reached for $p_{zb\to wz} = 1.0\%$ equal to the case depicted in Fig. 3.3 For $p_{zb\to wz} = 1\%$ the most pronounced peak is now that at the wurtzite side. The signal originating from the shorter zinc-blende segments gives rise only to a plateau which becomes less pronounced as $p_{zb\to wz}$ increases. At the same time the peak of wurtzite becomes sharper and shifts further towards the center. We point out that the width of the wurtzite peak changes, although the mean length of wurtzite segments stays the same for all cases depicted in Fig. 3.4(b).

In summary, we observe a highly non-trivial shape of the Q_z-profiles of the $(111)_c$ Bragg reflection of GaAs nanowires, depending on wurtzite fraction and phase purity. Since the signals of wurtzite and zinc-blende GaAs are very close to each other in case of the $(111)_c$ reflection, interference effects between zinc-blende and wurtzite segments are non-negligible. For pure wires, we see sharp peaks with size oscillations at $Q_z^{GaAs,wz}$ and $Q_z^{GaAs,zb}$. As the phase purity decreases, we observe a broadening of these peaks together with a drift of these peaks towards the center. The drift and the broadening causes the both peaks to overlap so that only a single peak can be observed for nanowires of low phase purity. The position of the peak depends on the wurtzite fraction, whereas the shape depends on both, wurtzite fraction and phase purity. Therefore, we conclude that the determination of wurtzite fraction and phase purity of the nanowires from Q_z-profiles of the $(111)_c$ GaAs reflection needs prior modeling as in our case using a simple Markov model for the generation of the stacking. Since the positions of the peaks does not correspond to the native values for $Q_z^{GaAs,wz}$ and $Q_z^{GaAs,zb}$ (unless for very pure wires) even the spacing of wurtzite and zinc-blende layers cannot be extracted directly from the Q_z-profile of the $(111)_c$ GaAs reflection, if an ensemble of nanowires is considered. Returning to the experimental profile depicted in Fig. 3.2(b), we consequently have to expect that the values for the ratio $(d_{wz} - d_{zb})/d_{zb}$ extracted from this profile is lower than the native values, although we observe two distinct peaks suggesting a rather high phase purity. Consequently, the large statistical fluctuations of the segment lengths render ensemble measurements not suitable for the extraction of the lattice spacing of wurtzite and zinc-blende, unless the phase purity of both polytypes is sufficiently high, and the amount of prasitic GaAs crystallites is negligibe. Ideally, measurements of individual nanowires would be able to provide the needed information without being affected by these statistical fluctuations

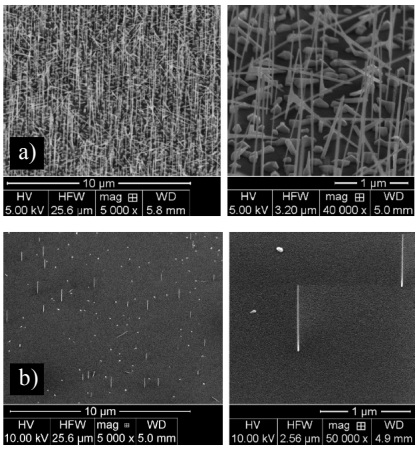

SEM summary		
	Sample 1	Sample 2
Nanowire density [1/µm^2]	2.2	0.0064
Nanowire mean heigth [µm]	2.22	1.15
Nanowire mean diameter [µm]	25	18
Nanowire mean volume [µm^3]	$1.1 \cdot 10^{-3}$	$2.9 \cdot 10^{-4}$
Crystallites density [1/µm^2]	5.32	0.56
Crystallites volume [µm^3]	$2.7 \cdot 10^{-3}$	$3.6 \cdot 10^{-4}$

Figure 3.5: Left: SEM images of the measured samples (sample 1 depicted in a); b) shows sample 2). Adapted from [156]. Reproduced with permission of the International Union of Crystallography. Right: Results of post-growth *ex-situ* SEM characterization.

3.2 Scattering from individual self-catalyzed GaAs nanowires and parasitic GaAs crystallites investigated by *ex-situ* X-ray diffraction using a nano-focus setup

Here we discuss X-ray measurements performed at the beamline ID13 at ESRF in Grenoble using a nano-focus setup. From these measurements we will obtain important information on the composition of ensemble signals as shown in Fig. 3.2(a), which will allow us to identify signals from individual nanostructures and distinguish the signals of GaAs nanowires from parasitic GaAs crystallites. Moreover, we will be able to estimate the ratio of the interplanar spacing $(d_{wz} - d_{zb})/d_{zb}$ in the nanowires. Those findings will be of great importance for the interpretation of time-resolved X-ray data obtained in ensemble measurements. These results have been published in Ref. [156] and are also presented in the PhD thesis of Martin Köhl [93].

Samples The two GaAs nanowire samples investigated here have been grown in the pMBE system at $T_S = 590\,°\text{C}$. Sample 1 was grown for 60 min at a V/III ratio of $F_{V/III} \approx 3$ and a Ga-flux corresponding to $R^{Ga}_{GaAs,100} = 45\,\text{nm/h}$ GaAs growth rate. Sample 2 was grown for 30 min at a lower $R^{Ga}_{GaAs,100} = 30\,\text{nm/h}$ and $F_{V/III} \approx 5$. Sample 1 features a rather high surface density of grown GaAs nanostructures (both, nanowires and crystallites), whereas a low density had been achieved for sample 2 which is of advantage for measurements requiring the illumination of single or few objects at a time. Representative SEM images of the two samples are depicted in Fig. 3.5 together with the results of a SEM analysis. The obtained diameters and heights correspond to the estimated values based on the growth calibration presented earlier in Chapter 2.

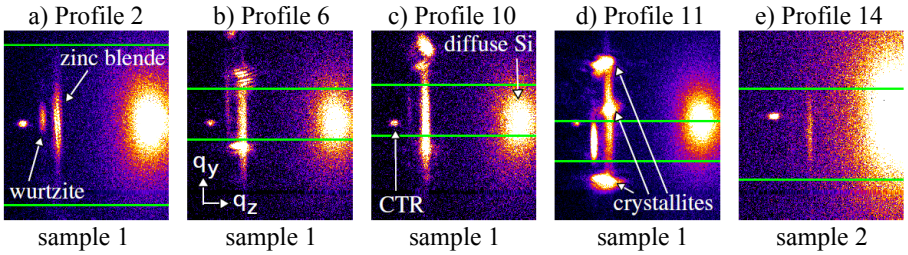

Figure 3.6: Detector frames best suited for the determination of the interplanar spacing of wurtzite and zinc-blende in our GaAs nanowires. In every frame, we observe the diffuse cloud of the Si(111) substrate and the cut with the CTR. The nanowires give rise to sharp signals in Q_z- direction but a broad extended signal in Q_y-direction with their centers close to the axis spanned by the CTR and the Si(111). Depending on the polytype the signals are located at different Q_z positions. Crystallites scatter at the same Q_z positions but their centers spread along Q_y indicating that the crystallites are tilted with respect to the $[111]_c$-direction. Taken from [156]. Reproduced with permission of the International Union of Crystallography.

Experiment The nano-focus setup available there provided an X-ray beam size with approx. 250 nm FWHM at a photon energy of E = 14.9 keV. We investigated two samples featuring GaAs nanowires with a certain amount of parasitic growth. By use of a piezo-nanostage we sampled different areas at the sample in a fine grid illuminating single or few objects at a time. The incidence angle was close to $\Theta^{\mathrm{GaAs}}_{(111)_c}$ and kept constant during the scan. Thereby we recorded regions in reciprocal space close to the GaAs Bragg reflection which essentially correspond to a cut parallel to the Q_y, Q_z-plane in reciprocal space for different non-overlapping spatial positions on the sample. The scattered signal was recorded by a MAXIPIX detector with 55 µm pixel size placed at 67 cm distance to the sample.

The detector frames recorded during the measurements always contain a diffuse cloud of intensity which stems from the Si(111) substrate and the CTR. At the GaAs position we observe additional signals, depending on the number and type of illuminated nanostructures. In Fig. 3.6 four such detector frames are depicted showing the signal originating from different locations of sample 1 and one frame showing a signal from sample 2.

As already seen from SEM, the surface density of GaAs nanostructures is higher for sample 1, therefore usually parts of multiple objects are illuminated and contribute to the scattering. For sample 2 the surface density was sufficiently low so that individual GaAs objects could be illuminated at a time. Compared to the signals from sample 1, the signals from sample 2 are weaker which is expected due to the lower diameter and therefore lower scattering volume of the GaAs structures grown on sample 2.

Results & Discussion Fig. 3.6(a) shows scattering attributed to rather extended segments of zinc-blende and wurtzite in the nanowires giving raise to two well separated peaks with high aspect ratio. In Fig. 3.6(d) in addition to nanowires, also crystallites are illuminated which can be identified by the rather circular shape of their signals. We classified the signals at the detector frames as follows: From SEM and the X-ray beam size we expect the nanowires to provide signals

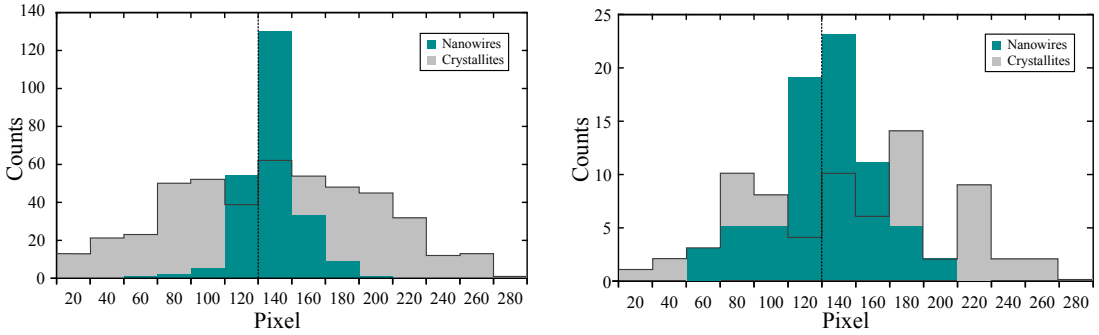

(a) 465 Crystallites: Mean= 129.2; StDev =58.7 and 234 Nanowires: Mean= 127.6; StDev =16.3

(b) 140 Crystallites: Mean= 137,0; StDev =59.2 and 74 Nanowires: Mean= 122.3; StDev =30.0

Figure 3.7: Distribution of the centers of individual signals originating from either nanowires or crystallites with respect to the position of the CTR. The wire signals have their centers close to the position of the CTR and the substrate (indicated by the vertical line). The standard deviations obtained for the crystallite-distribution exceeds the one of the nanowires at least by a factor of 2.

with a large aspect ratio $\delta Q_y/\delta Q_z$, whereas the signals from crystallites have an aspect ratio close to unity. In this way, we classified the frames into separate groups containing scattering from nanowires or crystallites only. Then, we attributed each signal to either scattering from crystallite or nanowire and registered the center of the respective signal. Thereby we obtain separate distributions of the signals from nanowires and crystallites along both Q_y and Q_z directions.

The distribution of the so obtained centers of the signals from nanowires and crystallites along the Q_y-direction have been plotted in Fig. 3.7. For both samples, the signals are distributed around a mean value close to the Q_y-position of the CTR, indicated by the vertical line. The distribution of the crystallite-signals has a width of approx. 60 pixels for both samples, whereas the distribution of the nanowire-signals is more narrow. This observation allows us to understand the origin of the high aspect ratio ($\delta Q_y/\delta Q_z$) of the ensemble signal. The Q_y- extension of the ensemble signal depicted in Fig. 3.2(a) is therefore not only given by shape function of the small diameter of the nanowires but may be additionally a consequence of small tilts of the GaAs structures around the $[111]_c$ direction. These tilts are more pronounced for crystallites than for nanowires indicating that the epitaxial relation of the crystallites to the Si(111) substrate is bad causing the crystallites to grow in random orientation. This conclusion is consistent with our findings from RHEED shown in Fig. 2.4, where we observed Debye-Scherrer rings passing through reflections of zinc-blende and twinned zinc-blende only, the powder rings appear during growth and are independent of the RHEED azimuth.

Now, we investigate the cumulative signals of nanowires and crystallites along the Q_z-direction, which contains crystallographic information regarding polytypism. We therefore integrate the detector frames along Q_y and obtain intensity profiles along the Q_z-direction. We fit

a Pearson VII function to the diffuse signal of silicon and thereby obtain the Q_z-position of its center. All profiles are then normalized to the signal of silicon and shifted such that the center of silicon is at zero position. For these shifts a linear interpolation of the data has been performed, since the center of silicon usually is a non-integer value. After the shifts and summation of the individual signals in the classes "nanowires" and "crystallites" we obtain the respective cumulative profiles. In Fig. 3.8(a), these profiles are depicted for three separate scans performed at different spatial positions of sample S2. Scan 1 is composed of 6 frames containing nanowires and 16 frames containing crystallites. Scan 2 consists of 16 frames with nanowire signals and 32 frames with signals of crystallites. Scan 3 is accumulated from 19 nanowire frames and 37 crystallite frames. If we regard the profiles from the nanowires, we observe considerable fluctuations between the scans. These fluctuations imply a large variation of the polytypic properties of the inspected nanowires such as wurtzite fraction and mean segment length.

All three nanowire profiles depicted in In Fig. 3.8(a) exhibit an asymmetric shape with its center of mass near the position of zinc-blende, indicating that the nanowires consist of mainly zinc-blende. However, scan 2 shows two distinct peaks indicated by the vertical lines. The main peak at position $p_1 = -128.0 \pm 1.0$ is attributed to zinc-blende, the second peak close to $p_2 = -148 \pm 1.5$ pixels is attributed to wurtzite. Scan 1 also shows a peak at p_1, however no peak at p_2 is observed which is attributed to the low number of nanowires contained in the scan and to a low phase purity causing the intensity plateau in between the zinc-blende and wurtzite positions. Scan 3 exhibits a broad peak close to $p_2 = -148 \pm 1.5$ slightly shifted towards larger values which is compatible with a low phase purity and small wurtzite segments. Consequently, the peak at the zinc-blende position is shifted to smaller values which is compatible with the simulations discussed in Sec. 3.1. In contrast to the nanowire signals, the shape of the profile from crystallites is close to a Gaussian and very similar for each scan. In particular, the center of the crystallite profiles is very close to $p_3 = -135$ clearly in between the signals of zinc-blende and wurtzite. This indicates that the GaAs crystallites are strained exhibiting a larger lattice constant in $[111]_c$ direction caused by compressive lateral strain from the Silicon substrate.

In Fig. 3.8(b), we compare the overall signals from crystallites and nanowires of the samples S1 and S2. For better comparison, the signals have been scaled in such a way, that the strongest profiles have equal maximum intensity. Threby, we can directly compare the shape of the crystallite signals, which is very similar for both samples. However, the signal from the nanowires differs. Whereas only one peak close to zinc-blende with a tail towards lower positions for sample S1 can be observed, S2 exhibits a fine structure and shows, besides the main peak close to zinc-blende a second peak at lower positions due to wurtzite. We attribute the differences in the signals of the nanowires to the difference in growth conditions for both samples, resulting in different polytypic properties. The gaussian shape, as well as the position of the center of the crystallite signal will be of high importance when correcting X-ray data obtained in ensemble measurements of the $(111)_c$ Bragg reflection in order to be comparable to the simulations obtained by the Markov model.

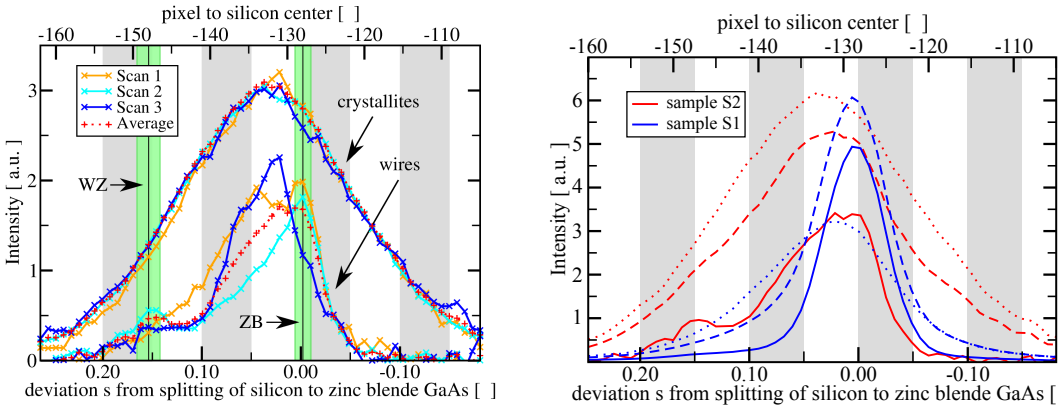

(a) Cumulative Q_z-profiles of nanowires and crystallites of three different scans performed on different spatial positions on sample S2. The profiles were normalized to equal weight of the crystallite signal.

(b) Comparison of the cumulative Q_z-profiles for nanowires and crystallites of the two samples S1 and S2. Crystallites are depicted in dotted lines. Solid lines correspond to nanowires and the dashed lines show the overall signal of all measured frames.

Figure 3.8: Taken from [156]. Reproduced with permission of the International Union of Crystallography.

We now will investigate the difference in the spacing of the atomic layers for wurtzite and zinc-blende in the nanowires in more detail. We therefore express the splitting of wurtzite and zinc-blende in reciprocal space as a fraction of the distance s between the zinc-blende GaAs and the Silicon signals:

$$s = \frac{Q_{zb} - Q_{wz}}{Q_{Si} - Q_{zb}}. \tag{3.1}$$

We then can express the ratio of the interplanar spacings of the atomic layers in wurtzite and zinc-blende [93, 156]:

$$\frac{d_{wz}}{d_{zb}} = \frac{Q_{zb}}{Q_{wz}} = \frac{1}{1 - (Q_{zb} - Q_{wz})/Q_{zb}} \tag{3.2}$$

$$= \left[1 - s \cdot \frac{Q_{Si} - Q_{zb}}{Q_{zb}}\right]^{-1} \tag{3.3}$$

$$= \left[1 - s \cdot \frac{d_{zb} - d_{Si}}{d_{Si}}\right]^{-1} \tag{3.4}$$

$$= \left[1 - s \cdot \frac{a_{zb} - a_{Si}}{a_{Si}}\right]^{-1} \tag{3.5}$$

$$\approx 1 + s \left(\frac{a_{zb} - a_{Si}}{a_{Si}}\right) \tag{3.6}$$

We obtain $(a_{zb} - a_{Si})/a_{Si} = 4.092\%$ if we assume bulk values for $a_{zb}^{GaAs} = 5.65325$ Å and

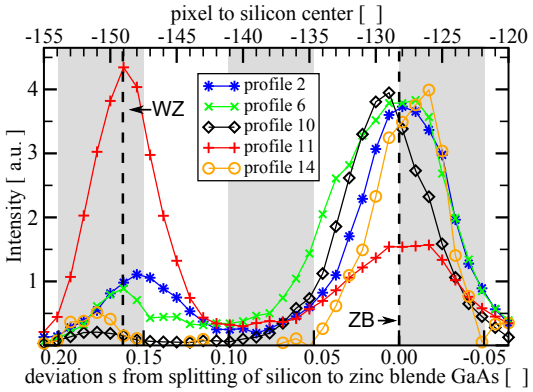

(a) Q_z-profiles of nanowires from frames depicted in Fig. 3.6 obtained by Q_y-integration in the region of interest indicated by the green lines. The profiles were shifted and corrected for background, as described in the text. The dashed vertical lines correspond to the average of the centers of zinc-blende and wurtzite signals obtained from the five profiles.

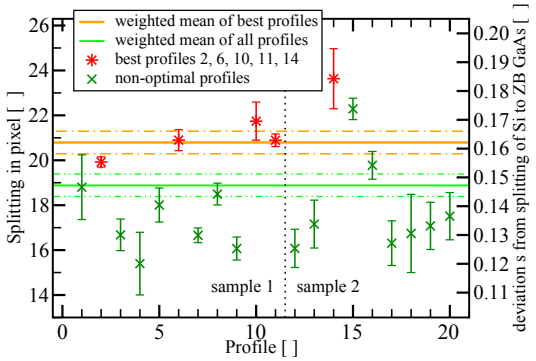

(b) Distance of the wurtzite and zinc-blende GaAs peaks in reciprocal space. The best profiles (see Figs. 3.6 and 3.9(a) originating from scattering at extended segments are depicted by red stars. The splittings obtained by other profiles are likely to underestimate the difference due to low phase purity of the illuminated segments.)

Figure 3.9: Taken from [156]. Reproduced with permission of the International Union of Crystallography.

$a_{Si} = 5.43102$ Å. Applying the values for p_1 and p_2 from the cumulative signals in Fig. 3.8(a), we obtain for the nanowire 'ensemble' measured by nanofocus: $s_{e,nf} = 15.6\% \pm 1.9\%$ or $[(d_{wz} - d_{zb})/d_{zb}]^{e,nf} = 0.64\% \pm 0.08\%$. This value is compatible with the value obtained from ensemble measurements presented in Sec. 3.1, where we reported on $[(d_{wz} - d_{zb})/d_{zb}]^{e} = 0.63\% \pm 0.04\%$. However, both values are likely to underestimate the ratio, since low phase purity of one or both polytypes shift the maxima of the respective peaks towards each other as can be seen in Fig. 3.3. Therefore, we are aiming at signals from long extended segments which are consequently better candidates for estimating the difference in the atomic spacing in wurtzite and zinc-blende. This is most likely the case, if both peaks in the profile are well separated and have no fine structure, i.e. are Gaussian-shaped. Additionally, the photon counts in the center between the peaks have to be as low as possible.

We identified 20 frames which show a nanowire signal that exhibits both zinc-blende and wurtzite. From the profiles obtained from these 20 frames, we depict the five profiles which best fulfill the requirements stated above in Fig. 3.9(a). All 20 profiles were then fitted by two Gaussian distributions, and the centers of the fits were used to determine the splitting as depicted in Fig. 3.9(b). The five profiles fulfilling our requirements for extended segments clearly show the most pronounced splitting, whereas the values obtained from the other candidates is systematically lower. The extracted values are $s_5 = 16.2\% \pm 0.4\%$ and $s_{20} = 14.7\% \pm 0.4\%$ which relates to $[(d_{wz} - d_{zb})/d_{zb}]_5 = 0.66\% \pm 0.02\%$ and $[(d_{wz} - d_{zb})/d_{zb}]_{20} = 0.60\% \pm 0.02\%$.

Compared to the values obtained by the ensemble signals and $[(d_{wz} - d_{zb})/d_{zb}]_{20}$, the value obtained by the best five profiles $[(d_{wz} - d_{zb})/d_{zb}]_5$ is larger since we avoid the effect of segments

of low phase purity. The value $[(d_{wz} - d_{zb})/d_{zb}]_{20} = 0.60\% \pm 0.02\%$ is however even smaller than the values obtained by the ensemble profiles which is owed to strong fluctuations of the phase purity between individual wires.

In summary, employing X-ray diffraction together with the nano-focus setup at ID13, we extracted the interplanar spacing of the atomic layers in zinc-blende ($(111)_c$) and wurtzite ($(00.2)_{h,wz}$) in thin, freestanding self-catalyzed GaAs nanowires grown on Si(111) substrates covered with native oxide. We found that the spacing of wurtzite layers in the wires is $0.66\% \pm 0.02\%$ larger than that of zinc-blende layers. Our results are compatible with the values reported by Biermanns [92] ($0.70\% \pm 0.05\%$) which is very close to our best estimate and the value reported by Breuer (0.62% [86]) which is very close to our values obtained for nanowire ensembles. However, our results are not compatible with the values reported by Mariager et al. [98] ($1.49\% \pm 0.06\%$). Finally, the value reported by Tchernycheva et al. [32] (0.52%) is outside of our range of error. Additionally, we identified the contribution of parasitic GaAs crystallites to the scattering signal which provides valuable information for the interpretation and processing of data obtained in X-ray diffraction of an ensemble of GaAs nanowires.

3.3 Evolution of polytypism during the growth of self-catalyzed GaAs nanowires

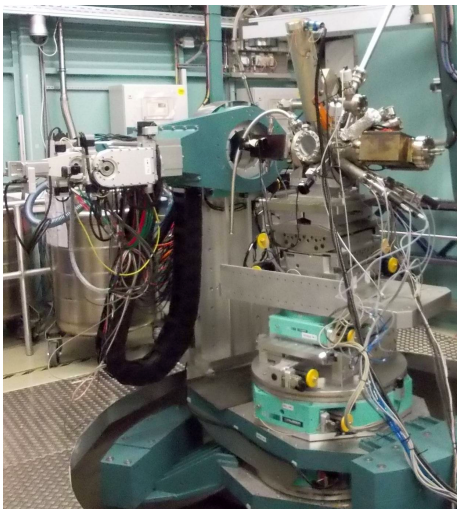

Figure 3.10: The portable MBE installed at the heavy-load diffractometer at the NANO beamline at ANKA. The downstream Be-window is visible. Also the cells for As, Ga and In at the right ca be seen. During the experiment the MBE was cooled with liquid N_2. The detector arm at the left holds a 1D Mythen strip detector used for calibration. The wiggler insertion device provided a flux of 10^{11} ph/s at an X-ray energy of $E = 14$ keV monochromatized by a double-crystal monochromator [157].

In this section we present results obtained from time-resolved *in-situ* X-ray diffraction during the growth of self-catalyzed GaAs nanowires grown on a Si(111) substrate covered with native oxide. Our results will give insight into the evolution of polytypism during the growth of the nanowires. We will infer key-parameters of polytypism such as mean phase fraction and phase purity and their evolution during growth, and discuss implications on the growth dynamics.

3.3.1 Experiment setup and data evaluation

In the following, we will discuss the experimental setup including measurement geometry and sample description. Further we will detail the route for data processing which is prerequisite for further interpretation of the time-resolved X-ray scattering data.

Experiment The measurements have been performed at the NANO beamline of the synchrotron radiation source ANKA at the Karlsruhe Institute of Technology employing the pMBE system. For this purpose, the growth chamber of the pMBE has been installed at the heavy load diffractometer at NANO. This diffractometer allows to translate and turn heavy equipment up to a total weight of 500 kg. With 175 kg, the pMBE growth chamber is well below this limit. A wiggler insertion device provided a photon flux of 10^{11} ph/s at an X-ray energy of E = 14 keV at $\delta E/E \approx 10^{-4}$ obtained by a double-crystal monochromator. We used a 2-dimensional Pilatus 100K detector with a pixel size of 172 µm x 172 µm placed at approx. 1m distance to the sample and monitored the intensity distribution in the vicinity of the $(111)_c$ Bragg reflection of GaAs. The Bragg angles for GaAs and Si at this energy are are $\Theta^{\mathrm{GaAs}}_{(111)_c} = 7.797°$ and $\Theta^{\mathrm{Si}}_{(111)_c} = 8.119°$ respectively. At this configuration and employing s_5, we expect the signals of wurtzite and zinc-

blende GaAs to be separated by approx. 11 pixels at the detector. Before and after the growth of the sample discussed here, three dimensional reciprocal space maps have been measured. The 3-dimensional intensity distribution was then integrated along the Q_y- direction in order to obtain the 2-dimensional reciprocal space maps of the Q_x, Q_z-plane. During the growth, detector frames at a fixed position of sample and detector with a frame rate of 0.83 frame/s have been recorded. The incidence angle for the time-resolved measurements was chosen to be close to the Bragg angle of GaAs zinc-blende. Thus the recorded 2 dimensional intensity distribution at each frame essentially corresponds to the intensity distribution in the Q_y, Q_z-plane in reciprocal space. The intensity is summed up along the Q_y-direction to obtain one-dimensional intensity profiles along Q_z which contain the crystallographic information on polytypism in the GaAs nanowires. The processing of the so obtained data and the successive correction for the signal of the GaAs crystallites was a joint work with Martin Köhl and is discussed in detail in his PhD thesis [93]. He also prepared the basis for the interpretation of the experimental data in the frame of the Markov model. Moreover, our results have been published in Ref. [113].

The setup of the experiment at the NANO beamline is shown in Fig. 3.10. The pMBE growth chamber is installed on the heavy duty Huber table of the diffractometer. A special adapter plate connects the growth chamber and the tower and shifts the center of the pMBE, and therefore the sample inside towards the level of the X-ray beam. The RHEED gun of the pMBE system was offline. Due to radiation-safety reasons, a simultaneous operation of RHEED and XRD was not possible, since the copper covers of the Be-windows had to be removed for the XRD measurements. RHEED operation is however only possible, while these covers are attached. During the experiment, the growth chamber was cooled by liquid N_2 and pumped by a 150 l/s ion-pump. Samples for the *in-situ* investigations could be transferred into the growth chamber from the storage compartment directly attached to the growth chamber. The temperatures of the evaporation cells, substrate heater as well as the motors for shutters and substrate rotation were remotely controlled from the beamline control room.

Sample The sample which is subject to this discussion has been grown on Si(111) substrates covered by native oxide. The wafer has been provided by the Paul-Drude Institut für Festkörperelektronik and belongs to the same batch of wafers which were used for the growth calibrations in Chapter 2. The substrate was annealed prior to growth at $T_S = 750\,°C$. During growth a comparatively high As-flux resulting in a background pressure in the growth chamber of $P_{gc} = 2.9 \cdot 10^{-7}$ mbar and a V/III ratio of approx. 5 was applied. The Ga-flux was equal to a growth rate of $R^{Ga}_{GaAs,100} = 30\,\text{nm/h}$ on GaAs(100) substrates. The growth was performed for 1 hour at $T_S = 590\,°C$ substrate temperature. After that, the shutters were closed and the substrate temperature was decreased to $T_S = 100\,°C$ in 8 minutes.

A post-growth SEM image of the *in-situ* grown sample taken at an angle of 60° from the surface normal is shown in Fig. 3.12. Thin and vertical nanowires with a low surface density were grown. The nanowires have a mean diameter of $d = 17\,\text{nm} \pm 5\,\text{nm}$ and mean height of $h = 2.2\,\mu\text{m} \pm 0.25\,\mu\text{m}$. In addition to the nanowires, parasitic growth without pronounced

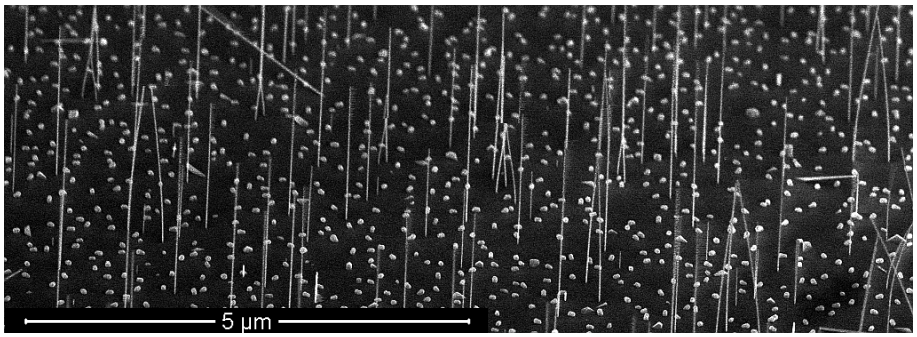

Figure 3.11: SEM image of the sample post-growth. Thin vertical nanowires with mean diameters of approx. $d = 17\,\text{nm}\pm5\,\text{nm}$ diameter and mean height of $h = 2.2\,\mu\text{m}\pm0.25\,\mu\text{m}$ as well as parasitic growth are visible.

faceting is visible. Again the values for diameter and height are within our expectations and in agreement with the growth calibrations.

Results Before and after the growth process we recorded a full 3-dimensional reciprocal space map of the $(111)_c$ GaAs Bragg reflection. The intensity has been integrated along the Q_y-direction in order to obtain the intensity distribution in the Q_x, Q_z- plane as shown in Fig. 3.12 . Before the growth, only the signal of the Si(111) substrate at $Q_z = 2.0038\,\text{Å}^{-1}$, the CTR and an oblique streak due to air scattering at the Bragg condition is visible. After the growth, a diffuse cloud of scattered intensity is visible at lower Q_z values. This cloud has an interesting shape suggesting, that the crystal structure of the nanowires may be composed by a mixture of cubic zinc-blende and hexagonal wurtzite GaAs. However, parasitic crystallites contribute as well to this signal. The extraction of detailed information on polytypism and it's evolution during growth from the shape of the GaAs signal will be discussed later.

During the growth, we restricted ourselves to measure the scattered intensity at a fixed position in reciprocal space instead of recording full reciprocal space maps, in order to achieve a time-resolution as good as possible. This chosen position is close to the GaAs Bragg peak and indicated by a black line in Fig. 3.12. Examples of the so obtained detector frames at three different growth times are depicted in Fig. 3.13(a). At the beginning, the frame only shows a cut through the diffuse part of the Si(111) signal centered around channel 60 and the cut with the CTR at channel 130. In a later stage of the growth, a signal from GaAs arises below the CTR between channel 130 and 150 visible as a diffuse cloud at first. At the final stage the GaAs signal shows an interesting shape caused by scattering from zinc-blende and wurtzite segments in the nanowires. The experimental geometry and thus the signals visible therein corresponds essentially to the geometry used for the frames measured during the nano-focus experiments at the ESRF, presented in Sec. 3.2. However, here the signal at the GaAs position arises from scattering of an *ensemble* of nanowires and crystallites. In a later step, the intensity distribution was summed up along the full Q_y-direction. Thereby we obtained a one-dimensional profile for each frame. All recorded profiles are depicted in Fig. 3.13(b). In total 2975 detector frames

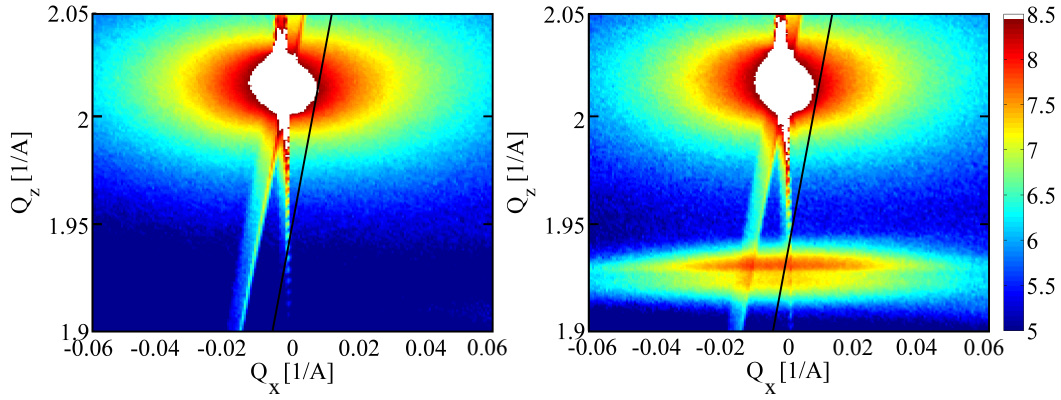

Figure 3.12: Reciprocal space maps of the $(111)_c$ Bragg reflections of Si and GaAs before and after the growth of GaAs nanowires. The GaAs signal exhibits a non-trivial shape and contains information on polytypism in the nanowires. The position of the frames recorded *in-situ* is depicted by the black solid line.

were recorded at 1 second exposure during the 1 hour growth . The digital processing of the frames resulted in an effective measurement time of 1.20 seconds per frame. The signal of GaAs between channels 130 and 150 starts to visibly appear at frame 500 which corresponds to a growth time of 10 minutes. The maximum intensity of the broad signal from Si(111) located at vertical channel 60 decreases slightly during growth which caused by a successive decrease of the incoming X-ray flux. This decrease is a result of the decrease of the electron current in the storage ring of the synchrotron. Consequently, the decrease in the incoming X-ray flux needs to be taken into account during further data analysis.

We now describe the processing steps which have been applied to this experimental raw data. First the decrease in the incoming X-ray flux was corrected for each detector frame. In order to increase the signal-to-noise ratio, 197 frames have been averaged, lowering the effective time-resolution to 4 minutes per time-step. We then averaged the first 100 detector-frames in order to get an estimate of the silicon signal and of the CTR. This average was then normalized and subtracted for each time step. The residual signal from the CTR was linearly interpolated. As a result, only the signals from GaAs remain. After Q_y-integration, we obtain the Q_z-profiles depicted in Fig. 3.14(a). We observe, that the overall intensity, as well as the shape of the profile changes with advancing growth time. Until 26 minutes of growth a rather broad plateau is visible, similar to the shape of the simulated profile for symmetric transition probabilities $p_{wz\to zb} = p_{zb\to wz} = 1.5\%$ in Fig. 3.3. For later growth times, the shape of the profile clearly obtains an asymmetric shape with a pronounced peak close to the position of GaAs zinc-blende. As the growth commences, this asymmetry becomes even more pronounced. The ratio between the peak at zinc-blende and the plateau at wurtzite increases from approx. 1 at 26 minutes growth time to approx. 1.6 after 58 minutes of growth.

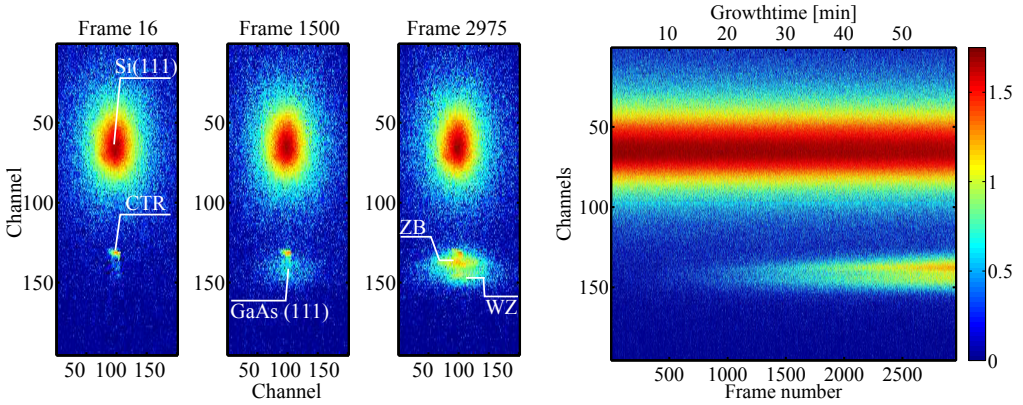

(a) Detector frames: Frame 16, 1500, 2975. At frame 16, the Ga shutter was opened.

(b) Intensity profiles along Q_z (decreasing channels correspond to increasing Q_z). A frame took 1 second for exposure and 0.20 seconds for saving.

Figure 3.13: Detector raw frames and Intensity profiles obtained during time-resolved X-ray diffraction during the growth experiment.

Regarding the shape of the profiles, there is broad background visible in the regions below $Q_z \leq 1.905\,\text{Å}^{-1}$ and above $Q_z \geq 1.935\,\text{Å}^{-1}$. Comparing to our numerical simulations of the ensemble Q_z-intensity profile shown previously in Fig. 3.3 and Fig. 3.4, we would expect the signal to decay rapidly towards zero intensity. From our nano-focus measurements, we know that the ensemble signal is composed of the signal from the nanowires and of the signals from the crystallites. Whereas the individual signals of the nanowires were sharp in Q_z direction and polytypism caused an interesting and asymmetric shape of the cumulative signal (compare Fig. 3.8(a)), the signal of the crystallites did not show such a fine structure, but is rather described by a broad Gaussian like signal. Thereby its width in Q_z, as well as in Q_y-direction exceeds that of the nanowire signal. Consequently, we attribute the signal in the tails of the Q_z-profile in Fig. 3.14(a) to scattering mostly originating from crystallites.

The evolution of the overall intensity of the GaAs signal with growth time is depicted in Fig. 3.14(b). We integrate over the whole GaAs signal, thus besides the nanowires, the crystallites contribute to the signal as well. Therefore, conclusions on the crystal structure and growth processes in the nanowires can not be made, unless the contributions of crystallites and nanowires in the signals depicted in Fig. 3.14 are separated.

After such a separation, we could obtain information on radial and axial growth processes in nanowire growth, given the total scattered intensity of the reflection is recorded in a time-resolved way. For example, we would expect a strictly linear increase of the intensity, proportional to the increase of the nanowire height for the absence of radial growth since the integrated intensity scales with the scattering volume. But, from the growth calibrations in Chapter 2 we know, that in addition to a rapid axial growth of the nanowire height, non-catalytic radial growth

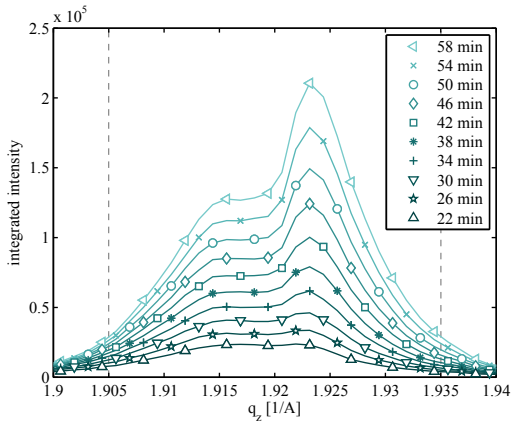

(a) Intensity profiles after averaging. The resulting time-resolution is 4 min. With time, the asymmetry of the profile becomes more pronounced and a peak close to GaAs zinc-blende emerges. At the tails of the profile, a broad Gaussian background can be observed.

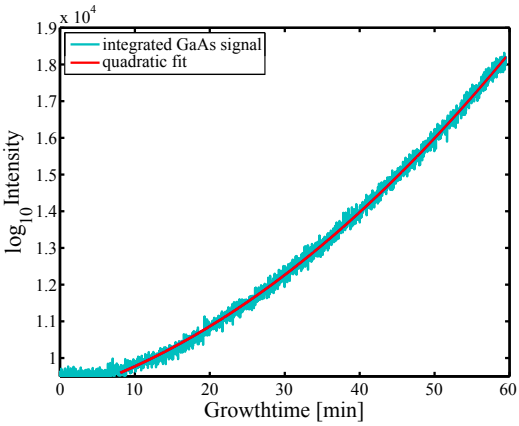

(b) Intensity integrated in a range $1.90\,\text{Å}^{-1} < Q_z < 1.94\,\text{Å}^{-1}$ and a quadratic fit for times larger 10 minutes are depicted. At earlier stages, the scattered intensity is too low and only noise is contributing.

Figure 3.14: Time-evolution of the shape of Q_z intensity profiles during growth, and the integrated scattered intensity. The scattered intensity originates from GaAs nanowires, as well as parasitic GaAs crystallites.

at the nanowire facets takes place which increases the nanowire diameter with growth time. Simultaneous radial growth may e.g. cause an interesting scaling behavior of nanowire length and radius [93, 55].

A detailed signal analysis of the recorded two-dimensional intensity distributions (compare Fig. 3.13(b)) is presented in [93]. Here, we aim on the separation of nanowire and crystallite signal in the measured one-dimensional profiles. Therefore, we extracted the crystallite signal from the two-dimensional intensity distribution in the detector frames. Doing so, more data points are available for the fitting and therefore will increase the robustness of the fit-parameters as compared to a fit of the tails in the one-dimensional Q_z-profiles. In the two-dimensional frames, the tails of the signal in Q_y- and Q_z-direction were fitted by a two-dimensional Gaussian distribution. Fig. 3.15(b) shows the result of this approach. The Q_z-profiles normalized to equal maximum intensity before the background subtraction are depicted in Fig. 3.15(a). After correction for the broad crystallite background the essential features of the profile remain and become even more pronounced. For comparison, the ratio between zinc-blende peak and wurtzite plateau after 58 minutes of growth is now approx. 2.2 instead of 1.6 before correction of the background. In addition, the corrected profile is much sharper in Q_z-direction, resulting from the subtraction of the broad crystallite signal which was the major contribution to the tails of the profiles. Regarding the time-evolution, besides the increasing asymmetry between wurtzite and zinc-blende, the width in Q_z-direction decreases with increasing growth time. At the same time we observe a monotonic drift of the center of mass of the scattered intensity towards the

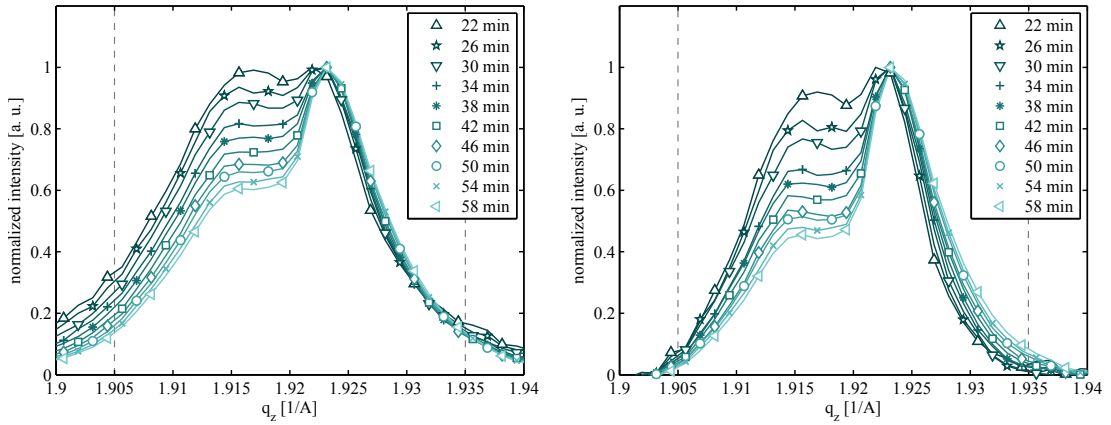

(a) Normalized Q_z-profiles before correction of the crystallite background.

(b) Normalized Q_z-profiles after correction of the crystallite background employing a Gaussian.

Figure 3.15: The contribution of the GaAs crystallites to the scattering signal. After subtraction of a 2-dimensional Gaussian distribution fitted to the tails of the GaAs signal at the detector frames, the asymmetry of the intensity distribution in Q_z-direction is more pronounced.

native zinc-blende position. This drift already implies a change in the properties of the crystal structure of the growing nanowires (e.g. wurtzite fraction and phase purity) with increasing height, although the external growth parameters have been kept constant during the growth.

In a first attempt to investigate the Q_z-splitting of the signals of wurtzite and zinc-blende, we fit two Gaussian functions to the profile taken after 58 min of growth in Fig. 3.15(b), and obtain $Q_z^{zb} = 1.924\,\text{Å}^{-1} \pm 0.000\,\text{Å}^{-1}$ for the signal close to GaAs $(111)_c$, and $Q_z^{wz} = 1.915\,\text{Å}^{-1} \pm 0.001\,\text{Å}^{-1}$ near to the GaAs $(00.2)_{h,wz}$ reflection. In analogy to previous investigations presented in Sec. 3.1, we evaluate the ratio of the vertical spacing between wurtzite and zinc-blende layers for this profile. As result, we obtain $[(d_{wz} - d_{zb})/d_{zb}]_{20} = 0.47\% \pm 0.05\%$ which is lower than $[(d_{wz} - d_{zb})/d_{zb}]_{20} = 0.63\% \pm 0.04\%$ reported in 3.1 indicating a lower phase purity of wurtzite segments in the current nanowires. However, in order to gain deeper insight into the evolution of polytypism a more sophisticated modeling, beyond simple signal analysis using Gaussians, is required.

3.3.2 Interpretation of time-resolved scattering data in the frame of a Markov model for the stacking sequences

In the following, we will interpret the time-resolved *in-situ* data in the framework of the Markov model. We will therefore introduce time-dependent transition probabilities, in order to account for the dynamics in the Q_z-profiles. From the simulated profiles best describing the experimental data, we will extract the evolution of wurtzite fraction and the phase purity with increasing height of the nanowires. In a next step, we connect the so obtained transition probabilities to

the difference of the nucleation barriers for growing either a layer wurtzite on zincblende or vice versa.

Let us first assume, no time-resolved data was available, but only *ex-situ* X-ray data after the growth of a nanowire sample - corresponding to one of the profiles in Fig. 3.15(b). Each of these single profiles could be well described by a simulation based on a suitable set of static transition probabilities as shown in Fig. 3.4(a) and Fig.3.4(b). Moreover, additional ambiguities might arise e.g. various distributions of the segment lengths - different from an exponential one - might be consistent with the case of static transition probabilities [93, 112]. Finally, the so obtained X-ray data averages over the whole volume of the nanowire and therefore is incapable of resolving gradients in the polytypic properties of the nanowires along their growth axis, given the large fluctuations of the segment lengths in each wire (compare Fig. 1.6(b) and [93, 112]). Consequently, each experimental profile could be fitted by a different set of static transition probabilities used to generate the stacking of the whole wire [113, 93, 112]. However, since phase transformations during growth are unlikely, the differences in the Q_z-profiles in Fig. 3.14(a) arise during the growth of the same ensemble of nanowires, in our case during 4 minutes of growth. Therefore, the newly growing part of the wires cause the difference in the profiles of successive time-steps. Consequently, static transition probabilities are *incompatible* with the observed time-resolved X-ray data. We attribute the change in the profiles to a gradient in the structural properties of the nanowires with increasing height. Thus we consider time-dependent (or layer-dependent) transition probabilities in the following.

As a first approximation, we assume a linear gradient for the transition probabilities since no abrupt changes in the temporal evolution of the profile shape is visible

$$p_{zb\to wz}(n) \;=\; u_{zb\to wz} + v_{zb\to wz}\cdot n \tag{3.7}$$

for switching from zinc-blende stacking to wurtzite, and

$$p_{wz\to zb}(n) \;=\; u_{wz\to zb} + v_{wz\to zb}\cdot n \tag{3.8}$$

vice versa, depending on the current layer n. In order to extract the parameters u and v, we employ $d_{wz}/d_{zb} = 1.007\%$ [92], and assume a linear increase of the nanowire height with growth time, and an experimental resolution in reciprocal space of $\delta q_z \approx 0.003\,\text{Å}^{-1}$. We then generated $N_1 = 3000$ sets of random parameters. The gradient v was varied in the range $-2.5\cdot10^{-6} \le v_{wz\to zb} \le 2.5\cdot10^{-6}$ and $-5.0\cdot10^{-6} \le v_{zb\to wz} \le 2.5\cdot10^{-6}$, and $u_{wz\to zb}$ and $u_{zb\to wz}$ was varied in the range from 0.25% to 5.00%. From the best 60 fits for the experimental data shown in Fig. 3.15(b), another reduced parameter space with $N_2 = 3000$ sets of parameters was defined with the limits corresponding to the 10% and 90% quantiles of the respective parameters: $-1.8\cdot10^{-6} \le v_{wz\to zb} \le 2.0\cdot10^{-6}$; $-3.8\cdot10^{-6} \le v_{zb\to wz} \le 1.2\cdot10^{-6}$, and $0.0093\% \le u_{wz\to zb} \le$

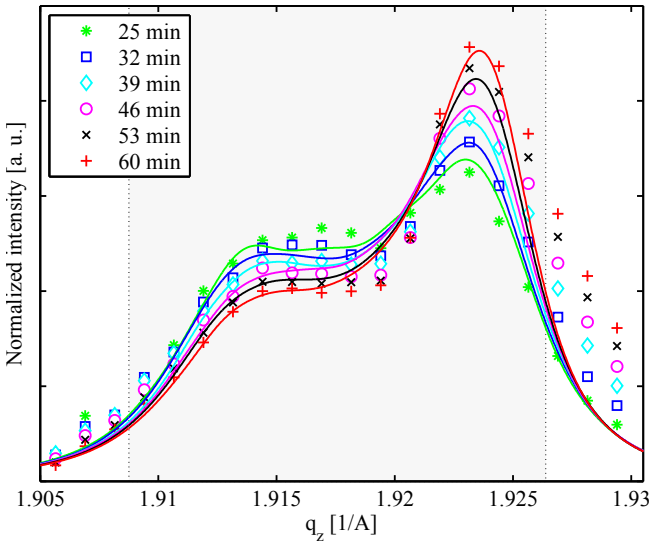

Figure 3.16: Experimental Q_z-profiles and best fit (solid lines) obtained by the Markov model assuming layer-dependent transition probabilities. The depicted growth times correspond to the following mean nanowire heights expressed in total number of layers: $N_{25} = 2792$, $N_{32} = 3573$, $N_{39} = 4355$, $N_{46} = 5137$, $N_{53} = 5918$ and $N_{60} = 6700$. The simulated profiles contain the contributions of 2500 nanowires, and have been smoothed by the resolution element using a Gaussian distribution with FWHM approx. $0.003\,\text{Å}^{-1}$.

2.1% and $0.0074\% \leq u_{zb\to wz} \leq 2.4\%$. Thus in total 6000 sets of random parameters were generated and served as a data basis for the fit of the experimental data. The simulated X-ray profiles based on the best fit in this framework are depicted in Fig. 3.16. In order to increase the signal to noise ratio and to reduce computational time, we reduced the time-resolution to steps of 7 minutes. For comparison with the experimental data, we restricted to the gray area shown, since the tails of the profiles might be strongly influenced by the correction of the crystallite contribution [93]. As a matter of fact, the experimental profiles are not well described by the model in the area $Q_z \geq 1.927\,\text{Å}^{-1}$ outside the region used for the fit. We attribute this discrepancy to e.g. thermal effects and the pre-processing (imperfect subtraction of CTR, or crystallite signal), since such a signal is not present neither in the nano-focus measurements nor at the ensemble measurements, both performed at room temperature. Besides the region $Q_z \geq 1.927\,\text{Å}^{-1}$, the fit describes the experimental profiles at all growth times very well.

The extracted transition probabilities according to Eqs. 3.7 and 3.8 as function of the layer n and the growth time are depicted in Fig. 3.17(a). The best fit is shown as solid lines, $p_{zb\to wz}$ marked by squares and $p_{wz\to zb}$ indicated by circles. The bold broken and dotted lines indicate the respective mean obtained from the 60 best fits, enclosed by dashed lines representing the 25% and 75% quantiles thereof as an error estimate. The transition probability $p_{zb\to wz}$ decreases from approx. 1.20% at the beginning of growth to 0.60% at the end, whereas $p_{wz\to zb}$ increases from approx. 1.15% to 1.80% with growth time.

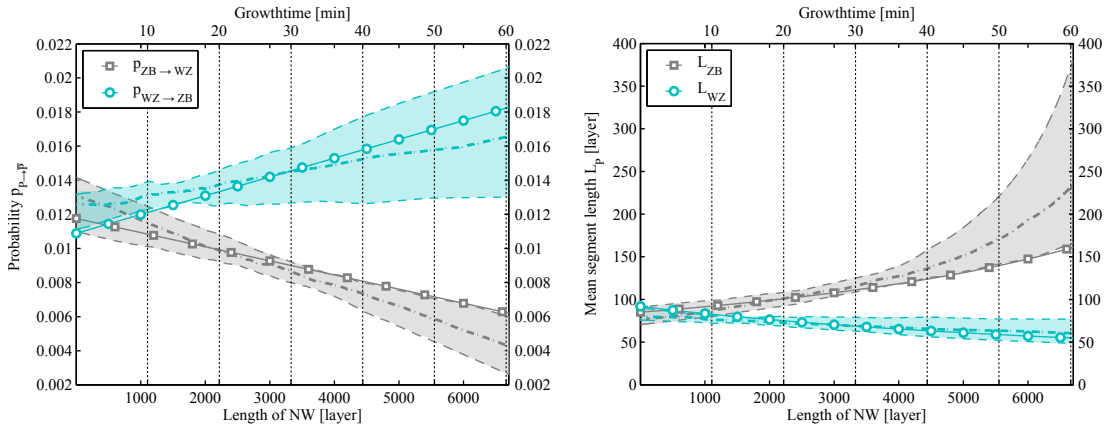

(a) Transition probabilities $p_{zb\to wz}$, and $p_{wz\to zb}$.

(b) Mean segment length of wurtzite and zinc-blende segments.

Figure 3.17: Transition probabilities and mean segment length as function of the actual nanowire height (expressed in layers), as well as the growth time. The values below 25 minutes of growth are obtained by extrapolation. The symbols connected by the solid line represent the best fit. The broken and dotted lines represent the mean value taken from the 60 best fits. As error estimate, the mean value is enclosed by the 25 % and 75 % quantiles given by the dashed lines.

For small gradients $|v_{wz\to zb}| \ll 1$, the average wurtzite segment thickness L_{wz} is still well approximated by $L_{wz} \approx 1/p_{wz\to zb}$ as obtained for static transition probabilities. The same holds for zinc-blende segments respectively. The so obtained mean segment lengths as a function of the layer n and the growth time are depicted in Fig. 3.17(b). Whereas zinc-blende and wurtzite segments are almost equally thick at early times of growth $L_p \approx 80$ layers ≈ 260 Å, the average thickness of zinc-blende segments increases to $L_{zb} \approx 200$ layers ≈ 650 Å after 60 minutes of growth. This is approx. 3.5 times larger than the mean segment length of wurtzite at this time.

It is important to mention, that the values for growth times below 20 minutes are extrapolated and should be treated with care. Due to the weak signal of the GaAs nanowires at these times no evaluation was possible. Moreover, effects due to the choice of the initial probabilities as discussed in Sec. 1.4 may not be negligible at times corresponding to a nanowire heigth larger than 2000 layers in general. However, the X-ray profile at 25 minutes growth time does not exhibit two separated peaks which would indicate small transition probabilities $p_{wz\to zb}, p_{zb\to wz} < 0.01$, therefore we assume $p_{wz\to zb} + p_{zb\to wz} > 0.015$ for the growth of the first 25 minutes (or 2792 layers). Consequently, the influence of the initial transition probabilities is negligible for the fitted growth times depicted in Fig. 3.16 and the transition probabilities for early growth times < 25 minutes cannot be reliably estimated from our experimental data. We also point out, that strain due to the lattice mismatch of 4.1% between GaAs and Si is already relaxed close to the interface [158, 159] and can be neglected for layers less than 2000.

However for layers larger than 2000, the effect of strain between the polytype segments might

be non-negligible. Especially very short segments of e.g. wurtzite in a surrounding of extended zinc-blende segments could be strained to match the surrounding polytype. Therefore we assume in a first *rough* approximation, that the in-plane lattice constant of the wurtzite layers a_{wz} is strained to the value of the surrounding zinc-blende polytype $a_{zb} = a_{wz,strained}$. Further, from [97] we know that $a_{wz} < a_{zb}$ and $a_{wz} = 0.9965 \cdot a_{zb}$, and $c_{wz} \approx 1.007\ c_{zb}$ from [92]. Under elastic deformation, the unit cell strives to preserve its volume

$$\frac{3}{2}\sqrt{3}\ a_{wz}^2\ c_{wz} \approx \frac{3}{2}\sqrt{3}\ a_{wz,strained}^2\ c_{wz,strained} \tag{3.9}$$

$$= \frac{3}{2}\sqrt{3}\ a_{zb}^2\ c_{wz,strained} \tag{3.10}$$

and

$$c_{wz,strained} = \frac{a_{wz}^2}{a_{zb}^2}\ c_{wz} = 0.993 \cdot 1.007\ c_{zb} = c_{zb} \tag{3.11}$$

Consequently this very short wurtzite segments would not be visible in the experiment since the difference in the vertical layer-spacing between zinc-blende and strained wurtzite vanishes. Hence, we would systematically overestimate the mean segment lengths. In the following, we therefore estimate the effect on the resulting mean segment length. We assume a very short wurtzite segment with a length of b layers is completely strained to the surrounding zinc-blende segments with lengths $a \gg b$. The probability of such a segment is given by (compare Sec.1.4)

$$f_{wz}^{short} = \int_0^b dx \left(\frac{1}{\mu_{wz}} e^{-\frac{x}{\mu_{wz}}} \right). \tag{3.12}$$

The length b of the short wurtzite segment is much smaller than the mean segment length of zinc-blende and that of wurtzite. Otherwise we would obtain a different X-ray signal in our case. Therefore, $b \ll \mu_{wz}$ and the probability for such a segment is $f_{wz}^{short} \approx b/\mu_{wz} \ll 1$. The probability, that such a single short segment is strained is $(1 - f_{wz}^{short}) \cdot f_{wz}^{short}$. In this case, the length of the segment sequence "ZB|WZ(short)|ZB" would be misinterpreted as one long segment of zinc-blende with length $2\mu_{zb} + O(b/\mu_{wz})$. With the probability $(1 - f_{wz}^{short}) \cdot (f_{wz}^{short})^2$, two successive short wurtzite segments are strained and overseen. The stacking sequence "ZB|WZ(short)|ZB|WZ(short)|ZB" would then be interpreted as zinc-blende segment with length $3\mu_{zb} + O(b/\mu_{wz})$. As a consequence such stacking sequences appear as one large zinc-blende segment and lead to an effective overestimation of the mean zinc-blende segment length $\mu_{zb}^{eff} > \mu_{zb}$. If we continue the above series to an infinite number n of overseen short wurtzite segments, the effective mean length μ_{zb}^{eff} can be expressed by

$$\mu_{zb}^{eff} = (1 - f_{wz}^{short})\ \mu_{zb}\ [1 + 2\ (f_{wz}^{short})^2 + 3\ (f_{wz}^{short})^3 + ...] \tag{3.13}$$

$$= (1 - f_{wz}^{short})\ \mu_{zb}\ \sum_{n=0}^{\infty}(n+1)(f_{wz}^{short})^n \tag{3.14}$$

$$= (1 - f_{wz}^{short})\ \mu_{zb}\ \left(\frac{1}{(1 - f_{wz}^{short})}\right)^2 \tag{3.15}$$

$$= \frac{\mu_{zb}}{1 - f_{wz}^{short}}. \tag{3.16}$$

We point out, that strain in the nanowires at an atomically sharp interface is limited to very few layers close to the interface in $(111)_c$- direction. For comparison: Larsson et al. [160] investigated an atomically sharp hetero-interface of InAs/InP (lattice mismatch of 3.1%) in InAs nanowires and found a deviation from the native lattice constants only up to approx. 2 nm from the interface (approximately 6 layers).

As example, we assume that segments up to 6 layers are completely strained to the surrounding polytype. With a mean segment length of e.g. $\mu_{wz} = 80$ layers, we obtain

$$f_{wz}^{short} \approx \frac{6}{80} = 0.075 \tag{3.17}$$

and

$$\frac{\mu_{zb}^{eff}}{\mu_{zb}} = 1.081. \tag{3.18}$$

Consequently, we would overestimate μ_{zb} only by approximately 8%. If we consider even smaller segments, the error reduces down to approximately 1% for short segments of 1 layer mean length. Therefore, and as long as the Markov model is valid for the generation of the stacking, short strained wurtzite segments (or stacking faults) do not lead to a dramatic overestimation of the mean segment length of zinc-blende for significantly pure wires.

Given that (i) our mean segment sizes (50-400 layers) are significantly larger than these 2 nm or respectively 6 layers and (ii) the in-plane strain at the interface of the polytypes in GaAs nanowires is approximately one order of magnitude smaller (0.3 according to Biermanns et al.[161]) and thus smaller than the lattice contrast in $[111]_c$ growth direction, we neglect the influence of strain for evaluation of our experiment.

Compared to literature, *statistical* data on polytypism in nanowires is only available for NWs with low phase purity - typically with mean phase segments smaller than 10 layers [44, 106, 2, 162], however, the distribution of the segment lengths has been found to follow an exponential distribution. This is also a property of the Markov model employed in our simulations. In case of higher phase purity, segment lengths similar to our mean segment lengths are reported in literature: e.g. zinc-blende segments up to 600 Å (184 layers) and wurtzite segments up to 400 Å (123 layers) have been reported by Biermanns et al. [159] for self-catalyzed GaAs nanowires,

Soshnikov et al. [163] obtained zinc-blende and wurtzite segments around 1000 Å (306 layers) for gold-catalyzed GaAs nanowires, and Spirkoska et al. [164] found nanowires with zinc-blende segments of up to 500 Å (153 layers) length and wurtzite segments up to 100 Å (31 layers). However, the values in all these references are obtained from one or few wires only and are consequently of limited statistical significance only.

3.3.3 Implications on the growth dynamics

Here, we will conclude on the differences in the nucleation barriers for switching the current polytype as implied by the time-dependent transition probabilities. We therefore relate the transition-probabilities to the nucleation barriers by a Boltzmann approach.

We now assume, that the nucleation process is close to the thermodynamic equilibrium. We also regard the transition probabilities to $p_{p\to p}$ and $p_{\bar{p}\to p}$, either to remain in the current polytype p or to switch to the other polytype $\bar{p}$.

Then the transition probabilities are linked to the nucleation barriers by [107, 106, 81, 57, 63]

$$p_{p\to p}(n) = \frac{c_{p\to p}(n)\ e^{-\beta E_{p\to p}(n)}}{c_{p\to p}(n)\ e^{-\beta E_{p\to p}(n)} + c_{p\to\bar{p}}(n)\ e^{-\beta E_{p\to\bar{p}}(n)}} \tag{3.19}$$

with $\beta = 1/(k_B\ T)$, where β is the Boltzmann constant and T is the absolute temperature of the system. The pre-factors $c_{p\to p}$ and $c_{p\to\bar{p}}$ account for the total number of possible nucleation sites for nuclei with energy barriers $E_{p\to p}$ and $E_{p\to\bar{p}}$. The differences in the nucleation barriers for switching from one polytype p to the other polytype $\bar{p}$ at layer n are then given by

$$\begin{aligned}
\delta E_{p\to\bar{p}}(n) &= E_{p\to\bar{p}}(n) - E_{p\to p}(n) && (3.20)\\
&= k_B T \cdot \left[ln\left(\frac{p_{p\to p}(n)}{p_{p\to\bar{p}}(n)}\right) + ln\left(\frac{c_{p\to\bar{p}}(n)}{c_{p\to p}(n)}\right)\right] && (3.21)\\
&= k_B T \cdot \left[ln\left(\frac{1-p_{p\to\bar{p}}(n)}{p_{p\to\bar{p}}(n)}\right) + ln\left(\frac{c_{p\to\bar{p}}(n)}{c_{p\to p}(n)}\right)\right]. && (3.22)
\end{aligned}$$

For the following evaluation, we assume $c_{p\to p}(n) \approx c_{p\to\bar{p}}(n)$ and are therefore neglected in a first approximation. The determination of $c_{p\to p}(n)$ and $c_{p\to\bar{p}}(n)$ requires a detailed modeling of the nucleation process, involving the growth temperature, the supersaturation of the liquid Ga-droplet, and the difference in the chemical potential of a III/V-pair between liquid and solid phase [57]. Most importantly, the transition probabilities, extracted from the X-ray data are *independent* of a particular geometric model of the nucleus, and do not rely on the nucleation mechanism or the dynamics of the Ga-droplet [147, 107, 151, 8, 59, 165, 166, 81, 63] but depend on the validity of the Markov model for the generation of the stacking sequences.

The nanowires were grown at $T = 590\,°\mathrm{C}$, therefore, $k_B T = 74.4\,\mathrm{meV}$. If we employ these values and the transition probabilties depicted in Fig. 3.17(a) to Eq. 3.22, we obtain the energy

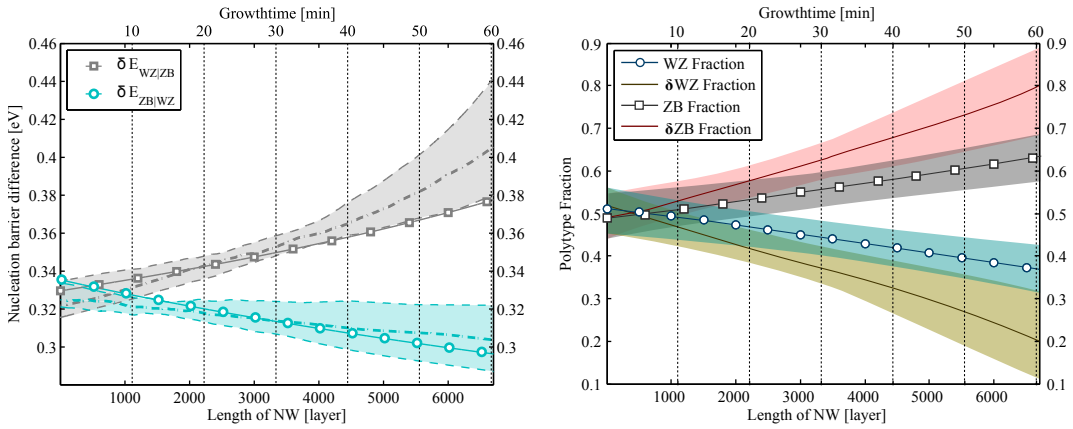

(a) Best fit for the difference in the energy barriers for nucleating a layer of wurtzite on a zinc-blende segment $\delta E_{WZ|ZB}$ (squares) and for nucleation of a zinc-blende layer on a wurtzite segment $\delta E_{ZB|WZ}$ (circles). The broken dotted line represents the mean value obtained from the best 60 fits, the dashed lines represent the 25 % and 75 % quantiles as an error-estimate.

(b) Time evolution of the polytype fractions. Squares indicate the zinc-blende fraction, and the circles depict the fraction of wurtzite. The differential polytype fraction δZB and δWZ respectively are given as solid lines. For further details we refer the reader to the appendix of [93].

Figure 3.18: The differences in the energy barriers and the polytype fractions as function of the actual nanowire height (expressed in layers), as well as the growth time.

barrier differences depicted in Fig. 3.18(a). The result obtained by the values of the best fit are indicated by markers. The mean values are given by the bold dotted and dashed lines, as well as the corresponding error estimates. Exemplary, we obtain $\delta E_{zb\to wz}(6700) = 380\,\text{meV}$ for $p_{zb\to wz} = 0.60\%$ and $\delta E_{wz\to zb}(6700) = 298\,\text{meV}$ for $p_{wz\to zb} = 1.80\%$ respectively.

Compared to literature, only Johansson et al. [44] provide a rough estimate of $\delta E_{zb\to wz} = 920\,\text{meV}$ for the difference of the nucleation barriers between regular plane and twin plane formation for gold-assisted GaP NW with very short ZB segments. Compared to our results for $\delta E_{zb\to wz} = 350\,\text{meV} - 400\,\text{meV}$ for self-catalyzed GaAs NWs, their value is larger than our result.

We remind the reader that we have assumed that there are no phase transformations taking place during growth. Additionally, we have assumed that the nanowires to have no tapering and a linear axial growth speed. The latter two requirements have been validated by our *ex-situ* SEM studies in Chapter 2. The first assumption is valid, as long as the gradient in the transition probabilities is sufficiently small. The transition probabilities for a given growth time t_g in Fig. 3.17(a) do not directly relate to the total wurtzite fraction $\tilde{p}_{wz}(t_g)$ of the ensemble of nanowires at time t_g but to the differential fraction of wurtzite $\delta\tilde{p}_{wz}$ which corresponds to the amount of wurtzite in the acually growing segments between the growth times t_g and $t_g + \delta t_g$.

With the above assumptions we extract the wurtzite fraction from our results obtained by the Markov model, following the preparations in the appendix of [93]. We can express the total wurtzite fraction at the time $t_g + \delta t_g$ as

$$\tilde{p}_{wz}(t_g + \delta t_g) = \left(\frac{t_g}{t_g + \delta t_g}\right) \tilde{p}_{wz}(t_g) + \left(\frac{\delta t_g}{t_g + \delta t_g}\right) \delta\tilde{p}_{wz}(t_g, \delta t_g). \tag{3.23}$$

Our results depicted in Fig. 3.18(b) indicate, that with increasing growth time, the total fraction of wurtzite decreases. Whereas the total fractions of zinc-blende and wurtzite are almost equal at the beginning of growth, we obtain $\tilde{p}_{wz} \approx 37\% \pm 5\%$ at the end. This is a consequence of the drop in the differential fraction of wurtztite. Further, it can be seen, that there is almost pure zinc-blende growing at the end of the growth, resulting in a differential zinc-blende fraction of $\delta\tilde{p}_{zb} \approx 80\% \pm 10\%$. A similar trend was observed by Biermanns et al. [92], where the results were obtained by *ex-situ* X-ray diffraction on a series of nanowire samples grown for different growth times. In contrast to the results presented here, the authors could not conclude on the phase purity of their investigated samples.

With the wurtzite fraction, the mean segment length obtained by the Markov model, we can conclude the following: Our self-catalyzed GaAs nanowires grow rather short segments on zinc-blende and wurtzite at the beginning of growth. At this time, the wurtzite fraction is approximately 50%. As the growth commences, the phase purity of wurtzite decreases, and the wurtzite segments become smaller. At the same time, the phase purity of zinc-blende increases, as well as the zinc-blende fraction. This trend continues until the growth is stopped after 60 minutes. Consequently, the difference in the nucleation barrier for growing a zinc-blende layer on top of a wurtzite layer decreases below the value of the difference in the nucleation barrier for growing a wurtzite layer on top of a zinc-blende one. The latter increases with growth time, effectively increasing the phase purity of zinc-blende segments and making the nucleation of new wurtzite layers less probable.

We attribute this trend to the dynamics of the liquid gallium droplets at the top of the nanowires. As proposed by Krogstrup et al. [81] on the one hand, the shape of the liquid droplet has a strong impact on the growing phase. On the other hand, the supersaturation of the liquid Ga droplet is an important factor as shown by Yamaguchi et al. [162]. Since the supersaturation of the droplet mainly depends on the As-flux - and we do not observe any indications for an increase nor a decrease which would also result in an increased (reduced, and therefore tapering may be likely) axial growth speed - we may rule out a gradual increase of supersaturation as an explanation for our observed trend. However, the relevant changes in the supersaturation may be too small to be detected in post-growth SEM. Another possibility for the increasing phase purity and fraction of zinc-blende could be a change in the shape of the liquid droplet. A reduction of the liquid volume of the Ga droplet may arise due to a reducion of the Ga-flux into the droplet provided by diffusion via the side-walls as the nanowires grow longer [31, 38, 167]. Since we do not observe tapering (which would indicate a reduction of the diameter of the droplet), the reduction of the liquid volume most likely causes a decrease in the wetting angle of the droplet pinned to the edges of the $(111)_c$ top facet. Such a behavior may also favour the nucleation zinc-blende over wurtzite [81].

In conclusion, we investigated the growth of an ensemble of self-catalyzed GaAs nanowires by

X-ray diffration. We obtained time-resolved scattering data in the vicinity of the $(111)_c$ GaAs Bragg reflection. Employing a Markov model for the generation of the stacking sequences in the nanowires, we were able to extract the evolution of key parameters of polytypism such as the phase fraction and phase purity. Under certain assumptions, even the difference in the nucleation barriers could be estimated. These results depend on the proper treatment of the contribution of parasitic GaAs crystallites on the one hand. On the other hand the results base on the validity of the Markov model for the generation of the stacking sequences, which is however founded on a well-established basis [44, 162, 168] and describes our X-ray data well. Nevertheless, deviations from the Markov model exhibiting a similar scale of fluctuations as compared to their mean value of the segment length may not be visible in the $(111)_c$-profiles but lead to systematic errors if evaluated by the Markov-approach [93, 112]. Consequently, additional theoretical modeling e.g. including the ANNNI model [111] as well as additional experimental investigation thereof need to be performed in future.

3.4 Distinguishing the contribution of parasitic growth and epitaxial nanowires by asymmetric *ex-situ* X-ray diffraction

In this section, we will discuss how the contribution of parasitic GaAs crystallites to the scattering intensity distribution around phase selective Bragg reflections can be distinguished from the contribution of vertical GaAs nanowires. Accounting for the contribution of parasitic growth in X-ray diffraction experiments of an ensemble of nanowires is of great importance. If neglected, the contribution of the parasitic crystallites which are of cubic zinc-blende (or twinned zinc-blende) GaAs will strongly affect the obtained results. As a consequence the obtained value for the fraction of wurtzite will not correspond to the wurtzite inside the nanowires but rather in all grown GaAs structures, including the parasitic islands.

In Sec. 3.2, we have demonstrated by nanofocus X-ray measurements, that epitaxial alignment with respect to the [111]-direction of the zinc-blende crystallites differs from the alignment of the nanowires. The crystallites were found to have a way broader directional distribution around the [111]-surface normal (see Fig. 3.7(b)) as compared to the nanowires. Measurements in asymmetric scattering geometry support these findings: In Fig. 3.19 a reciprocal space map displays the scattered intensity from an ensemble of self-catalyzed GaAs nanowires (for SEM compare Fig. 2.2) along the lowest order asymmetric truncation rod in the vicinity of the cubic GaAs Bragg reflections $(220)_{\mathrm{c}}$ and $(311)_{\mathrm{c}}$, the hexagonal $(10.3)_{\mathrm{h,wz}}$ reflection, and the $(311)_{\mathrm{c}}$ Silicon reflection. We observe two oblique and pronounced streaks passing through the $(220)_{\mathrm{c}}$ and $(311)_{\mathrm{c}}$ reflections of GaAs at $Q_z = 2.56\,\text{Å}^{-1}$ and $Q_z = 3.21\,\text{Å}^{-1}$. These streaks are slightly curved and are in fact arcs of a Debye-Scherrer ring with center at the reciprocal origin. Important to note is, that this arc is missing or at least not detectable for the $(10.3)_{\mathrm{h,wz}}$ reflection of GaAs wurtzite at $Q_z = 2.87\,\text{Å}^{-1}$. Moreover, we observe that the intensity of the arc is centered around the respective Bragg reflection and decays with increasing distance. Therefore, the crystallites may obtain a certain directional orientation along the [111]-direction (comparable to texturing) instead of being completely randomly oriented. In addition, a diffuse streak due to stacking-faults in the nanowires along Q_z connecting the GaAs reflections is visible. Also, a facet streak perpendicular to Q_z can be observed at the $(220)_{\mathrm{c}}$ reflection. From SEM we infer the mean diameter of the nanowires $d_{NW} = 54\,\text{nm} \pm 4\,\text{nm}$ and the mean lateral size of the crystallites $d_{Cr} \approx 500\,\text{nm} \pm 100\,\text{nm}$.

In the following, we evaluate the distribution of the scattered intensity along the Debye-Scherrer arcs of $(220)_{\mathrm{c}}$ and $(311)_{\mathrm{c}}$ GaAs Bragg reflections and compare their widths with the width of the $(10.3)_{\mathrm{h,wz}}$ wurtzite GaAs reflection. The full-width-at-half-maximum (FWHM) of a Bragg reflection may be employed as approximate measure for the size of the scattering nanocrystal (or the coherently illuminated volume thereof) [169, 110]. Therefore, the widths along Q_y of all three GaAs reflections should be comparable, if the reflections originate from the same

objects (either nanowires or crystallites, i.e. structures with comparable diameter, or lateral size and epitaxial alignment). Additional broadening may arise due to strain inside the nano-crystals or may be caused by a misorientation of the crystals with respect to the $[111]_c$-direction.

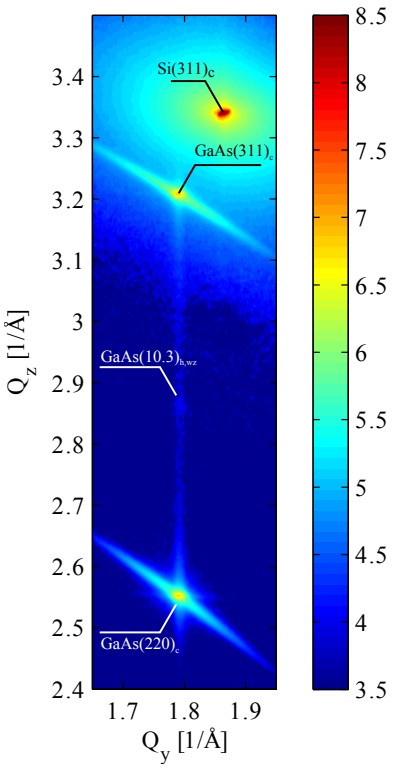

Figure 3.19: Reciprocal space map of the asymmetric Bragg reflections of GaAs twinned zinc-blende $(220)_c$, zinc-blende $(311)_c$, and wurtzite $(10.3)_{h,wz}$. Debye-Scherrer arcs pass through the zinc-blende and twinned zinc-blende reflections. A weak facet streak, perpendicular to Q_z is visible at the $(220)_c$ reflection. In the upper right, the Si $(311)_c$ substrate reflection is located.

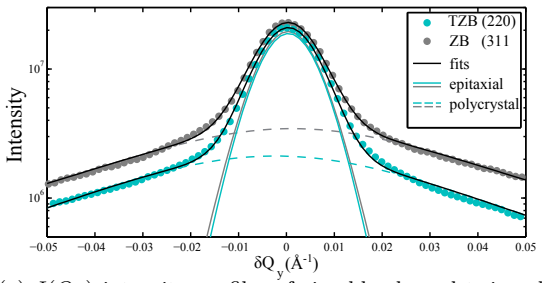

(a) $I(Q_y)$ intensity profiles of zinc-blende and twinned zinc-blende Bragg reflections. Experimental data is given as filled circles. Pearson VII functions were fitted to the experimental profiles.

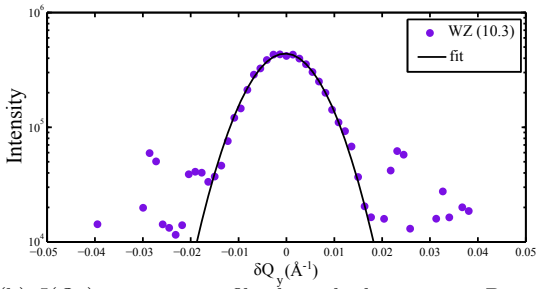

(b) $I(Q_y)$ intensity profile through the wurtzite Bragg reflection with Pearson VII fit function.

Figure 3.20: a) Intensity profiles of the GaAs Bragg reflections $(220)_c$ and $(311)_c$. The profiles are composed of a narrow and a broad signal. The narrow signal is attributed to nanowires with epitaxial alignment whereas the broad signal originates from tilted polycrystalline (twinned) zinc-blende structures. b) Intensity profile of the wurtzite GaAs Bragg reflection $(10.3)_{h,wz}$. Here the background is caused by noise. The FWHM of the central peak in Q_y-direction is comparable to the one of the epitaxial (twinned) zinc-blende structures.

After correction for structure factor and background, we perform line fits of the intensity profiles using two Pearson VII functions of the form

$$I(q_y) = \sum_{i=1}^{2} \frac{2a_i\sqrt{2^{1/m_i}-1}}{\beta(m_i - 0.0, 0.5) \cdot \left(1 + 4(\frac{q_y - b_i}{s_i})^2 \cdot (2^{1/m_i} - 1)\right)^{m_i}}. \tag{3.24}$$

The Pearson VII function is a comfortable choice since, depending on m, it becomes a Lorentzian (for $m \to 1$), and approaches a Gaussian (for $m \to \infty$). The fits are constituted of two contributions, a broad and a narrow signal (depicted as broken and solid colored lines in fig 3.20(a)). We obtain widths $s_{220}^{epi} = 0.0141\,\text{Å}^{-1} \pm 0.0001\,\text{Å}^{-1}$ and $s_{311}^{epi} = 0.0143\,\text{Å}^{-1} \pm 0.0001\,\text{Å}^{-1}$ for the narrow signals and $s_{220}^{cryst} = 0.0840\,\text{Å}^{-1} \pm 0.0053\,\text{Å}^{-1}$ and $s_{311}^{cryst} = 0.0856\,\text{Å}^{-1} \pm 0.0047\,\text{Å}^{-1}$ for the broad part. For the intensity profile of the [10.3] wurtzite reflection, a single Pearson VII is sufficient and the fit yields $s_{103}^{epi} = 0.0138\,\text{Å}^{-1} \pm 0.0021\,\text{Å}^{-1}$. Therefore, the FWHM of the narrow signals are compatible for the reflections of cubic and hexagonal GaAs, implying that the same type of structures contribute to their scattering signal. If we estimate the average lateral size of the scattering wurtzite and zinc-blende segments by $\bar{d}_i \approx 2 \cdot 2.78/s_i$ (which relates the FWHM to the correlation length via the sinc^2 function), we obtain $\bar{d}_{220}^{epi} = 39.4\,\text{nm} \pm 0.3\,\text{nm}$, $\bar{d}_{311}^{epi} = 38.9\,\text{nm} \pm 0.3\,\text{nm}$ and $\bar{d}_{103}^{epi} = 40.3\,\text{nm} \pm 3.9\,\text{nm}$ which is in the range of the facet distance of the nanowires estimated by SEM: $d_{NW,facet} = \frac{\sqrt{3}}{2} d_{NW} = 46.7\,\text{nm} \pm 3.4\,\text{nm}$. For the broad crystallite signals we obtain $\bar{d}_{cryst} < 10\,\text{nm}$. Whereas the results for the width of the narrow part correspond well to the observed nanowire diameter (more precisely its facet distance) no corresponding signal-width was found in case of the parasitic crystallites. Rather, the poly-crystallites seem to be more randomly oriented and therefore scatter along the Debye-Scherrer arc passing through the cubic Bragg reflections. Therefore, by the presented procedure, the contribution of parasitic crystallites to the scattering signal of asymmetric Bragg reflections can be estimated, assuming that parasitic growth contributes to scattering located at a Debye-Scherrer arc and the nanowires are epitaxially oriented and free of strain. Based on these assumptions, successive correction of the integrated intensities therefore allows a reliable quantitative determination of the phase fraction in the nanowires. This will be of importance for the discussion presented in the following section.

3.5 Comparison of phase fractions of polytypic nanowires determined by symmetric and asymmetric X-ray diffraction

In Sec. 3.3 we inferred information on polytypism in growing GaAs nanowires by time-resolved symmetric X-ray diffraction. We therefore had to simulate the X-ray diffraction intensity profiles of the $(111)_c$-GaAs Bragg reflection along Q_z based on stacking sequences generated with a Markov model which was then compared to the experimental intensity profiles.

In the following, we will take advantage of a methodical benefit arising from measurements of asymmetric phase selective reflections (e.g. $(220)_c$, $(311)_c$ and $(10.3)_{h,wz}$), in addition to the intensity profiles of the GaAs $(111)_c$ reflection. From the phase selective reflections, we can straightforwardly determine the integral intensity of the scattering signals originating from zinc-blende, twinned zinc-blende and wurtzite segments in the nanowires. This can be accomplished without any deeper modeling, since the contribution of parasitic growth can be distinguished as e.g. proposed in Sec. 3.4, and the phase selective Bragg reflections are well separated in reciprocal space. We thereby gain a way to independently cross-check the results obtained by the Markov model for the measurements in symmetric XRD.

Samples Three different droplet engineered GaAs nanowire samples grown on Si(111) serve as a basis for this comparison (for details on the growth procedure refer to the PhD thesis of J. Jakob, KIT). The samples A and B have been grown at $T_S = 600\,°C$ using a nominal V/III ratio of approx. 3 and a 2D GaAs growth rate of $R_{GaAs} = 45\,nm/h$, the only difference is their growth time which is for $t_g = 0.5\,h$ for sample A resulting in a mean length $l_A = 377\,nm \pm 30\,nm$ and mean diameter $d_A = 51\,nm \pm 6\,nm$. On sample B nanowires with $l_B = 4000\,nm \pm 100\,nm$ and $d_B = 100\,nm \pm 40\,nm$ have grown for $t_g = 4.5\,h$. Sample C was grown at $T_S = 590\,°C$ for 1 hour using a nominal V/III ratio of approx. 5. Sample C features nanowires with mean length $l_C = 2000\,nm \pm 100\,nm$ and diameter $d_C = 40\,nm \pm 5\,nm$ (This sample has been introduced in Sec. 3.1).

Experiment For these samples we recorded 3D reciprocal space maps of the symmetric $(111)_c$, and the three phase selective reflections $(220)_c$, $(311)_c$ and $(10.3)_{h,wz}$. After transformation into reciprocal space, the three dimensional intensity distribution was projected on the $Q_y - Q_z$ plane. The reciprocal space maps of the symmetric reflections were integrated along Q_y in order to obtain profiles $I(Q_z)$. From these profiles the background of the Si $(111)_c$ reflection was subtracted. From the background corrected profiles, a broad Gaussian was subtracted, accounting for scattering from the crystallites. The resulting profiles were fitted by simulated profiles, obtained from an ensemble of 3000 nanowires with 4000 layers each, created by the Markov model applying static transition probabilities transition probabilities $p_{zb\to wz}$ and $p_{wz\to zb}$.

The Bragg reflections located at the asymmetric truncation rod differ in their scattering strength (as calculated by Eq. 1.9). Therefore, the reciprocal space maps of the asymmetric

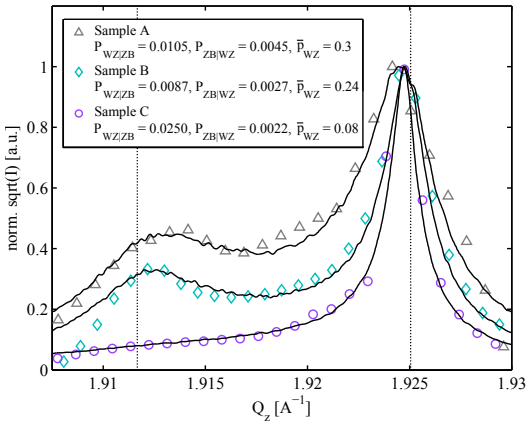

(a) $I(q_z)$ profiles of the symmetric $(111)_c$ Bragg reflection of GaAs and calculated profiles obtained by the Markov model (solid lines). The vertical dotted lines depict the reference Q_z-values for wurtzite and zinc-blende GaAs.

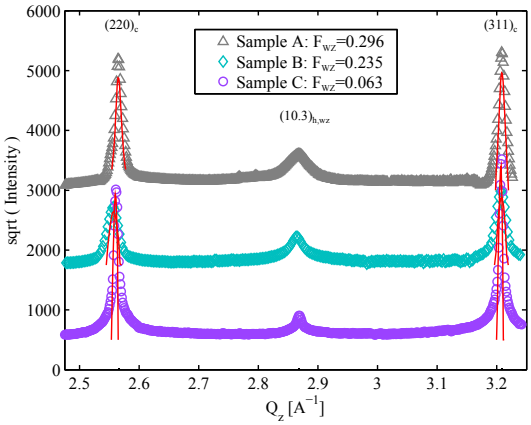

(b) $I(q_z)$ profiles along the asymmetric truncation rod containing the $(220)_c$,$(10.3)_{h,wz}$ and $(311)_c$ GaAs Bragg reflections.

Figure 3.21: A comparison of $\bar{p}_{WZ}$ obtained by the Markov model and the integrated intensity of phase selective Bragg reflections along an asymmetric truncation rod.

reflections were structure-factor corrected and then integrated along Q_y. Successively, the background of the Si $(311)_c$ reflection was subtracted, as well as the contribution of the crystallites estimated from scattering along the Debye-Scherrer arc. From the resulting $I(Q_z)$ profiles the integrated intensity of the phase selective reflections was determined and used for the calculation of the phase fraction.

Results & Discussion In Fig. 3.21(a) the intensity profiles of the GaAs $(111)_c$ reflection are depicted, together with the corresponding fits from the Markov model. The respective parameters are given in the figure. The intensity profiles of the asymmetric truncation rods of the samples are given in Fig. 3.21(b). The red solid curves are obtained after correction for the parasitic crystallites. The area below these curves are used to calculate the integrated intensity of the cubic reflections.

In a model free way, $\bar{p}_{WZ}$ can be extracted from the integrated intensities I_p of the phase selective reflections located at the asymmetric truncation rod

$$\bar{p}_{WZ} = \frac{I_{WZ}}{I_{TZB} + I_{ZB} + I_{WZ}}. \tag{3.25}$$

The wurtzite fraction $\bar{p}_{WZ}$ obtained by the Markov model is calculated via Eq. 1.24. Comparing both, the determined values for $\bar{p}_{WZ}$ from the Markov model are close to the values obtained from the asymmetric truncation rod measurement (see Fig. 3.21). In contrast to the time-resolved X-ray investigations presented in Sec. 3.3, it is not possible from these *ex-situ* measurements to obtain the distribution of mean segment lengths along the nanowire growth axis. However, from the static transition probabilities $p_{\bar{P}\to P}$ and $p_{P\to\bar{P}}$, the mean segment lengths

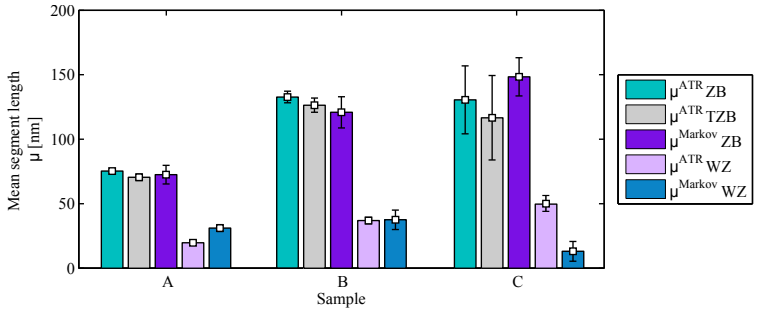

Figure 3.22: Comparison of mean segment lengths μ^p obtained by the Markov model and by the FWHM in Q_z-direction obtained from the phase selective GaAs reflections $(220)_{\mathrm{c}}$,$(10.3)_{\mathrm{h,wz}}$ and $(311)_{\mathrm{c}}$.

$\mu_{\bar{P},P}$ obtained from the Markov model, and from the width in δQ_z of the crystallite-corrected phase selective GaAs Bragg reflections, can be estimated and quantitatively compared.

We employ $\mu_P^{Markov} = 1/p_{P\to\bar{P}}$ for evaluating the results from the Markov model and we use the Scherrer equation [169, 170] with $k = 0.9$ for the estimation of the mean segment length from δQ_z. The resulting mean lengths of polytype segments are depicted in Fig. 3.22. A reasonable agreement between the values inferred by the Markov model and the signal analysis of the phase selective Bragg reflections $(220)_{\mathrm{c}}$,$(103)_{\mathrm{h,wz}}$ and $(311)_{\mathrm{c}}$ is obtained. Whereas the agreement is good, as either polytype fraction and segment length is large (Sample A and B), the results for the wurtzite segment length in case of Sample B differ considerably. We account this to the influence of corrections for crystallite contribution and substrate background which may have a strong influence, especially if the wurtzite-fraction is small as given in Sample C. Therefore, we argue that the Markov model may deliver reliable results on phase purity and polytype fraction only within a limited range of $\bar{p}_{WZ}$. We can estimate a lower bound for this limit with $\bar{p}_{WZ} > 8\%$ in our case.

Therefore, we found that information on polytypism in GaAs nanowires extracted by the Markov model is consistent to model free information extracted from phase selective GaAs Bragg reflections - at least for the ranges of mean segment lengths and wurtzite fractions of the investigated samples. Whereas each measurement geometry alone has its drawbacks e.g. complicated separation of the crystallite signal in the $(111)_{\mathrm{c}}$ reflection or more time-intensive measurements of the asymmetric-truncation rod, we propose that the benefits arising from a combination of the two geometries even out their drawbacks by far and allow for a robust microstructure characterization:

In a combined measurement, as presented for *ex-situ* XRD in this section one would first extract $\bar{p}_{WZ}$ model-free from the asymmetric truncation rod since the separation of crystallite contribution to the integrated intensities of twinned zinc-blende and zinc-blende reflections is easy. In a second step, the obtained value for $\bar{p}_{WZ}$ is compared to the set of simulations given in Sec. 4.3 in Ref. [93]. In Fig. 4.2.9 a) in Ref. [93] one set of the parameters standard deviation

and skewness of $I(Q_z)$ around the $(111)_c$ reflection of GaAs (after correction for background and crystallites) defines $p_{ZB\rightarrow WZ}$. These parameters can readily be extracted from the experimental $I(Q_z)$ and compared to the corresponding charts. Finally, with the knowledge of $\bar{p}_{WZ}$, the complementary transition probability $p_{WZ\rightarrow ZB}$ can be calculated by Eq. 1.24. Step two therefore provides a suitable starting point for further refinements of the fit of $I(Q_z)$ by the Markov model. As a result of this fit, estimates of $\mu_{P,\bar{P}}^{Markov}$ are obtained and can be compared to the respective values for δQ_z extracted from the asymmetric truncation rod.

Summarizing, the combination of phase selective asymmetric and symmetric Bragg reflections has strong advantages, given a careful consideration of the contribution of parasitic growth. The results obtained by the Markov model and the phase selective Bragg reflections for the set of samples investigated here are compatible. The presented procedure provides a way to review the limits of the Markov-approach since discrepancies are expected for e.g. an enhanced occurrence of the 4H polytype - which is not covered by the Markov model as presented in Ref. [113]. Further, detailed investigations of the shape of symmetric [111]-intensity profiles simulated by the Markov-model, and proposed expansions thereof are given in Ref. [112]. Therefore, further investigations of nanowires containing a large fraction of 4H are suggested in order to extend the review of the Markov model.

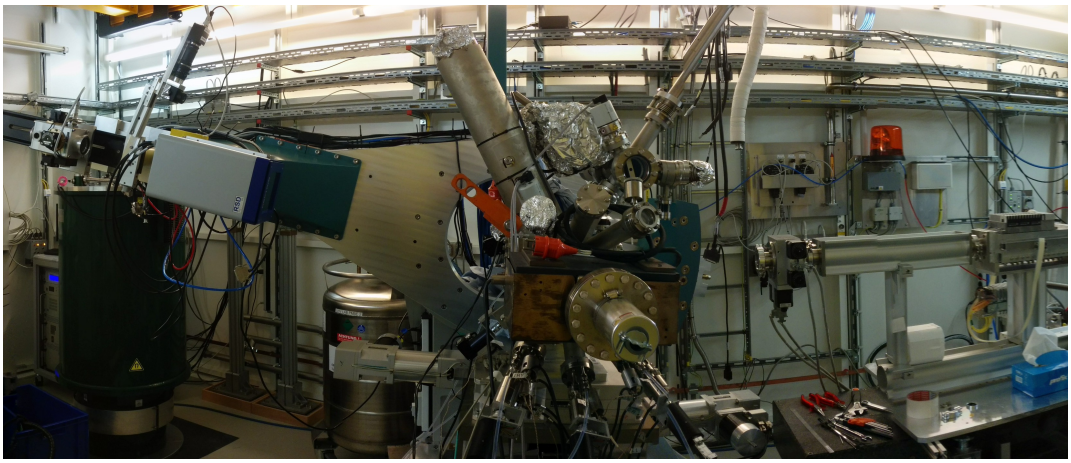

Figure 3.23: Setup of the *in-situ* X-ray experiments during MBE growth of nanowires at the Resonant Scattering and Diffraction beamline P09 at PETRA III. The growth chamber of the pMBE system is seen in the center mounted on the heavy load Psi-diffractometer. The X-rays incoming from the right, scatter at the sample inside the chamber and get detected by the Pilatus 300K on the left, mounted at the diffractometer arm. LN_2 cooling was provided by two 200 litre dewars in the back.

3.6 Evolution of the crystal-structure of self-catalyzed GaAs nanowires during growth monitored by time-resolved X-ray diffraction in asymmetric geometry

Here, we report on time-resolved *in-situ* asymmetric X-ray diffraction during growth of self-catalyzed GaAs nanowires. The monitoring of phase selective Bragg reflections in a time resolved way during growth will allow us to take advantages of the separation of wurtzite and zin-blende signals in reciprocal space. As a consequence, structural information on the evolution of polytypism can be obtained without requiring a statistical model for the stacking sequences.

Experiment The X-ray experiment was performed at the beamline P09 at PETRA III (compare Sec. 3.1). A photograph of the experiment setup can be seen in Fig. 3.23. We used a highly monochromatic X-ray beam with an energy of 15 keV and a size of 145 µmx50 µm. The undulator insertion device provided a photon flux of $\approx 10^{13}$ ph/s. Employing a Pilatus 300K detector, we measured the scattered intensity in the vicinity of the cubic $(311)_c$ reflection of zinc-blende, the wurtzite $(10.3)_{h,wz}$ reflection and the $(220)_c$ reflection of twinned zinc-blende GaAs in a time resolved manner during the growth of droplet-engineered GaAs nanowires. After the growth, at growth temperature, full 3D reciprocal space maps of the symmetric $(111)_c$ reflection and the asymmetric reflections have been measured. After the cooldown process 3D reciprocal space maps were measured in symmetric and asymmetric geometry. This way, we obtain time-resolved information on GaAs zinc-blende and its twin, and the wurtzite polytype during the growth,

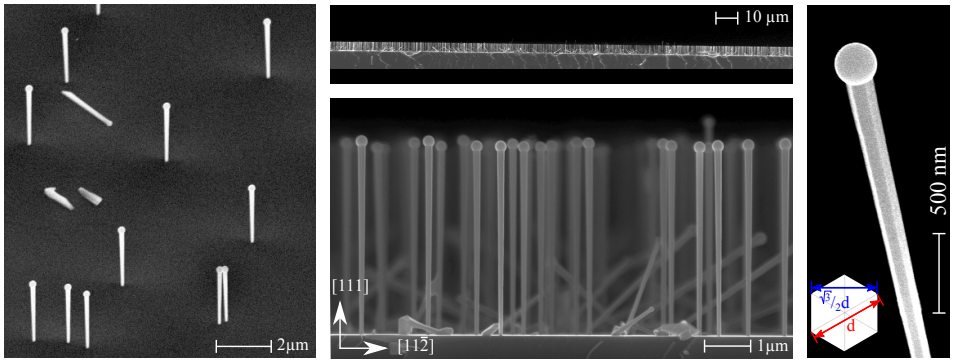

Figure 3.24: Representative scanning electron images of the grown NW ensemble. Left, a 30° tilt view is shown. The large field of view at the upper center gives an impression on the homogeneity of the NW ensemble. At the lower center, the inverse tapering of the wires is visible. In both images, the view-direction coincides with the normal of one (110)-type side-facet which allows us to calculate the facet distance. The high magnification image at the right shows a single NW from a tilted view. The (110)-type side-facets and a pronounced Ga droplet at its tip are visible.

whereas we obtain complementary information from symmetric and asymmetric reflections at two important late stages of the growth.

Sample The growth of the GaAs nanowires was performed on n-doped Si(111) wafers covered by native oxide at $T_S = 600\,°\text{C}$ substrate temperature and a comparably low V/III ratio in order to achieve low axial growth rates and to obtain nanowires with a pronounced droplet and a large diameter. Prior to the growth, the substrate was annealed for 30 minutes. Afterwards, Ga-droplets were deposited on the substrate. The nanowire growth was then initiated by increasing the As-flux. The Ga shutter was opened when the first GaAs material started to nucleate. This moment has been calibrated by RHEED before. After 255 minutes of growth, approx. 4000 nm long and 80-160 nm thick (edge distance) nanowires are present at the surface with pronounced Ga-droplets at their tips with a contact angle $\beta_{SEM} \approx 135° \pm 2°$ observed after growth. Since the view-direction in SEM is along the [111]-direction and coincides with the facet normal, the measured diameter actually corresponds to the distance of opposing edges of the hexagonal nanowire cross-section. Importantly, the facet distance, which will be discussed later is by a factor of $\sqrt{3}/2$ smaller than the edge distance. In the following, we will address the facet distance by using the term 'diameter'. Consequently, the values obtained from SEM will be multiplied by $\sqrt{3}/2$ in order to obtain the facet distance. Besides vertical GaAs nanowires, parasitic growth is mostly constituted by non-vertical GaAs nanowires (see Fig.3.24). All the nanowires appear to be tapered, which we attribute to an excessive Ga-flux into the droplet as a result of the low axial nanowire growth rate of $v_a = 15.68\,\text{nm/min}$ at a V/III ratio of $\text{F}_{\text{V/III}} = 2.6$ and Ga-limited 2D GaAs growth rate $R_{GaAs} = 45\,\text{nm/h}$.

Results & Discussion In the following, we evaluate the time-resolved X-ray data obtained in asymmetric scattering geometry in order to gain insight into the evolution of the microstructure

of the growing self-catalyzed GaAs nanowires. We aim on estimating phase-composition, and mean segment length without requiring a model for the stacking sequences and finally compare the values to results obtained from symmetric X-ray diffraction and the thereon applied Markov model.

Since time-resolved X-ray data is available, we can infer information on the time dependence of the average phase fraction. Here the mean phase fraction of wurtzite $\bar{p}_{wz}$ may be estimated from comparing the integrated intensities of suitable asymmetric reflections. For the extraction of the phase fraction, the measured data of the $(311)_{\mathrm{c}}$, $(10.3)_{\mathrm{h,wz}}$, and $(220)_{\mathrm{c}}$ reflections was corrected for the diffuse background caused by the Si substrate and was then integrated in a small Q_y-range ($\delta Q_y = \pm 0.008\,\text{Å}^{-}1$) around the truncation rod, in order to select scattering from mostly the vertically grown nanowires. The contribution of parasitic crystallites to the zinc-blende reflections was estimated from the Debye-Scherrer arc. The integrated intensity was then corrected for the structure factor of the respective reflection, and are shown in Fig. 3.25(a). Interestingly, we first observe an increase of the intensity of the wurtzite reflection before the zinc-blende reflections start to appear. Only after approximately $t_g = 25\,\text{min}$ of growth, corresponding to approximately 450 nm of nanowire height, the zinc-blende $(220)_{\mathrm{c}}$ twin reflection appears. The onset of the GaAs zinc-blende $(311)_{\mathrm{c}}$ reflection happens even later, however the strong background of the $(311)_{\mathrm{c}}$ reflection of the silicon substrate may superpose the weak GaAs signal at the beginning. Concomitantly with the onset of the zinc-blende reflections, we observe a change in the course of the wurtzite signal. Whereas the wurtzite signal increase is comparable to the one of the zinc-blende reflections at first, its gradient decreases drastically after 20 min. After 60 min of growth, corresponding to approximately 900 nm of nanowire height, both zinc-blende reflections exceed the intensity of wurtzite and increase further. This increase may be explained first by the axial growth and second by radial growth of the nanowires. In this case, the radial growth is composed of two contributions. The uniform growth of the nanowire facets, as observed before by SEM, and the height dependent increase of the diameter or tapering caused by an increase of the liquid Ga droplet due the excessive Ga-flux. The exact mechanisms of radial nanowire growth will be addressed later.

From the ratios of the time-dependent integrated intensities, we can estimate the phase fractions (Fig. 3.25(b)) in the nanowires after a certain growth time or length of the wires. Regarding the phase fraction, the nanowires seem to be composed mainly of wurtzite GaAs at the beginning of growth. After $t_g = 30$ min, however the wurtzite fraction decreases as a function of the growth time. A crossover is reached after approx. 50 min of growth, where the nanowires are composed equally of the cubic and hexagonal GaAs phase. For later growth times the wurtzite fraction decreases further resulting in a wurtzite fraction $\bar{p}_{wz} < 10\%$ for $t_g > 100\,\text{min}$. Consequently, the nanowires consist of mainly zinc-blende and twinned zinc-blende after $t_g = 160\,\text{min}$, whereas twinned zinc-blende and zinc-blende are of approximately equal abundance. This observation is similar to the findings of Biermanns [92], who found a length dependence of the wurtzite fraction $\bar{p}_{wz}$ from *ex-situ* XRD investigations. Qualitatively,

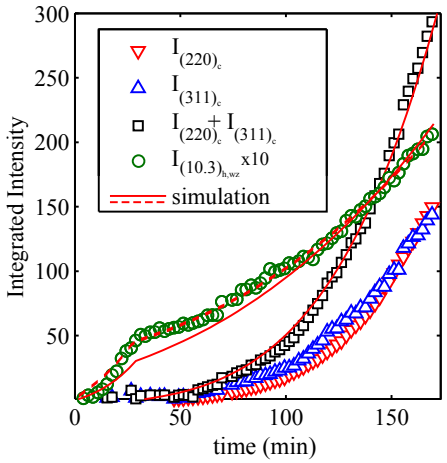

(a) Integrated intensity of the asymmetric zinc-blende, twinned zinc-blende and wurtzite reflections. The intensity of wurtzite is multiplied by a factor $a = 10$ for better illustration.

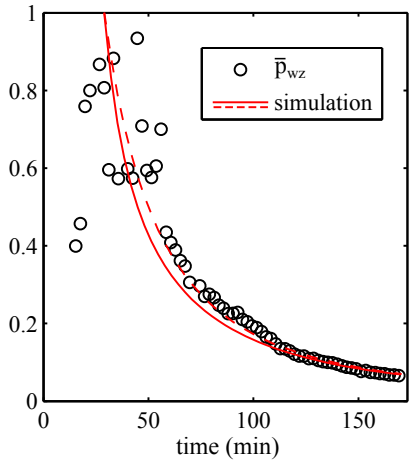

(b) Evolution of the wurtzite fraction $\bar{p}_w z$ during growth.

Figure 3.25: Time-resolved intensity and polytype phase fractions during growth. The simulated lines are obtained from calculations employing results presented in Sec. 3.7.

we observe the same trend as in our previous *in-situ* experiment, although the growth parameters differ, resulting in different quantitative values of the wurtzite fraction.

In the following, we will investigate the FWHM of the asymmetric reflections along the Q_z-direction which can be used in order to estimate a correlation length $\mu^p(t)$ along the [111]-direction, which may be interpreted as mean polytype segment length and the evolution thereof during growth. Therefore, the 2-dimensional data at the detector was integrated only in Q_y-direction in a small range around the reflection ($\delta Q_y = \pm 0.008\,\text{Å}^-1$). In order to relate the FWHM in reciprocal space and a correlation length in real space, we employ the Scherrer equation [169, 170]. However, the correlation length obtained by the Scherrer equation provides only a rough estimate, at best a lower bound of the segment size, since stacking faults, crystallite contribution or experimental resolution may cause additional peak broadening. In the following, we account for the experimental resolution estimated by the size of the CTR at the detector (approx. 1 px) which corresponds to $\delta Q_z \approx 0.0016\,\text{Å}^{-1}$.

The corresponding FWHM are depicted in Fig. 3.26(a). At the beginning of the growth no meaningful fit was possible due to the low signal intensity and background noise. After $t \approx 20\,\text{min}$, we observe, that the width of the $(10.3)_{h,wz}$ wurtzite reflection remains rather constant during growth. In contrast, the reflections of zinc-blende and its twin become more sharp as the growth proceeds and their FWHM decreases. Evaluated by the Scherrer equation (see Fig. 3.26(b)), we obtain estimates for the mean segment length of wurtzite segments $\mu^{wz} \approx 65\,\text{nm}$ which remains rather constant all over the measured growth time. The segment lengths of zinc-blende and twinned zinc-blende however, evolve from $\mu^{tzb}(30\,\text{min}) \approx 50\,\text{nm}$ to $\mu^{tzb}(160\,\text{min}) \approx$

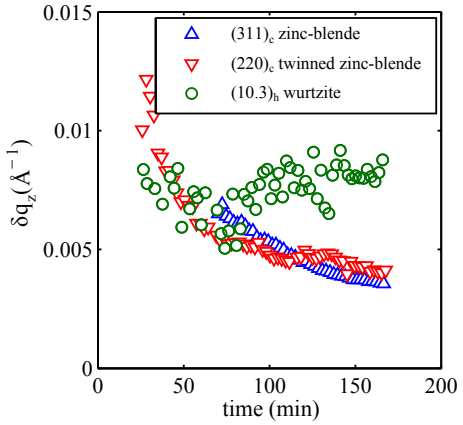

(a) Time-evolution of the width of the phase selective Bragg reflections in Q_z-direction.

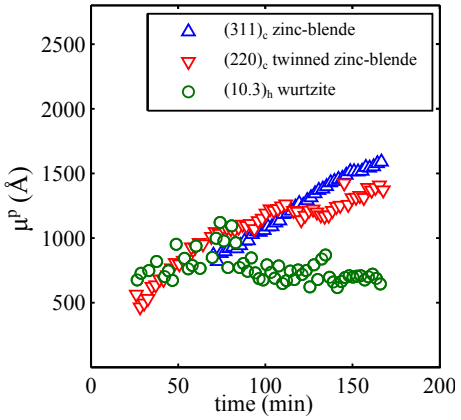

(b) Estimated correlation length $\mu^p(t)$ from the wurtzite and zinc-blende and zinc-blende twin reflections.

Figure 3.26: Time-dependece of the extracted FWHM of the phase selective asymmetric Bragg reflections along Q_z estimated by a Gaussian fit. From the FWHM, the correlation length $\mu^p(t)$ is estimated by applying the Debye-Scherrer formula.

140 nm and respectively $\mu^{zb}(160\,\text{min}) \approx 165\,\text{nm}$ at the end of growth. However, we state that these values are only estimates for the mean segment lengths, especially for the values of the wurtzite segments and should be treated rather as qualitative measures. Therefore, it may be only concluded, that the mean length of zinc-blende segments becomes larger, meaning that the phase purity of zinc-blende increases with growth time, measured by the FWHM, and in average segments of zinc-blende and its twin are approx. 2-3 times larger than the average wurtzite segment. If we correlate these findings with the evolution of the integral intensities, we may state, that after $t_g = 30\,\text{min}$ of growth, mainly extended zinc-blende and twin zinc-blende segments grow since the corresponding intensities increase. The FWHM of wurtzite however remains almost constant, indicating that only a small fraction of wurtzite is grown in additional segments after $t_g = 30\,\text{min}$. Therefore, we assume that the main part of wurtzite has been formed in the first 20 minutes of growth and the increase of $I_{10.3}$ is mainly caused by radial facet growth.

After the time resolved monitoring, full reciprocal space maps of the asymmetric truncation rod containing the $(311)_\text{c}$ reflection of Silicon and GaAs, the $(10.3)_\text{h,wz}$, and $(220)_\text{c}$, as well as of the symmetric $(111)_\text{c}$, reflections have been measured at growth temperature. After $t_g = 255\,\text{min}$, the growth was stopped by simultaneously closing the shutters for Ga and As. Subsequently, the sample has been rapidly cooled down to room temperature. At room temperature, the measurements detailed above have been repeated. In Fig. 3.27 the respective reciprocal space maps of the asymmetric reflections are depicted, next to the corresponding Q_z-intensity profiles. Clearly, the diffuse background originating from the Silicon substrate is considerable and most pronounced for the measurement performed at growth temperature. Below the Si $(311)_\text{c}$ Bragg

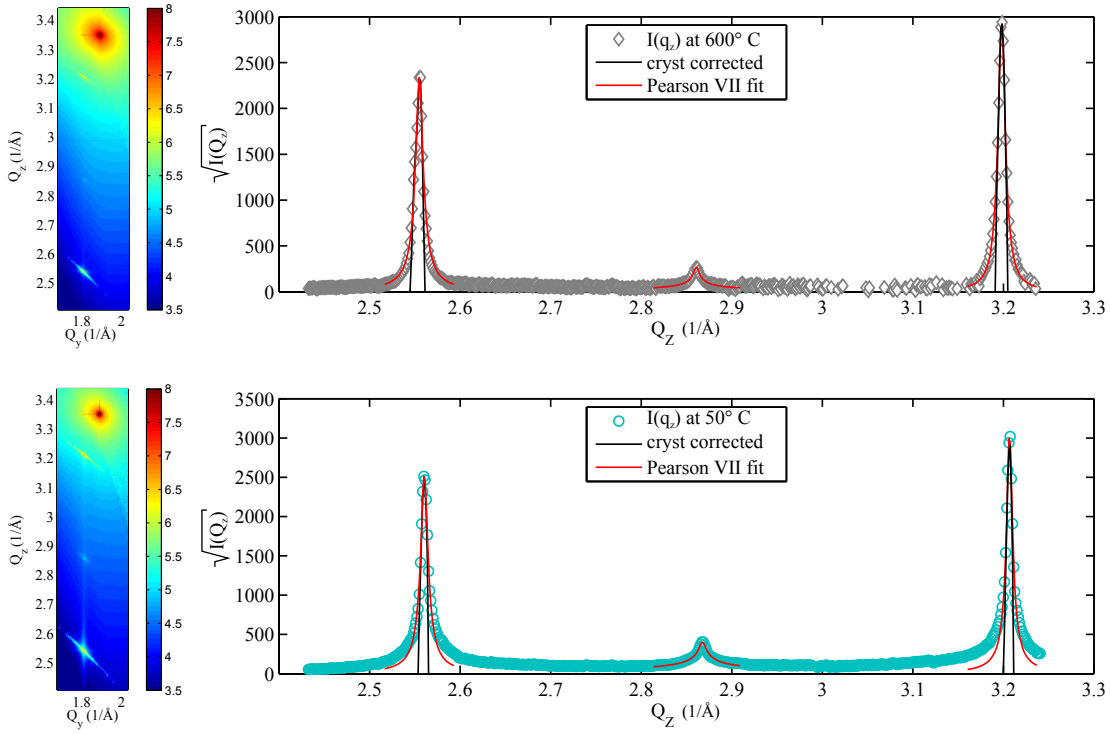

Figure 3.27: Left: Reciprocal space maps of the asymmetric truncation rod including the $(311)_c$ reflection of Silicon and GaAs, as well as the $(10.3)_{h,wz}$, and $(220)_c$ reflections. Right: Q_z-intensity profiles along the crystal truncation rod. Pearson VII fits to the centers of the Bragg peaks are shown in red. The black lines show the twinned zinc-blende, and zinc-blende contribution, after correction for parasitic GaAs crystallites. After cooldown at room temperature the diffuse scattering around the GaAs reflections, and along the crystal truncation rod is enhanced.

peak the GaAs $(311)_c$ can bee seen at $Q_z = 3.20\,\text{Å}^{-1}$. The wurtzite signal is visible at $Q_z = 2.87\,\text{Å}^{-1}$ and finally the $(220)_c$ Bragg peak of twinned GaAs zinc-blende is located at $Q_z = 2.56\,\text{Å}^{-1}$. An interesting feature of the cubic GaAs reflections, most pronounced at the $(220)_c$ reflection, is the oblique arc passing through the reflections' center. This arc can be attributed to GaAs structures which are tilted with respect to the $[111]_c$ direction. As we know from RHEED and our nano-focus experiments these structures are mostly crystallites which scatter at positions distributed at a Debye-Scherrer ring centered at the origin of the reciprocal space with radius equal to the magnitude of the scattering vector of the respective Bragg reflection. The $(10.3)_{h,wz}$ wurtzite reflection in contrast, does not show such a pronounced arc of a Debye-Scherrer ring.

If we inspect the fine structure of the $(220)_c$ reflection further, we observe a distinct streak perpendicular to the Q_z-direction. This streak is caused by scattering from the side-facets of vertical nanowires (similar to the facet streak observed in RHEED) and will be investigated in more detail later. Employing the method presented in Sec. 3.4, we are able to distinguish scattering from crystallites and vertically oriented nanowires in the asymmetric truncation rod.

We use this information for the correction of the Q_z-profiles depicted at the right, given by the black solid lines. Let us first consider the intensity profile measured at growth temperature at the top. The grey symbols constitute the Q_z-profile resulting from a Q_y-integration around $Q_y = 3.18\,\text{Å}^{-1}$ after subtraction of the diffuse Si-background and correction for the structure factor. The red solid lines depict fits to the centers of the Bragg peaks before correction for the tilted structures using a Pearson VII function. The black solid lines depict the GaAs peaks after this correction, for which we subtracted the averaged signal from areas besides the Q_y-center of the truncation rod. These areas contain only the Debye-Scherrer arcs. Whereas the width of the two cubic GaAs reflections considerably reduces by the correction, the wurtzite peak at $Q_z = 2.87\,\text{Å}^{-1}$ is not affected. Therefore, mainly tilted structures consisting of cubic GaAs cause a peak broadening of the cubic asymmetric GaAs reflections along Q_z and moreover contribute to the integral intensity. Consequently, the contribution of the tilted parasite structures needs to be accounted for. Otherwise the values obtained for phase fraction and the estimates for the mean segment width obtained from uncorrected Q_z-profiles may not be representative for the crystal structure of the vertical nanowires.

If we compare the measurements of the asymmetric reflections at growth temperature and room temperature, we observe two interesting differences. First, the peak positions shift slightly towards higher Q-values due to thermal contraction during cooldown. Second, the diffuse intensity distributed along the crystal truncation rod becomes more pronounced after cooldown and increases by a factor of 3. At the same time, the background corrected maximum intensity of the wurtzite reflection increases by a factor of 2, whereas the intensities of the cubic GaAs reflections remain constant. This corresponds to an increase of the wurtzite fraction from $\bar{p}_{wz}(600\,°\text{C}) \approx 2\%$ to $\bar{p}_{wz}(50\,°\text{C}) \approx 6\%$ or an increase by a factor of approx. 3. Since the measurement at growth temperature depicted in Fig. 3.27 has been performed at the end of growth, after 255 minutes, we can compare the wurtzite fraction $\bar{p}_{wz}(600\,°\text{C}) \approx 2\%$ with an extrapolated value obtained from the time-resolved measurement shown in Fig. 3.25(b). Extrapolation yields a wurtzite fraction of $\bar{p}^{e}_{wz}(600\,°\text{C}) \approx 2.5\%$ which is close to the result for the wurtzite fraction obtained by the time-resolved measurement.

The resulting estimates for the mean segment lengths are $\mu^{tzb}(600\,°\text{C}) \approx 120\,\text{nm}$ and $\mu^{tzb}(50\,°\text{C}) \approx 120\,\text{nm}$ for twinned zinc-blende, $\mu^{zb}(600\,°\text{C}) \approx 125\,\text{nm}$ and $\mu^{zb}(50\,°\text{C}) \approx 160\,\text{nm}$ for zinc-blende and $\mu^{wz}(600\,°\text{C}) \approx 72\,\text{nm}$ and $\mu^{wz}(50\,°\text{C}) \approx 50\,\text{nm}$ for wurtzite segments. This suggests, that after the shutters have been closed, the newly grown material may be composed mainly of wurtzite, although having a very low phase purity thus containing many stacking-faults.

Next we discuss the additional growth of wurtzite after the closing of the shutters on basis of measurements of the $(111)_c$-reflection at growth temperature and after the cooldown. The reciprocal space maps are given in Fig. 3.28(a): On the left the measurement at growth temperature is shown. The measurement at room temperature after the cooldown is depicted on the right. At growth temperature, we observe a pronounced diffuse background, and a shift of the Bragg peaks

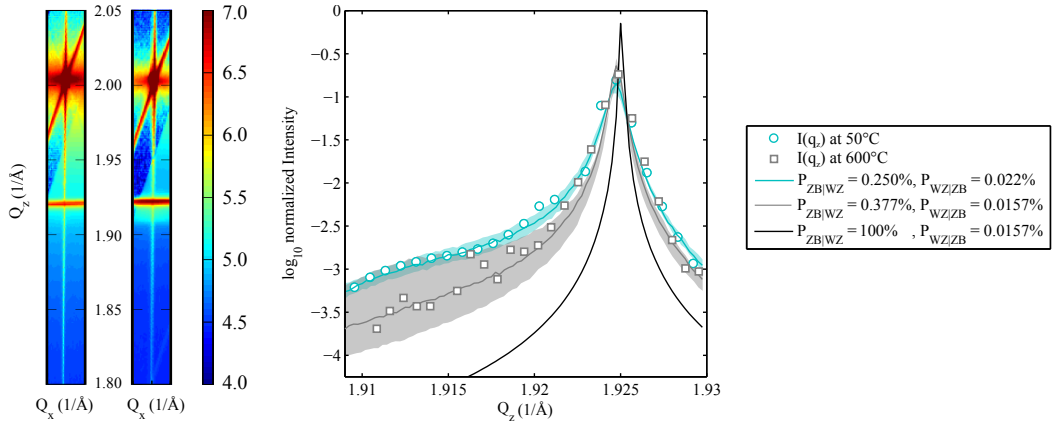

(a) Reciprocal space maps of the $(111)_c$ reflection at growth temperature (left) and room temperature (right)

(b) Intensity profiles after background correction. Simulations by the Markov model are given as solid lines. The shaded areas correspond to simulations in the given error range for the wurtzite fraction (see text). As reference, the intensity profile of nanowires containing only zinc-blende and twinned zinc-blende segments is depicted by the black solid line.

Figure 3.28: The reciprocal space maps at growth temperature and room temperature (a) have been integrated along Q_x, corrected for background and normalized (b). Fits obtained by a Markov model are given by the colored solid lines.

of the signals to smaller Q_z-values, due to thermal expansion. Most interestingly, the shape of the GaAs signal is different. After cooldown the GaAs signal obtained a diffuse cloud below the Q_z-position of GaAs zinc-blende, which was not observable at growth temperature. Fig. 3.28(b) shows the Q_z-intensity profiles obtained after integration of the reciprocal space maps in Fig. 3.28(a) along Q_y and successive background correction. The background correction contains the subtraction of the diffuse substrate signal, and the subtraction of a Gaussian for the crystallite contribution. Clearly, the slope towards lower Q_z-values changed after growth and a broad diffuse signal emerged in between $1.910\,\text{Å}^{-1} \leq Q_z \leq 1.915\,\text{Å}^{-1}$. We attribute this additional signal to wurtzite with low phase purity which could have been formed during the cooldown. Employing the Markov model using static transition probabilities to the depicted profiles, we can estimate the average wurtzite fraction. A good agreement with the experimental data was obtained for the fits presented by the solid lines in Fig.3.28(b), resulting in a wurtzite fraction at growth temperature of $\bar{p}_{wz}(600\,°\text{C}) = 4.0\% \pm 2.9\%$ and $\bar{p}_{wz}(50\,°\text{C}) = 8.1\% \pm 1.8\%$ after cooldown. The mean segment length of zinc-blende segments at room temperature obtained from the Markov model is $L_{zb} \approx L_{tzb} \approx 150\,\text{nm}$ similar to the values obtained from the asymmetric reflections. However the Markov model yields smaller values for wurtzite segments $L_{wz} \approx 13\,\text{nm}$. Comparable to the results from the asymmetric reflections, we observe that segments of zinc-blende (and its twin) are up to 10 times larger that wurtzite segments. We find an increase in the wurtzite fraction after cooldown, however the quantitative values differ and have in case of the Markov model huge errors. Therefore, we argue that for nanowires with $\bar{p}_{wz} < 10\%$ we may have reached the

limit of the applicability of the Markov model to intensity profiles of the $(111)_c$ reflection. The low amount of wurtzite in the nanowires, as well as the low phase purity of wurtzite segments cause the wurtzite signal to spread over a large Q_z-range. In addition, errors in the background correction of crystallite and substrate contributions cause uncertainties. Together, these factors may lead to a non uniqueness of the solution obtained by the Markov model. In particular, an experimental profile may be equally well described by simulations based on different sets of transition probabilities (compare shaded areas in Fig. 3.28(b)) with different phase purity for zinc-blende and wurtzite segments, but similar wurtzite-fraction. As we discussed in Sec. 3.5, combined measurements in symmetric and asymmetric geometry yield consistent results, given that the wurtzite fraction and phase purity is sufficiently large. One way to overcome the limitations of the $(111)_c$-reflection imposed by low phase purity could be the measurement of the $(333)_c$ -reflection [112]. This Bragg reflection is, however not accessible with the current growth equipment.

In summary, we grew self-catalyzed GaAs nanowires and simultaneously monitored the X-ray scattering of the phase-selective $(311)_c$, $(10.3)_{h,wz}$, and $(220)_c$ reflections in a time resolved way. We observe, that wurtzite forms first resulting in a wurtzite fraction $\bar{p}_{wz} > 50\%$ for the first 50 minutes of growth (or equivalently approx. 750 nm nanowire length). After 30 minutes of growth, the nucleation of zinc-blende and its twin sets in, and appears to be more favorable than wurtzite. As a result the wurtzite fraction reduces to $\bar{p}_{wz} \approx 2\%$ at the end of the growth. At the same time, zinc-blende and twin zinc-blende segments grow longer which is expressed by the decrease of the Q_z-FWHM of the $(311)_c$ and $(220)_c$ reflections. In contrast, the Q_z-width of the $(10.3)_{h,wz}$ reflection remains constant during growth.

The state of the microstructure at the end of the growth at growth temperature and room temperature, was investigated by combined measurements of the $(311)_c$, $(10.3)_{h,wz}$, and $(220)_c$ reflections, and the symmetric $(111)_c$-reflection. The results imply that after the growth was stopped, additional wurtzite was formed in the nanowires. We attribute this to subsequent nucleation of material solved in the liquid droplet and a change in growth conditions after the supply of Ga and As was stopped [34, 60]. Recently Rieger et al. [83] showed, that the shape of the droplet, in particular its wetting angle with the top facet has a strong impact on the crystal structure grown during this stage. Interestingly in this case, a transition area with a high number of stacking-faults is formed, before the growth proceeds in wurtzite stacking [34, 60]. This is again compatible with our observations that after the supply of growth species was stopped, a small amount of wurtzite with low phase purity was grown.

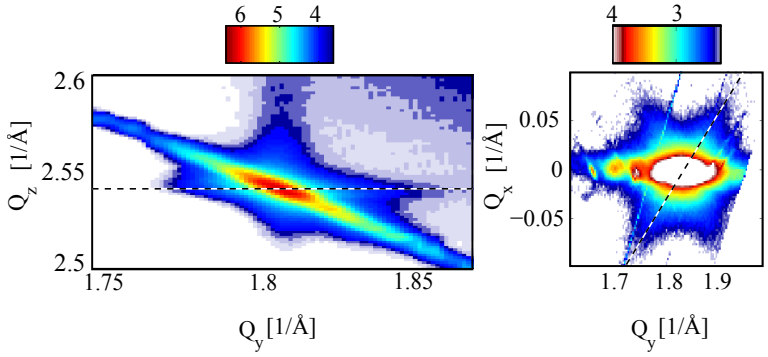

Figure 3.29: 2D projections of the 3D scattered intensity distribution around the $(220)_c$ reflection. Left: $Q_y - Q_z$ - RSM of the $(220)_c$ reflection. Right: $Q_x - Q_y$ - RSM of the $(220)_c$ reflection.

3.7 Time-resolved monitoring of radial growth of self-catalyzed GaAs nanowires: tapering and facet growth

After investigating the crystal structure of the nanowires of the nanowire sample presented in Sec. 3.6, we will now extract information on their shape and its evolution during growth by detailed inspection of scattering features originating from the (110)-type nanowire side-facets. Therefore, we resort to the same set of experimental data, used for the determination of the structural evolution in Sec. 3.6. From this data, we will extract key-features which will allow us to conclude on radial growth processes at the base of the nanowire, and – by correlation with *ex-situ* SEM – at the nanowire tip during growth. Thereby, we will be able to distinguish non-catalytic facet growth at the nanowire side walls from catalytic growth processes involving the liquid Ga-droplet at the nanowire tip. We will further compare our experimental findings to simulations of the X-ray scattering features. By extending and applying theoretical growth models to our *in-situ* results, we will obtain quantitative estimates for the effective diffusion length of Ga, and will infer information on the evolution of shape and volume of the liquid Ga-droplet *during* growth.

For the investigation of the facet streaks, we focus on the twinned zinc-blende $(220)_c$ reflection. Inspecting the fine-structure of the $(220)_c$ reflection in Fig. 3.29, we observe two distinct features: 1) the oblique Debye-Scherrer arc with its center at the origin of the reciprocal space, and 2) a streak at constant Q_z passing through the $(220)_c$-Bragg peak. A cross-section through the Bragg peak in the Q_x-Q_y plane at this Q_z-level reveals the hexagonal symmetry of this signal which we relate to scattering from the nanowire (110)-type side facets.

For a vertical self-catalyzed GaAs nanowire, its growth direction is parallel to the $[111]_c$-direction of the substrate normal, which is parallel to the Q_z-direction in our geometry. If a nanowire is coherently illuminated by X-rays, we would expect a scattering signal proportional to the square modulus of the Fourier transform of its electron density which is given by the

Fourier transform of its shape [171]. Therefore, the Q_x-Q_y parallel to the substrate surface provides information on the corresponding cross-section of the scattering nanowire which is in our case a hexagon bounded by (110)-type facets. Indeed, a projection of the $(220)_c$-Bragg peak into the Q_x-Q_y-plane reveals a signal with a sixfold symmetry. Originating from the truncation of the nanostructure the side facets give rise to crystal truncation rods, visible as diffuse streaks forming a sixfold star in the Q_x-Q_y-plane. However, we do not observe distinct size oscillations along the streaks, as we would expect for a given hexagon (see Fig. 3.29). The vanishing of these features may be a result of fluctuations of individual nanowire diameters around a certain mean value, or a non-constant nanowire diameter along the growth axis (tapering) which cause the size oscillations to smear out. For the X-ray evaluation, we will use the terms 'diameter' and 'radius', referring to the distance of two opposing nanowire (110)-type side facets. For later comparison, the values obtained by SEM measurements (e.g. extracted from side view SEM images as given in Fig. 3.24) have to be multiplied by a factor of $\sqrt{3}/2$, since here the diameter is evaluated along the $[11\bar{2}]$ direction.

3.7.1 Distinguishing non-catalytic facet-growth and catalytic growth processes by scattering features obtained by time-resolved *in-situ* X-ray diffraction

In the following, we will investigate the intensity distribution $I(q,t)$ along such facet streaks during growth, by evaluating certain key-features of the intensity profiles: the full-width-half-maximum $q^p_{fwhm}(t)$ of the central maximum, as well as the position of the first-order maximum $q^p_{max}(t)$ as a function of growth time t. Since the distribution of twinned zinc-blende and zinc-blende segments along a nanowire is random, the $(220)_c$-Bragg reflection from an ensemble of nanowires contains information on the average lateral dimension over the whole nanowire length (excluding the small wurtzite segment at the base). These key-features will then be interpreted as correlation length in the frame of a sinc^2 function. In case of wurtzite this correlation length may serve as estimate for the mean radius of the respective wurtzite segments at the nanowire base. Having the time-evolution of the radius at the nanowire base *during* growth, and the height-dependent radius *after* growth inferred from SEM, will allow us to conclude on the shape-evolution of the nanowire during the growth process.

For the extraction of the key-features, the time-resolved 2D cuts through the $(220)_c$-Bragg peak and $(10.3)_{h,wz}$-Bragg peak were corrected for background, and then integrated along $\delta q_z = \pm 0.0016$ Å^{-1}. This results in an intensity profile $I(q)$ essentially along a side-facet streak as indicated by the dotted lines in Fig. 3.29 for the $(220)_c$ Bragg reflection. Then a Gaussian function was fitted to the central peak in order to obtain q^{ZB}_{fwhm}. The position of the first order maximum q^{ZB}_{max}, was obtained by a fit using a Gaussian, as well. The time-evolution of $I(q,t)$ is given in the top panel of Fig. 3.30 up to a growth time $t = 168$ min. In case of the twinned zinc-blende reflection in Fig. 3.30(a) the central maximum at $q = 0$ Å^{-1} can be fitted after

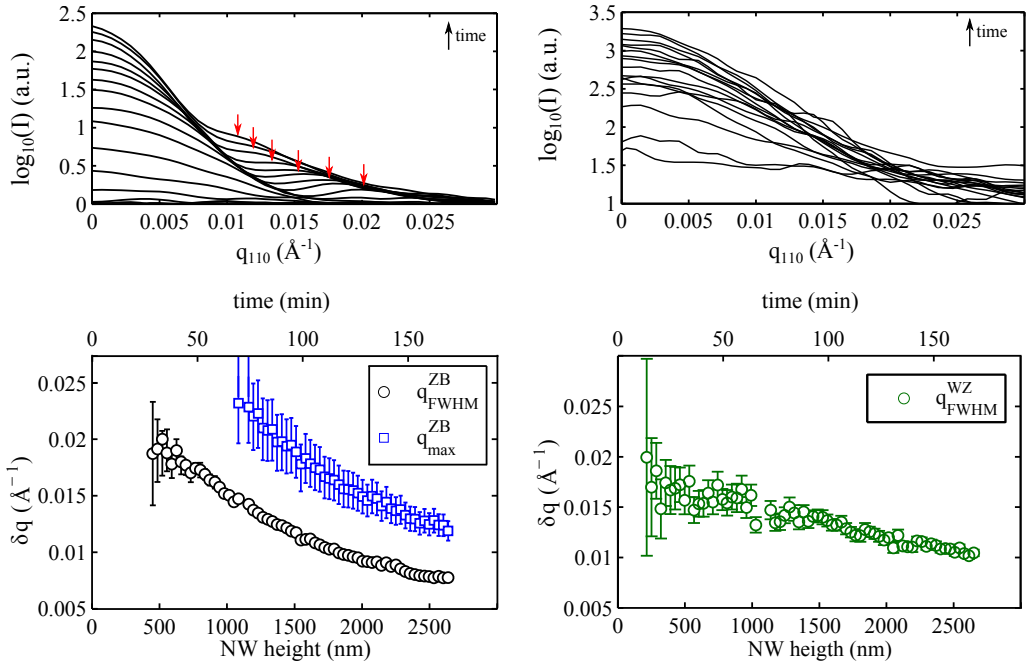

(a) Time-resolved intensity profiles $I(q_{110})$ of the $(220)_c$ reflection. Extracted values for $q_{fwhm}(t)$ and $q_{max}(t)$. On top, exemplary positions of q_{max} are indicated by the red arrows.

(b) Time-resolved intensity profiles $I(q_{110})$ of the $(10.3)_{h,wz}$ wurtzite Bragg reflection and extracted $q_{fwhm}(t)$.

Figure 3.30: The background-corrected intensity-profiles $I(q_{110})$, obtained by an integration along $\delta q_z = \pm 0.0016$ Å^{-1} around the respective Bragg reflection, are given on top. Additionally, the values were smoothed by a running average. On the bottom, the values of the extracted key-features are given.

$t \approx 30$ min, and shows weak but detectable satellite peaks as exemplary indicated by the red arrows. At earlier times $t < 60$ min the satellite peaks are too weak and cannot be evaluated. As time increases, the intensity of the central maximum increases and the satellite peaks move closer to the central peak. Below, the corresponding values of $q^{ZB}_{fwhm}(t)$ and $q^{ZB}_{max}(t)$ extracted from the intensity profiles are shown. Both values, FWHM as well as position of the first order maximum decrease with increasing growth time. However with rater large uncertainties in case of $q^{ZB}_{max}(t)$. In Fig. 3.30(b), we accordingly evaluate the intensity profiles $I(q,t)$ for the $(10.3)_{h,wz}$ wurtzite Bragg reflection. In contrast to the twinned zinc-blende reflection, only a central peak but no satellite peaks are observable. However, $q^{WZ}_{fwhm}(t)$ can be evaluated beginning already at $t = 11$ min. At these early times ($t < 30$ min), $q^{WZ}_{fwhm} \approx q^{ZB}_{fwhm}$. As for the FWHM of twinned zinc-blende $q^{ZB}_{max}(t)$, the FWHM of wurtzite $q^{WZ}_{max}(t)$ decreases with increasing growth-time.

Further, we relate $q_{fwhm}(t)$ and $q_{max}(t)$ to the FWHM and the position of the first order side maximum of a sinc^2 function

$$I(q) \propto \left(\frac{\sin(q \cdot \mu)}{q \cdot \mu} \right)^2 \tag{3.26}$$

and are thereby able to estimate a time-dependent correlation length $\mu^p(t)$ along the $[1\bar{1}0]$-direction for both polytypes twinned zinc-blende and wurtzite separately. We approximate $\mu^p(t)$ by

$$\mu^p(t) \approx 2.78/q^p_{fwhm}(t) \tag{3.27}$$

$$\mu^p(t) \approx 4.49/q^p_{max}(t). \tag{3.28}$$

The resulting values for the correlation length $\mu^p(t)$ are given in Fig. 3.32(a). First, consistent values of $\mu^{ZB}(t)$ are obtained by the FWHM and the first order side peak position. This is of great importance, since it implies that the central peak, as well as the satellite peaks originate from the same type of nanostructures which most probably undergo the same size-evolution during growth. This size-evolution is expected to be different in case of parasitic crystallites. An increase in $\mu^{ZB}(t)$ is further compatible with the observed inverse tapering of the nanowires by SEM shown in Fig. 3.24. For the correlation length extracted from the wurtzite Bragg reflection, we observe values compatible with $\mu^{ZB}(t)$ for times $t < 50\,\text{min}$. However, for $t > 50\,\text{min}$ the correlation length of the two polytypes differ. The increase of $\mu^{WZ}(t)$ with time is slower as compared to the increase of the correlation length $\mu^{ZB}(t)$ and follows a linear behavior. Including observations from Fig. 3.25(a), indicating that the bottom of the nanowire consists mainly of wurtzite GaAs, whereas the part grown after $t \approx 20\,\text{min}$ is predominantly zinc-blende or twinned zinc-blende GaAs, we can interpret $\mu^{WZ}(t)$ as the mean bottom radius of the nanowire $r^{WZ}_{NW}(t)$. Assuming, that the evolution of the mean radius $r^{WZ}_{NW}(t)$ of the wurtzite segments after $t \approx 20\,\text{min}$ is caused by radial growth of existing wurtzite segments at the nanowire base only, and no new wurtzite segments are formed at the nanowire tip.

The increase of the correlation length of twinned zinc-blende segments $\mu^{ZB}(t)$ however, is additionally connected to the nucleation of new layers at the tip of the nanowire, directly below the droplet. These newly grown layers have larger radius than the layers below, as consequence of the inverse tapering. Therefore, we can not directly relate the correlation length $\mu^{ZB}(t)$ to the mean radius of the zinc-blende segments during growth. For an interpretation, a weight function is required, which accounts for the different scattering volume of (111)-bilayers with different cross-sectional area.

We now introduce a basic model for radial growth of self-catalyzed GaAs nanowires including tapering due to catalytic growth and non-catalytic, homogeneous side-wall growth. In this context, catalytic growth refers to changes in the shape of the liquid Ga-droplet during growth. By applying this model to our *in-situ* X-ray results, we will be able to distinguish the contributions of facet growth and catalytic growth to the overall radial growth of self-catalyzed GaAs nanowires.

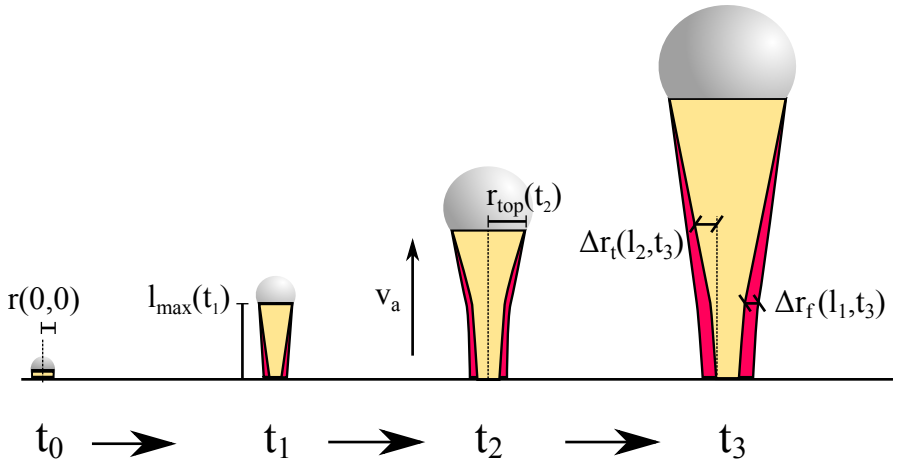

Figure 3.31: Illustration of the radial growth of $r_{NW}(l,t)$ according to Eq. 3.30 at different growth times t_i. The initial nanowire radius $r(0,0)$ at $t_0 = 0$ is given. The nanowire height at time t_1 is indicated by $l_{max}(t_1)$. The radius of the top-facet $r_{top}(t_2)$ is shown, as well as the contribution of tapering $\Delta r_t(l_2,t_3)$ and of facet growth $\Delta r_f(l_1,t_3)$.

Finally, we apply recent theoretical growth models of tapering due to catalytic growth in GaAs nanowires to our results.

GaAs nanowires grown via the self-catalyzed method feature a liquid Ga droplet at their tip acting as a catalyst for axial growth. The contact area of the liquid Ga particle and the top facet determines the size of newly nucleating layers at the growth front. In contrast to Au-catalyzed nanowires where the size of the catalyst particle remains constant, the Ga-droplet may change its size during growth at non-steady state conditions. The droplet may either inflate due to excessive Ga influx, or deflate if the rate of Ga atoms which are incorporated into the solid nanowire exceeds the rate of Ga atoms entering the droplet by impingement or diffusion. As a result, growth at non-steady state conditions usually leads to (inverse) tapering. In addition to catalytic growth, non-catalytic growth takes place at the side facets of the nanowire. This results in a subsequent radial growth all along the grown nanowire.

Whereas *in-situ* XRD offers access to the radial evolution of the nanowires at certain growth time t, *ex-situ* SEM reveals the evolution of the radius along the nanowire growth axis in its final state corresponding to t_f. Here, the radius of the nanowire, r_{SEM} at a certain height l above the substrate is measured, revealing inverse tapering.

In the following, we discuss how the results of XRD and SEM can be related and how the correlation length in case of the tapered twinned zinc-blende segments may be interpreted. Therefore, we model the growth of nanowire length and radius, where we allow radial growth processes containing contributions of tapering and facet growth. Supposing the initial nanowire radius is $r(0,0)$ at growth time $t = 0$ min and height $l = 0$ nm, we express the nanowire radius $r_{NW}(l,t)$ as

$$r_{NW}(l,t) = r(0,0) + \Delta r_{radial}(l,t) \tag{3.29}$$
$$= r(0,0) + \Delta r_t(l,t) + \Delta r_f(l,t) \tag{3.30}$$

assuming that the radial growth of the nanowire can be described by two independent quantities constituted by tapering $\Delta r_t(l,t)$, and subsequent facet or side-wall growth $\Delta r_f(l,t)$, both depending on nanowire length l and growth time t in general. The components of radial growth are illustrated in Fig. 3.31. The overall height of the nanowire at time t is given by $l_{max}(t)$. Whereas $\Delta r_t(l,t) = \Delta r_t(l_{max}(t)) = \Delta r_t(t)$ describes the radial growth of the top-facet due to tapering [172, 145] at $l_{max}(t)$, the term $r_f(l,t)$ accounts for subsequent non-catalytic side-wall growth. Further, we assume that the facet growth rate is homogeneous and constant along the nanowire ($dr_f/dl \propto dr_f/dt = const.$), and $\Delta r_f(l_{max},t) = 0$. Moreover, we assume that the nanowire grows with a constant axial growth rate $dl/dt = v_a = const.$ resulting in the nanowire length $l_{max} = v_a \cdot t$ at time t. At our growth conditions we obtain $v_a = 15.68$ nm/min, and $\Delta r_f(l,t)$ can be expressed with $t_0(l) = l/v_a$ as

$$\Delta r_f(l,t) = \left.\frac{\mathrm{d}r_f}{\mathrm{d}t}\right|_{t\geq t_0(l)} (t - t_0(l)) \tag{3.31}$$
$$= \frac{m_{facet}}{v_a}\,(v_a\, t - l). \tag{3.32}$$

We note, that $\Delta r_f(l,t) = 0$, if $l(t_0) > l_{max}(t)$, or equivalent $t_0 > t$. From the linear fit of $\mu_{WZ}(t > 60\,\mathrm{min})$ in Fig. 3.32, we obtain the facet growth rate $dr_f/dt = m_{facet} = 0.095$ nm/min $\pm$ 0.006 nm/min which defines $r_{NW}(0,t)$. In addition, we obtain the initial radius $r_{NW}(0,0) = 11.1\,\mathrm{nm} \pm 0.8$ nm from linear extrapolation of $\mu_{WZ}(t)$ at $t = 0$.

The values r_{SEM} measured by SEM can then be expressed by

$$r_{SEM}(l) = r_{NW}(l,t_f) = r(0,0) + \Delta r_t(t_f) + \Delta r_f(l,t_f). \tag{3.33}$$

The initial radius $r(0,0)$, as well as the facet growth rate m_{facet} can be extracted from the X-ray experiment. With Eq. 3.32, and $r_{SEM}(l)$, and assuming homogeneous facet growth, this allows us to conclude on the nanowire shape during growth. More precisely, we obtain $r_t(l_{max},t)$ empirically by

$$\Delta r_t(l_{max}(t)) = r_{NW}(l_{max}(t),t_f) - \Delta r_f(l_{max}(t),t_f) - r(0,0). \tag{3.34}$$

After determining $\Delta r_t(t)$, the nanowire shape follows according to Eq. 3.30. Here, *in-situ*

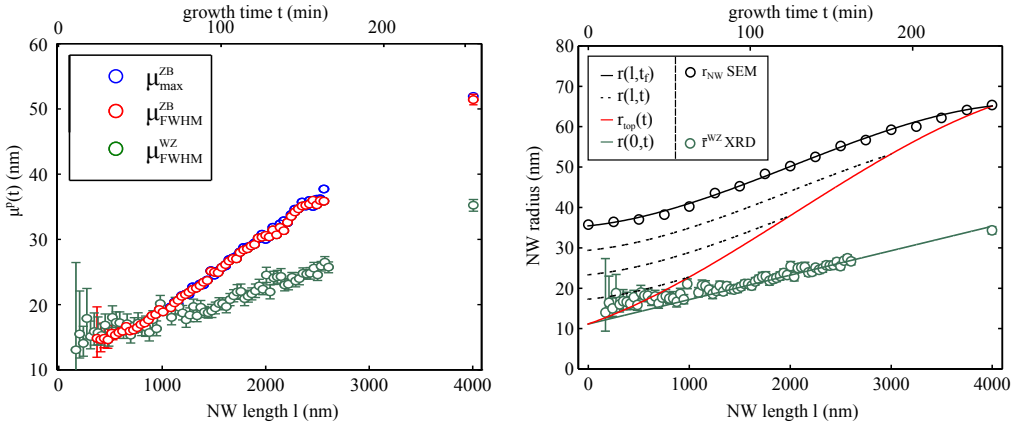

(a) Correlation length $\mu^p(t)$ for zinc-blende and wurtzite segments as function of growth time. In addition, values obtained from the reciprocal space maps (compare Fig. 3.27) taken after growth at $t_f = 255$ min are given.

(b) Calculated nanowire shape $r_{NW}(l,t)$ for various growth times, top facet radius $r_{top}(t)$, bottom radius $r_{NW}(0,t)$ and $r_{SEM}(l)$.

Figure 3.32: Correlation lengths $\mu^p(t)$ allow calculation of the nanowire shape during growth via Eq. 3.30.

XRD and *ex-situ* SEM provide sufficient input data, and no further model for Δr_t is required for calculation of the nanowire shape and its evolution during growth. The resulting curves are given in Fig. 3.32. The solid black line, $r_{NW}(l,t_f)$ is a fit to $r_{SEM}(l)$ using a third order polynomial. The dotted black lines represent $r_{NW}(l,t)$, for several growth times t. In red, the top-facet radius $r_{top}(t) = \Delta r_t(t) + r_{NW}(0,0)$ is given, and $r(0,t)$, the linear fit to $r^{WZ}(t)$ is given by the green line. Both so obtained values for the initial radii $r_{NW}(0,0) = 11.1$ nm $\pm$ 0.8 nm and $r_{top}(0) = 11.1$ nm $\pm$ 1.5 nm are compatible. Moreover, the value at the end of growth $r_{NW}(0,t_f) = 35.5$ nm $\pm$ 1.5 nm is consistent with the measurement by SEM at the nanowire bottom $r_{SEM}(0) = 35.3$ nm $\pm$ 1.2 nm.

3.7.2 Simulation of time-resolved intensity profiles $I(\vec{q},t)$ and comparison to the experimental *in-situ* data

Now, we calculate the two-dimensional scattered intensity distribution $I_{NW}(\vec{q},t)$ in t he $Q_x - Q_y$-plane for a single nanowire with non-uniform radius $r_{NW}(l,t)$ as given by Eq. 3.30 in kinematical approximation at certain growth times t. Therefore, we require $r_{NW}(l,t)$ as displayed in Fig. 3.32(b). We assume that the cross-section of a layer at height l and time t is given by a regular hexagon $\Omega_l(\vec{r},t)$. In order to calculate the in-plane intensity distribution from a nanowire $I_{NW}(\vec{q},t)$ with varying radius along its length, we build the sum over the squared absolute values of the two-dimensional Fourier transforms $\tilde{\Omega}_l(\vec{q},t)$ of the hexagonal cross-sections of the nanowire

$\Omega_l(\vec{r},t)$ for $l=0$ to $l=l_{max}$

$$I_{NW}(\vec{q},t) = \sum_{l=0}^{l_{max}} |\tilde{\Omega}_l(\vec{q},t)|^2. \tag{3.35}$$

Then, we evaluate the intensity profile along a nanowire facet streak $I_{NW}(q,t)$ at a certain time t as shown in the top panel of Fig. 3.33(a), and as indicated by the dotted line in the two-dimensionl in-plane calculation of $I_{NW}(\vec{q},t)$ below. In the bottom panel of Fig. 3.33(a), the simulated intensity profiles (black) are compared exemplary for three growth times to the experimental profiles (red) and the intensity profile of a sinc^2 - function (blue) using the weighted mean radius $\bar{r}_w(t)$ as argument. Here, we employ the area of a layer at height l at a given time t, $A_{layer}(l,t)$ as weight and write

$$\bar{r}_w(t) = \int_0^{l_{max}(t)} w(l,t)\; r^p_{NW}(l,t)\; dl \tag{3.36}$$

with the weight

$$w(l,t) = \frac{A_{layer}(l,t)}{\int_0^{l_{max}(t)} A_{layer}(l,t)dl}. \tag{3.37}$$

The position of the first-order side maximum $q^{NW}_{max}(t)$ is indicated by the vertical dotted line and coincides for experiment, simulation and sinc^2 in the three depicted cases. This can be understood as hint (but not as a proof), that the weighted mean radius $\bar{r}_w(t)$ may serve for interpretation of the correlation length $\mu^{ZB(t)}$ in our case. In the following however, we resort to the comparison of the key-features of simulated and measured intensity profiles, since we therefore do not require a real-space interpretation of the key-features. We evaluate the position of the first-order side-maximum $q^{NW}_{max}(t)$ and the FWHM $q^{NW}_{fwhm}(t)$ from the simulated profiles in order to compare the calculated values to the ones obtained from the $(220)_c$ twinned zinc-blende Bragg reflection.

The top panel in Fig. 3.33(a) shows the calculated profiles $I^{NW}(q,t)$ normalized to the maximum intensity at each time t (or equivalent nanowire height $l_{max}(t)$) in log scale. As the nanowire grows longer, both $q^{NW}_{fwhm}(t)$ and $q^{NW}_{max}(t)$ decrease (compare Fig. 3.30(a)). From these calculated profiles, the values of the key-features (red solid line) are extracted. From a comparison to the experimental values in Fig. 3.33(b), we find a good agreement with the experiment. This confirms that the shape-evolution shown in Fig. 3.32(b) is consistent with our X-ray data extracted from the $(220)_c$ twinned zinc-blende Bragg reflection. Below, the corresponding values $q^{WZ}_{fwhm}(t)$ obtained from the $(10.3)_{h,wz}$ wurtzite reflection are compared to the calculated values obtained by $r_{NW}(0,t) = m_{facet}\cdot t + r(0,0)$ and Eq. 3.28, given by the red solid line.

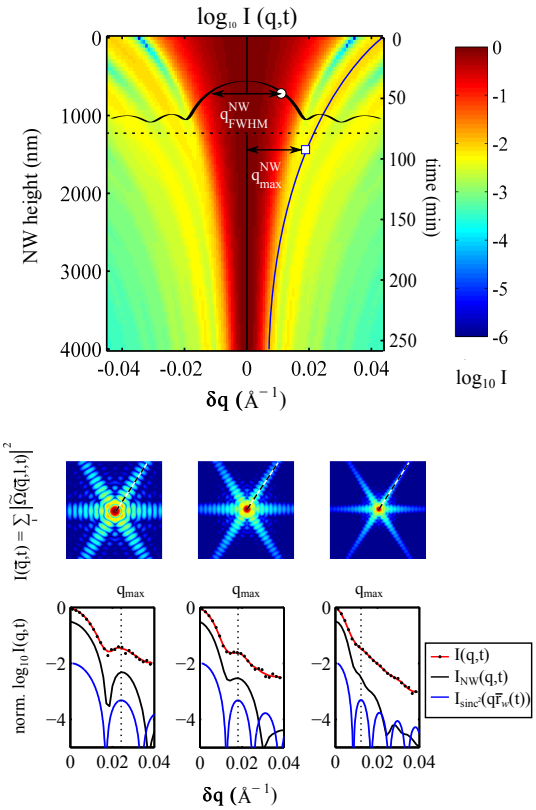

(a) The top panel shows the calculated intensity profiles $I_{NW}(q,t)$ evaluated along a facet streak during growth. In the bottom panel, the calculated two-dimensional intensity distribution in the $Q_x - Q_y$-plane for three different growth times are given. Below, exemplary measured and calculated intensity profiles are depicted.

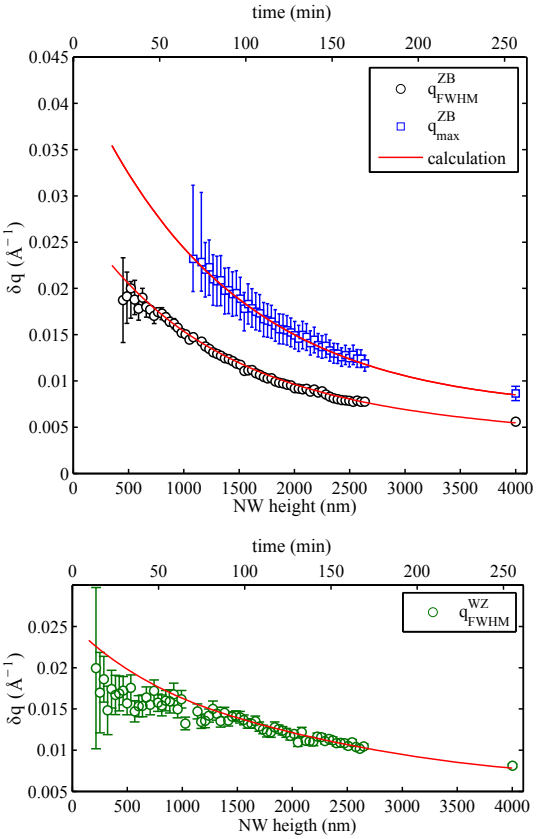

(b) Comparison of key-features, extracted from experiment (symbols) and simulation (red solid lines). The calculated values are obtained from the calculated profiles shown in the top panel of Fig. 3.33(a).

Figure 3.33: The top panel of Fig. 3.33(a) shows the calculated intensity profiles $I_{NW}(q,t)$ evaluated along a facet streak during growth. For illustration, one profile is depicted in black. Below, the two-dimensional scattered intensity $I(\vec{q},t)$ for the depicted growth-times ($t_1 = 69\,\text{min}$, $t_2 = 105\,\text{min}$, and $t_3 = 168\,\text{min}$) is given. The direction along the one-dimensional intensity-profile $I_{NW}(q,t)$ (facet streak) is evaluated, is indicated by the broken line. At the bottom the normalized intensity-profiles from experiment $I(q,t)$ (red), from the calculation $I_{NW}(q,t)$ and from $I_{sinc^2} = \text{sinc}(q\ \bar{r}_w(t))^2$ are compared. The position of the first-order side-maximum is indicated by the vertical broken line. Fig. 3.33(b) gives the comparison of key-features extracted from the simulation of the X-ray intensity profiles depicted by the red solid lines with values obtained by the experiment given by square ($q^{NW}_{max}(t)$), and circle ($q^{NW}_{fwhm}(t)$) symbols. The simulated values were obtained for the shape evolution $r_{NW}(l,t)$ shown in Fig. 3.32.

Since we now have a model for the evolution of the scattering volume given by $r_{NW}(l,t)$ and the axial growth rate v_a, we can moreover compare the integrated intensities $I_{(hkl)}(t)$ already introduced in Sec. 3.6 to the summed intensities of the calculated profiles $I^p_{calc}(t) = \sum I_{NW}(q,t)$.

We first calculate the integrated intensity or wurtzite. In Fig. 3.25(a), we observe a change in the slope of $I_{(10.3)_{h,wz}}$ at $t \approx 30\,\text{min}$. Based on the linear axial growth rate v_a, this time corresponds to a length $l_{max}(30\,\text{min}) = 450\,\text{nm}$. At the same time, integrated intensity of the twinned zinc-blende $(220)_c$ and zinc-blende $(311)_c$ reflections is basically a result of noise and thus compatible with zero.

In order to model polytypism, we can therefore assume, that the nanowire grows in wurtzite phase for the first 450 nm. Therefore, the modeled shape includes radial and axial growth until $l_{max} = 450\,\text{nm}$. Afterwards, only radial growth contributes to the volume increase of the wurtzite base segment, since the axial growth continues in zinc-blende phase. Complementary, we assume growth of pure zinc-blende phase after $l_{max} = 450\,\text{nm}$.

The calculated values are then compared to $I_{(10.3)}(t)$ as a measure of the nanowire volume constituted by wurtzite GaAs, and to the sum of zinc-blende and twinned zinc-blende $I_{(220)}(t) + I_{(311)}(t)$ as measure for the remaining nanowire volume constituted by cubic GaAs. For a direct comparison to the experiment, we further have to normalize the calculated intensities by a scaling factor, which is in our case, $k = 9.377e^{-13}$.

As depicted by red solid lines in Fig. 3.25(a), the calculated intensity for zinc-blende fits well to the sum of of zinc-blende and twinned-zinc-blende. The intensity calculated for the wurtzite nanowire part reproduces the change of the slope of the experimental values at 450 nm quite well. However, the calculated intensity underestimates the experimental values at early times. This is possibly caused by nucleation of new nanowires in wurtzite phase at the beginning of growth, which is not covered by our model which describes the growth of a single nanowire. If we instead assume an additional volume increase by a factor of $f_{nuc} = 1.75$ due to nucleation of new nanowires until $l_{max} = 400\,\text{nm}$, we obtain the dotted line for the simulated integrated intensity of the wurtzite phase (grown up to $l_{max} = 400\,\text{nm}$) which is in good agreement to the experiment. The same holds for the wurtzite fraction $\bar{p}_{wz}$ depicted in Fig. 3.25(b). For our model, the calculated fraction of wurtzite lower than observed in the experiment. By accounting for additional nucleation of new nanowires in wurtzite phase at the beginning of growth, a good agreement with the experiment could be achieved.

So far, we were able to reconstruct the time-evolution of the nanowire radius $r_{NW}(l,t)$ during growth of self-catalyzed GaAs nanowires by combining $\Delta r_f(l,t)$ determined by key-features (q^p_{fwhm} and q^p_{max}) from *in-situ* XRD, and $r_{NW}(l,t_f)$ obtained by *ex-situ* SEM. Exploiting information on polytypism, we obtained an estimate for non-catalytic facet growth at the nanowire base radius from the in-plane FWHM of the $(10.3)_{h,wz}$ wurtzite reflection. Together with the radius after growth $r_{NW}(l,t_f)$ obtained by SEM, this allowed us to calculate the radius of the top facet $r_{top}(t)$ during growth, assuming homogeneous facet growth. Having $r_{NW}(l,t)$, we calculated the corresponding in-plane XRD intensity distribution $I(\vec{q},t)$ from which we evaluated

the intensity profiles $I(q,t)$ along facets streaks in analogy to our experiment. We found that the XRD simulation based on the evolution of $r_{NW}(l,t)$ is compatible with the values obtained by our *in-situ* XRD experiment. Therefore, we gained insight in the evolution of the top-facet radius $r_{top}(t)$. This is of particular interest, since $r_{top}(t)$ is in contact with the liquid Ga-droplet which acts as the catalyst for axial nanowire growth. In the following, we will apply a growth model that links the radial growth of $r_{top}(t)$ to the shape of the Ga-droplet. Such an application to our data is only feasible due to the disentanglement of non-catalytic facet growth from tapering caused by the liquid Ga-catalyst.

3.7.3 Models for catalytic radial nanowire growth

In the following, we briefly introduce two but essentially equivalent models for the evolution of the top-facet radius $r_{top}(t)$ in dependence of the growth parameters. At given growth parameters, we will be able to express $r_{top}(t)$ as a function of the growth time t, or equally the nanowire length $l_{max}(t)$ at this time. Most importantly, these growth models allow conclusions on the shape of the liquid Ga-droplet. For further reading, the reader is kindly referred to the publications of Vladimir Dubrovskii [173] (model 1) and Jerry Tersoff [172] (model 2).

Model 1: Self-equilibration of nanowire diameter

According to Ref. [173] the time-dependent radius of an individual GaAs nanowire grown by the self-catalyzed method is given by

$$x = r_0 - r + ln\left(\frac{r_0 - 1}{r - 1}\right) \tag{3.38}$$

with the scaled time $x = t/\tau$, the scaled radius of the nanowire $r = R/R_c$, and the scaled radius $r_0 = R_0/R_c$ at $t = 0$. R and R_0 are the nanowire radii in nm, R_c is the critical nanowire radius towards which the system tries to equilibrate in the time scale defined by the relaxation time τ.

We now solve Eq. 3.38 by the use of the Lambert W-function for $R(t)$:

$$R(t) = R_c \quad W_{\text{Lambert}}\left[\left(e^{(-\frac{t}{\tau}+\frac{R_0}{R_c}-1)}\right)\cdot\left(\frac{R_0}{R_c}-1\right)\right] + R_c \tag{3.39}$$

The fit parameters are defined as

$$A = \frac{\Omega_{Ga}}{\Omega_{GaAs} f(\beta)}\left(\frac{v_a}{\chi\nu}\right); \qquad B = \frac{2\Omega_{Ga}}{\pi\Omega_{GaAs} f(\beta)}\nu\lambda_{Ga}\sin\alpha \tag{3.40}$$

and relate to the relaxation time $\tau = R_c/A$, and the critical diameter $R_c = B/A$.

Further,

$$f(\beta) = \frac{(1-\cos\beta)(2+\cos\beta)}{(1+\cos\beta)\,\sin\beta} \tag{3.41}$$

is a geometrical factor which depends on the contact angle between droplet and top facet β, which in turn is important for $\chi = 1/sin^2\beta$ in our case for $\beta \geq \pi/2 + \alpha$. The angle α is the tilt angle of the molecular beams with respect to the surface and equals $\alpha = 28°$ for our portable MBE.

The remaining variables are identified as $\Omega_{Ga} = 0.02\,\mathrm{nm}^3$ the volume of Ga in liquid and $\Omega_{GaAs} = 0.0452\,\mathrm{nm}^3$ the volume of a GaAs pair in the solid. Besides these values, we find the axial nanowire growth rate $v_a = 15.68\,\mathrm{nm/min} = 0.26\,\mathrm{nm/s}$, the Ga deposition rate $\nu = 0.75\,\mathrm{nm/s}$ and the diffusion length for Ga adatoms λ_{Ga}.

Model 2: The kinetic self-regulation of the nanowire diameter

Within Ref. [172] we find an expression for the radial growth rate of the top facet radius r_{top} as a function of nanowire length

$$\frac{dr_{top}}{dl} = \frac{2\Omega_{Ga}/\Omega_{GaAs}}{\eta_{eq}(3+\eta_{eq}^2)}\left[F_{V/III}^{-1}\left(1+\frac{\lambda_{Ga}}{(1+\eta_{eq}^2)r_{top}}\right)-1\right] \tag{3.42}$$

the only undefined parameters in Eq. 3.42 are V/III ratio $F_{V/III}$ and the equilibrium droplet shape factor η_{eq} that relates the height of the liquid droplet to the radius of the nanowire top-facet via $\eta = h_D/r_{top}$.

The contact angle β can be expressed with the help of the droplet shape η:

$$\beta = 180° - sin^{-1}\left(\frac{2\,\eta}{1+\eta^2}\right) \tag{3.43}$$

The corresponding droplet Volume V_D is given by Eq. 7 in Ref. [172] as

$$V_D = \frac{\pi}{6}\,\eta\cdot(3+\eta^2)\cdot r_{top}^3. \tag{3.44}$$

We employ Eq. 3.42 from Ref.[172] in order to model the evolution of the nanowire top radius due to tapering at a certain growth time t by

$$r_{top}(t) = \int_0^t \frac{dr_{top}(t)}{dt}\cdot dt + r_{NW}(0,0), \tag{3.45}$$

and

$$\frac{dr_{top}(t)}{dt} = \frac{2\Omega_{Ga}/\Omega_{GaAs}}{\eta_{eq}(3+\eta_{eq}^2)}\left[F_{V/III}^{-1}\left(1+\frac{\lambda_{Ga}}{(1+\eta_{eq}^2)r_{top}(t)}\right)-1\right]+m_{facet}, \tag{3.46}$$

which we extend by the radial facet growth rate m_{facet}. Further, $\Omega_{Ga}/\Omega_{GaAs} = 0.42$ [172], where Ω_{Ga} is the volume of Ga in liquid and Ω_{GaAs} is the volume of a GaAs pair in the solid. The diffusion length of Ga-atoms at (110)-type facets is given by λ_{Ga}. $F_{V/III}$ is the V/III ratio, and η_{eq} is the equilibrium droplet shape factor that relates the height of a spherical droplet to the

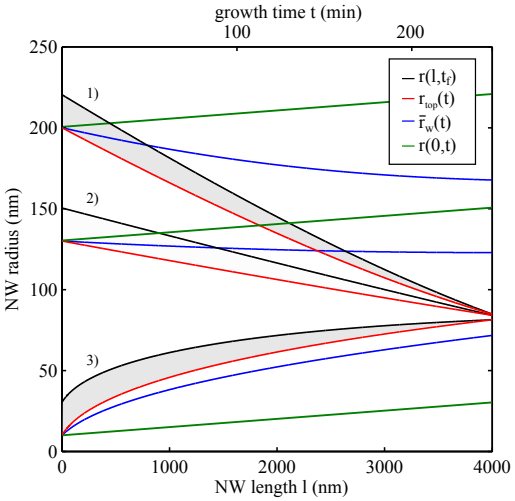

Parameters			
	1)	2)	3)
r(0,0) [nm]	200	130	10
m_{facet} [nm/min]	0.08	0.08	0.08
η_{eq} [ ]	3	2	3
$F_{V/III}$ [ ]	5.5	6	3
λ[µm]	1	1	1

Figure 3.34: Calculated radii according to Eq. 3.46 for various parameters. The solid lines represent the length-dependent nanowire radius after growth $r_{NW}(l, t_f)$ (black) as accessible by *ex-situ* SEM, the weighted mean radius $\bar{r}_w(t)$ for illustration for *in-situ* XRD (blue), and the radius of the top-facet below the droplet $r_{top}(, t)$ during growth (red). Additionally, the radius at the nanowire base $r(0, t)$ is given (green). As example, parameters were chosen that result in similar final radii, and demonstrating 1) tapering and decreasing $\bar{r}_w(t)$, 2) tapering and quasi constant $\bar{r}_w(t)$, and finally 3) inverse tapering and increasing $\bar{r}_w(t)$. The overall contribution of facet growth $\Delta r_f(l, t_f)$ is illustrated by the gray area.

radius of the nanowire top-facet.

Our choice for model 2 is motivated by the possibility of the straightforward integration of the non-catalytic side-wall growth rate m_{facet}. The introduction of m_{facet} in the model for r_{top} is at this point not strictly required, but can also not be excluded. For the following discussion, we assume $m_{facet} > 0$ in Eq. 3.46 smaller than the facet growth rate obtained in the experiment. For small values of $m_{facet} \leq 0.1$ nm/min, the quantitative values will change slightly, however the qualitative behavior of $r_{NW}(l, t)$ and $r_{top}(t)$ will remain the same. For completeness however, we will later compare results for which we consider $m_{facet} = 0$ in Eq. 3.46 and discuss the quantitative differences resulting for the model parameters.

In Fig. 3.34, we show the evolution of the shape of three different nanowires, calculated according to Eqs. 3.30, 3.32, and 3.46 for different growth conditions. Here, we chose an axial growth rate equal to v_a. The equilibrium radius can be defined by a combination of droplet shape η_{eq}, Ga-diffusion length λ and V/III-ratio $F_{V/III}$. Depending on the starting conditions given by the initial radius $r(0, 0)$ the nanowire moves towards this equilibrium value by either reducing or increasing its top-radius $r_{top}(t)$ during growth. This results in (inverse) tapering if the initial radius is (smaller) larger than the equilibrium value. The presence of non-catalytic facet growth changes the nanowire shape successively. For illustration, the radius of the nanowire base $r(0, t)$ during growth is shown. The overall contribution of $\Delta r_f(l, t_f)$, introduced in Eq. 3.32, after

growth is given by the gray area between the curves $r_{NW}(l, t_f)$ and $r_{top}(t)$.

In our discussion so far, we assumed a constant value for the Ga-droplet shape η_{eq} independent of its volume and the top-facet radius $r_{top}(t)$. This requires an easy mechanism for tapering, e.g. if the sidewalls are not oriented along stable surface facets [174, 172]. Then the nanowire radius below the droplet can be readily adjusted in order to maintain η_{eq}. In case of self-catalyzed GaAs nanowires, the side-facets are composed of (110)-type surfaces however. Therefore, the actual droplet shape $\eta(t)$ may differ from its equilibrium value but may change during growth in order to approximate t he equilibrium value η_{eq}. Consequently, tapering is a result of the mismatch between $\eta(t)$ and η_{eq} [172]. However, the exact functional behavior of $\eta(t)$ is unknown.

We employ a Fermi-function in order to model the behavior of $\eta(t)$. This is advantageous, since we can express $\eta(t)$ as function of initial η_i and equilibrium value η_{eq}, whereas the transition between both limits is described by the width f_w of the Fermi-function and the transition time t_0

$$\eta(t) = \eta_i - \frac{\eta_i - \eta_{eq}}{e^{-(t-t_0)/f_w} + 1}. \tag{3.47}$$

We further substitute η_{eq} in Eq. 3.46 by Eq. 3.47.

In order to probe the effect of a non-constant $\eta(t)$, we investigate the shape-evolution of a nanowire for different starting values η_i but otherwise identical growth parameters illustrated in Fig. 3.35. We hereby limit the investigation to values of $\eta > 1 (\beta > 90°)$, and $\eta_i > \eta_{eq}$ in order to obtain cases $dr_{NW}(l, t_f)/dl \geq 0$ as compatible with our experiment. Further, we set $t_0 = 0$. It appears, that the nanowire tapers easily for smaller values of $\eta(t)$, whereas tapering is reduced for large $\eta(t)$ (see cases 1 and 4 in Fig. 3.35(b)).

3.7.4 Comparison of model and experiment: the evolution of droplet shape $\eta(t)$ during growth of self-catalyzed GaAs nanowires, and the Ga-diffusion length λ_{Ga}

Since we have a model for the calculation of the evolution of the nanowire radius $r_{NW}(l, t)$ depending mainly on the growth parameters, we can now search for a set of parameters which describe simultaneously our experimental *in-situ* XRD results, as well as the *ex-situ* SEM data. Therefore, a sampling of the parameter space given by λ, $r(0, 0)$, m_{facet}, $F_{V/III}$, and η_i, η_{eq}, t_0 and f_w is required. From our growth calibrations, we obtain the value for $F_{V/III} = 2.6$. Also values for $r(0, 0) = 11.1\,\text{nm}$, and $m_{facet} = 0.095\,\text{nm/min}$ are known from the X-ray experiment. From SEM we obtain $\beta_{SEM} = 135° \pm 2°$ which allows us to limit a probable range of $\eta_{eq} \in \{2.00, 4.3\}$ with a certain safety margin to higher values. The remaining parameter space is bounded by $\lambda \in \{550, 4500\}$, $\eta_i \in \{2.45, 11.5\}$, $f_w \in \{6, 65\}$ and $t_0 \in \{0, 65\}$. In total 477360 sets of parameters were evaluated, and the resulting $\bar{r}_w(t)$, and $r(l, t_f)$ were compared to the results from the X-ray experiment, and SEM respectively.

We find solutions, which describe the radii as well as the value for the wetting angle β_{SEM}

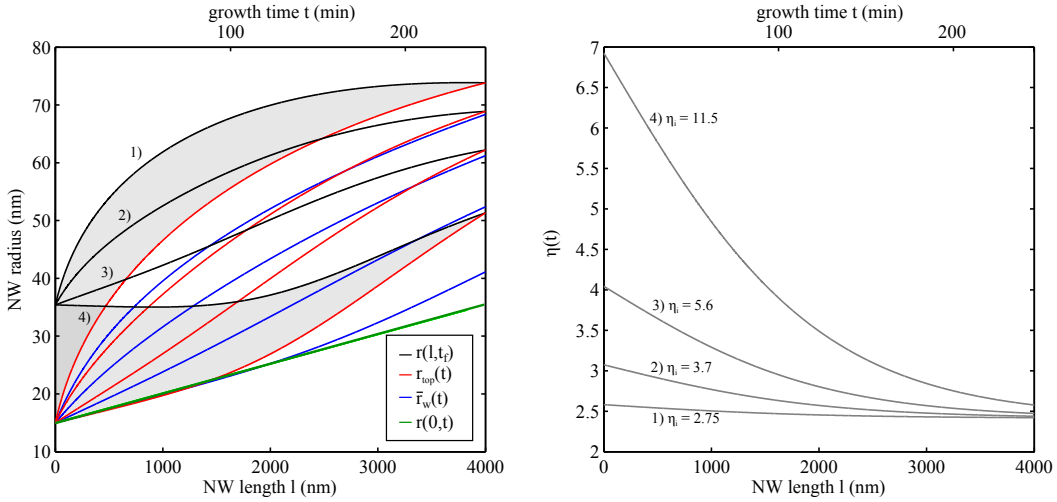

(a) Calculated radii $r(l,t_f)$ (black), $\bar{r}_w(t)$ (blue), $r_{top}(t)$ (red), and $r(0,t)$ (green) for four different $\eta(t)$. For the cases 1) and 4), the overall contribution of facet growth is illustrated by the gray area.

(b) Four different courses of $\eta(t)$ calculated by Eq. 3.47 using $\eta_{eq} = 2.4$ equivalent to $\beta_{eq} = 135°$ and four different starting values η_i given in the figure.

Figure 3.35: Effect of different $\eta(t)$ on the shape-evolution of a nanowire. Only cases with $\eta_i > \eta_{eq}$ are considered here. Thereby we limit the investigation to cases $dr(l,t_f)/dl \geq 0$. The parameters used for this calculation are $\lambda = 1\,\mu m$, $r(0,0) = 15\,nm$, $m_{facet} = 0.08\,nm/min$, $F_{V/III} = 3$,$t_0 = 0\,min$, and $f_w = 65\,min$.

very well. The corresponding parameters of one example are given in the caption of Fig. 3.36(a), the respective course of $\eta(t)$ is shown in Fig. 3.36(b). The measured radii by SEM given by the grey circles and the calculated values $r_{NW}(l,t_f)$ show a good agreement. Also, the radii obtained by our *in-situ* X-ray experiment $\bar{r}_w^{ZB}$ and $\bar{r}_w^{WZ}$ are well reproduced by the calculated values for the weighted mean radius $\bar{r}_w(t)$ and the radius at the nanowire base $r(0,t)$. In addition, the final value $\eta(t_f) = 2.46$ which results in a wetting angle $\beta(t_f) \approx 135.0°$ is compatible with the measured wetting angle by SEM $\beta_{SEM} \approx 135° \pm 2°$ as observed after growth.

Further, we show the time-dependent values for the droplet volume $V_D(t)$ in Fig. 3.36(b). The droplet volume increases during the growth as a consequence of excessive Ga-influx.

Regarding the parameters used for the solutions presented in Fig. 3.36, we state that these parameters are not the only set of parameters within the sampled parameter space that result in a very good agreement with the radial evolution obtained from the experiment. Another result for such an alternative set of parameters is given by the dotted lines in Fig. 3.36. This calculation was achieved for the parameters $\lambda = 3.7\,\mu m$, $r(0,0) = 11.1\,nm$, $m_{facet} = 0.095\,nm/min$, $F_{V/III} = 2.6$, and $\eta_i = 10.4$, $\eta_{eq} = 4.3$ and $f_w = 44.6\,min$ (compare dotted lines in Fig. 3.37(a)). Regarding only the experimental results for the radii depicted in Fig. 3.36(a), both parameter sets are able to describe the data with similar values for least σ^2 (sum of squared residuals). It might even be possible, that the calculated curves for the radii become identical, by using a smaller sampling

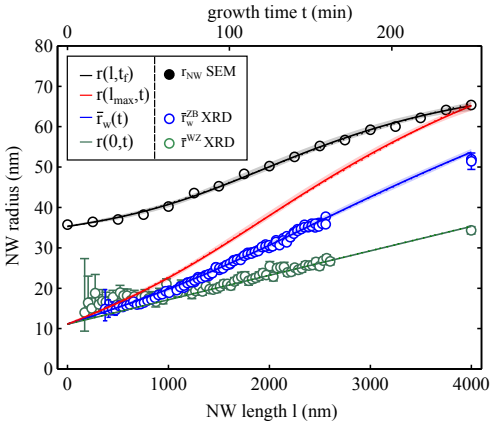

(a) Solid lines: calculated nanowire radius at the end of growth $r_{NW}(l, t_f)$ (black), the weighted mean radius $\bar{r}_w(t)$ (blue), the top facet radius $r_{top}(, t)$ (red), and the base radius $r(0, t)$ (green) obtained for $\lambda = 0.85\,\mu m$, $r(0, 0) = 11.1\,nm$, $m_{facet} = 0.095\,nm/min$, $F_{V/III} = 2.6$, and $\eta_i = 7.6$, $\eta_{eq} = 2.4$ and $f_w = 65\,min$ in best agreement with the experimental data (given by the circle symbols). Dotted lines: alternative, but almost identical solution for $\lambda = 4.0\,\mu m$. The corresponding values for $\eta(t)$ for both solutions differ and are given in Fig. 3.36(b).

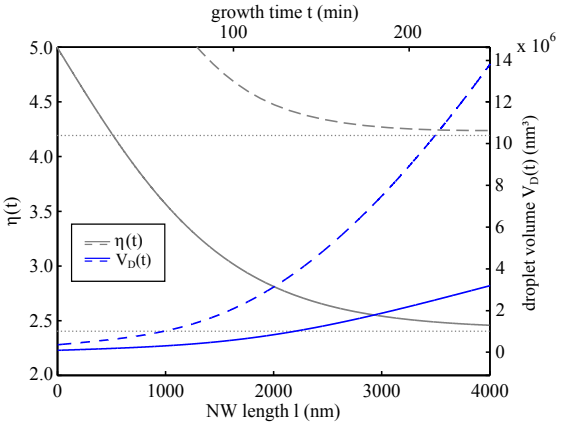

(b) Droplet shape $\eta(t)$ calculated by Eq. 3.47 with $\eta_i = 7.6$, $\eta_{eq} = 2.4$ and $f_w = 51.0\,min$corresponding to the calculated radii displayed as solid lines in Fig. 3.36(a). Broken line: $\eta(t)$ obtained for $\eta_i = 10.4$, $\eta_{eq} = 4.3$ and $f_w = 38.3\,min$ corresponding to the alternative solution shown in Fig. 3.36(a). The horizontal dotted lines represent the respective η_{eq} values. The corresponding droplet volume $V_D(t)$, calculated according to Eq. 3.44 is given as well.

Figure 3.36: Comparison of calculation according to the model and the *in-situ* experiment.

of the parameters around these two solutions. This ambiguity is inherent in the used growth model for $r_{top}(t)$ as long as at least two parameters are unknown, since variations in η, λ and $F_{V/III}$ may compensate each other. Therefore, it is possible to obtain similar $r_{top}(t)$ for different sets of parameters, if these parameters are not bounded or fixed by experimental constraints or measurements. Consequently, we have to include additional constraints e.g. provided by the droplet shape after growth $\eta(t_f)$. In our case, the alternative parameter set requires large $\eta(t)$, e.g. $\eta(t_f) = 4.3$ which equals a wetting angle of $\beta = 154.0°$. From SEM however, we can safely exclude this solution by employing experimental constraints on $\eta(t_f)$ obtained by SEM.

By a close investigation of the parameter space however, we find that a solution is not only possible for the two cases above. In fact, many sets of parameters are able to describe the experimental data (the radii obtained by SEM as well as by XRD, given in Fig. 3.36(a)) to a similar degree. For illustration, the sum of least squares $\sigma^2(\lambda, \eta_{eq})$ in the range $\sigma^2(\lambda, \eta_{eq}) \leq 4\ \sigma^2_{min}$ are shown in Fig. 3.37(a). We observe, that the solutions resulting in similar minimal $\sigma^2_{min}(\lambda, \eta_{eq})$ are located in a conjoined minimum which spreads across the sampled parameter space. The values of $\sigma^2_{min}(\lambda, \eta_{eq})$ are given in the inset. No distinguished solution can be found, since the values are of same magnitude. Therefore, additional input is required, such as the knowledge of either λ, or η_{eq}. Selecting for instance, $\beta_{SEM} = 135°$, we obtain the profiles $\sigma^2(\lambda)$ and $\sigma^2(\beta_{eq})$ along the dotted red and blue line respectively. These profiles are given in

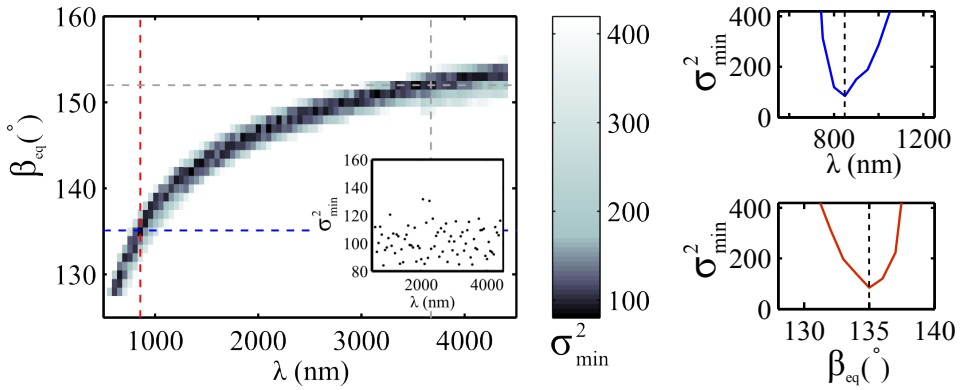

(a) Values for $\sigma^2_{min}(\lambda, \beta_{eq})$. The inset shows the minimal values $\sigma^2_{min}(\lambda)$ as function of λ.

(b) Cuts at fixed λ, and β_{eq}) positions.

Figure 3.37: The calculations describing the experimental values $r_{NW}(l,t)$ best are located in the black area shown in Fig. 3.37(a). Each pixel corresponds to one set of λ and β_{eq}. Fig. 3.37(b) shows cuts at the positions marked by the red and blue broken lines.

Fig. 3.37(b). $\sigma^2(\lambda)$ shows a parabolic behavior close to the minimum value for $\lambda_{min} = 850\,\text{nm}$. Therefore, knowledge of $\beta_{eq} = 135°$ is required for a unambiguous assignment of the diffusion length λ. Without such constraints, this solution can not be distinguished from other ambiguous combinations of λ and β_{eq}, e.g. $\lambda = 3.7\,\mu\text{m}$ and $\beta_{eq} = 154°$ as indicated by the dotted gray lines, from a comparison to the experimental radii alone.

In order to provide an overview of the parameter space, we give the solution space that contains the respective parameters allocated to the best calculations with least $\sigma^2_{min}(\lambda)$ in Fig. 3.38. For a given λ, the remaining parameters can be selected from the plots. All displayed set of parameters correspond to solutions with $\sigma^2 \leq 2\,\sigma^2_{min}$ and therefore describe the experimental radii very well. In a next step, we empirically fitted the parameters $\eta_i(\lambda)$, $\eta_{eq}(\lambda)$, $f_w(\lambda)$ and $t_0(\lambda)$. These fits are given by the red solid line respectively. Whereas $\eta_i(\lambda)$, $\eta_{eq}(\lambda)$ and $f_w(\lambda)$ can sufficiently be described by a power law, we describe $t_0(\lambda)$ by a linear function. Then, we calculate the radii for $\lambda \in \{550, 4500\}$ increasing by 10 nm steps and the corresponding remaining parameters which are defined by the empirical fits. The employed empirical fits for the model parameters are given in the table in Fig. 3.38. Then we use these fits in order to calculate $r_{top}(t)$, $\bar{r}_w(l)$ and $r_{NW}(l,t)$ for varying λ. The so calculated radii are contained within in the colored envelope shown in Fig. 3.36(a), with having $\sigma^2 \leq 3\,\sigma^2_{min}$, and therefore match the experimental radii very well. Further, this demonstrates the ambiguity inherent to the model in our case with unknown λ and $\eta(t)$.

As stated before, for each value of λ, we find a set of parameters that allows a description of the radii obtained by the XRD and SEM experiment. Further, each λ requires a certain trajectory of $\eta(t)$ as modeled by Eq. 3.47. Since the parameters used in Eq. 3.47 give only bounds for the actual values of $\eta(t)$, we investigated $\eta(t)$ for various values of λ shown in Fig. 3.39(a). For

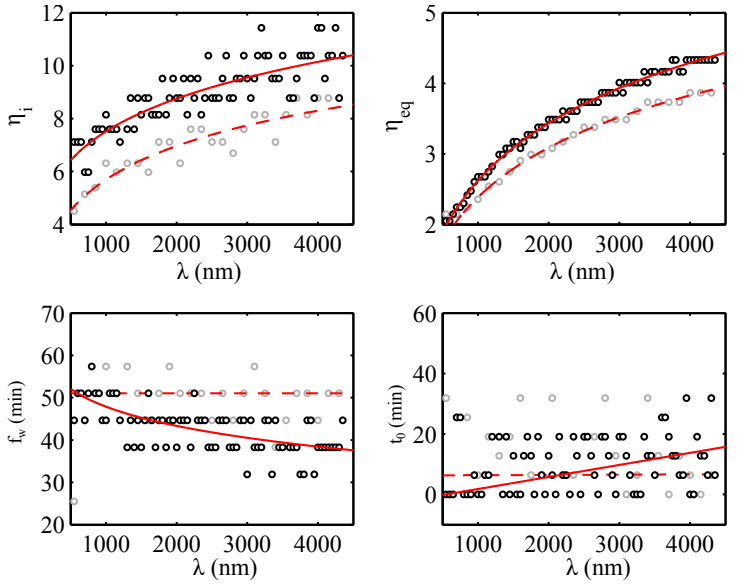

$f(\lambda) = a\lambda^b + c$			
	$\eta_i(\lambda)$	$\eta_{eq}(\lambda)$	$f_w(\lambda)$
a	-78.0	-1564.0	-420.3
b	-0.261	-0.582	0.110
c	177.7	166.3	1650.0

$f(x) = a\lambda + b$	
	$t_0(\lambda)$
a	0.0625
b	-34.37

Figure 3.38: Parameter values for the calculations with minimal $\sigma^2_{min}(\lambda)$. For the black circles, $m_{facet} = 0.95\,\mathrm{nm/min}$ in Eq. 3.46. In gray, m_{facet} was set to zero. The red lines represent fits to the parameters as function of λ. The fit parameters for $m_{facet} = 0.95\,\mathrm{nm/min}$ are given in the table at the right.

illustration $\eta(t)|_{\lambda=850\,\mathrm{nm}}$ resulting in $\eta(t_f) = 2.46$ is highlighted by the white solid line. This figure nicely demonstrates, that an increasing λ is compensated by an overall increase in $\eta(t)$ in order to result in radii able to describe our experimental results in Fig. 3.36(a). Further it can generally be observed that at fixed λ, $\eta(t)$ decreases with increasing t, implying a reduction of the wetting angle during the growth. Moreover, from this figure, we observe that the ambiguity between λ and η vanishes, if e.g. $\eta(t_f)$ is known since for each value $\eta(t_f)$ it exists a unique λ. Further, the parametrization via λ allows an investigation of the effect of the value of m_{facet} in Eq. 3.46. As we set $m_{facet} = 0$, we still are able to obtain a match for the experiment, but we observe a shift in the corresponding model parameters. For illustration the set of parameters for $m_{facet} = 0$ with minimal least σ^2 are given in Fig. 3.38 as gray circles. Still the qualitative behavior remains similar to the case before, however η_i and η_{eq} shift to lower values at same value of λ. Alternatively, if $m_{facet} = 0$ for the same values η a higher λ is needed to achieve the required radial growth rate, and compensate for m_{facet}. The same observation can be made for $\eta(t)$ in Fig. 3.39(a). Here $\eta(t)$ calculated for $m_{facet} = 0$ is given by the gray frame. Still, the qualitative behavior of $\eta(t)$ remains the same, only the values are collectively shifted.

By SEM, we can determine the wetting angle β of the liquid Ga droplet with the nanowire top-facet after growth. This value has been given before with $\beta_{SEM} = 135° \pm 2°$, or respectively $\eta_{SEM} = 2.42 \pm 0.12$. This value has been obtained after growth, and at room temperature. So far it is not clear whether the difference between growth and room temperature affects the wetting angle. However, an exposure to As atmosphere at growth temperature after shutting

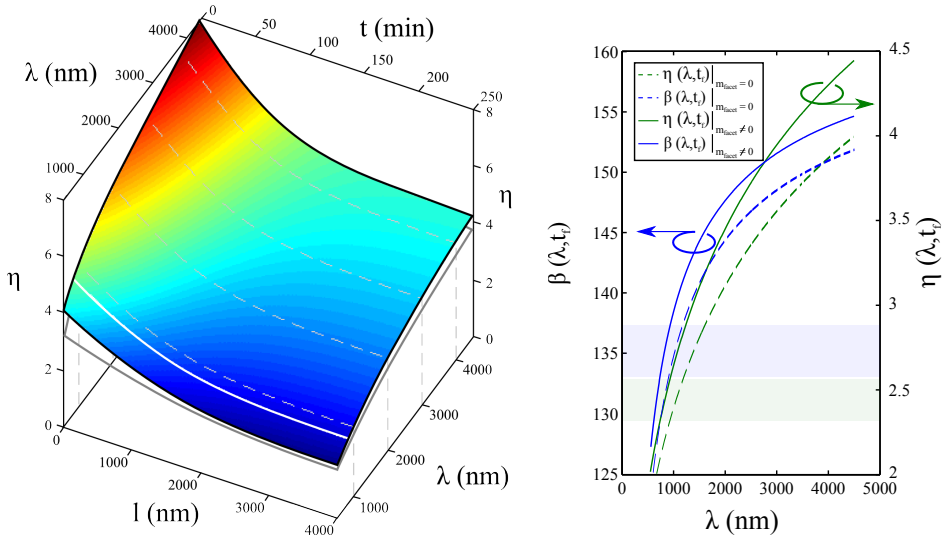

(a) Illustration of the droplet shape $\eta(\lambda, t)$ (illustrated by colorscale) in dependence of growth time t (or corresponding nanowire height $l_{max}(t)$) and Ga diffusion-length λ, calculated by Eq. 3.47.

(b) Wetting angle $\beta(\lambda, t_f)$ calculated from the droplet shape $\eta(\lambda, t_f)$ by Eq. 3.43. The dashed curves correspond to solutions obtained for setting $m_{facet} = 0$ in Eq. 3.46.

Figure 3.39: In Fig. 3.39(a) the time-evolution of $\eta(t)$ for various values of λ is shown. For the depicted trajectories $\eta(t)$ and respective value of λ, model 2 yields results for $r_{NW}(l, t)$ that are consistent with the experiment. Fig. 3.39(b) displays the wetting angle $\beta(\lambda, t_f)$ and droplet shape $\eta(\lambda, t_f)$ at end of growth as function of λ. Shaded area depicts the range for measured values of β_{SEM} and η_{SEM}.

down the Ga-flux was found to consume the droplet which was accompanied by a reduction of the wetting angle [83]. In our case, an As-atmosphere is still present in the growth chamber even after closing the shutters. However in our case, the sample is cooled down rapidly after growth. Therefore, a change of the wetting angle due to droplet-consumption or Ga-desorption is expected to be small. In order to estimate the maximum change of the droplet wetting angle β during cooldown, we employ the findings for 80 nm thick self-catalyzed GaAs nanowires of Rieger et al.[83]. Accounting for a consumption time at growth temperature of 2 min we obtained a reduction $\delta\beta = -2°$. Therefore, the potential reduction of β as a consequence of cooldown would not be larger than the error range from the SEM measurement. In Fig. 3.39(b) the values $\beta(\lambda, t_f)$ and $\eta(\lambda, t_f)$ resulting from our calculations are displayed. The broken lines correspond to the case $m_{facet} = 0$ in Eq. 3.46. With the limits for β_{SEM}, we obtain a for the Ga diffusion length $\lambda = 820^{+90}_{-120}$ nm (for the case $m_{facet} = 0$, we obtain $\lambda = 1010^{+140}_{-110}$ nm. Please note that always $m_{facet} = 0.095\,\mathrm{nm/min}$ in Δr_f in Eq. 3.32). Moreover, from our investigation alone, there is no indication so far, whether the side wall growth rate m_{facet} has to be included in Eq. 3.46 or not. Therefore, we give both values for the diffusion length separately. Compared to literature, Dubrovskii et al. [145] obtained similar values $\lambda = 750\,\mathrm{nm}$ applying model 1 to *ex-situ*

SEM data obtained from site-selective grown self-catalyzed GaAs nanowires. This value is close to ours, and the difference may be caused by different growth parameters used and the mean distance of neighboring nanowires. In contrast to that, our values are lower than Ga diffusion lengths $\lambda > 2$ μm on GaAs (110)-facets reported e.g. by Lopez et al.[50]. Such high values for λ would, in our case, require large $\eta(t_f)$ which are incompatible with our observations. This implies that either the diffusion length on Ga adatoms at nanowire (110)-type side-walls may be different as compared to extended plain GaAs(110) surfaces, or the growth conditions are not directly comparable to 2D layer growth. This may be caused by As re-evaporation effects in the case of nanowire growth [52, 124] or a lower effective Ga-diffusion length, reduced by the number density and mean distance of neigboring nanowires [145].

In conclusion, we investigated the growth of self-catalyzed inversely tapered GaAs nanowires on Si(111) using *in-situ* time-resolved X-ray diffraction and *ex-situ* SEM. By evaluation of the integrated intensity of polytype-sensitive Bragg reflections, we found indications that the nanowire base consists mainly of wurtzite, whereas the remaining nanowire consists of zinc-blende and its twin.

By investigating the in-plane key features FWHM q^p_{fwhm}, and the position of the first-order maximum q^p_{max} of the polytype sensitive $(10.3)_{h,wz}$, and $(220)_c$ reflections, we could infer information on the radial growth of the wurtzite nanowire base and the remaining nanowire separately. We found evidence for non-catalytic facet growth and could determine the radial growth rate m_{facet}.

In combination with SEM, we were able to conclude on the radial evolution of the nanowire radius $r_{NW}(l,t)$ during growth. Further, we simulated the in-plane X-ray scattering resulting from the so determined evolution of $r_{NW}(l,t)$, evaluated the key-features from the simulation and found good agreement to the experiment.

Applying a growth model for the evolution of the top-facet radius $r_{top}(t)$ of self-catalyzed GaAs nanowires we inferred values for the Ga diffusion length λ at (110)-type GaAs nanowire side walls. Further from this model, we obtain information on properties of the liquid Ga catalyst droplet at the nanowire tip during growth. These properties are droplet volume $V_D(t)$ and droplet shape $\eta(t)$, which are important factors of nanowire growth e.g. for the evolution of polytypism.

Therefore, combined *in-situ* and *ex-situ* growth experiments as presented here have a great potential for advancing the understanding of growth processes for further improvement of growth theories and modeling. Especially *in-situ* XRD can provide time-resolved information on microstructure and shape of the growing nanostructures.

For future experiments, tailoring the Ga droplets prior to growth will give the opportunity to study radial growth processes from varying starting points (i.e. above or below the equilibrium radius). Further, the presented methods are not limited to GaAs nanowires but are also applicable to nanowires grown in other material systems. Especially the role of the catalyst particle material could be investigated e.g. during the growth of Au-seeded GaAs nanowires.

3.8 Summary: X-ray studies of self-catalyzed GaAs nanowires

In this chapter we presented results of *ex-situ* and time-resolved *in-situ* X-ray experiments.

Employing an *ex-situ* nano-focus setup we were able to separate the contributions of parasitic growth and nanowires to the scattering signal of the $(111)_c$ Bragg reflection of GaAs and evaluated the ratio $(d_{wz} - d_{zb})/d_{zb} = 0.66\% \pm 0.02\%$ of the vertical spacing of wurtzite and zinc-blende layers *in the nanowires*.

In-situ X-ray experiments in symmetric geometry revealed the evolution of polytypism in a growing ensemble of GaAs nanowires. Employing a Markov model for the stacking sequences along $[111]_c$ direction, we calculated the experimental time-resolved Q_z intensity profiles and extracted the time-dependent transition probabilities $p_{zb\to wz}$ and $p_{wz\to zb}$. Further, we estimated the resulting differences in the layer-dependent nucleation barriers $\delta E_{p\to\bar{p}}(n)$ for switching between the different polytypes.

We demonstrated the separation of the contributions originating from parasitic GaAs growth and GaAs nanowires in the scattering signal asymmetric Bragg reflections *ex-situ*. We proved, that the crystallites consist of zinc-blende and twinned zinc-blende GaAs.

We proposed a robust *in-situ* compatible method for structural characterization of GaAs nanowires, by combining X-ray measurements of the $(111)_c$ reflection with measurements of the phase sensitive $(311)_c$, $(10.3)_{h,wz}$ and the $(220)_c$ reflections. We therefore compare results from the Markov model for Q_z intensity profiles of the $(111)_c$ Bragg reflection to results obtained by evaluation of the integrated intensities of $(311)_c$, $(10.3)_{h,wz}$ and the $(220)_c$ reflections.

By time-resolved *in-situ* X-ray experiments in asymmetric geometry, we obtained information on the evolution of polytypism in the nanowires i.e. phase fraction and segment length without requiring a model for the stacking sequences. We observed a switch in the crystal structure from wurtzite to zinc-blende at the beginning of growth which we relate to a change in the wetting conditions of the liquid Ga-droplet. Therefore, until the end of growth the nanowires consist mainly of zinc-blende, except the bottom part. During cooldown, after closing the shutters, we found evidence for the nucleation of highly faulted zinc-blende and wurtzite.

The evolution of the nanowire shape could be monitored during growth as well. Therefore the change of the intensity distribution along facet-streaks in the $(220)_c$ and $(10.3)_{h,wz}$ reflections originating from the (110)-type side-facets of twinned-zincblende and wurtzite segments in the nanowires were evaluated. Our results indicate that in our case radial growth is constituted by catalytic and non-catalytic processes responsible for tapering and side-wall growth. We were able to disentangle these contributions. Employing and expanding a theoretical model for radial nanowire growth at our growth conditions, we inferred values for the Ga-diffusion length, and obtained unique information on the evolution of the liquid Ga-droplet during growth, i.e. its wetting angle and its volume.

4 Conclusion & Outlook

In this work, we developed a methodical framework for the systematic application of time-resolved *in-situ* X-ray scattering methods for the structural characterization of semiconductor nanowires during MBE growth. This included the implementation of time-resolved X-ray scattering methods in symmetric and asymmetric non-coplanar geometry for the monitoring of the growth of self-catalyzed GaAs nanowires by MBE, and the developement of analysis strategies in order to characterize the structural properties of the nanowires and their evolution during growth. The time-resolved structural characterization of growing nanowire ensembles, enabled by this framework, provided valuable insights into dynamical processes taking place during the growth of self-catalyzed GaAs nanowires.

As preparation for the targeted *in-situ* investigations, the MBE growth of self-catalyzed GaAs nanowires under controlled conditions was realized in a specialized and portable MBE system. This system has been calibrated and the growth conditions have been optimized for the self-catalyzed growth of GaAs nanowires on Si(111) substrates. Further, the influence of substrate preparation, material fluxes, substrate temperature and growth time on the properties of the nanowires were investigated by *ex-situ* scanning electron microscopy and *in-situ* reflection-high-energy-electron-diffraction, and compared to predictions and findings from literature. As a result of these studies, an optimized parameter window for the portable MBE system with respect to *in-situ* X-ray scattering experiments was found which is characterized by high yield of vertical nanowires at minimal parasitic growth. In our particular case, substrate temperatures in the range of $570\,^{\circ}\mathrm{C} \leq T_S \leq 590\,^{\circ}\mathrm{C}$, low Ga-flux and high V/III ratios of 5 were found to be beneficial for the growth of self-catalyzed GaAs nanowires on Si(111) substrates covered by native oxide.

Using highly focused X-ray radiation provided by synchrotron radiation facilities, scattering from individual self-catalyzed GaAs nanowires as well as individual parasitic GaAs islands could be resolved. Thereby, a separation of the contributions from parasitic islands and GaAs nanowires in ensemble X-ray diffraction measurements became possible. Moreover, the ratio $(d_{wz} - d_{zb})/d_{zb}$ of the vertical spacing of wurtzite and zinc-blende layers *in the nanowires* could be evaluated.

Enabled by the results above, *in-situ* investigations of the growth of self-catalyzed GaAs nanowires were performed at the synchrotron radiation facilities ANKA and PETRA III. By time-resolved X-ray diffraction, and averaging over large ensembles of nanowires during MBE

growth, insight into the evolution of polytypism on a statistical level, and valuable information on the dynamics of the structural evolution of the nanowires could be obtained. Employing a Markov model for the stacking sequences along $[111]_c$ direction, the experimental time-resolved Q_z-intensity profiles could be calculated and the time-dependent transition probabilities $p_{zb\to wz}$ and $p_{wz\to zb}$ could be extracted. This way, the evolution of the wurtzite fraction $\bar{p}_{wz}$ and the mean polytype segment length L_p during growth could be determined. Whereas zinc-blende and wurtzite segments have been found to be of comparable length at early times of growth $L_p \approx$ 80 layers ≈ 260 Å, the average length of zinc-blende segments increases to $L_{zb} \approx 200$ layers $\approx$ 650 Å after 60 minutes of growth in our particular case. Further, the resulting differences in the layer-dependent nucleation barriers $\delta E_{p\to\bar{p}}(n)$ for switching between the different polytypes could be estimated. Exemplary, we found $\delta E_{zb\to wz} = 380\,\text{meV}$ for $p_{zb\to wz} = 0.60\%$ and $\delta E_{wz\to zb} = 298\,\text{meV}$ for $p_{wz\to zb} = 1.80\%$ at the end of growth.

Also, a robust *in-situ* compatible method for structural characterization of GaAs nanowires was proposed. It could be shown, that by combining X-ray measurements of the $(111)_c$ reflection in symmetric geometry, and subsequent modeling using the Markov approach, with measurements of the phase sensitive $(311)_c$, $(10.3)_{h,wz}$ and the $(220)_c$ reflections in a special asymmetric non-coplanar geometry with fixed incidence angle, consistent results on the structural properties of the nanowires could be obtained.

Moreover, the great value of time-resolved *in-situ* X-ray scattering experiments in combination with complementary *ex-situ* scanning electron microscopy has been demonstrated. From the integral intensity of phase sensitive reflections, the evolution of polytypism (i.e. the mean fraction of wurtzite $\bar{p}_{wz}$ and the mean polytype correlation length μ^p) during growth could be determined without requiring a model for the stacking sequences. Simultaneously, the evolution of the nanowire shape could be inferred from scattering features related to the (110)-type side-facets of twinned-zincblende and wurtzite segments in the nanowires. In combination with *ex-situ* scanning electron microscopy characterization, the two major radial growth processes, namely side-wall growth Δr_f and tapering Δr_t due to catalytic growth could be disentangled. Employing and expanding a theoretical model for radial nanowire growth at our growth conditions, values for the Ga-diffusion length $\lambda = 820^{+90}_{-120}$ nm were found, and information on the evolution of the shape η of liquid Ga-droplet during growth was obtained, i.e. its wetting angle β with the nanowire top-facet and its volume. In our case of inversely tapered GaAs nanowires, the droplet volume V_D increased from $V_D(0) \approx 1.0 \times 10^5\,\text{nm}^3$ to $V_D(t_f) \approx 3.2 \times 10^6\,\text{nm}^3$. Simultaneously, the droplet wetting angle was found to decrease from $\beta(0) = 157\,^\circ$ to $\beta(t_f) = 136\,^\circ$.

For future investigations, an upgrade of the growth equipment will improve both X-ray capabilities and control of the growth conditions. First, a UHV chamber with large Be-windows will increase the accessible angular range for XRD experiments to $\pm 23^\circ$ allowing to access a greater number of Bragg reflections e.g. the GaAs $(333)_c$ reflection. This will be beneficial for the structural characterization of nanowires with low phase purities.

Second, an As valved cracker cell will provide direct control over the As flux, and allow for

rapid changes of the V/III ratio. This will be of great importance for studying the growth of e.g. droplet-engineered GaAs nanowires. Moreover, the dynamic response of the GaAs nanowires (including changes of the Ga-droplet volume, radial growth rate and polytypism) to changes in the provided growth parameters can then by studied in detail.

Further, a combination of *in-situ* RHEED with *in-situ* X-ray diffraction may allow correlation of information on the evolution of polytypism obtained by surface sensitive diffraction at grazing conditions (RHEED) during simultaneous X-ray diffraction in non-grazing conditions.

Especially for the investigation of the early nucleation phase of GaAs nanowires, such combination will be highly beneficial and allow new insights into the nucleation process.

By introducing Indium as third growth species, structural characterization of the growth of InGaAs/GaAs core-shell nanowire heterostructures can be conducted. In particular, the capabilities of the nanowires for strain relaxation along the (110)-type side-walls can be probed by *in-situ* X-ray diffraction during growth and may shed light into the strain relaxation mechanism available for nanostructures with such high surface to volume ratio.

Finally, for taking advantage of highly focused X-ray radiation in time-resolved *in-situ* studies, the growth of nanowires on pre-defined nucleation sites has to be implemented and suitable focusing setup for X-ray radiation compatible with the growth equipment has to be designed. Such combination will allow for time-resolved *in-situ* X-ray diffraction on the level of few or even a single nanowire.

Bibliography

[1] O. Hayden, R. Agarwal, and W. Lu, "Semiconductor nanowire devices," *Nano Today*, vol. 3, pp. 12–22, Oct. 2008.

[2] K. Tomioka, T. Tanaka, S. Hara, K. Hiruma, and T. Fukui, "III-V nanowires on Si substrate: Selective-area growth and device applications," *IEEE Journal of Selected Topics in Quantum Electronics*, vol. 17, pp. 1112–1129, July 2011.

[3] S. Zhao, S. Y. Woo, M. Bugnet, X. Liu, J. Kang, G. A. Botton, and Z. Mi, "Three-dimensional quantum confinement of charge carriers in self-organized AlGaN nanowires: A viable route to electrically injected deep ultraviolet lasers," *Nano Letters*, vol. 15, no. 12, pp. 7801–7807, 2015.

[4] P. E. Landreman and M. L. Brongersma, "Deep-subwavelength semiconductor nanowire surface plasmon polariton couplers," *Nano Letters*, vol. 14, no. 2, pp. 429–434, 2014.

[5] T. P. H. Sidiropoulos, R. Roder, S. Geburt, O. Hess, S. A. Maier, C. Ronning, and R. F. Oulton, "Ultrafast plasmonic nanowire lasers near the surface plasmon frequency," *Nature Physics*, vol. 10, no. 11, pp. 870–876, 2014.

[6] A. I. Hochbaum, R. Chen, R. D. Delgado, W. Liang, E. C. Garnett, M. Najarian, A. Majumdar, and P. Yang, "Enhanced thermoelectric performance of rough silicon nanowires," *Nature*, vol. 451, pp. 163–167, Jan. 2008.

[7] K. L. Kavanagh, "Misfit dislocations in nanowire heterostructures," *Semiconductor Science and Technology*, vol. 25, p. 024006, Feb. 2010.

[8] H. J. Joyce, J. Wong-Leung, Q. Gao, H. H. Tan, and C. Jagadish, "Phase perfection in zinc blende and wurtzite III–V nanowires using basic growth parameters," *Nano Letters*, vol. 10, pp. 908–915, Mar. 2010.

[9] J. K. Hyun, S. Zhang, and L. J. Lauhon, "Nanowire heterostructures," *Annual Review of Materials Research*, vol. 43, no. 1, pp. 451–479, 2013.

[10] J. Xiang, W. Lu, Y. Hu, Y. Wu, H. Yan, and C. M. Lieber, "Ge/Si nanowire heterostructures as high-performance field-effect transistors," *Nature*, vol. 441, pp. 489–493, May 2006.

[11] K. Tomioka, M. Yoshimura, and T. Fukui, "A III–V nanowire channel on silicon for high-performance vertical transistors," *Nature*, vol. 488, pp. 189–192, Aug. 2012.

[12] B. Tian, X. Zheng, T. J. Kempa, Y. Fang, N. Yu, G. Yu, J. Huang, and C. M. Lieber, "Coaxial silicon nanowires as solar cells and nanoelectronic power sources," *Nature*, vol. 449, pp. 885–889, Oct. 2007.

[13] V. K. Narasimhan and Y. Cui, "Nanostructures for photon management in solar cells," *Nanophotonics*, vol. 2, no. 3, pp. 187–210, 2013.

[14] E. Dimakis, U. Jahn, M. Ramsteiner, A. Tahraoui, J. Grandal, X. Kong, O. Marquardt, A. Trampert, H. Riechert, and L. Geelhaar, "Coaxial multishell (In,Ga)As/GaAs nanowires for near-infrared emission on Si substrates," *Nano Letters*, vol. 14, no. 5, pp. 2604–2609, 2014.

[15] X. Duan, Y. Huang, R. Agarwal, and C. M. Lieber, "Single-nanowire electrically driven lasers," *Nature*, vol. 421, pp. 241–245, Jan. 2003.

[16] D. Saxena, S. Mokkapati, P. Parkinson, N. Jiang, Q. Gao, H. H. Tan, and C. Jagadish, "Optically pumped room-temperature GaAs nanowire lasers," *Nature Photonics*, vol. 7, pp. 963–968, Dec. 2013.

[17] J. B. Wright, S. Liu, G. T. Wang, Q. Li, A. Benz, D. D. Koleske, P. Lu, H. Xu, L. Lester, T. S. Luk, I. Brener, and G. Subramania, "Multi-colour nanowire photonic crystal laser pixels," *Scientific Reports*, vol. 3, Oct. 2013.

[18] K. H. Li, X. Liu, Q. Wang, S. Zhao, and Z. Mi, "Ultralow-threshold electrically injected AlGaN nanowire ultraviolet lasers on Si operating at low temperature," *Nature Nanotechnology*, vol. 10, pp. 140–144, Feb. 2015.

[19] C. Couteau, A. Larrue, C. Wilhelm, and C. Soci, "Nanowire lasers," *Nanophotonics*, vol. 4, pp. 90–107, 2015.

[20] Y. Cui, Q. Wei, H. Park, and C. M. Lieber, "Nanowire nanosensors for highly sensitive and selective detection of biological and chemical species," *Science*, vol. 293, pp. 1289–1292, Aug. 2001.

[21] E. Stern, J. F. Klemic, D. A. Routenberg, P. N. Wyrembak, D. B. Turner-Evans, A. D. Hamilton, D. A. LaVan, T. M. Fahmy, and M. A. Reed, "Label-free immunodetection with CMOS-compatible semiconducting nanowires," *Nature*, vol. 445, pp. 519–522, Feb. 2007.

[22] R. Egger, A. Zazunov, and A. L. Yeyati, "Helical luttinger liquid in topological insulator nanowires," *Physical Review Letters*, vol. 105, p. 136403, Sept. 2010.

[23] J. H. Bardarson, P. W. Brouwer, and J. E. Moore, "Aharonov-bohm oscillations in disordered topological insulator nanowires," *Physical Review Letters*, vol. 105, p. 156803, Oct. 2010.

[24] V. Mourik, K. Zuo, S. M. Frolov, S. R. Plissard, E. P. A. M. Bakkers, and L. P. Kouwenhoven, "Signatures of majorana fermions in hybrid superconductor-semiconductor nanowire devices," *Science*, vol. 336, no. 6084, pp. 1003–1007, 2012.

[25] J. Cartwright, "Qubit in a nanowire," *Nature News*, Dec. 2010.

[26] M. E. Reimer, G. Bulgarini, N. Akopian, M. Hocevar, M. B. Bavinck, M. A. Verheijen, E. P. A. M. Bakkers, L. P. Kouwenhoven, and V. Zwiller, "Bright single-photon sources in bottom-up tailored nanowires," *Nature Communications*, vol. 3, p. 737, Mar. 2012.

[27] R. G. Hobbs, N. Petkov, and J. D. Holmes, "Semiconductor nanowire fabrication by bottom-up and top-down paradigms," *Chemistry of Materials*, vol. 24, no. 11, pp. 1975–1991, 2012.

[28] M.-C. Sun, G. Kim, J. H. Lee, H. Kim, S. W. Kim, H. W. Kim, J.-H. Lee, H. Shin, and B.-G. Park, "Patterning of Si nanowire array with electron beam lithography for sub-22 nm Si nanoelectronics technology," *Microelectronic Engineering*, vol. 110, pp. 141 – 146, 2013.

[29] A. M. Munshi, D. L. Dheeraj, V. T. Fauske, D. C. Kim, J. Huh, J. F. Reinertsen, L. Ahtapodov, K. D. Lee, B. Heidari, A. T. J. van Helvoort, B. O. Fimland, and H. Weman, "Position-controlled uniform GaAs nanowires on silicon using nanoimprint lithography," *Nano Letters*, vol. 14, no. 2, pp. 960–966, 2014.

[30] E. I. Givargizov, "Fundamental aspects of VLS growth," *Journal of Crystal Growth*, vol. 31, pp. 20–30, Dec. 1975.

[31] V. Dubrovskii, N. Sibirev, G. Cirlin, J. Harmand, and V. Ustinov, "Theoretical analysis of the vapor-liquid-solid mechanism of nanowire growth during molecular beam epitaxy," *Physical Review E*, vol. 73, Feb. 2006.

[32] M. Tchernycheva, J. C. Harmand, G. Patriarche, L. Travers, and G. E. Cirlin, "Temperature conditions for gaas nanowire formation by au-assisted molecular beam epitaxy," *Nanotechnology*, vol. 17, no. 16, p. 4025, 2006.

[33] M. Tchernycheva, L. Travers, G. Patriarche, F. Glas, J.-C. Harmand, G. E. Cirlin, and V. G. Dubrovskii, "Au-assisted molecular beam epitaxy of InAs nanowires: Growth and theoretical analysis," *Journal of Applied Physics*, vol. 102, p. 094313, Nov. 2007.

[34] G. E. Cirlin, V. G. Dubrovskii, Y. B. Samsonenko, A. D. Bouravleuv, K. Durose, Y. Y. Proskuryakov, B. Mendes, L. Bowen, M. A. Kaliteevski, R. A. Abram, and D. Zeze, "Self-catalyzed, pure zincblende GaAs nanowires grown on Si(111) by molecular beam epitaxy," *Physical Review B*, vol. 82, p. 035302, July 2010.

[35] G. E. Cirlin, V. G. Dubrovskii, I. P. Soshnikov, N. V. Sibirev, Y. B. Samsonenko, A. D. Bouravleuv, J. C. Harmand, and F. Glas, "Critical diameters and temperature domains for MBE growth of III–V nanowires on lattice mismatched substrates," *physica status solidi (RRL) - Rapid Research Letters*, vol. 3, no. 4, pp. 112–114, 2009.

[36] R. S. Wagner and W. C. Ellis, "Vapor liquid solid mechanism of single crystal growth," *Applied Physics Letters*, vol. 4, no. 5, pp. 89–90, 1964.

[37] A. I. Persson, M. W. Larsson, S. Stenström, B. J. Ohlsson, L. Samuelson, and L. R. Wallenberg, "Solid-phase diffusion mechanism for GaAs nanowire growth," *Nature Materials*, vol. 3, pp. 677–681, Oct. 2004.

[38] C. Colombo, D. Spirkoska, M. Frimmer, G. Abstreiter, and A. Fontcuberta i Morral, "Ga-assisted catalyst-free growth mechanism of GaAs nanowires by molecular beam epitaxy," *Physical Review B*, vol. 77, p. 155326, Apr. 2008.

[39] V. Consonni, A. Trampert, L. Geelhaar, and H. Riechert, "Physical origin of the incubation time of self-induced GaN nanowires," *Applied Physics Letters*, vol. 99, no. 3, p. 033102, 2011.

[40] S. Breuer, C. Pfuüller, T. Flissikowski, O. Brandt, H. T. Grahn, L. Geelhaar, and H. Riechert, "Suitability of Au- and self-assisted GaAs nanowires for optoelectronic applications," *Nano Letters*, vol. 11, pp. 1276–1279, Mar. 2011.

[41] V. Schmidt, J. V. Wittemann, S. Senz, and U. Gösele, "Silicon nanowires: A review on aspects of their growth and their electrical properties," *Advanced Materials*, vol. 21, no. 25-26, pp. 2681–2702, 2009.

[42] C. O'Regan, S. Biswas, N. Petkov, and J. D. Holmes, "Recent advances in the growth of germanium nanowires: synthesis, growth dynamics and morphology control," *J. Mater. Chem. C*, vol. 2, pp. 14–33, 2014.

[43] X. Wu, J. S. Kulkarni, G. Collins, N. Petkov, D. Almécija, J. J. Boland, D. Erts, and J. D. Holmes, "Synthesis and electrical and mechanical properties of silicon and germanium nanowires," *Chemistry of Materials*, vol. 20, no. 19, pp. 5954–5967, 2008.

[44] J. Johansson, L. S. Karlsson, C. Patrik T. Svensson, T. Mårtensson, B. A. Wacaser, K. Deppert, L. Samuelson, and W. Seifert, "Structural properties of [111] b-oriented III-V nanowires," *Nature Materials*, vol. 5, pp. 574–580, July 2006.

[45] J.-C. Harmand, F. Glas, and G. Patriarche, "Growth kinetics of a single InP(1-x)As(x) nanowire," *Physical Review B*, vol. 81, p. 235436, June 2010.

[46] E. Dimakis, J. Lahnemann, U. Jahn, S. Breuer, M. Hilse, L. Geelhaar, and H. Riechert, "Self-assisted nucleation and Vapor-Solid growth of InAs nanowires on bare si(111)," *Crystal Growth & Design*, vol. 11, pp. 4001–4008, Sept. 2011.

[47] K. Kahen, I. A. Goldthorpe, and J. Minter, "Low temperature II–VI nanowire growth using Au–Sn catalysts," *Journal of Crystal Growth*, vol. 322, no. 1, pp. 57 – 62, 2011.

[48] L. E. Greene, B. D. Yuhas, M. Law, D. Zitoun, , and P. Yang, "Solution-grown zinc oxide nanowires," *Inorganic Chemistry*, vol. 45, no. 19, pp. 7535–7543, 2006.

[49] M. Borgström, K. Deppert, L. Samuelson, and W. Seifert, "Size- and shape-controlled GaAs nano-whiskers grown by MOVPE: a growth study," *Journal of Crystal Growth*, vol. 260, no. 1-2, pp. 18 – 22, 2004.

[50] M. López and Y. Nomura, "Surface diffusion length of Ga adatoms in molecular-beam epitaxy on GaAs (100) – (110) facet structures," *Journal of Crystal Growth*, vol. 150, Part 1, pp. 68–72, May 1995.

[51] V. G. Dubrovskii, N. V. Sibirev, J. C. Harmand, and F. Glas, "Growth kinetics and crystal structure of semiconductor nanowires," *Phys. Rev. B*, vol. 78, p. 235301, Dec 2008.

[52] M. R. Ramdani, J. C. Harmand, F. Glas, G. Patriarche, and L. Travers, "Arsenic Pathways in Self-Catalyzed Growth of GaAs Nanowires," *Crystal Growth & Design*, vol. 13, pp. 91–96, Jan. 2013.

[53] P. Krogstrup, R. Popovitz-Biro, E. Johnson, M. H. Madsen, J. Nygård, and H. Shtrikman, "Structural phase control in self-catalyzed growth of GaAs nanowires on silicon (111)," *Nano Letters*, vol. 10, pp. 4475–4482, Nov. 2010.

[54] F. Glas, "Vapor fluxes on the apical droplet during nanowire growth by molecular beam epitaxy," *physica status solidi (b)*, vol. 247, pp. 254–258, Feb. 2010.

[55] V. G. Dubrovskii, V. Consonni, L. Geelhaar, A. Trampert, and H. Riechert, "Scaling growth kinetics of self-induced GaN nanowires," *Applied Physics Letters*, vol. 100, no. 15, p. 153101, 2012.

[56] J. H. Paek, T. Nishiwaki, M. Yamaguchi, and N. Sawaki, "Catalyst free MBE-VLS growth of GaAs nanowires on (111)Si substrate," *physica status solidi (c)*, vol. 6, pp. 1436–1440, June 2009.

[57] F. Glas, M. R. Ramdani, G. Patriarche, and J.-C. Harmand, "Predictive modeling of self-catalyzed III-V nanowire growth," *Physical Review B*, vol. 88, p. 195304, Nov. 2013.

[58] F. Glas, J.-C. Harmand, and G. Patriarche, "Nucleation antibunching in catalyst-assisted nanowire growth," *Physical Review Letters*, vol. 104, p. 135501, Mar. 2010.

[59] A. D. Gamalski, C. Ducati, and S. Hofmann, "Cyclic supersaturation and triple phase boundary dynamics in germanium nanowire growth," *The Journal of Physical Chemistry C*, vol. 115, no. 11, pp. 4413–4417, 2011.

[60] T. Rieger, S. Heiderich, S. Lenk, M. I. Lepsa, and D. Grützmacher, "Ga-assisted MBE growth of GaAs nanowires using thin HSQ layer," *Journal of Crystal Growth*, vol. 353, pp. 39–46, Aug. 2012.

[61] J. Johansson, K. A. Dick, P. Caroff, M. E. Messing, J. Bolinsson, K. Deppert, and L. Samuelson, "Diameter dependence of the Wurtzite–Zinc blende transition in InAs nanowires," *The Journal of Physical Chemistry C*, vol. 114, pp. 3837–3842, Mar. 2010.

[62] V. G. Dubrovskii, N. V. Sibirev, G. E. Cirlin, I. P. Soshnikov, W. H. Chen, R. Larde, E. Cadel, P. Pareige, T. Xu, B. Grandidier, J.-P. Nys, D. Stievenard, M. Moewe, L. C. Chuang, and C. Chang-Hasnain, "Gibbs-thomson and diffusion-induced contributions to the growth rate of Si, InP, and GaAs nanowires," *Phys. Rev. B*, vol. 79, p. 205316, May 2009.

[63] V. G. Dubrovskii, *Nucleation Theory and Growth of Nanostructures*. NanoScience and Technology, Berlin, Heidelberg: Springer Berlin Heidelberg, 2014.

[64] J. W. Chen and A. G. Milnes, "Energy levels in silicon," *Annual Review of Materials Science*, vol. 10, no. 1, pp. 157–228, 1980.

[65] M. J. Tambe, S. Ren, and S. Gradečak, "Effects of gold diffusion on n-type doping of GaAs nanowires," *Nano Letters*, vol. 10, pp. 4584–4589, Nov. 2010.

[66] S. Kodambaka, J. B. Hannon, R. M. Tromp, , and F. M. Ross, "Control of Si nanowire growth by oxygen," *Nano Letters*, vol. 6, no. 6, pp. 1292–1296, 2006.

[67] J. B. Hannon, S. Kodambaka, F. M. Ross, and R. M. Tromp, "The influence of the surface migration of gold on the growth of silicon nanowires," *Nature*, vol. 440, no. 7080, pp. 69–71, 2006.

[68] T. Xu, J. P. Nys, A. Addad, O. I. Lebedev, A. Urbieta, B. Salhi, M. Berthe, B. Grandidier, and D. Stiévenard, "Faceted sidewalls of silicon nanowires: Au-induced structural reconstructions and electronic properties," *Phys. Rev. B*, vol. 81, p. 115403, Mar 2010.

[69] Y. Wang, V. Schmidt, S. Senz, and U. Gösele, "Epitaxial growth of silicon nanowires using an aluminium catalyst," *Nature Nanotechnology*, vol. 1, pp. 186–189, Dec. 2006.

[70] J. Arbiol, B. Kalache, P. R. i. Cabarrocas, J. R. Morante, and A. F. i. Morral, "Influence of Cu as a catalyst on the properties of silicon nanowires synthesized by the vapour-solid-solid mechanism," *Nanotechnology*, vol. 18, p. 305606, Aug. 2007.

[71] Q. Tang, X. Liu, T. I. Kamins, G. S. Solomon, and J. S. Harris, "Nucleation of ti-catalyzed self-assembled kinked si nanowires grown by gas source MBE," *Journal of Crystal Growth*, vol. 251, pp. 662–665, Apr. 2003.

[72] A. Fontcuberta i Morral, C. Colombo, G. Abstreiter, J. Arbiol, and J. R. Morante, "Nucleation mechanism of gallium-assisted molecular beam epitaxy growth of gallium arsenide nanowires," *Applied Physics Letters*, vol. 92, no. 6, p. 063112, 2008.

[73] M. Heiß, A. Gustafsson, S. Conesa-Boj, F. Peiró, J. R. Morante, G. Abstreiter, J. Arbiol, L. Samuelson, and A. F. i. Morral, "Catalyst-free nanowires with axial InxGa1-xAs/GaAs heterostructures," *Nanotechnology*, vol. 20, p. 075603, Feb. 2009.

[74] B. Mandl, J. Stangl, T. Martensson, A. Mikkelsen, J. Eriksson, L. S. Karlsson, G. Bauer, L. Samuelson, and W. Seifert, "Au-free epitaxial growth of InAs nanowires," *Nano Letters*, vol. 6, pp. 1817–1821, Aug. 2006.

[75] B. Mandl, J. Stangl, E. Hilner, A. A. Zakharov, K. Hillerich, A. W. Dey, L. Samuelson, G. Bauer, K. Deppert, and A. Mikkelsen, "Growth mechanism of self-catalyzed group III-V nanowires," *Nano Letters*, vol. 10, pp. 4443–4449, Nov. 2010.

[76] F. Jabeen, V. Grillo, S. Rubini, and F. Martelli, "Self-catalyzed growth of GaAs nanowires on cleaved Si by molecular beam epitaxy," *Nanotechnology*, vol. 19, p. 275711, July 2008.

[77] S. Plissard, K. A. Dick, G. Larrieu, S. Godey, A. Addad, X. Wallart, and P. Caroff, "Gold-free growth of GaAs nanowires on silicon: arrays and polytypism," *Nanotechnology*, vol. 21, p. 385602, Sept. 2010.

[78] B. Mandl, A. W. Dey, J. Stangl, M. Cantoro, L.-E. Wernersson, G. Bauer, L. Samuelson, K. Deppert, and C. Thelander, "Self-seeded, position-controlled InAs nanowire growth on Si: A growth parameter study," *Journal of Crystal Growth*, vol. 334, pp. 51–56, Nov. 2011.

[79] F. Matteini, G. z. Tütüncüoğlu, D. Rüffer, E. Alarcøn-Lladø, and A. Fontcuberta i Morral, "Ga-assisted growth of GaAs nanowires on silicon, comparison of surface SiOx of different nature," *Journal of Crystal Growth*, vol. 404, pp. 246–255, Oct. 2014.

[80] F. Matteini, G. Tütüncüoglu, H. Potts, F. Jabeen, and A. Fontcuberta i Morral, "Wetting of Ga on SiOx and Its Impact on GaAs Nanowire Growth," *Crystal Growth & Design*, vol. 15, pp. 3105–3109, July 2015.

[81] P. Krogstrup, S. Curiotto, E. Johnson, M. Aagesen, J. Nygård, and D. Chatain, "Impact of the liquid phase shape on the structure of III-V nanowires," *Phys. Rev. Lett.*, vol. 106, p. 125505, Mar 2011.

[82] D. S. Oliveira, L. H. G. Tizei, D. Ugarte, and M. A. Cotta, "Spontaneous periodic diameter oscillations in InP nanowires: The role of interface instabilities," *Nano Letters*, vol. 13, no. 1, pp. 9–13, 2013.

[83] T. Rieger, M. I. Lepsa, T. Schäpers, and D. Grützmacher, "Controlled wurtzite inclusions in self-catalyzed zinc blende III-V semiconductor nanowires," *Journal of Crystal Growth*, vol. 378, pp. 506–510, Sept. 2013.

[84] C. García Núñez, A. F. Braña, J. L. Pau, D. Ghita, B. J. García, G. Shen, D. S. Wilbert, S. M. Kim, and P. Kung, "Pure zincblende GaAs nanowires grown by Ga-assisted chemical beam epitaxy," *Journal of Crystal Growth*, vol. 372, pp. 205–212, June 2013.

[85] S.-G. Ihn, , J.-I. Song*, T.-W. Kim, D.-S. Leem, , T. Lee, S.-G. Lee, E. K. Koh, , and K. Song, "Morphology- and orientation-controlled gallium arsenide nanowires on silicon substrates," *Nano Letters*, vol. 7, no. 1, pp. 39–44, 2007.

[86] S. Breuer, *Molecular Beam Epitaxy of GaAs Nanowires and their Suitability for Optoelectronic Applications*. Dissertation, Humboldt-Universität zu Berlin, 2011.

[87] P. Krogstrup, H. I. Jørgensen, E. Johnson, M. H. Madsen, C. B. Sørensen, A. F. i Morral, M. Aagesen, J. Nygård, and F. Glas, "Advances in the theory of III–V nanowire growth dynamics," *Journal of Physics D: Applied Physics*, vol. 46, no. 31, p. 313001, 2013.

[88] P. Caroff, J. Bolinsson, and J. Johansson, "Crystal phases in III–V nanowires: From random toward engineered polytypism," *Selected Topics in Quantum Electronics, IEEE Journal of*, vol. 17, pp. 829–846, July 2011.

[89] F. Bastiman, H. Küpers, C. Somaschini, and L. Geelhaar, "Growth map for Ga-assisted growth of GaAs nanowires on Si(111) substrates by molecular beam epitaxy," *Nanotechnology*, vol. 27, no. 9, p. 095601, 2016.

[90] A. Biermanns, E. Dimakis, A. Davydok, T. Sasaki, L. Geelhaar, M. Takahasi, and U. Pietsch, "Role of liquid indium in the structural purity of wurtzite InAs nanowires that grow on si(111)," *Nano Letters*, vol. 14, no. 12, pp. 6878–6883, 2014.

[91] M. Koguchi, H. Kakibayashi, M. Yazawa, K. Hiruma, and T. Katsuyama, "Crystal Structure Change of GaAs and InAs Whiskers from Zinc-Blende to Wurtzite Type," *Japanese Journal of Applied Physics*, vol. 31, p. 2061, July 1992.

[92] A. Biermanns, *X-ray diffraction from single GaAs nanowires*. Dissertation, Universität Siegen, 2012.

[93] M. Köhl, *Analysis of nanostructures based on diffraction of X-ray radiation*. Dissertation, Karlsruhe Institute of Technology, 2014.

[94] N. Ashcroft and N. Mermin, *Festkörperphysik*. Oldenbourg Wissenschaftsverlag, 2007.

[95] C. Kittel and S. Hunklinger, *Einführung in die Festkörperphysik*. Oldenbourg Wissenschaftsverlag, 2013.

[96] C.-Y. Yeh, Z. W. Lu, S. Froyen, and A. Zunger, "Zinc-blende-wurtzite polytypism in semiconductors," *Phys. Rev. B*, vol. 46, pp. 10086–10097, Oct 1992.

[97] C. Panse, D. Kriegner, and F. Bechstedt, "Polytypism of GaAs, InP, InAs, and InSb: An *ab initio* study," *Phys. Rev. B*, vol. 84, p. 075217, Aug 2011.

[98] S. O. Mariager, S. L. Lauridsen, C. B. Sörensen, A. Dohn, P. R. Willmott, J. Nygård, and R. Feidenhansl, "Stages in molecular beam epitaxy growth of GaAs nanowires studied by x-ray diffraction," *Nanotechnology*, vol. 21, no. 11, p. 115603, 2010.

[99] M. I. McMahon and R. J. Nelmes, "Observation of a wurtzite form of gallium arsenide," *Phys. Rev. Lett.*, vol. 95, p. 215505, Nov 2005.

[100] A. Biermanns, S. Breuer, A. Davydok, L. Geelhaar, and U. Pietsch, "Structural evolution of self-assisted GaAs nanowires grown on Si(111)," *physica status solidi (RRL) - Rapid Research Letters*, vol. 5, no. 4, pp. 156–158, 2011.

[101] K. A. Dick, P. Caroff, J. Bolinsson, M. E. Messing, J. Johansson, K. Deppert, L. R. Wallenberg, and L. Samuelson, "Control of III-V nanowire crystal structure by growth parameter tuning," *Semiconductor Science and Technology*, vol. 25, p. 024009, Feb. 2010.

[102] K. A. Dick, J. Bolinsson, M. E. Messing, S. Lehmann, J. Johansson, and P. Caroff, "Parameter space mapping of InAs nanowire crystal structure," *Journal of Vacuum Science & Technology B*, vol. 29, p. 04D103, July 2011.

[103] T. Akiyama, K. Sano, K. Nakamura, and T. Ito, "An Empirical Potential Approach to Wurtzite-Zinc-Blende Polytypism in Group III-V Semiconductor Nanowires," *Japanese Journal of Applied Physics*, vol. 45, no. 9, pp. L275–L278, 2006.

[104] R. Magri, M. Rosini, and F. Casetta, "Structural stability of clean GaAs nanowires grown along the [111] direction," *physica status solidi (c)*, vol. 7, no. 2, pp. 374–377, 2010.

[105] M. Rosini and R. Magri, "Surface Effects on the Atomic and Electronic Structure of Unpassivated GaAs Nanowires," *ACS Nano*, vol. 4, pp. 6021–6031, Oct. 2010.

[106] J. Johansson, L. S. Karlsson, K. A. Dick, J. Bolinsson, B. A. Wacaser, K. Deppert, and L. Samuelson, "Effects of supersaturation on the crystal structure of gold seeded III-V nanowires," *Crystal Growth & Design*, vol. 9, pp. 766–773, Feb. 2009.

[107] F. Glas, J.-C. Harmand, and G. Patriarche, "Why does wurtzite form in nanowires of III-V zinc blende semiconductors?," *Physical Review Letters*, vol. 99, p. 146101, Oct. 2007.

[108] S. Breuer, L.-F. Feiner, and L. Geelhaar, "Droplet Bulge Effect on the Formation of Nanowire Side Facets," *Crystal Growth & Design*, vol. 13, pp. 2749–2755, July 2013.

[109] M. Schmidbauer, *X-Ray Diffuse Scattering from Self-Organized Mesoscopic Semiconductor Structures*. Springer Tracts in Modern Physics, Berlin, Heidelberg: Springer Berlin Heidelberg, 2004.

[110] U. Pietsch, V. Holy, and T. Baumbach, *High-Resolution X-Ray Scattering*. Berlin, Heidelberg: Springer-Verlag New York, 2004.

[111] J. Johansson, J. Bolinsson, M. Ek, P. Caroff, and K. A. Dick, "Combinatorial approaches to understanding polytypism in III-V nanowires," *ACS Nano*, vol. 6, no. 7, pp. 6142–6149, 2012.

[112] M. Köhl, P. Schroth, and T. Baumbach, "Perspectives and limitations of symmetric X-ray Bragg reflections for inspecting polytypism in nanowires," *Journal of Synchrotron Radiation*, vol. 23, pp. 487–500, Mar 2016.

[113] P. Schroth, M. Köhl, J.-W. Hornung, E. Dimakis, C. Somaschini, L. Geelhaar, A. Biermanns, S. Bauer, S. Lazarev, U. Pietsch, and T. Baumbach, "Evolution of polytypism in gaas nanowires during growth revealed by time-resolved *in situ* x-ray diffraction," *Phys. Rev. Lett.*, vol. 114, p. 055504, Feb 2015.

[114] T. Slobodskyy, P. Schroth, D. Grigoriev, A. A. Minkevich, D. Z. Hu, D. M. Schaadt, and T. Baumbach, "A portable molecular beam epitaxy system for in situ x-ray investigations at synchrotron beamlines," *Review of Scientific Instruments*, vol. 83, pp. 105112–105112–7, Oct. 2012.

[115] P. Schroth, T. Slobodskyy, D. Grigoriev, A. Minkevich, M. Riotte, S. Lazarev, E. Fohtung, D. Hu, D. Schaadt, and T. Baumbach, "Investigation of buried quantum dots using grazing incidence x-ray diffraction," *Materials Science and Engineering: B*, vol. 177, no. 10, pp. 721 – 724, 2012.

[116] M. Helfrich, P. Schroth, D. Grigoriev, S. Lazarev, R. Felici, T. Slobodskyy, T. Baumbach, and D. M. Schaadt, "Growth and characterization of site-selective quantum dots," *physica status solidi (a)*, vol. 209, no. 12, pp. 2387–2401, 2012.

[117] P. Krogstrup, M. Hannibal Madsen, W. Hu, M. Kozu, Y. Nakata, J. Nygård, M. Takahasi, and R. Feidenhansl, "In-situ x-ray characterization of wurtzite formation in GaAs nanowires," *Applied Physics Letters*, vol. 100, no. 9, pp. –, 2012.

[118] M. Takahasi, M. Kozu, T. Sasaki, and W. Hu, "Mechanisms determining the structure of gold-catalyzed GaAs nanowires studied by in situ x-ray diffraction," *Crystal Growth & Design*, vol. 15, no. 10, pp. 4979–4985, 2015.

[119] F. Matteini, G. z. Tütüncüoğlu, D. Rüffer, E. Alarcøn-Lladø, and A. Fontcuberta i Morral, "Untangling the role of oxide in Ga-assisted growth of GaAs nanowires on Si substrates," *arXiv preprint arXiv:1307.6113*, 2013.

[120] A. Wolkenberg, "A mechanism for the effect of doping on the silicon native oxide thickness," *physica status solidi (a)*, vol. 79, no. 1, pp. 313–322, 1983.

[121] C. Okada, H. Kobayashi, I. Takahashi, J. Ryuta, and T. Shingyouji, "Growth of native oxide and accumulation of organic matter on bare Si wafer in air," *Japanese Journal of Applied Physics*, vol. 32, no. 8A, p. L1031, 1993.

[122] M. H. Madsen, M. Aagesen, P. Krøgstrup, C. Sørensen, and J. Nygård, "Influence of the oxide layer for growth of self-assisted InAs nanowires on Si(111)," *Nanoscale Research Letters*, vol. 6, p. 516, Aug. 2011.

[123] S. Plissard, G. Larrieu, X. Wallart, and P. Caroff, "High yield of self-catalyzed GaAs nanowire arrays grown on silicon via gallium droplet positioning," *Nanotechnology*, vol. 22, p. 275602, July 2011.

[124] T. Rieger, S. Heiderich, S. Lenk, M. I. Lepsa, and D. Grützmacher, "Ga-assisted MBE growth of GaAs nanowires using thin HSQ layer," *Journal of Crystal Growth*, vol. 353, pp. 39–46, Aug. 2012.

[125] Z. Y. AbuWaar, Z. M. Wang, J. H. Lee, and G. J. Salamo, "Observation of Ga droplet formation on (311)A and (511)A GaAs surfaces," *Nanotechnology*, vol. 17, p. 4037, Aug. 2006.

[126] J. H. Lee, Z. M. Wang, and G. J. Salamo, "Observation of change in critical thickness of In droplet formation on GaAs(100)," *Journal of Physics: Condensed Matter*, vol. 19, p. 176223, Apr. 2007.

[127] M.-Y. Li, Y. Hirono, S. D. Koukourinkova, M. Sui, S. Song, E.-S. Kim, J. Lee, and G. J. Salamo, "Formation of Ga droplets on patterned GaAs (100) by molecular beam epitaxy," *Nanoscale Research Letters*, vol. 7, p. 550, Oct. 2012.

[128] S. Wright and H. Kroemer, "Reduction of oxides on silicon by heating in a gallium molecular beam at 800 °C," *Applied Physics Letters*, vol. 36, pp. 210–211, Feb. 1980.

[129] C. N. Cochran and L. M. Foster, "Vapor Pressure of Gallium, Stability of Gallium Suboxide Vapor, and Equilibria of Some Reactions Producing Gallium Suboxide Vapor," *Journal of The Electrochemical Society*, vol. 109, pp. 144–148, Feb. 1962.

[130] A. J. SpringThorpe, S. J. Ingrey, B. Emmerstorfer, P. Mandeville, and W. T. Moore, "Measurement of GaAs surface oxide desorption temperatures," *Applied Physics Letters*, vol. 50, no. 2, p. 77, 1987.

[131] J. Drelich, "The Effect of Drop (Bubble) Size on Contact Angle at Solid Surfaces," *The Journal of Adhesion*, vol. 63, pp. 31–51, June 1997.

[132] J.-Y. Park, M.-Y. Ha, H.-J. Choi, S.-D. Hong, and H.-S. Yoon, "A study on the contact angles of a water droplet on smooth and rough solid surfaces," *Journal of Mechanical Science and Technology*, vol. 25, pp. 323–332, Mar. 2011.

[133] A. Calvimontes, *Thermodynamic equilibrium in the wetting of rough surfaces: on the role of the topography in the formation of energy barriers of wetting and the prediction of metastable equilibrium regions and apparent contact angles on hydrophilic and hydrophobic surfaces.* Raeligh, NC: Lulu Press, 2014.

[134] T. Young, "An Essay on the Cohesion of Fluids," *Philosophical Transactions of the Royal Society of London*, vol. 95, pp. 65–87, Jan. 1805.

[135] V. Veselovsky and V. N. Pertzov *Phys. Chem. USSR.*, vol. 8, p. 5, 1936.

[136] L. Boruvka and A. Neumann *J. Chem. Phys.*, vol. 66, p. 5464, 1977.

[137] S. C. Hardy, "The surface tension of liquid gallium," *Journal of Crystal Growth*, vol. 71, pp. 602–606, May 1985.

[138] M. Schrader, P. Virnau, and K. Binder, "Simulation of vapor-liquid coexistence in finite volumes: A method to compute the surface free energy of droplets," *Physical Review E*, vol. 79, June 2009.

[139] V. Veselovsky and V. N. Pertzov *J. Chem. Phys.*, vol. 17, p. 333, 1949.

[140] T. F. Nonnenmacher, "Size effect on surface tension of small droplets," *Chemical Physics Letters*, vol. 47, no. 3, pp. 507–508, 1977.

[141] M. C. Plante and R. R. LaPierre, "Control of GaAs nanowire morphology and crystal structure," *Nanotechnology*, vol. 19, p. 495603, Dec. 2008.

[142] G. Priante, S. Ambrosini, V. G. Dubrovskii, A. Franciosi, and S. Rubini, "Stopping and Resuming at Will the Growth of GaAs Nanowires," *Crystal Growth & Design*, vol. 13, pp. 3976–3984, Sept. 2013.

[143] M. Heiß, E. Riedlberger, D. Spirkoska, M. Bichler, G. Abstreiter, and A. F. i. Morral, "Growth mechanisms and optical properties of GaAs-based semiconductor microstructures by selective area epitaxy," *Journal of Crystal Growth*, vol. 310, pp. 1049–1056, Mar. 2008.

[144] S. Koshiba, Y. Nakamura, M. Tsuchiya, H. Noge, H. Kano, Y. Nagamune, T. Noda, and H. Sakaki, "Surface diffusion processes in molecular beam epitaxial growth of GaAs and AlAs as studied on GaAs (001) – (111)B facet structures," *Journal of Applied Physics*, vol. 76, pp. 4138–4144, Oct. 1994.

[145] V. G. Dubrovskii, T. Xu, A. D. Álvarez, S. R. Plissard, P. Caroff, F. Glas, and B. Grandidier, "Self-Equilibration of the Diameter of Ga-Catalyzed GaAs Nanowires," *Nano Letters*, July 2015.

[146] C. Somaschini, S. Bietti, A. Trampert, U. Jahn, C. Hauswald, H. Riechert, S. Sanguinetti, and L. Geelhaar, "Control over the Number Density and Diameter of GaAs Nanowires on Si(111) Mediated by Droplet Epitaxy," *Nano Letters*, vol. 13, pp. 3607–3613, Aug. 2013.

[147] R. Wagner and W. Ellis, *Vapor-liquid-solid mechanism of crystal growth and its application to silicon*. Bell Telephone Laboratories, 1965.

[148] M. H. Huang, Y. Wu, H. Feick, N. Tran, E. Weber, and P. Yang, "Catalytic Growth of Zinc Oxide Nanowires by Vapor Transport," *Advanced Materials*, vol. 13, pp. 113–116, Jan. 2001.

[149] N. V. Sibirev, M. Tchernycheva, M. A. Timofeeva, J.-C. Harmand, G. E. Cirlin, and V. G. Dubrovskii, "Influence of shadow effect on the growth and shape of InAs nanowires," *Journal of Applied Physics*, vol. 111, p. 104317, May 2012.

[150] S. J. Gibson, *Ga-Assisted Nanowire Growth on Nano-Patterned Silicon*. PhD thesis, 2015.

[151] M. Moseler, F. Cervantes-Sodi, S. Hofmann, G. Csányi, and A. C. Ferrari, "Dynamic catalyst restructuring during carbon nanotube growth," *ACS Nano*, vol. 4, no. 12, pp. 7587–7595, 2010.

[152] V. A. Nebol'sin, A. A. Shchetinin, A. A. Dolgachev, and V. V. Korneeva, "Effect of the Nature of the Metal Solvent on the Vapor-Liquid-Solid Growth Rate of Silicon Whiskers," *Inorganic Materials*, vol. 41, pp. 1256–1259, Dec. 2005.

[153] N. Moll, A. Kley, E. Pehlke, and M. Scheffler, "GaAs equilibrium crystal shape from first principles," *Physical Review B*, vol. 54, pp. 8844–8855, Sept. 1996.

[154] V. G. Dubrovskii and N. V. Sibirev, "Growth thermodynamics of nanowires and its application to polytypism of zinc blende III-V nanowires," *Physical Review B*, vol. 77, p. 035414, Jan. 2008.

[155] U. König and W. Keck, "Contact Angles Between III-V Melts and Several Substrates," *Journal of The Electrochemical Society*, vol. 130, pp. 685–686, Mar. 1983.

[156] M. Köhl, P. Schroth, A. A. Minkevich, J.-W. Hornung, E. Dimakis, C. Somaschini, L. Geelhaar, T. Aschenbrenner, S. Lazarev, D. Grigoriev, U. Pietsch, and T. Baumbach, "Polytypism in GaAs nanowires: determination of the interplanar spacing of wurtzite GaAs by X-ray diffraction," *Journal of Synchrotron Radiation*, vol. 22, pp. 67–75, Jan 2015.

[157] S. Bauer. private communication, 2012.

[158] A. Davydok, S. Breuer, A. Biermanns, L. Geelhaar, and U. Pietsch, "Lattice parameter accommodation between GaAs(111) nanowires and si(111) substrate after growth via au-assisted molecular beam epitaxy," *Nanoscale Research Letters*, vol. 7, p. 109, Feb. 2012.

[159] A. Biermanns, S. Breuer, A. Davydok, L. Geelhaar, and U. Pietsch, "Structural polytypism and residual strain in GaAs nanowires grown on Si(111) probed by single-nanowire X-ray diffraction," *Journal of Applied Crystallography*, vol. 45, pp. 239–244, Apr 2012.

[160] M. W. Larsson, J. B. Wagner, M. Wallin, P. Hakansson, L. E. Fröberg, L. Samuelson, and L. R. Wallenberg, "Strain mapping in free-standing heterostructured wurtzite InAs/InP nanowires," *Nanotechnology*, vol. 18, no. 1, p. 015504, 2007.

[161] A. Biermanns, S. Breuer, A. Trampert, A. Davydok, L. Geelhaar, and U. Pietsch, "Strain accommodation in Ga–assisted GaAs nanowires grown on silicon (111)," *Nanotechnology*, vol. 23, no. 30, p. 305703, 2012.

[162] M. Yamaguchi, J.-H. Paek, and H. Amano, "Probability of twin formation on self-catalyzed GaAs nanowires on Si substrate," *Nanoscale Research Letters*, vol. 7, p. 558, Oct. 2012.

[163] I. Soshnikov, G. Cirlin, A. Tonkikh, Y. Samsonenko, V. Dubovskii, V. Ustinov, O. Gorbenko, D. Litvinov, and D. Gerthsen, "Atomic structure of MBE-grown GaAs nanowhiskers," *Physics of the Solid State*, vol. 47, no. 12, pp. 2213–2218, 2005.

[164] D. Spirkoska, J. Arbiol, A. Gustafsson, S. Conesa-Boj, F. Glas, I. Zardo, M. Heigoldt, M. H. Gass, A. L. Bleloch, S. Estrade, M. Kaniber, J. Rossler, F. Peiro, J. R. Morante, G. Abstreiter, L. Samuelson, and A. Fontcuberta i Morral, "Structural and optical properties of high quality zinc-blende/wurtzite GaAs nanowire heterostructures," *Physical Review B*, vol. 80, p. 245325, Dec. 2009.

[165] P. Caroff, J. Bolinsson, and J. Johansson, "Crystal phases in III-V nanowires: From random toward engineered polytypism," *IEEE Journal of Selected Topics in Quantum Electronics*, vol. 17, no. 4, pp. 829–846, 2011.

[166] A. D. Gamalski, J. Tersoff, R. Sharma, C. Ducati, and S. Hofmann, "Metastable crystalline AuGe catalysts formed during isothermal germanium nanowire growth," *Phys. Rev. Lett.*, vol. 108, p. 255702, Jun 2012.

[167] V. Pankoke, S. Sakong, and P. Kratzer, "Role of sidewall diffusion in GaAs nanowire growth: A first-principles study," *Physical Review B*, vol. 86, p. 085425, Aug. 2012.

[168] G. Priante, J.-C. Harmand, G. Patriarche, and F. Glas, "Random stacking sequences in III-V nanowires are correlated," *Phys. Rev. B*, vol. 89, p. 241301, Jun 2014.

[169] P. Scherrer *Göttinger Nachrichten Gesell*, vol. 2, p. 98, 1918.

[170] A. Patterson, "The scherrer formula for x-ray particle size determination," *Phys. Rev.*, vol. 56, no. 10, pp. 978–982, 1939.

[171] A. Biermanns, A. Davydok, H. Paetzelt, A. Diaz, V. Gottschalch, T. H. Metzger, and U. Pietsch, "Individual GaAs nanorods imaged by coherent X-ray diffraction," *Journal of Synchrotron Radiation*, vol. 16, pp. 796–802, Nov 2009.

[172] J. Tersoff, "Stable Self-Catalyzed Growth of III–V Nanowires," *Nano Letters*, vol. 15, pp. 6609–6613, Oct. 2015.

[173] V. G. Dubrovskii, T. Xu, A. D. Álvarez, S. R. Plissard, P. Caroff, F. Glas, and B. Grandidier, "Self-Equilibration of the Diameter of Ga-Catalyzed GaAs Nanowires," *Nano Letters*, July 2015.

[174] K. W. Schwarz and J. Tersoff, "From droplets to nanowires: Dynamics of vapor-liquid-solid growth," *Phys. Rev. Lett.*, vol. 102, p. 206101, May 2009.

Danksagung - Acknowledgements

Ich danke Prof. Dr. Tilo Baumbach und Prof. Dr. Ullrich Pietsch, welche diese Arbeit betreut und über all die Jahre begleitet haben, für ihre Förderung und Unterstützung. Für die gute Zusammenarbeit danke ich, stellvertretend für alle meine Kollegen am IPS, Anton Plech, Svetoslav Stankov und Bärbel Krause, auf deren Rat und Unterstützung ich mich immer verlassen konnte. Des weiteren möchte ich mich bei Hans Gräfe für seine Hilfe bei technischen Angelegenheiten im UHV-Labor bedanken. Annette Weißhardt danke ich für ihre Unterstützung im Chemielabor.

Ich danke Thomas Keller am Nanolab (DESY) für die Hilfe bei elektronenmikroskopischen Messungen, sowie Sondes Bauer und Jörg Strempfer für die Unterstützung während der Messungen an den Strahlrohren NANO bei ANKA und P09 bei DESY. Darüber hinaus möchte ich mich bei Emmanouil Dimakis und Lutz Geelhar für ihre Unterstützung am Paul-Drude-Institut für Festkörperelektronik in Berlin bedanken.

Besonderer Dank gilt meinem guten Freund Martin Köhl, der mir in unzähligen abendfüllenden Diskussionen, und durch seine konstruktive Kritik stets weitergeholfen hat.

Ganz besonders danke ich meiner Familie und Nathalie, für einfach alles.

Teile dieser Arbeit wurden durch das *Bundesministerium für Bildung und Forschung* (BMBF) innerhalb der Projekte 05ES7CK, und 05K13PS3 gefördert.

Parts of this work have been supported by the *Bundesministerium für Bildung und Forschung* (BMBF) within the research projects 05ES7CK, and 05K13PS3.

Hiermit bestätige ich, dass ich die vorliegende Arbeit selbstständig und nur unter Verwendung der angegebenen Literatur und Hilfsmittel angefertigt habe.

Siegen, den 19. Juli 2016 Philipp Schroth